

UNCLASSIFIED

AD NUMBER

AD893825

NEW LIMITATION CHANGE

TO

Approved for public release, distribution
unlimited

FROM

Distribution authorized to U.S. Gov't.
agencies only; Test and Evaluation; APR
1972. Other requests shall be referred to
Air Force Flight Dynamics Lab.,
Wright-Patterson AFB, OH 45433.

AUTHORITY

AFFDL ltr, 13 Mar 1981

THIS PAGE IS UNCLASSIFIED

AFFDL-TR-71-5

Part II, Vol. I

62

AD 893825

SUBSONIC UNSTEADY AERODYNAMICS FOR GENERAL CONFIGURATIONS

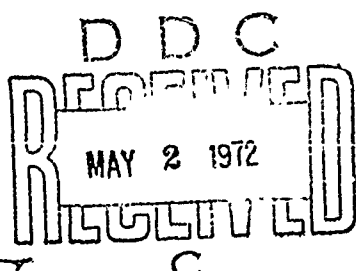
PART II

VOLUME I. APPLICATION OF THE DOUBLET-LATTICE METHOD AND THE
METHOD OF IMAGES TO LIFTING-SURFACE/BODY INTERFERENCE

J. P. GIESING
T. P. KALMAN
W. P. RODDEN

TECHNICAL REPORT AFFDL-TR-71-5, PART II, VOLUME I

APRIL 1972



Distribution limited to U.S. Government agencies only; test and evaluation; statement applied in September 1971. Other requests for this document must be referred to AF Flight Dynamics Laboratory, (FY), Wright-Patterson AFB, Ohio 45433.

AIR FORCE FLIGHT DYNAMICS LABORATORY
AIR FORCE SYSTEMS COMMAND
WRIGHT-PATTERSON AIR FORCE BASE, OHIO

NOTICE

When Government drawings, specifications, or other data are used for any purpose other than in connection with a definitely related Government procurement operation, the United States Government thereby incurs no responsibility nor any obligation whatsoever; and the fact that the government may have formulated, furnished, or in any way supplied the said drawings, specifications, or other data, is not to be regarded by implication or otherwise as in any manner licensing the holder or any other person or corporation, or conveying any rights or permission to manufacture, use, or sell any patented invention that may in any way be related thereto.

ACCESSION for	
CGSTI	WHITE SECTION <input type="checkbox"/>
DDG	BUFF SECTION <input checked="" type="checkbox"/>
UNANNOUNCED	<input type="checkbox"/>
JUSTIFICATION	
.....	
BY	
DISTRIBUTOR/AVAILABILITY CODES	
DIST.	AVAIL. and/or SPECIAL
<i>B</i>	

Copies of this report should not be returned unless return is required by security considerations, contractual obligations, or notice on a specific document.

6

SUBSONIC UNSTEADY AERODYNAMICS FOR GENERAL CONFIGURATIONS

PART II.

VOLUME I. APPLICATION OF THE DOUBLET-LATTICE METHOD AND THE METHOD OF IMAGES TO LIFTING-SURFACE/BODY INTERFERENCE.

(1) Tasks init rpt. Dec 69-Aug 71,

(11) Apr 72

(12) 255 p.

(15) F-36R-7Ae-117

1370

137223

JOSEPH
TEIGER
WILLIAMS
10
Y.P. GIESING,
Y.P. KALMAN
Y.P. RODDEN

PLM 102-147-525L (Pt 1 V2)

(14) MDG-JD944-Pt 2-V1 1

(18) AFFDL

TR-71-5-Pt-2-V1-1

Distribution limited to U.S. Government agencies only; test and evaluation; statement applied in September 1971. Other requests for this document must be referred to AF Flight Dynamics Laboratory, (FY), Wright-Patterson AFB, Ohio 45433.

198
11/71

FOREWORD

This report was prepared by the Douglas Aircraft Company, Aircraft Division, Long Beach, California, for the Aerospace Dynamics Branch, Vehicle Dynamics Division, Air Force Flight Dynamics Laboratory, Wright-Patterson Air Force Base, Ohio under contract F33615-70-C-1167. This research was conducted under Project 1370, "Dynamic Problems in Military Flight Vehicles," and Task 137003, "Prevention of Dynamic Aeroelastic Instabilities in Advanced Military Aircraft." Mr. S. J. Pollock of the Aerospace Dynamics Branch was Task Engineer.

This report consists of two parts with two volumes for each part. This volume, Volume I of Part II, contains a method which uses an image system and an axial singularity system to account for the effects of the bodies. Volume I of Part I contains the method of direct application of nonplanar lifting surface elements, Volume II of Part I is the Computer Program H7WC, and Volume II of Part II is the Computer Program NCKA. The volumes containing the computer programs are available upon request from the Air Force Flight Dynamics Laboratory/FY, Wright-Patterson AFB, Ohio 45433.

The work reported herein was conducted during the period of December 1969 to August 1971.

The Principal Investigator was Joseph P. Giesing. Mrs. T. P. Kalman was responsible for the computer programming and Dr. W. P. Rodden was a McDonnell Douglas Company Consultant. Others have made significant contributions to this project including Messrs. D. H. Larson, D. S. Warren, and W. E. Henry.

The contractor's designation of this report is MDC-J0944. The report was released by the authors in August 1971 for publication as an AFFDL Technical Report.

This technical report has been reviewed and is approved.

16, 1971
WALTER J. MYKYTOW
Asst. for Research & Technology
Vehicle Dynamics Division

ABSTRACT

A technique for predicting steady and oscillatory aerodynamic loads on general configurations has been developed which is based on the Doublet-Lattice Method and the method of images. Chord- and spanwise loading on lifting surfaces and longitudinal body load distributions are determined. Configurations may be composed of an assemblage of bodies (elliptic cross sections and a distribution of width or radius) and lifting surfaces (arbitrary planform and dihedral, with or without control surfaces). Loadings predicted by this method are required for flutter, gust, frequency response and static aeroelastic analyses and may be used to determine static and dynamic stability derivatives. Volume I presents the theory and calculated results while Volume II presents the details of the computer program used to implement the theory.

CONTENTS

	Page
1.0 INTRODUCTION	1
2.0 THEORETICAL DEVELOPMENT	4
2.1 Outline of the Problem and Solution	4
2.2 The Normalwash Boundary Conditions	9
2.2.1 Polynomial Modes	9
2.2.2 Numerical Input	11
2.2.3 Aerodynamic Influence Coefficients	12
2.3 The Lifting Surface	12
2.4 The Isolated Body	16
2.4.1 Axial Singularity Strength Using Slender Body Theory	21
2.4.2 Far Field Representation	26
2.4.3 Matrix Representation	30
2.5 Interference	32
2.5.1 The Method of Images	32
2.5.2 The Method of Images for Circular Cross Sections	34
2.5.3 The Method of Images for Noncircular Cross Sections	36
2.5.4 The Method of Images for Unsteady Flow	40
2.5.5 Formation of the Influence Matrix With Images . .	42
2.5.6 The Residual Interference Flow	45
2.5.7 The Use of Surface Singularities for the Residual Interference Flow	53
2.5.8 The Image System for Wing-tail Configurations . .	54
2.6 Body Force and Moment Distributions	57
2.6.1 Reduction of All Singularity Distributions to Pressure Doublet Distributions	58
2.6.2 Calculation of Force and Moment on a Body in the Presence of a Point Pressure Doublet . .	62
2.6.3 Effects of Symmetry, Ground Effect and Images . .	73
2.6.4 Redistribution of Body Loads for Alternate II . .	76

CONTENTS (Cont.)

	Page
2.7 Generalized Forces and Aerodynamic Parameters	77
2.7.1 Generalized Forces	77
2.7.2 Aerodynamic Parameters	79
3.0 CALCULATED RESULTS	82
3.1 Parameter Variation Studies	82
3.1.1 The Effect of Body Radius	82
3.1.2 The Effect of Cross Sectional Shape	82
3.1.3 The Effects of Frequency	83
3.1.4 A High-Wing Configuration	84
3.1.5 End Plating Effects	85
3.1.6 The Effect of Pick-up Point Location	86
3.2 Correlation of the Present Method with Other Methods and Experimental Data	86
3.2.1 Wing-Fuselage Combinations (Emphasis on Wing Loads)	86
3.2.2 Wing-Fuselage Combinations (Emphasis on Fuselage Loads)	88
3.3 T-tail Fuselage Combinations	92
3.4 Wing and Tip Mounted Nacelle Combination	93
3.5 Wing-Nacelle-Fuselage Combination	98
4.0 CONCLUSIONS AND RECOMMENDATIONS	101
4.1 Conclusions	101
4.2 Recommendations for Further Work	104
REFERENCES	107
APPENDIX A Basic Singularities	176
APPENDIX B Discretization of Surface and Axial Integrals . . .	184
APPENDIX C Image Points	189
APPENDIX D Longitudinal Integration of the Surface Pressure, on a Body of Arbitrary Cross Section, for Force and Moment	196

CONTENTS (Cont.)

	Page
APPENDIX E Numerical Evaluation of the Force and Moment Integrals for Bodies of Elliptic Cross Section	205
APPENDIX F Evaluation of the Steady Lift For Circular Cross Sections	215
APPENDIX G Circumferential Integration of the Pressure for Bodies of Circular Cross Section in Both Steady and Oscillatory Flow	221
APPENDIX H Integration of $\partial(\bar{F}/q)/\partial x$ Over a Body Element	232

NOMENCLATURE

A	Reference total area
a	Average body width
a_0	Local body width
\bar{a}	Radius of curvature
b	Average body height
b_0	Local body height
\bar{c}	Position vector to center of curvature
c_ℓ	Rolling moment coefficient (moment/ qA_S) (+ right wing down)
c_m	Pitching moment coefficient (moment/ $qA\bar{c}$) (+ nose up)
c_n	Yawing moment coefficient (moment/ qA_S) (+ nose right)
c_p	Pressure coefficient
c_y	Side force coefficient (Force/ qA) (+ out right wing)
c_z	Vertical force coefficient (Force/ qA) (+ up)
c	Local chord length
\bar{c}	Reference chord length
c_m	Local pitching moment coefficient
c_n	Local normal force coefficient
c.p.	Center of pressure
D	Matrix relating normalwash to lifting pressures for lifting surface elements
D_I	Matrix relating normalwash to lifting pressures for image elements
\bar{D}	Matrix relating normalwash to lifting pressures for elements and all their images
$\bar{\bar{D}}$	Matrix relating normalwash to lifting pressures for elements plus their images plus the contributions due to symmetry and ground effect

D_T	Partitioned matrix $[D \mid E]$, relating normalwash to lifting pressures and doublet strengths
D_0	Matrix relating the flow normal to a body surface (at the meridian angle θ) to the lifting pressure for elements and their images
$D(y), D(z)$	Matrix relating the average side- or upwash at a body due to lifting surface elements
D_{2D}	Matrix relating the doublet strength to the local up- or sidewash using quasi-steady, two-dimensional slender-body theory
d	Spacing of doublets or vortices within slender bodies (simulation of body aspect ratio (b/a)))
E	Matrix relating normalwash to axial doublet strengths
\bar{E}	Matrix relating normalwash to axial doublet strengths with the effects of symmetry and ground effect included
$E(y), E(z)$	Matrix relating the normalwash to y - or z -oriented axial doublets
e	Lifting surface element semi-width; also cross-sectional element semi-width
$F_z^{(z)}, F_z^{(y)}, F_y^{(z)}, F_y^{(y)}$	Total force on a body due to a point pressure doublet. Subscript indicates direction of force; superscript indicated direction of pressure doublet
f	Nondimensional deflection. Also function involving Hankel functions
$H_v^{(2)}$	Hankel function of the second kind of order v
h	Deflections normal to a lifting surface
h_y, h_z	Deflections of a body in y - and z -directions, respectively
$\vec{i}, \vec{j}, \vec{k}$	Unit vectors in x -, y - and z -directions, respectively
\vec{i}_F	Unit vector in the direction of the body force
K	Velocity kernel function; the normalwash due to a point pressure doublet; also $(a_0^2 - b_0^2)/4$
K_ϕ	Potential kernel function; the potential due to a point pressure doublet
k_r	Reduced frequency $(\omega C / 2U_\infty)$
\bar{k}	$\omega r^M / U_\infty$

L	The normalwash due to a potential doublet
L_ϕ	The potential due to a potential doublet
M	Mach number; also normalwash due to a point source; also moment
\vec{n}	Orientation of pressure doublet
\vec{n}, \vec{t}	Outward normal and tangent vectors
p	Function involving Hankel functions
Q	Generalized force; also modified acceleration potential
q	Dynamic pressure
\bar{q}	Generalized modal coordinate
R	$\sqrt{(x - \zeta)^2 + \beta^2 r^2}$
r	$\sqrt{(y - n)^2 + (z - \zeta)^2}$
\hat{r}	$(a + b)/2$
s	semi-span
U_∞	Freestream velocity
w	Normalwash boundary values
w_i	Normalwash due to image lifting surface elements
w_n	Normalwash due to body interference doublet distribution
w_R	$w_S + w_I$
w_s	Normalwash due to lifting surface elements
$w_{\bar{I}}$	$w - \Delta w$
\bar{w}	Normalwash in the circle plane
x,y,z	Coordinates of a receiving point
XM	Coordinate about which moments are taken
α	angle of attack
β	$\sqrt{1 - M^2}$
γ	Dihedral angle: γ_r , receiving point, γ_s , sending point
r	Vortex strength

ΔC_p	Lifting pressure
$\Delta \bar{Q}$	Modified acceleration potential jump
Δw	Normalwash due to slender body elements
Δx	Longitudinal length of lifting surface box
$\Delta \xi$	Longitudinal length of axial element
$\Delta \varphi$	Potential jump
δ	Symmetry plane indication (1 symmetry, 0 no symmetry, -1 anti-symmetry); also a delta function; also a virtual displacement
δA	Elemental area
ϵ	Ground-effect indication (-1 ground effect, 0 no ground effect, 1 antiground effect)
ζ	z-coordinate of sending point
η	y-coordinate of sending point
\bar{n}	Lateral coordinates in the plane of the lifting surface
θ	Meridian angle for a body of circular cross section
λ	Sweep of 1/4-chord of lifting surface element; also inclination angle in z-y-plane of a cross-sectional surface element
μ_d	Quadrupole strength
μ_n	Doublet strength of interference-body elements
μ_s	Doublet strength of slender-body elements
$\bar{\mu}_v$	Multipole strength in circle plane; v gives order of pole
$\hat{\mu}_y, \hat{\mu}_z$	Doublet strength of modified acceleration potential distribution in y- and z-directions; also reduction factors for image doublets
ξ	x-coordinate of sending point
\bar{o}	Distance from center curvature to external singularity
σ	Source strength
ϕ	Velocity potential
Ω	Acceleration potential
ω	Frequency

ξ_c	Center of axial-body element
ξ_1	Leading edge of body element
ξ_2	Trailing edge of body element

Subscripts and Superscripts

a	Body axis
b	Body
I	Image
LL	Lower left-hand quadrant
LR	Lower right-hand quadrant
n	Residual or interference flow
r,s	Receiving and sending points, respectively
UL	Upper left-hand quadrant
UR	Upper right-hand quadrant
s	Steady
y,q	y- and z-directions
α	On the body surface
1,2	Planar and nonplanar parts, respectively
1/4	Quarter chord of element

1.0 INTRODUCTION

Until several years ago the kernel function procedure was the best known and most widely used lifting surface theory. The classic report on this procedure is by Watkins, Runyan and Cunningham.¹ There have been many variations of this procedure; however, it is not our purpose to present a survey of them. Ashley, Widnall and Landahl² have already prepared an excellent survey of the lifting surface theory.

The use of lattice methods in steady flow goes back to Falkner³ and even further. Recent developments and improvements made by Rubbert⁴, Dulmovits⁵, Hedman⁶, Belotserkovskii⁷, Giesing⁸ and others have rejuvenated and popularized this method. The lattice method produces very accurate results even though the numerical technique is relatively simple. James⁹ has analyzed a two-dimensional model of the steady lattice theory. He has proven that when the vortex is placed at the 1/4-chord point of each element and the control point is placed at the 3/4-chord point of each element (the lifting surface is divided into a number of elements), then the following is true: 1) the lift and moment are exactly correct, 2) the Kutta condition is satisfied automatically without the use of loading functions, 3) in the limit of a large number of elements the correct leading edge singularity and correct trailing edge zero are obtained, and 4) the method works just as well for cambered surfaces whose distributions are continuous.

The lattice method is simple, versatile and accurate. The accuracy has already been discussed. The simplicity arises from the fact that no loading functions are required. The method is versatile because no prior knowledge of the solution is required as with the kernel function procedure. Loading functions appropriate to the particular problem must be chosen ahead of time for the kernel function procedure. It has been demonstrated that the lattice method can handle a very wide variety of configurations, including: 1) wings of arbitrary planform, 2) wings with partial span control surfaces, 3) T-tails, wing-pylons, wing-tails, 4) wings in ground effect, and 5) annular wings, wings with arbitrary dihedral.

Since the steady lattice method has met with such success, it seems only natural that it should be extended to unsteady (oscillatory) flow. Albano and Rodden¹⁰ have done just that. (A completely independent unsteady lattice procedure was developed by Stark¹¹.)

The new unsteady method has been termed the Doublet-Lattice Method (DLM). Further extensions, applications and refinements of the DLM are found in references 12 through 18. The DLM has proven as versatile as the Vortex Lattice Method and can handle the same wide variety of configurations (see references 13, 18 and Part I of this report). The attributes of the Vortex Lattice Method, i.e., simplicity, accuracy and versatility can be applied equally well to the DLM. Because of these attributes it was selected as the basis of the present method.

Of major interest in this report is the interaction of bodies (e.g., fuselage, nacelle, store) with lifting surfaces (e.g., wing, tail, pylon, etc.). There are two basic approaches to this problem: 1) one in which elements are placed on the body surfaces, and 2) one in which images are placed within the bodies. Recent advances in the first of these approaches have been made by Woodward¹⁹, Labrujere²⁰, and Bradley and Miller²¹ for steady flow. Part I of this report presents an extension of these methods of oscillatory flow. Recent advances in the second of these approaches have been made by Giesing⁸, Spangler and Mendenhall²², Borland²³, and Chou²⁴ for steady Flow. This report (Part II) presents an extension of these methods to oscillatory flow and very general configurations.

The approach of this report is to use the method of images directly replacing the steady vortex lattice on the lifting surfaces and image surfaces with an unsteady vortex lattice DLM. The advantage of using images over other methods is the fact that images do not introduce any new unknowns into the problem.

This approach furnishes a practical method for handling general configurations efficiently. Specifically, the configurations considered may include a collection of bodies (e.g., fuselage, nacelles, stores) and lifting surfaces (e.g., wing, tail, pylon, etc.). The configuration may oscillate in any mode,

rigid or flexible, and may operate in or out of ground effect. Outputs from the method are: generalized forces and aerodynamic parameters such as span loads, center of pressure, lift, moment, etc. The method can also be used to obtain dynamic stability derivatives (reference 14).

2.0 THEORETICAL DEVELOPMENT

2.1 Outline of the Problem and Solution

The velocity normal to an oscillating surface or body, $W = U_\infty \operatorname{Re}(w_s e^{i\omega t})$ is related to the lifting pressure $\Delta p = q \operatorname{Re}(\Delta C_p e^{i\omega t})$ by the following integral equation derived in Appendix A:

$$w_s(x, y, z, \gamma_r) = \frac{1}{8\pi} \iint_{L.S.} K(x - \xi, y - \eta, z - \zeta, \gamma_s, \gamma_r, k_r, M) \Delta C_p(\xi, \eta, \zeta) d\xi d\eta$$
(2.1-1)

where L.S. indicates integration over all lifting surfaces. This is the familiar integral equation of lifting surface theory for surfaces alone. Here γ_s, γ_r are the sending and receiving surface dihedral angles. If a body is introduced, there are additional contributions to the normal velocity. The first contribution may be called the slender body term and represents the flow field generated by bodies without considerations of interference.

$$\Delta W(x, y, z, \gamma_r) = \frac{1}{8\pi} \int_B L(x - \xi, y - \eta_a, z - \zeta_a, \gamma_s, \gamma_r, k_r, M) \tilde{\mu}_s(\xi) d\xi + \frac{1}{4\pi} \int_B M(x - \xi, y - \eta_a, z - \zeta_a, \gamma_r, M) \sigma(\xi) d\xi$$
(2.1-2)

The limit B. indicates integration over all bodies; these integrals are also derived in Appendix A. The subscript a on η and ζ indicate the location of body axes.

Here the term $\tilde{\mu}_s(\xi)*$ represents an axial multipole distribution (dipole, quadrupole, etc.) whose orientation is given by γ_s . The second integral exists only in steady flow and is a source distribution used to represent the body volume effects. The slender body terms are known since $\tilde{\mu}_s(\xi)$ and $\sigma(\xi)**$ are determined using an appropriate slender body theory.

*Actually $\tilde{\mu}_s(\xi)$ is twice the classic doublet strength $\mu_1(\xi)$.

**Currently in the Present Method sources are excluded since they do not exist for unsteady flow and have a small effect even in steady flow.

A second contribution to the normalwash flow field caused by the introduction of bodies into the flow field arises from "image" lifting surface elements. These are placed within the body to help divert the flow around a body in the presence of a lifting surface. The strength of the image elements is the same as the external elements.

$$w_I(x, y, z, \gamma_r) = \frac{1}{8\pi} \iint_{L.S.} K(x - \xi, y - n_I, z - \zeta_I, \gamma_{SI}, \gamma_r, k_r, M) \Delta C_p(\xi, n, \zeta) d\xi \quad (2.1-3)$$

The subscript I on n, ζ and γ_S indicates the image position on the image surface.

A third contribution to the normalwash flow field caused by the bodies is generated by an interference doublet distribution $\tilde{\mu}_n(\xi)$.

$$w_n(x, y, z, \gamma_r) = \frac{1}{8\pi} \int_B L(x - \xi, y - n_a, z - \zeta_a, \gamma_s, \gamma_r, k_r, M) \tilde{\mu}_n(\xi) d\xi \quad (2.1-4)$$

The form of this equation is identical to the first integral of equation (2.1-2). The reason it is not combined with $\tilde{\mu}_S$ is the fact that $\tilde{\mu}_S$ is known while $\tilde{\mu}_n$, like ΔC_p , is unknown.

In the direct problem, the normalwash boundary conditions are specified and the lifting pressure, ΔC_p , and body interference distribution, $\tilde{\mu}_I$, are solved for:

$$w = w_s + \Delta w + w_I + w_n \quad (2.1-5)$$

Here w is the prescribed normalwash on lifting surfaces and bodies. If the known quantities are placed on the left-hand side while the unknown quantities are placed on the right, then the following equation results:

$$\begin{aligned} w - \left(\frac{1}{8\pi} \int_B L \tilde{\mu}_S d\xi + \frac{1}{4\pi} \int_B M d\xi \right) &= \frac{1}{8\pi} \iint_{L.S.} K \Delta C_p d\xi + \frac{1}{8\pi} \iint_{L.S.} K_I \Delta C_p d\xi \\ &\quad + \frac{1}{8\pi} \int_B L \tilde{\mu}_n d\xi \end{aligned} \quad (2.1-6)$$

Here the subscript I on K indicates $K(x - \xi, y - n_I, z - \zeta_I, \gamma_{SI}, \gamma_r, k_r, M)$.

$$w - \Delta w = \frac{1}{8\pi} \iint_{L.S.} (K + K_I) \Delta C_p ds + \frac{1}{8\pi} \int_B L \tilde{\mu}_n d\xi \quad (2.1-7)$$

There are still further contributions to the normal wash and these arise from planes of symmetry and ground effect. If the assumption is made that the right half of the aircraft lies in the upper right-hand quadrant of the z-y plane, then a subscript UR may be applied to contributions made from lifting surfaces in this quadrant. Similarly, UL indicates upper left which contains the contribution from the left side of the aircraft. The subscript LR indicates lower right and, in this quadrant, the ground effect of the right side is contained. The subscript LL indicates lower left and this quadrant contains the contribution of the ground effect of the left half of the aircraft. Equation (2.1-7) may be expanded to include these contributions as follows:

$$\begin{aligned} w - (\Delta w_{UR} + \delta \Delta w_{UL} + \varepsilon \Delta w_{LR} + \varepsilon \delta \Delta w_{LL}) \\ = \frac{1}{8\pi} \iint \left\{ (K + K_I)_{UR} + \varepsilon (K + K_I)_{UL} + \varepsilon (K + K_I)_{LR} + \varepsilon \delta (K + K_I)_{LL} \right\} \Delta C_p ds \\ + \frac{1}{8\pi} \int_B \left\{ L_{UR} + \delta L_{UL} + \varepsilon L_{LR} + \varepsilon \delta L_{LL} \right\} \tilde{\mu}_n d\xi \end{aligned} \quad (2.1-8)$$

The quantities δ and ε are the symmetry and ground effect indicators. For instance, $\delta = 1, 0, -1$ indicates symmetry, no symmetry, and antisymmetry, respectively. Similarly, $\varepsilon = -1, 0, 1$ indicates ground effect, no ground effect, and anti-ground effect, respectively. The changes to the argument lists denoted by these subscripts are as follows:

$$UR: n = n, \quad \xi = \xi, \quad \gamma_S = \gamma_S$$

$$UL: n = -n, \quad \xi = \xi, \quad \gamma_S = -\gamma_S$$

$$LR: n = n, \quad \xi = -\xi, \quad \gamma_S = -\gamma_S$$

$$LL: n = -n, \quad \xi = -\xi, \quad \gamma_S = \gamma_S$$

The basic method of solution of Eq. (2.1-8) is to discretize the lifting surfaces into small boxes and the bodies into small axial elements. The unknowns are assumed constant over these elements and the normalwash boundary condition is applied to each box and element. This forms as many equations as unknowns and the system may be solved. Eq. (2.1-8) becomes:

$$w_T = \sum_{s=1}^{N1} \Delta C_p_s \iint_{\text{ELEMENT}_s} K_{Trs} ds + \sum_{s=1}^{N2} \tilde{u}_n_s \int_{\text{ELEMENT}_s} L_{Trs} d\xi \quad (2.1-9)$$

where s and r indicate sending and receiving points, respectively, and

$$w_T = w - \Delta w_T$$

$$\Delta w_T = (\Delta w_{UR} + \delta \Delta w_{UL} + \epsilon \Delta w_{LR} + \epsilon \delta \Delta w_{LL})$$

$$K_T = \frac{1}{8\pi} \left\{ (K + K_I)_{UR} + \delta(K + K_I)_{UL} + \epsilon(K + K_I)_{LR} + \epsilon\delta(K + K_I)_{LL} \right\}$$

$$L_T = \frac{1}{8\pi} \left\{ L_{UR} + \delta L_{UL} + \epsilon L_{LR} + \epsilon \delta L_{LL} \right\}$$

$N1$ = number of lifting surface boxes for all surfaces

$N2$ = number of axial body elements for all bodies

In matrix notation:

$$\begin{Bmatrix} w_T \end{Bmatrix} = [D_T] \begin{Bmatrix} \Delta C_p \\ \tilde{u}_n \end{Bmatrix} \quad (2.1-10)$$

where

$$[D_T] = [\bar{D} \mid \bar{E}] \quad (2.1-11)$$

in which

$$\begin{aligned} \bar{D} = & \left\{ (D + D_I)_{UR} \right. \\ & + \delta(D + D_I)_{UL} \\ & + \epsilon(D + D_I)_{LR} \\ & \left. + \epsilon\delta(D + D_I)_{LL} \right\} \end{aligned} \quad (2.1-12)$$

Here

$$D_{rs} = \iint_{\text{ELEMENT}} \frac{1}{8\pi} K ds$$

$$D_{I,rs} = \iint_{\text{ELEMENT}} \frac{1}{8\pi} K_I ds = \iint_{\text{ELEMENT}} \frac{1}{8\pi} K(x - \xi, y - n_I, z - \zeta_I, \gamma_r, \gamma_s, k_r, M) ds \quad (2.1-13)$$

The matrix elements D_{rs} have the subscript r on the receiving point quantities, x, y, z, γ_r and the subscript s on the sending element quantities ξ, n, ζ, γ_s , ELEMENT. The matrix partition E is:

$$\bar{E}_{rs} = \frac{1}{4\pi} \{ E_{UR} + \delta E_{UL} + \epsilon E_{LR} + \epsilon \delta E_{LL} \} \quad (2.1-14)$$

$$E = \iint_{\substack{\text{BODY} \\ \text{ELEMENT}}} L d\xi$$

Once w_T is known, ΔC_p and μ_n can be found, and these can be used to find the loads on the lifting surfaces and bodies.

The calculation of the flow field due to the slender body terms, i.e., μ_s and σ , is performed using the same discretization technique.

$$\Delta w_r = \frac{1}{8\pi} \sum_{s=1}^{N3} \tilde{\mu}_s \int_{\substack{\text{BODY} \\ \text{ELEMENT}_s}} L_{rs} d\xi + \frac{1}{4\pi} \sum_{k=1}^{N3} \sigma_k \int_{\substack{\text{BODY} \\ \text{ELEMENT}_s}} M_{rs} d\xi \quad (2.1-15)$$

where $N3$ is the number of slender body elements. If symmetry planes and ground effect are accounted for and matrix notation is introduced, then Eq. (2.1-15) becomes:

$$\{\Delta w_T\} = [L_T^{-1}] \{\tilde{\mu}_s\} + [M_T] \{\sigma\} \quad (2.1-16)$$

where

$$M_T = \frac{1}{4\pi} \{ M_{UR} + \delta M_{UL} + \epsilon M_{LR} + \epsilon \delta M_{LL} \}$$

Slender body theory states that \tilde{u}_s is directly proportional to the local velocity normal to the body axis (the direction of u_s is parallel to this velocity).

$$\tilde{u}_s = w D2D \quad (2.1-17)$$

where $D2D$ is the proportionality constant which is dependent on local body cross section. The values of w which act normal to the body axis (Eq.(2.1-17)) are part of the larger set that acts normal to all surfaces and bodies.

2.2 The Normalwash Boundary Conditions

The normalwash w must be determined at each lifting surface element (or box) and at each axial body element in both the z - and y -directions. The normalwash boundary conditions are obtained by taking the substantial derivative of the modal deflections. There are various methods of describing these modes and several of these will be discussed. Only the first of these methods has been incorporated into the present method (the polynomial approach). The polynomial approach lends itself to scientific investigation where the modes are simple. When the modes become complicated, however, it may be desirable to incorporate other more practical modal input methods.

2.2.1 Polynomial Modes

The total deflection distribution of a lifting surface normal to itself is made up of a set of modes, f_i .

$$h = \bar{c} \sum_{i=1}^{NM} \bar{q}_i f_i \quad (2.2-1)$$

where \bar{q}_i are the generalized coordinates and NM is the number of modes. The total normalwash is likewise

$$w = \frac{W}{U_\infty} = \sum_{i=1} \bar{q}_i w_i \quad (2.2-2)$$

where

$$w_i = - \left\{ \frac{df_i}{d(x/c)} + i \frac{\omega c}{U_\infty} f_i \right\}$$

or

$$w_i = - \left\{ \frac{df_i}{d(x/c)} + ik_r^2 f_i \right\}$$

Here

$$k_r = \frac{\omega c}{2U_\infty}$$

For lifting surfaces the modes may be approximated by

$$f_i = \sum_{n=0}^5 \sum_{m=0}^5 a_{inm} \left(\frac{x}{c}\right)^n \left(\frac{\tau}{c}\right)^m \quad (2.2-3)$$

$$\frac{df_i}{d(x/c)} = \sum_{n=0}^5 \sum_{m=0}^5 n a_{inm} \left(\frac{x}{c}\right)^{n-1} \left(\frac{\tau}{c}\right)^m \quad (2.2-4)$$

where τ is the lateral distance in the plane of the lifting surface.

Eqs. (2.2-3) and (2.2-4) represent fifth-degree polynomials in both the lateral and longitudinal directions.

When dealing with bodies, two separate directions of motion are possible: z -motion and y -motion. However, bodies have no lateral coordinate, thus the mode shapes are as follows:

$$f_{z_i} = \sum_{n=0}^5 a_{zin} \left(\frac{x}{c}\right)^n \quad (2.2-5)$$

$$f_{y_i} = \sum_{n=0}^5 a_{yin} \left(\frac{x}{c}\right)^n \quad (2.2-6)$$

$$\frac{df_{zi}}{d(x/c)} = \sum_{n=0}^5 naz_{in} \left(\frac{x}{c}\right)^{n-1} \quad (2.2-7)$$

$$\frac{df_{yi}}{d(x/c)} = \sum_{n=0}^5 nay_{in} \left(\frac{x}{c}\right)^{n-1} \quad (2.2-8)$$

The w_i arrays have the following order: first, all of the lifting surface normal wash values, w , are determined, then the z - or upwash values, w_z , and then the y - or sidewash values, w_y .

$$\{w\}_i = \begin{Bmatrix} w \\ w_z \\ w_y \end{Bmatrix}_i \quad (2.2-9)$$

2.2.2 Numerical Input

In many instances it is inconvenient to determine polynomial coefficients from modal data. The values of w and f could then be supplied directly.

An alternate scheme is to supply only h and require the program to take the necessary derivatives numerically. Various fitting techniques could be used including the spline fit of Harder²⁵.

A second alternate is to supply only the values of $df_i/d(x/c)$ and integrate for the values of f_i . Also needed is one value of f_i at each spanwise station to establish the level of f_i .

Interpolation schemes could be used to reduce the number of input values. Instead of supplying deflection data at each spanwise strip, it could be supplied at intervals along the span and interpolated at the intermediate spanwise locations.

2.2.3 Aerodynamic Influence Coefficients

There are many schemes for generating aerodynamic influence coefficients (AICs) and some of these are discussed in Part I of this report (page 28). The basic idea of the AIC approach is to derive a set of elementary modes which can be used to build up any desired mode shape. These elementary mode shapes are independent of the mass or stiffness properties of the aircraft and, thus, can be used to build up a solution for various fuel conditions, for example. One way to derive elementary mode shapes is to deflect a series of modal deflection points on the structure one at a time while holding all the others fixed. Once the generalized forces for this set of elementary modes are known for a particular aircraft planform, Mach number and frequency, aerodynamic solutions for all mass and stiffness distributions can be found simply by a matrix multiplication of the modal deflections and the AIC matrix.

$$Q_{ij} = \{f_j\}^T [AIC] \{f_i\} \quad (2.2-10)$$

where f_j is a set of modal deflections for mode j and f_i is the same for mode i .

The type of curve fit used for the generation of the elementary mode shapes may vary. Part I of this report offers several possibilities (see page 31). Recent work by Harder, et.al.²⁵ already referred to, on two-dimensional surface spline fitting of deflected surfaces may offer a very accurate and versatile technique for generating elementary mode shapes. For bodies the usual one-dimensional spline could be used.

2.3 The Lifting Surface

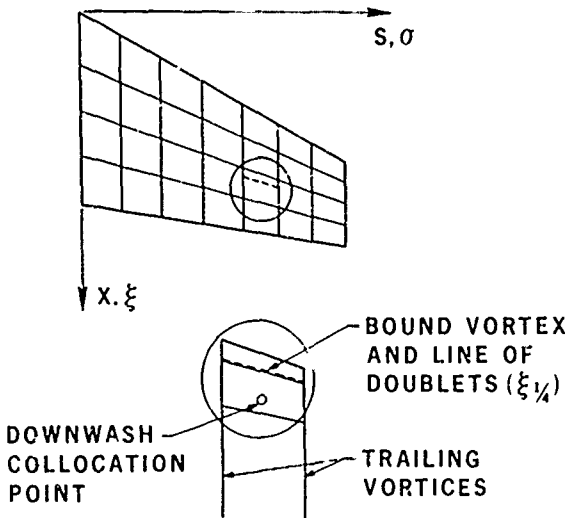
The basic technique employed to represent the lifting surfaces is the Doublet Lattice Method (DLM). The DLM is an extension of the steady flow Vortex-Lattice Method to oscillatory flow. Developments of the Vortex-Lattice Method include those of Rubbert⁴, Dulmovits⁵, Hedman⁶, Belotserkovskii⁷, and Giesing⁸ who extended the method to wing-body combinations. The original extension of the steady Vortex-Lattice Method to unsteady flow was made by Albano and Rodden¹⁰. Adaptation of the DLM to AIC generation was done by

Stahl, et al.¹² Extensive correlations for nonplanar configurations were made by Kalman, et al.¹³ A refinement of the method for nearly coplanar configurations is reported in Part I of this report (section 2.1, appendices A, B and C) and also by Rodden, et al.¹⁸ The use of the method for stability derivatives is given by Rodden and Giesing¹⁵, and its use in gust analysis is given by Giesing and Rodden¹⁶. An extension to induced drag distribution was made by Kalman, et al.¹⁷

The DLM has proven to be a simple, versatile and accurate method for the solution of unsteady nonplanar lifting surface problems. The general nature of the solution need not be known in advance as with the kernel function techniques which utilize a standard set of pressure loading functions. Elimination of the loading functions simplifies the analysis since the complicated and time consuming quadrature integrations of the loading functions and kernel are eliminated. The method is versatile since there are essentially no restrictions on the configurations that can be handled. It has been shown to be accurate by James⁹ who performed analytic studies on the steady two-dimensional version, and through the many correlations with experimental data and other analytical methods.

The flow singularities used to model the lifting surface are steady horseshoe vortices and oscillatory doublets along the bound vortex. The doublet line is equivalent, at zero frequency, to the horseshoe vortex, and thus the horseshoe vortex need not be used. However, since the effects of the vortex system can be analyzed exactly, while the effects of a doublet line can only be approximated, improved accuracy is obtained by using both the vortex and doublet systems. In this way, the vortices represent the steady-flow effects, and the doublets represent the incremental effects of oscillatory motion.

The configuration is idealized by dividing the surface(s) into small trapezoidal elements (boxes) arranged in strips parallel to the freestream so that surface edges, fold lines, and hinge lines lie on box boundaries (sketch 2.3-1). Then, to represent the steady-flow effects, a horseshoe vortex is placed on each of the boxes such that the bound vortex of the horseshoe system coincides with the quarter-chord line of the box. To represent the oscillatory increment, a distribution of acceleration potential doublets (which have the steady-flow acublet strength subtracted) of uniform strength



Sketch 2.3-1. Surface Idealization into Boxes and Location of Vortices, Doublets and Collocation Points

is superimposed on the bound vortex. The surface boundary condition is a prescribed normalwash applied at the control point of each box. The control point is centered spanwise on the three-quarter-chord line of the box (sketch 2.3-1). The influences of all vortices and doublets are summed for each control point to obtain the total dimensionless normalwash, w , at the control point.

The expressions for D_{rs} , the elements of the influence matrix, are well documented in Part I and will not be repeated here. A general description of the method of integration will suffice. The expression for D_{rs} is given in Eq. (2.1-13).

$$D_{rs} = \frac{1}{8\pi} \iint_{\text{ELEMENT}} K_{ds} \quad (2.3-1)$$

The kernel K is split up into the following components

$$K = \left\{ \frac{T_1 K_1^{(s)}}{r^2} + \frac{T_2^* K_2^{(s)}}{r^4} \right\}$$

$$+ \left\{ \frac{T_1 (K_1 - K_1^{(s)})}{r^2} \right\} \quad (2.3-2)$$

$$+ \left\{ \frac{T_2^* (K_2 - K_2^{(s)})}{r^4} \right\}$$

where the sending and receiving subscripts (s,r) have been dropped for convenience. The first term in braces is the steady part of the kernel while the second and third terms are the planar and nonplanar parts, respectively, of the unsteady increment. Integration in the ξ -direction (parallel to the freestream) is done by lumping the value of the integrand at the one-quarter-chord point of the box. The integration of the steady term in the spanwise direction is done using the law of Biot and Savart. Spanwise integration of the planar and nonplanar terms is done by approximating the numerators by parabolas. The resulting expressions are analytically integrable.

$$D = D^{(s)} + D^{(1)} + D^{(2)} \quad (2.3-3)$$

$$D^{(s)} = \frac{\Delta x}{8\pi} \int_{-e}^e \left\{ \frac{T_1 K_1^{(s)}}{r^2} + \frac{T_2^* K_2^{(s)}}{r^4} \right\} d\bar{n} \quad (2.3-4)$$

$$D^{(1)} = \frac{\Delta x}{8\pi} \int_{-e}^e \frac{A_1 \bar{n}^2 + B_1 \bar{n} + C_1}{r^2} d\bar{n} \quad (2.3-5)$$

$$D^{(2)} = \frac{\Delta x}{8\pi} \int_{-e}^e \frac{A_2 \bar{n}^2 + B_2 \bar{n} + C_2}{r^4} d\bar{n} \quad (2.3-6)$$

where

$$A_1 \bar{n}^2 + B_1 \bar{n} + C_1 \approx T_1 (K_1 - K_1^{(s)}) \quad (2.3-7)$$

$$A_2 \bar{n}^2 + B_2 \bar{n} + C_2 \approx T_2^* (K_2 - K_2^{(s)})$$

the coefficients A, B, and C are found by evaluating the kernel at the center and both edges of the element. Here \bar{n} is a spanwise coordinate in the plane of the element centered on the sending element, e is the semi-width of the sending element and the subscripts (r,s) have been dropped again for convenience. The result of integrating Eq. (2.3-4), i.e., an expression for the steady horseshoe vortex, is found in Part I, Appendix C, Vol. I, page 68. The integrations indicated in Eqs. (2.3-5) and (2.3-6) are found also in Part I, Vol. I, Appendix B, page 58. Two expressions for $D^{(2)}$ are found on pages 59 and 60 of Part I, Vol. I, Appendix B.

The matrix formulation for an isolated lifting surface without ground effect, symmetry or images, given in terms of the influence coefficient matrix [D], is then

$$\{w\} = [D] \{\Delta C_p\} \quad (2.3-8)$$

2.4 The Isolated Body

It is desirable to use an axial system of singularities to simulate the effect of bodies in the fluid since they require much less computational effort than do surface singularity distributions. Generally, axial distributions are associated with slender body theory.

Slender body theory has had a long history and it is not the purpose of this report to detail its development. Only some of the more important works will be mentioned. The doctoral thesis by Revell (see reference 26) gives a very elegant and detailed description and cites over 200 references.

Munk²⁷ is generally the first of any references relating to steady slender body theory. Kármán²⁸ applied a modified version of Munk's theory to airship hulls (Kármán's method will be discussed later in this section). Lighthill²⁹ may be mentioned next along with Jones³⁰ for extensions to slender wings and Miles³¹ for extension to unsteady flow. Many attempts have been made to extend the slender body theory to higher order. Ward³² has given second-order effects for the nonlifting component of the pressure for supersonic flow. Adams and Sears³³ have extended this method to subsonic flow using the Fourier transform. Van Dyke³⁴ attempted a second-order "lifting" solution and was only partially successful. Van Dyke suggests using the first-order solution for the lifting components (doublets) but suggests using

the higher order axial flow solution along with a higher-order pressure formulation to find the pressures and forces. Such a formulation allows the coupling of the cross flow with the axial flow. This coupling does have an effect on the axial loading; however, for many bodies (shown in reference 34) the first-order solution is very good over a wide range of Mach number.

The only completely consistent second-order theory has been developed by Revell²⁶. Revell attacks the second-order solution by a complicated iteration scheme.

The methods of Hess and Smith³⁵ and Landweber³⁶ may be mentioned in passing. These methods are exact, surface singularity methods. They are, however, only valid for steady, compressible flow or unsteady incompressible flow and cannot be used here.

In all of the axial singularity methods described (except for Revell), the lifting part of the solution is given by the first-order slender body theory. Various improvements have been suggested for determining the loading associated with this distribution; however, the distribution itself is determined using first-order theory.

The basic approach of slender body theory is to consider only the near field effects of the axial singularities of the bodies on themselves. In the near field the flow is both two-dimensional and quasi-steady. When the body surface lies close to the axis, the surface sees only the local axial singularity distribution. Also, when the body surface lies close to the axis, the characteristic wave length associated with the solution of the wave equation is long compared to the distance from the body axis to its surface; this renders the problem quasi-steady. In all of the axial singularity methods described, only one isolated body is considered. Any method developed would have to properly generate a flow field away from the body surface where the slender body assumptions are no longer valid (so that the mutual interference of bodies can be accounted for).

A possible solution to this problem would be to use the exact three-dimensional unsteady compressible flow solution for the effect of the axial singularity system. The axial integral could be discretized (see Appendix B) giving a piecewise constant singularity distribution. For such a distribution the axis is divided up into a series of short axial elements. The singularity

strengths are held constant over each element but varied from element to element. The boundary conditions would be made to hold along a line on the surface of each of the bodies. Multiple bodies of arbitrary thickness should be handled easily and the flow fields could be calculated easily.

Kármán used this approach to predict pressures and loads on airship hulls at angle of attack. He used sources for the volume effect and doublets for the crossflow lifting effect. Kármán's method was a velocity potential approach (Appendix B, Eq. (B-2)). Other approaches could be used, however, for instance, the pressure potential method given by Eq. (B-4) (Appendix B) or the modified acceleration potential approach given by Eq.(B-15) (Appendix B). For steady flow the modified acceleration potential method is the same as the velocity potential method.

The unsteady pressure potential and modified acceleration potential methods, discretized as described above, were implemented on the computer so that they could be investigated. The formulas for the flow field due to a short element of pressure potential doublet and modified acceleration potential doublet are as follows:

$$E_{rs} = \frac{1}{8\pi} \Delta\xi_s K(x_r - \xi_{1/4s}, y_r - n_{as}, z_r - \zeta_{as}, \gamma_r, k_r, M)$$

Pressure Potential (2.4-1)

$$E_{rs} = \frac{1}{8\pi} \left\{ e^{i\omega\Delta\xi_s/2U_\infty} K(x_r - \xi_{1s}, y_r - n_{as}, \dots) - e^{-i\omega\Delta\xi_s/2U_\infty} K(x_r - \xi_{2s}, y_r - n_{as}, \dots) \right\}$$

Modified Acceleration Potential (2.4-2)

The terms ξ_{1s} , ξ_{2s} and $\xi_{1/4s}$ are the leading edge, trailing edge and 1/4-chord point of the sending axial element (indexed by the subscript s). The index r indicates the receiving point. The boundary condition was enforced at one point per element. For the pressure potential method this point was located as follows:

Pressure Potential

$$\begin{aligned}x_r &= x_{3/4r} \quad (3/4\text{-chord point of element}) \\y_r &= \eta_a \\z_r &= \zeta_a + a_r\end{aligned}\tag{2.4-3}$$

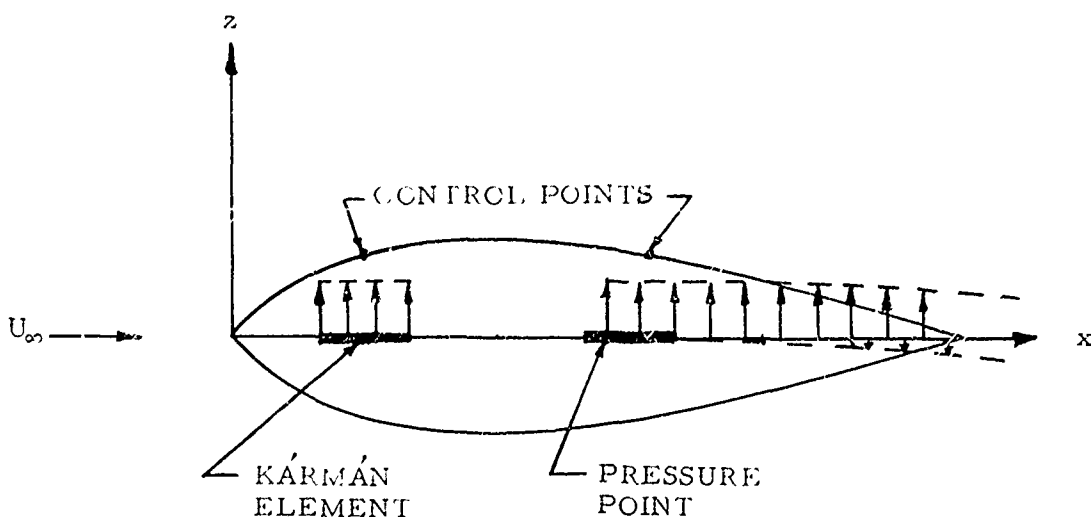
where a_r is the radius at the point $x_{3/4r}$.

Modified Acceleration Potential

$$\begin{aligned}x_r &= x_{1/2r} \quad (\text{mid-chord point of element}) \\y_r &= \eta_a \\z_r &= \zeta_a + a_r\end{aligned}\tag{2.4-4}$$

Unlike slender body theory each element affects all control points.

The pressure point doublet in steady flow is just an ordinary doublet line of constant strength originating at the pressure point and terminating at downstream infinity. The pressure point doublet in steady flow then is just a semi-infinite doublet line.



Sketch 2.4-1

The two approaches previously outlined are essentially the same for bodies that close (eliminating the wake). The only difference is that the elements for the pressure doublet method are shifted aft by 1/4 of an element length. This difference disappears with increasing numbers of elements. The numerical results for either method were found to be almost identical for the cases considered. Figure 1 shows one such case. A pointed body of parabolic shape is made to pitch about its leading edge with a reduced frequency ($k = \omega L/U_\infty$) of 0.1. The calculated axial loading* is compared to that obtained using the method of J. W. Miles³¹. For this case the axis was divided up into ten equal elements. A pressure doublet was placed on each element. The results for a thickness ratio, (R_{\max}/L), of 0.1 are essentially in perfect agreement with those of Miles. As the thickness increases, however, the calculated results start to oscillate about the correct solution. For very thick bodies the results are meaningless. It has been found that the ratio of diameter to element length plays an important role in determining the accuracy of the results. It has been found that the diameter should not be much greater than 2 to 4 times the element length. Von Kármán used a diameter-to-element length ratio of about 3, and thus obtained very satisfactory results for the airship hulls he considered.

The reason for the failure of this method is not known. The supersonic version of this method, as developed by Kármán and Moore³⁷ and Tsien³⁸, seems to work very well. It is suspected that the reason the supersonic method works while the subsonic method runs into trouble, is the fact that in supersonic flow, singularities or discontinuities are propagated to the body surface from the axis while they are not in subsonic flow. It is obviously impossible to produce a discontinuity in upwash on the body surface due to axial singularities unless discontinuities can propagate to the surface of the body from the axis. It is then obvious that in subsonic flow the closer the singularities are to the surface (i.e., the more slender the body) the more accurate the solution will be. It seems logical that there is a restricted family of upwash distributions or boundary conditions that a subsonic axial singularity system can satisfy on the surface of the body. The method by which one determines whether a specific upwash boundary condition qualifies for a solution is not yet known.

*The assumption was made that the axial doublet strength could be used directly to obtain the loading in the calculation.

Kármán²⁸ commented that the doublet distribution obtained by his method agrees very well with the doublet distribution obtained using Munk's slender body theory. He went on to suggest that very accurate solutions for the pressure could be found if the exact non-linearized pressure formula were used in conjunction with the doublet distribution obtained using either his or Munk's theory.

Kármán has thus suggested a solution to our problem. For an isolated body, slender body theory should be used to determine the axial doublet strength. Classical slender body theory does not account for interference between the isolated body and lifting surfaces or other bodies. A solution to this problem would be to keep the finite element or Kármán approach for interreference purposes but to use slender body theory for the effect of a body on itself. Stated in terms of influence coefficients this would mean that slender body theory should be used for the calculation of influence coefficients of the bodies on themselves, producing diagonal matrices, and general three-dimensional wave equation solutions should be used for the calculation of influence coefficients of the bodies on 1) lifting surfaces and 2) other bodies. The interference matrices would be full matrices.

2.4.1 Axial Singularity Strength Using Slender Body Theory

Slender body theory states that the flow field very near the body is two-dimensional and quasi-steady. At each longitudinal station the flow field depends only on the local upwash (or sidewash) and local body cross-sectional shape. The axial singularity can then be determined from this two-dimensional quasi-steady flow. For the case of a circular cross section a simple doublet suffices to divert the flow around the cross section.

$$\mu_s = 2\pi w a_0^2 \quad (2.4-5)$$

where a_0 is the local radius and w is the local up- or sidewash.

For noncircular cross sections a simple doublet will not suffice. In general, a multipole expansion would be required to simulate the cross section in the far field. An alternative approach which requires no new basic singularities is to use doublets spaced laterally a distance from the axis. This produces

the same effect in the far field as do higher order singularities. This approach can be matched to the proper expansion through the second term (quadrupole) to give the value of the distance of the doublet from the origin. An integrated doublet, i.e., two vortices, can also be used in the same manner.

Consider the flow about a body of elliptic cross section where a_0 is the semi-major axis and b_0 is the semi-minor axis. The slender body theory gives the near field solution as the two-dimensional flow about an ellipse. Let F be the complex potential in the complex plane.

$$F = -iwZ + \frac{i\tilde{r}^2 w}{Z} \quad (2.4-6)$$

where Z is the complex coordinate in the circle plane. The transformation to the ζ or ellipse plane ($\zeta = y + iz$) is

$$\zeta = Z + K^2/Z$$

$$\zeta = y + iz$$

$$\tilde{r} = (a_0 + b_0)/2 \quad (2.4-7)$$

$$K = (a_0^2 + b_0^2)/4$$

$$w = \text{upwash at the cross section}$$

In the usual procedure for inner-outer matching, the inner solution will be expanded in terms of the outer variable. Basically, what is wanted is the multipole expansion of the inner or slender body solution. Expanding the expression for F and ζ gives:

$$\begin{aligned} F = iw & \left[- \left\{ \zeta - K^2/\zeta - K^4/\zeta^3 - \dots \right\} \right. \\ & \left. + \tilde{r}^2 \left\{ \zeta - K^2/\zeta - K^4/\zeta^3 - \dots \right\}^{-1} \right] \end{aligned}$$

or retaining one term past the doublet gives:

$$F = i w \left\{ -\zeta + a_0 \left(\frac{a_0 + b_0}{2} \right) \zeta^{-1} + \left(\frac{a_0 + b_0}{2} \right)^2 \left(\frac{a_0 - b_0}{2} \right) a_0 \zeta^{-3} + \dots \right\} \quad (2.4-8)$$

↑
onset flow ↑ doublet ↑ quadrupole

The appropriate doublet and quadrupole strengths, needed to represent the elliptic cross section, are:

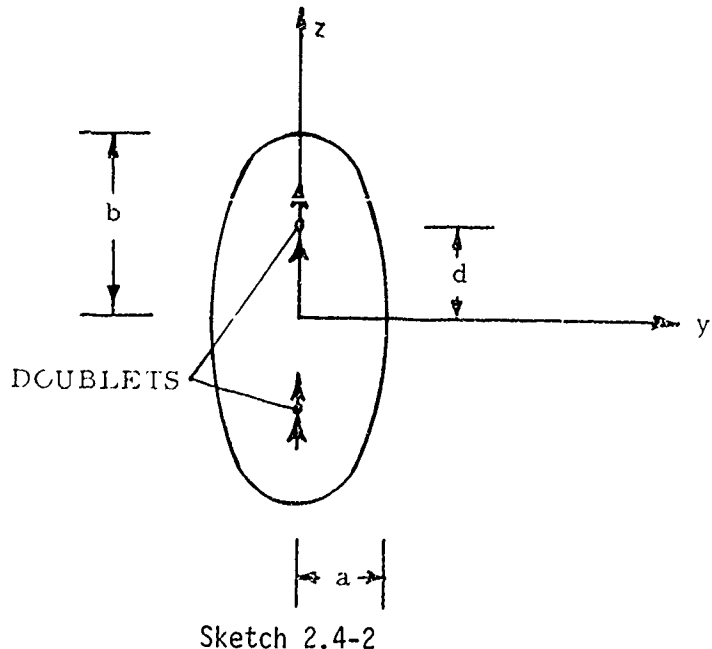
$$\mu_s = D2Dw \quad \text{doublet}$$

$$D2D = 2\pi a_0 (a_0 + b_0)/2 \quad (2.4-9)$$

$$\mu_q = w 2\pi a_0 \left(\frac{a_0 + b_0}{2} \right)^2 \left(\frac{a_0 - b_0}{2} \right) \quad \text{quadrupole}$$

The flow about the ellipse is replaced by the flow about a doublet of strength μ_s and a quadrupole of strength μ_q . The approach is to replace the doublet and quadrupole with two doublets each spaced a distance d from the axis of the cross section.

Two cases will be considered: 1) $b > a$, i.e., major axis smaller than minor axis, and 2) $a > b$. For the first case, $b > a$, two doublets will be used (see sketch 2.4-2). One doublet placed at $+id$ and the other at $-id$.



The complex potential due to these doublets is:

$$F = i w \left\{ -\zeta + \frac{\mu_s/4\pi}{\zeta-id} + \frac{\mu_s/4\pi}{\zeta+id} \right\} \quad (2.4-10)$$

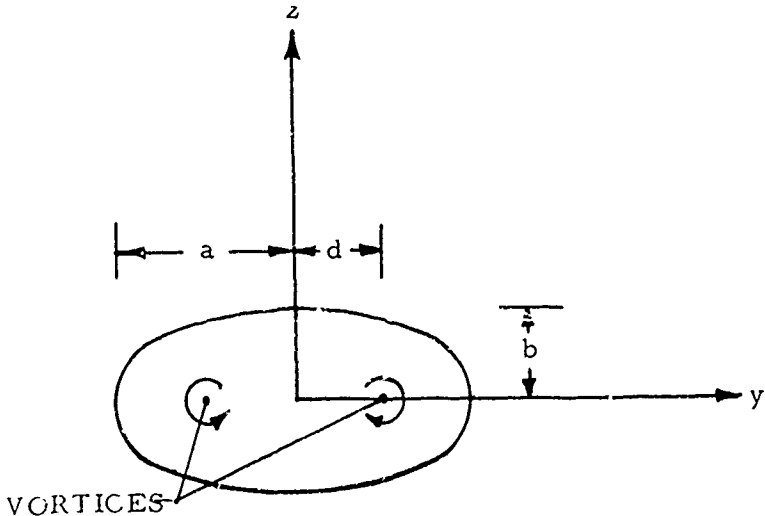
Expanding Equation (2.4-10) gives:

$$F = i w \left\{ -\zeta + (\mu_s/2\pi)\zeta^{-1} - (\mu_s d^2/2\pi)\zeta^{-3} + \dots \right\} \quad (2.4-11)$$

The term $-\mu_s d^2$ is the quadrupole strength. Equating this to μ_q given in (2.2-4) gives an expression for d .

$$d = \sqrt{\frac{b_0^2 - a_0^2}{4}} = K \quad (2.4-12)$$

The second case, where the major axis is larger than the minor axis, $a > b$, is now described. In this case an integrated doublet is used. This integrated doublet gives two vortices; one positive vortex at $+d$ and one negative vortex at $-d$. Sketch 2.4-3 gives the geometry.



Sketch 2.4-3

The complex potential for the two vortices is:

$$F = i w \left\{ -\zeta + \frac{\Gamma}{2\pi} \ln \left(\frac{\zeta + d}{\zeta - d} \right) \right\} \quad (2.4-13)$$

Expanding this equation gives:

$$F = i w \left\{ -\zeta + \left(\frac{2rd}{2\pi}\right) \zeta^{-1} + \left(\frac{2rd^3}{2\pi}\right) \zeta^{-3} + \dots \right\} \quad (2.4-14)$$

Equating Equations (2.4-14) and (2.4-8) gives:

$$\begin{aligned} 2dr &= \mu_s \\ \mu_s &= D2D \\ D2D &= 2\pi a_0(a_0 + b_0)/2 \\ d &= \sqrt{3} \sqrt{\frac{a_0^2 - b_0^2}{4}} = \sqrt{3} K \end{aligned} \quad (2.4-15)$$

Equations (2.4-15), (2.4-12) and (2.4-9) give the appropriate doublet strength or vortex strength and spacing d to properly represent the doublet and quadrupole strengths of the elliptic cross section. The far field may now be determined by using the exact wave equation solution for these singularities coupled with the appropriate singularity strength and spacing as derived above.

The multipole expansions used are terminated after the quadrupole. Thus the cross section will not exactly be an ellipse. Specifically, the ratio a/b or b/a may not exactly be the aspect ratio of the body. Figures 2 and 3 give examples of body shapes obtained using two-doublets and two vortices. In many instances it is not important to maintain an elliptic cross section exactly since the ellipse itself is an approximation to body shapes with unequal semi-major and semi-minor axes. The main idea is to match the ratio of a/b or b/a of the ellipse or approximate ellipse to the physical aircraft cross section. In some instances the body cross-sectional shapes shown in Figures 2 and 3 are more representative of the physical shape than is the ellipse. In any case it may be more important to correctly associate the values of doublet strength and spacing d with the ratio a/b or b/a for the approximate ellipse.

2.4.2 Far Field Representation

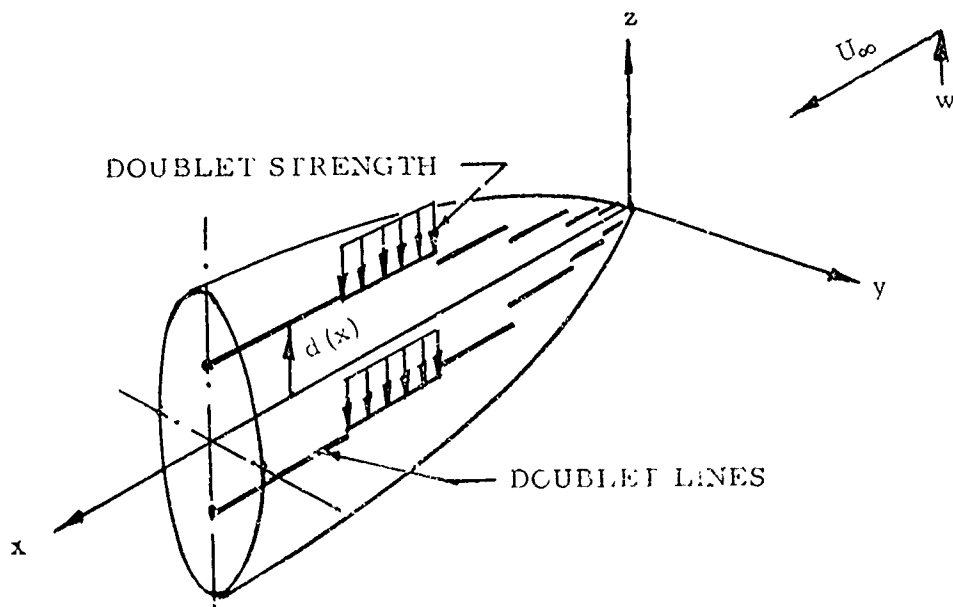
As stated in the foregoing discussion, exact formulas are to be used for the effect of the body on lifting surfaces and other bodies. The cross-sectional area and shape usually varies along the length of practical bodies. Thus, the strength and spacing d must vary along the length of a body. Numerically, it seems reasonable to assume that the cross section is piecewise constant over short lengths. The body is then divided up into short elements (see sketch 2.4-4). The two-dimensional doublet becomes a line doublet the length of the element. One line doublet lies at $n = +d$ and one at $n = -d$. Each line doublet or vortex, will, in general, lie at a different value of d . The exact solution for a constant strength doublet has not been derived. However, an expression for a doublet varying like $e^{-i\omega(\xi-\xi_c)/U_\infty}$ over the element (from ξ_1 to ξ_2 where $\xi_c = (\xi_1 + \xi_2)/2$) has been derived in Appendix B. This is the modified acceleration potential method. The influence function at a field point then is the sum of two expressions, one for the doublet element lying at $n = n_a + d$ and one for the doublet element lying at $n = n_a - d$.

$$E_{rs} = \frac{1}{16\pi} \left\{ e^{+i\omega(\xi_s - \xi_1)/2U_\infty} [K(x_r - \xi_{1s}, y_r - (n_{as} - d_s), z_r - \zeta_{as}, \dots) + K(x_r - \xi_{1s}, y_r - (n_{as} + d_s), z_r - \zeta_{as}, \dots)] - e^{-i\omega(\xi_s - \xi_2)/2U_\infty} [K(x_r - \xi_{2s}, y_r - (n_{as} - d_s), z_r - \zeta_{as}, \dots) + K(x_r - \xi_{2s}, y_r - (n_{as} + d_s), z_r - \zeta_{as}, \dots)] \right\} \quad (2.4-16)$$

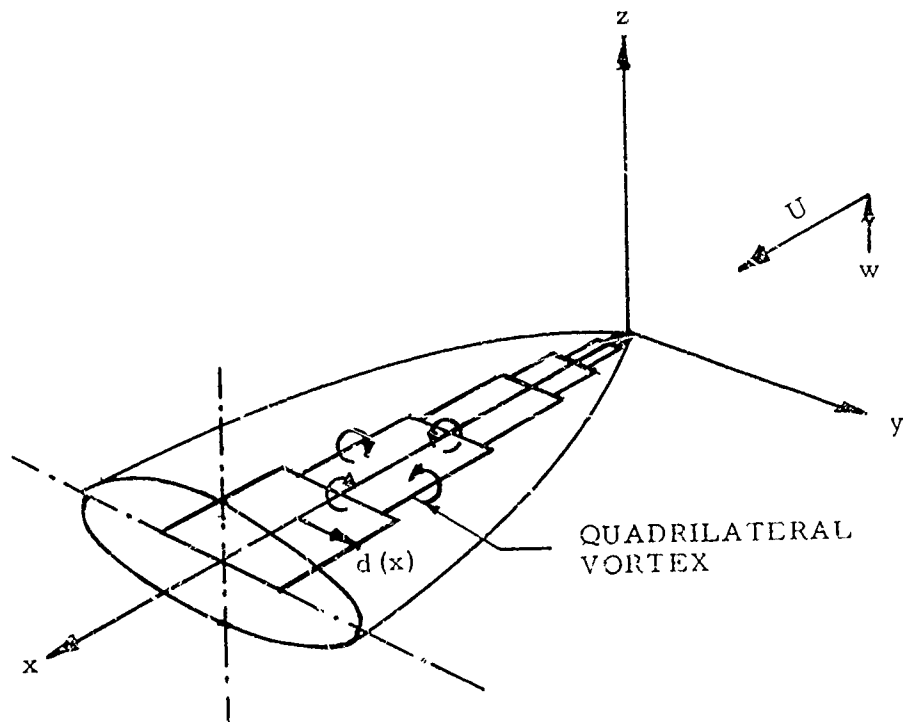
The term K is the classic kernel of lifting surface theory and is derived in Appendix A. The terms ξ_1 and ξ_2 are the element end points. The term E_{rs} gives the velocity at the point x_r, y_r, z_r normal to a surface of dihedral γ_r due to the doublet line segment of unit doublet strength.*

If the short segment of line doublets is integrated laterally, as outlined in Appendix B, then the result is an unsteady trapezoidal vortex; see Sketch 2.4.5.

*For convenience the modified doublet ($i\omega \neq 2\mu$) is used in this analysis, see Eqs. 2.4-26, -27.



Sketch 2.4-4



Sketch 2.4-5

$$E_{rs} = \frac{1}{8\pi} \int_{-d}^d \frac{1}{2d} \left[e^{i \omega \Delta \xi_s / 2U_\infty} K(x_r - \xi_1 s, y - n, \dots) - e^{-i \omega \Delta \xi / 2U_\infty} K(x_r - \xi_2 s, y - n, \dots) \right] dn \quad (2.4-17)$$

The division by $2d$ appearing in Eq. (2.4-17) reduces the quadrilateral vortex strength per unit area to a doublet strength (modified) per unit length.

Expanding K into its three component parts, as given by Eq. (2.3-2),

$$E_{rs} = E_{rs}^{(s)} + E_{rs}^{(1)} + E_{rs}^{(2)} \quad (2.4-18)$$

$$E^{(s)} = \frac{1}{16\pi d} \int_{-d}^d K^{(s)}(x - \xi_1, y - n, \dots) T_1 / r^2 dn$$

$$- \frac{1}{16\pi d} \int_{-d}^d K_1^{(s)}(x - \xi_2, y - n, \dots) T_2^* / r^4 dn \quad (2.4-19)$$

$$E^{(1)} = \frac{1}{16\pi d} \int_{-d}^d T_1 \left\{ \frac{e^{i \omega \Delta \xi / 2U_\infty} K_1(x - \xi_1, \dots) - K_1^{(s)}(x - \xi_1, \dots)}{r^2} - \frac{e^{-i \omega \Delta \xi / 2U_\infty} K_1(x - \xi_2, \dots) + K_1^{(s)}(x - \xi_2, \dots)}{r^2} \right\} dn \quad (2.4-20)$$

$$E^{(2)} = \frac{1}{16\pi d} \int_{-d}^d T_2^* \left\{ \frac{e^{i \omega \Delta \xi / 2U_\infty} K_2(x - \xi_1, \dots) - K_2^{(s)}(x - \xi_1, \dots)}{r^4} - \frac{e^{-i \omega \Delta \xi / 2U_\infty} K_2(x - \xi_2, \dots) + K_2^{(s)}(x - \xi_2, \dots)}{r^4} \right\} dn \quad (2.4-21)$$

where the subscripts r and s have been dropped in Eq. (2.4-19) through (2.4-21) for convenience. The subscript r is attached to the receiving point quantities x_r, y_r, z_r, γ_r , etc., whereas the sending point subscript s is attached to the sending element quantities, $\Delta\xi_s, \xi_1, \xi_2, d_s$, etc. The steady term $E^{(s)}$ is associated with a trapezoidal vortex of constant strength located around the edge of the element and can be determined using the law of Biot and Savart. The second and third terms, $E^{(1)}$ and $E^{(2)}$ can be evaluated in a manner analogous to that for $D^{(1)}$ and $D^{(2)}$ given in Eqs. (2.3-5) and (2.3-6).

$$E^{(1)} = \frac{1}{16\pi d} \int_{-d}^d \frac{A_1 n_2 + B_1 n + C_1}{r^2} dn \quad (2.4-22)$$

$$E^{(2)} = \frac{1}{16\pi d} \int_{-d}^d \frac{A_2 n^2 + B_2 n + C_2}{r^4} dn \quad (2.4-23)$$

$$A_1 n^2 + B_1 n + C_1 = \text{Numerator of (2.4-20)}$$

$$A_2 n^2 + B_2 n + C_2 = \text{Numerator of (2.4-21)}$$

This formulation of $E^{(1)}$ and $E^{(2)}$ becomes very inaccurate when $r = 0$ and the receiving point is downstream of the element. The $1/r^2$ and $1/r^4$ singularities exist only on the length of the element; no such singularities exist downstream. These singularities are eliminated in the numerator in a limiting process. However, when the numerator is approximated by a parabola the singularities are not cancelled properly. A way around this difficulty is to fit the entire integral with parabolas.

$$E^{(1)} = \frac{1}{16\pi d} \int_{-d}^d (A_3 n^2 + B_3 n + C_3) dn = \frac{1}{16\pi d} \left(\frac{2}{3} A_3 d^3 + 2dC_3 \right) \quad (2.4-24)$$

$$E^{(2)} = \frac{1}{16\pi d} \int_{-d}^d (A_4 n^2 + B_4 n + C_4) dn = \frac{1}{16\pi d} \left(\frac{2}{3} A_4 d^3 + 2dC_4 \right) \quad (2.4-25)$$

$$A_3 n^2 + B_3 n + C_3 = \text{Integrand of (2.4-20)}$$

$$A_4 n^2 + B_4 n + C_4 = \text{Integrand of (2.4-21)}$$

The coefficients $A_3, B_3, C_3, A_4, B_4, C_4$ are calculated by evaluating the integrands at three points: $n = -d, 0, d$, that is, the left edge, center and right edge of the element. When a field point lies close to one of these locations (downstream of the element) then r becomes very small and accuracy can be lost in the calculation. To avoid this difficulty, a two-point formula is used when $r \leq 0.01d$. The offending point is simply eliminated from the calculation.

$$B_3 n + C_3 = \text{Integrand of (2.4-20)}$$

$$B_4 n + C_4 = \text{Integrand of (2.4-21)}$$

If a field point lies close to an element edge, for instance, B and C are determined using the value of the integrand as evaluated at the other edge and the center. This simplification of the integration scheme gives rise to irregularities in the normalwash flow field of the trapezoidal vortex in a region downstream of the element. These irregularities do not, however, invalidate the calculation. Problems involving $1/r^2$ and $1/r^4$ could be eliminated if the velocity potential approach were taken and new formulas developed for the line and area integrals. The general form of these integrals are given in Appendix B, Eqs. (B-1) and (B-2). Details of the integration over a small element have not yet been developed but no problems are envisioned.

2.4.3 Matrix Representation

In the last two subsections, expressions have been derived for the singularity strengths and far field effects of short element lengths. The total effect, Δw , is obtained by summing the effects of all elements. In matrix form

$$\tilde{\mu}_S = 2.0 D2Dw \quad (2.4-26)$$

$$\{\Delta w\} = [E^{(z)}] \{\tilde{\mu}_S^{(z)}\} + [E^{(y)}] \{\tilde{\mu}_S^{(y)}\} \quad (2.4-27)$$

where Δw is the flow field caused by the bodies. Specifically, Δw is the normalwash at: 1) lifting surface elements, and 2) body interference elements (these will be discussed later) that lie off the surface of the sending body.

The superscripts z and y indicate the doublet orientation in response to velocities in the z - and y -directions. Various expressions are used for $E^{(z)}$ and $E^{(y)}$ depending on the ratio a/b of the cross section and depending on the location of the receiving point. The far field formulas (2.4-16) and (2.4-17) are used when the receiving points fall on lifting surfaces and on bodies other than the sending body. The effect of a body on itself is determined simply by the inverse of the expression for \tilde{w}_s given in Eq. (2.4-26). This means that the value of w used as a boundary condition is obtained as the effect of the body on itself. The final boundary condition on lifting surfaces and interference body elements is the difference of $w - \Delta w$. The result of this difference is zero for interference body elements lying on the sending body. Rather than go through this operation, the term w (excluding the effect of other slender bodies) is set to zero there. Thus, the effect of a body on itself is set to zero.

$$E^{(z)} = E^{(y)} = 0 \text{ when receiving elements lie on sending body} \\ w = 0 \text{ for interference body elements on the sending body} \quad (2.4-28)$$

when $b/a \geq 1$

$$E^{(z)} = \text{Equation (2.4-16) with } \gamma_s = 0 \quad (2.4-29) \\ E^{(y)} = \text{Equation (2.4-17) with } \gamma_s = -90^\circ$$

when $b/a < 1$

$$E^{(z)} = \text{Equation (2.4-17) with } \gamma_s = 0 \quad (2.4-30) \\ E^{(y)} = \text{Equation (2.4-16) with } \gamma_s = -90^\circ$$

The receiving points for lifting surfaces are, as usual, the 3/4-chord point centered spanwise. The receiving points for body interference elements are on the receiving body axis $y_r = n_{ar}$, $z_r = n_{ar}$ and centered longitudinally. For geometrical purposes, bodies are represented by constant section tubes to which lifting surfaces are attached. In some instances (e.g., a tail) this idealization moves the surface so that the proper Δw is not calculated. A provision has been made to shift surfaces (receiving points) back to their proper position.

2.5 Interference

The first step in the determination of interference has been taken in section 2.4. Specifically, the incremental normalwash Δw due to the isolated bodies has been found, Eq. (2.4-23). The resulting normalwash is

$$w_T = w - \Delta w \quad (2.5-1)$$

and is known at all lifting surfaces and bodies. This may be viewed as a new normalwash distribution to be satisfied by the lifting surfaces and bodies and need not be considered further. Simply replace w with w_T .

The basic approach to be taken in the solution of this new modified boundary value problem is to: 1) generate an approximate Green's function for lifting surfaces in the presence of several bodies, and 2) generate a residual flow used to render the Green's function exact. In simpler terms, an image system is generated within each body to divert the flow around that body when it is in the presence of the lifting surface. The image system is not completely effective in doing this, however, and a residual flow must be added. This residual potential is a simple axial singularity distribution, very similar to the axial system discussed in section 2.4.

2.5.1 The Method of Images

The method of images is not new. Lennertz³⁹ in 1927 and later Koeing⁴⁰ were two of the first to use the method for steady flow. The basic idea of the method is to match each singularity external to the body with one internal to the body at the "image" point. The strength of the internal or image singularity is directly related to that of the external singularity strength so that no new unknown distributions are introduced. The image singularity exists to negate the flow through the body surface generated by the external singularity.

The method of images has been put to use in different ways. In most of the approaches the residual flow is ignored. Exceptions are Rehorst⁴¹ and Wu and Talmadge⁴² who generated complicated expressions for the residual flow fields.

Zlotnick and Robinson⁴³ used images of unswept horseshoe vortices that are placed along the 1/4-chord point of a swept wing. The calculation of induced velocity due to a particular bound horseshoe vortex includes the image as well. The resulting integral equation for the span load is solved using a discretized Weissinger approach. Some attempts were made to account for the effect of body thickness ratio on the lift of the body.

Gray and Schenk⁴⁴ used a more approximate method. The basic approach was to: 1) determine the span load excluding the fuselage; 2) form the image system of the known loading; 3) calculate the resultant upwash distribution generated by the image system on the wing, and 4) repeat the span load calculation using the new upwash distribution.

Multhopp's method⁴⁵ and extensions of it by Weber, Kirby and Kettel⁴⁶ require a mapping of the fuselage to a vertical or horizontal slit. The fuselage is effectively reduced to either a plane of symmetry or a segment of the lifting surface. In either case the resulting simplified problem can be solved using standard methods. Such an approach ignores entirely the residual flow field. This method cannot be extended much further and generalization to more complicated configurations seems unlikely.

Giesing⁸ recently has incorporated the method of images into the lifting surface theory. All horseshoe vortices, both external and image, possess sweep. Non-midplane configurations are considered. In addition, the residual potential is accounted for using an axial doublet distribution. The approach described in the present report is an extension of this method. Spangler and Mendenhall²² have developed a similar method for more general configurations.

Extensions of the method of Gray and Schenk have recently been made. Borland²³ has extended the method to fuselage cross sections of elliptic shape. Chou²⁴ has generalized the image procedure to include nacelles. Also, an attempt was made to generalize the image approach to account for longitudinal variations in cross-sectional area.

Other approaches have been taken into account for wing-fuselage interference. For instance, slender body theory has been generalized, refined and extended to determine the flow about very slender wing-body combinations. No attempt will be made to review all of the slender configuration approaches.

Instead, reference will be made to an excellent survey paper written by Lawrence and Flax⁴⁷. This approach has not been considered for the present method since more than just slender configurations are considered.

2.5.2 The Method of Images for Circular Cross-Sections

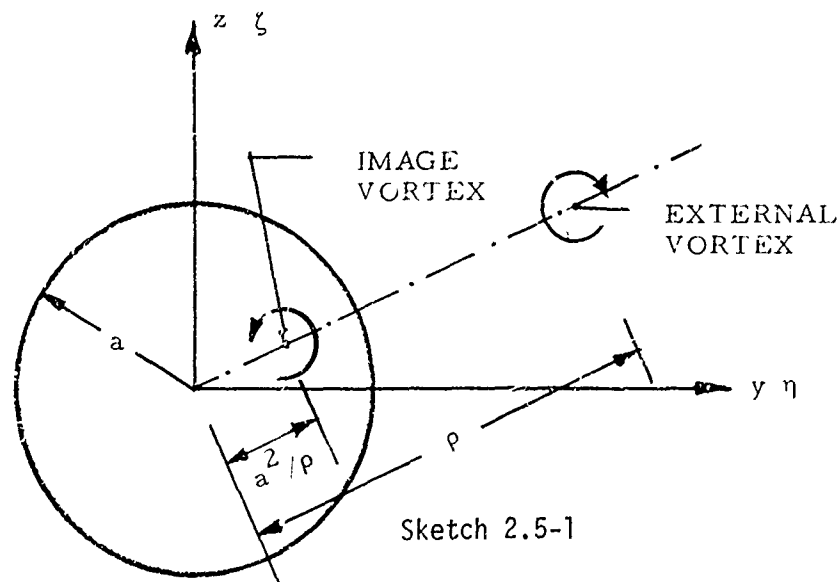
The image point and singularity strength are determined using two-dimensional theory. Appendix C shows how the Thompson Circle Theorem is applied to obtain the image point location and strengths for three types of external singularities in the presence of a body of circular cross section. The three types of singularities are: 1) the vortex, 2) the source, and 3) the doublet. The results are given in Appendix C in Equations (C-2), (C-3) and (C-5), respectively. For an external vortex of strength Γ located at η, ζ , the image strength Γ_I and location η_I, ζ_I are given as:

$$\begin{aligned}\Gamma_I &= -\Gamma \\ \eta_I &= (a^2/\rho^2)\eta \\ \zeta_I &= (a^2/\rho^2)\zeta\end{aligned}\tag{2.5-2}$$

where

$$\rho^2 = \eta^2 + \zeta^2$$

Here it is assumed that the axis of the circular body is at the origin of coordinates. Sketch (2.5-1) gives a graphical description of these results.



For the source of strength σ , there are two images

$$\begin{aligned}
 \sigma_{I_1} &= \sigma \\
 n_{I_1} &= (a^2/\rho^2)n \\
 \zeta_{I_1} &= (a^2/\rho^2)\zeta \\
 \sigma_{I_2} &= -\sigma \\
 n_{I_2} &= 0 \\
 \zeta_{I_2} &= 0
 \end{aligned} \tag{2.5-3}$$

For a doublet of strength $u(y)$ and $u(z)$ in the y and z directions, respectively, the image strengths and positions are given by:

$$\begin{aligned}
 u_I(y) &= \frac{-a^2}{\rho^4} [u(y)(n^2 - \zeta^2) + u(z)2\zeta n] \\
 u_I(z) &= \frac{a^2}{\rho^4} [u(z)(n^2 - \zeta^2) + u(y)2\zeta n] \\
 n_I &= (a^2/\rho^2)n \\
 \zeta_I &= (a^2/\rho^2)\zeta
 \end{aligned} \tag{2.5-4}$$

The location of the image in the x -direction is identical with that of the external singularity. That is, the image singularity matches the external singularity both in length and position in the longitudinal direction.

The use of a multipole expansion or singularity distribution along the axis of the body requires that the surface boundary condition (the residual normal wash generated by the external singularity and its image) must be finite and continuous on the body surface. One of the basic requirements of the image then is to render the boundary condition regular even when the external singularity lies very close to the body surface. It can be shown that such is the case. In the limit as the singularity approaches the surface from the outside,

the image singularity approaches the surface from the inside. In the limit the singularity and its image render that portion of the body surface lying between them a plane of symmetry. The flow normal to the body surface in that region is then zero. This can be shown from the expression for the image coordinates η_I , ζ_I . Consider the case $\zeta = 0$ and $\eta = a + \epsilon$. Equation (2.5-4) then gives:

$$\begin{aligned}\eta_I &= a - \epsilon + O(\epsilon^2) \\ \mu_I^{(y)} &= -\mu^{(y)} + O(\epsilon^2) \\ \mu_I^{(z)} &= \mu^{(z)} + O(\epsilon^2)\end{aligned}$$

when

$$\eta = a + \epsilon$$

This equation shows that in the limit as $\epsilon \rightarrow 0$ the surface $\eta = a$ is a symmetry plane. This is a two-dimensional result. It can be shown, however, that it also holds in three-dimensions.

As a summary of the above discussion it may be stated that:

1. The image singularity furnishes the major part of the disturbance flow necessary to satisfy the boundary condition on a body in the presence of an external singularity.
2. The boundary conditions for the residual potential (needed in addition to the image potential) is everywhere regular even when the external singularity approaches the body surface.

2.5.3 The Method of Images for Noncircular Cross Sections

Borland²³ has developed an image system for elliptic cross sections. The image point is obtained by transforming the circle image points. The transformation is the one that carries the circle to the ellipse. The image coordinates given in complex form are:

$$\eta_I + i\zeta_I = \frac{\tilde{r}^4 + (1/4)K^2(A + iB)^2}{(1/2)\tilde{r}^2(A + iB)} \quad (2.5-5)$$

where

$$A + iB = n - i\zeta + \sqrt{(n - i\zeta)^2 - 4K^2}$$

$$\tilde{r} = (a + b)/2$$

$$K^2 = \frac{a^2 - b^2}{4}$$

The terms a and b are the semi-major and semi-minor axes, respectively. This formula is not valid for singularities lying outside of the region bounded by the ellipse

$$\frac{\zeta^2}{(\tilde{r}^2/|K| - K^2|K|/\tilde{r}^2)^2} + \frac{n^2}{(r^2/|K| - K^2|K|/r^2)^2} = 1$$

since the image point then lies on the wrong Riemann sheet. This is not a serious deficiency since the image system is intended mainly to eliminate the nonuniform flow field associated with singularities that lie close to the body surface. Under this circumstance the behavior of the image is identical to that described in the last subsection. In a small region near the singularity the surface of the body becomes a plane of symmetry in the limit as the singularity approaches the surface.

As anticipated, the image approach is not as effective for noncircular cross section as it is for circular cross section. The image does not render the ellipse a streamline even in the two-dimensional cross section plane. The residual potential then will be larger for noncircular cross sections.

A second method of determining the image point for noncircular cross sections is given in Appendix C. The method is based on the concept of local center and radius of curvature. If the radius and center of curvature are known on that part of the body cross section which lies closest to the external singularity, then an image point may be found using the circle produced by that center and radius. The image is calculated using the formulas for the circular cross section where the circle center and radius vary depending on the position of the external singularity relative to the cross section. Sketch C-2 in Appendix C gives an illustration.

The formulas for the radius and center of curvature have been developed for an elliptic cross section in Appendix C. If \vec{C} is the vector from the center of the ellipse to the center of curvature and \bar{a} is the local radius of curvature, then:

$$\vec{C} = \vec{j} \left(\frac{a^2 - b^2}{a} \right) \cos^3 \theta + \vec{k} \left(\frac{b^2 - a^2}{b} \right) \sin^3 \theta \quad (2.5-6)$$

$$\bar{a} = \frac{(a^2 \sin^2 \theta + b^2 \cos^2 \theta)^{3/2}}{ab} \quad (2.5-7)$$

where the parameter θ is related to y and z as follows:

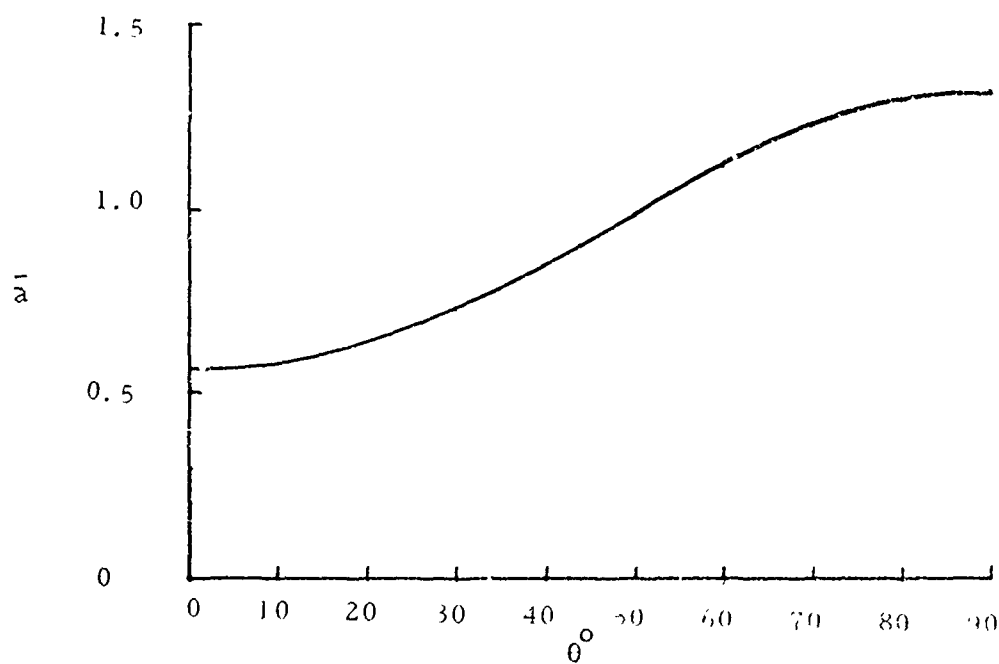
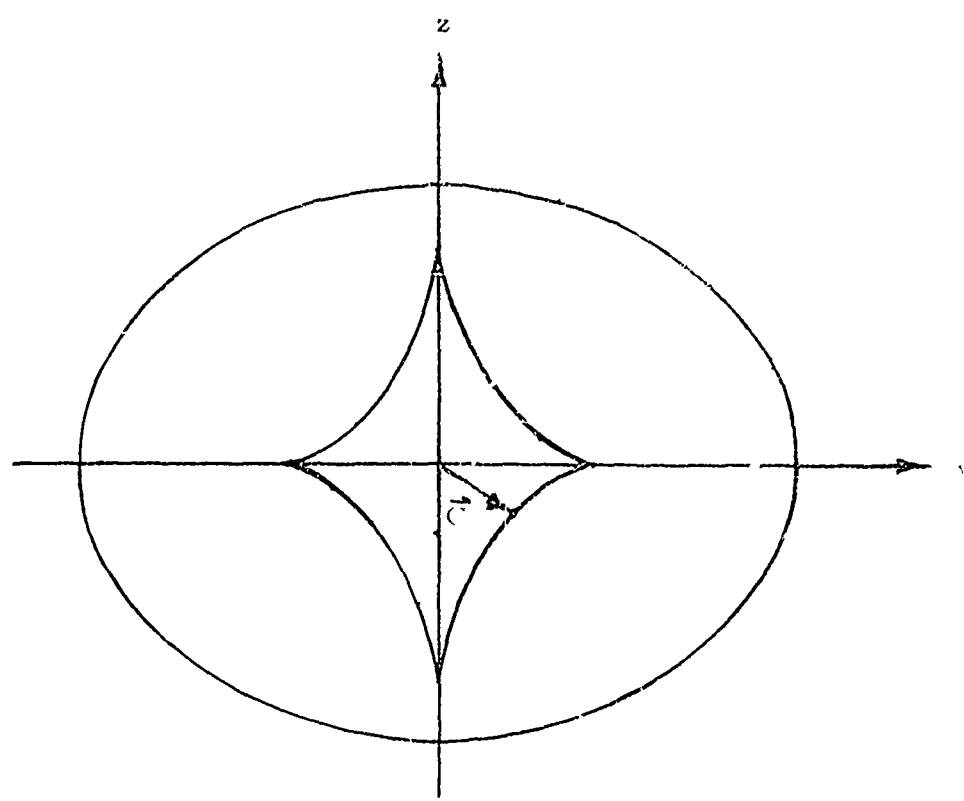
$$y = a \cos \theta$$

$$z = b \sin \theta$$

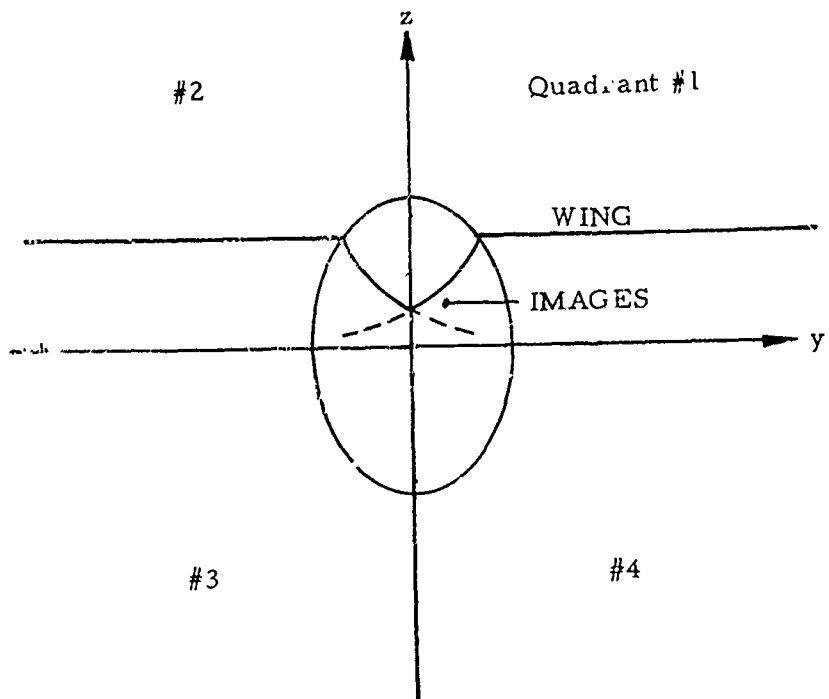
The unit vectors \vec{j} and \vec{k} are in the y - and z -directions, respectively. Sketch 2.5-2 presents a plot of the locus of \vec{C} which is the evolute of the ellipse and a plot of \bar{a} for an ellipse of b/a ratio of 0.75.

As the ratio b/a is reduced, the center of curvature eventually passes outside of the ellipse, thus allowing the possibility that the image may pass outside of the ellipse. This method, like the last, works best for singularities that lie close to the body. The determination of which method is best — either Borland's or the method just described — remains to be seen. In any case, it is anticipated that there will be restrictions on the ratio b/a and on the position of the external singularities as far as images are concerned.

The present method uses the local center of curvature approach with a further restriction: the image point must lie in the same quadrant as the external singularity. If it does not, it is ignored. This restriction eliminates the overlapping of image sheets within the body. That part of the image surface indicated by a dashed line in the example of Sketch 2.5-3 is the part that is ignored.



Sketch 2.5-2



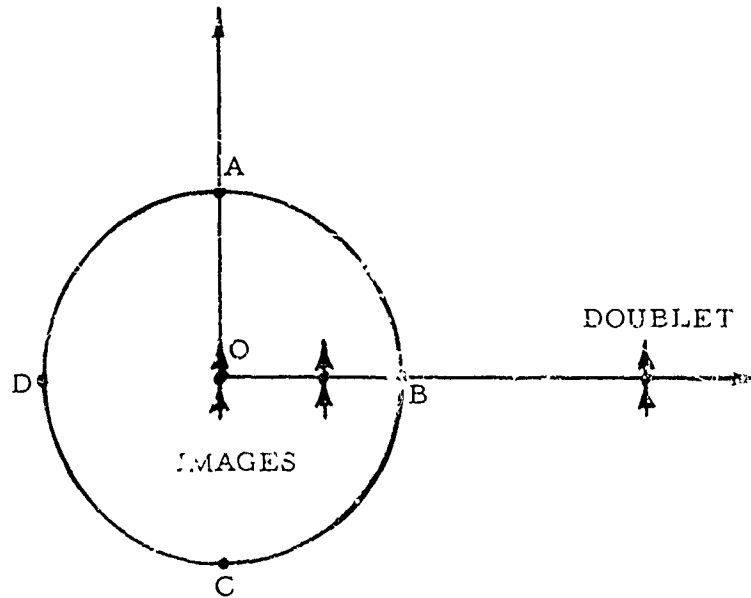
Sketch 2.5-3

2.5.4 The Method of Images for Unsteady Flow

The method of images can be taken over into the unsteady regime essentially unchanged. Attempts to refine the image to account for unsteady effects have led to the conclusion that unsteady effects can be lumped into the residual potential.

Consider the cross section given in Sketch 2.5-4. Attempts to refine the image system so that unsteady effects are accounted for include:

1. An adjustment of the strength and location of the image such that the boundary conditions at A, B and C are satisfied in unsteady flow;
2. Adjustment of the strength of a second doublet located at "0" and the position of the image doublet such that the boundary conditions at A, B and C are satisfied in unsteady flow; and
3. Adjustment of the strength of the second doublet (at "0") and the strength of the image doublet so that the boundary conditions at A, B and C are satisfied in unsteady flow.



Sketch 2.5-4

All of the approaches are based on the assumption that the similarity variable $\bar{k} = k_r r/\bar{c}$ is small. Consistent with this approximation is the use of Laschka's simplified expression⁴⁸ for the kernel downstream of a pressure doublet. (The expression is valid if $(\beta r/(x - \xi))$ is small.) This expression is expanded in terms of \bar{k} and terms up to $\bar{k}^2 \ln \bar{k}$ and \bar{k}^2 are retained. In all of the attempts outlined, the changes in strength and position of the image are small (proportional to $\bar{k}^2 \ln \bar{k}$ and \bar{k}^2) so that products of high-order terms are ignored.

The basic idea of the first attempt is to adjust the image strength so that the boundary condition at A (and by symmetry at C) is satisfied for any image position. The boundary condition at A and C requires that there be a stagnation point at A and C. The next step is to calculate the value of the stream function on the body surface at A and C. The image position is then adjusted so that the value of the stream function at B matches the value calculated at A and C.

It was found that the boundary condition at A and C could not be maintained when the external and image singularities approached the circular surface.

The second attempt was meant to correct this condition. Instead of using the image strength to satisfy the boundary condition at A and C, a second doublet was introduced at the origin to do so. Again the stream function was calculated at A and C and the image location adjusted until the stream function at B matched that calculated at A. This method works except when the external singularity is at a large distance from the body. This is not a serious drawback since the basic expansion in terms of $k_r r/\bar{c}$ fails there also. The basic drawback with this method as with the first one is that an adjustment of distance is involved. The image position is adjusted. This adjustment, however, must vary in the longitudinal direction; the correction to the position of the image varies like $e^{-i \omega x/U_\infty}$. Changing the position of the image with x is practical only when the frequency is small. This type of correction is complicated and not worth the effort.

The third attempt was directed toward the development of a correction that does not involve adjustment of any distance. The idea is to adjust the strength of the doublet at the origin for any strength image so that the boundary condition at A and C is satisfied. The strength of the image was then adjusted until the stream function at B was equal to that calculated at A and C. This approach has no real deficiencies except that the status of the boundary condition at D and in between A, B, C, and D is unknown. Also, this method like the second method fails for singularities located at large distances from the body.

The conclusions drawn after analyzing the above three attempts to correct the image is that it is better to lump unsteady effects into the residual potential. The last two attempts described actually use a correction flow (the new doublet at the origin) to correct for unsteadiness. Rather than generate a residual solution for each singularity and image separately, it seems logical to generate the residual potential only once. The description of the residual potential is given in section 2.5.6.

2.5.5 Formation of the Influence Matrix with Images

Each lifting surface element has its image. For each unsteady horseshoe vortex exterior to the body, there may be an image unsteady horseshoe vortex within the body. The expression for the normalwash influence matrix for

elements exterior to the body may be rewritten from Eq. (2.3-1) as

$$D = \frac{\Delta X}{8\pi} \int_{-e}^e K d\eta \quad (2.5-8)$$

The influence matrix from the image element is:

$$D_I = \frac{\Delta X}{8\pi} \int_{-e_I}^{e_I} K_I d\tilde{\eta} \quad (2.5-9)$$

The required image quantities are determined from the edge locations of the image element. If η_1, ζ_1 are the coordinates of the inboard edge of the exterior surface element, and η_2, ζ_2 are the outboard coordinates, and $\bar{\eta}_a$ and $\bar{\zeta}_a$ are the coordinates of the local center of curvature, then the corresponding image locations are:

$$\begin{aligned} \eta_{I_1} &= \bar{\eta}_a + \frac{\bar{a}^2}{\rho_1} (\eta_1 - \bar{\eta}_a) \\ \zeta_{I_1} &= \bar{\zeta}_a + \frac{\bar{a}^2}{\rho_1} (\zeta_1 - \bar{\zeta}_a) \\ \rho_1^2 &= (\eta_1 - \bar{\eta}_a)^2 + (\zeta_1 - \bar{\zeta}_a)^2 \end{aligned} \quad (2.5-10)$$

Similarly, for η_{I_2} and ζ_{I_2} . These expressions are slightly different from those of (2.5-2) because it is no longer assumed that the body on ζ is at the origin.

$$\begin{aligned} e_I &= \sqrt{(\eta_{I_2} - \eta_{I_1})^2 + (\zeta_{I_2} - \zeta_{I_1})^2} \\ \cos \gamma_I &= -\frac{(\eta_{I_2} - \eta_{I_1})}{e_I} \\ \sin \gamma_I &= -\frac{(\zeta_{I_2} - \zeta_{I_1})}{e_I} \end{aligned} \quad (2.5-11)$$

The sweep angle of the image element, λ_I is given by

$$\sin \lambda_I = \frac{\Delta \xi}{\sqrt{\Delta \xi^2 + e_I^2}} \quad (2.5-12)$$

$$\cos \lambda_I = \frac{e_I}{\sqrt{\Delta \xi^2 + e_I^2}}$$

Each body in the flow may possess an image of the external lifting surface image. For the sake of efficiency, it is not required that each body have a complete image system. That is, every lifting surface element need not have an image in every body. Only those bodies that lie close to the lifting surface element are required to possess an image of the element. Also, if a lifting surface element lies out of the range of the body longitudinally, then no image exists. Taking into account all image elements, the normal wash becomes:

$$\begin{aligned} \{w_R\} &= [\bar{D}] \{\Delta C_p\} \\ \bar{D} &= D + \sum_{b=1}^{NAB(s)} D_I^{(b)} \end{aligned} \quad (2.5-13)$$

where the superscript b ranges over all bodies that must have images associated with the element. The velocity w_R is the sum of the velocity due to lifting surface elements, w_s , and their images, w_I .

$$w_R = w_s + w_I$$

It is convenient at this point to include the effects of symmetry and ground effect. The effect of symmetry is to introduce a system of lifting surface elements, plus their images, on the left-hand side of the $y = 0$ plane. The η -coordinates of the sending elements are changed from η to $-\eta$. Similarly, the dihedral angle changes from γ_s to $-\gamma_s$. Elements lying on the symmetry plane (in the $y = 0$ plane) have no image. The effect of the ground plane is to introduce a system of lifting surface elements, plus images, below the $z = 0$ plane. The ζ -coordinates of the sending

elements are changed from ζ to $-\zeta$. The dihedral angle changes from γ_s to $-\gamma_s$. The interaction of ground effect and symmetry is to change n to $-n$, ζ to $-\zeta$ and leave γ_s unchanged.

$$\bar{D} = \bar{D}(n, \zeta, \gamma_s) + \delta\bar{D}(-n, \zeta, -\gamma_s) + \epsilon\bar{D}(n, -\zeta, -\gamma_s) + \delta\epsilon\bar{D}(-n, -\zeta, \gamma_d)$$

Note that the effect of images is included in Eq. (2.5-13) because of its inclusion in \bar{D} . Eq. (2.5-13) may be rewritten as

$$\{w_R\} = [\bar{D}] \{\Delta C_p\} \quad (2.5-14)$$

2.5.6 The Residual Interference Flow

The image singularity, of course, is not completely effective in diverting the flow, generated by the external singularity, around the body. The reason is that two-dimensional theory was used to develop the image. It is surprising, however, how well it does work. Wu and Talmadge⁴² have attempted to solve the full three-dimensional problem of a semi-infinite line doublet in the presence of a shape that has a circular cross section and is infinite in length*. Their approach is to break the potential into two parts: ϕ_1 due to a doublet and its image (as discussed above) and ϕ_2 an incremental potential used to render the solution exact. The basic approach is to calculate the flow normal to the surface as generated by the singularity and its image, i.e., as generated by ϕ_1 . Then a Fourier-Bessel series is used to negate this residual normalwash. Basically, what this series represents is a distribution of singularities along the axis of the body. Near the axis the Bessel function can be approximated by the functions $1/r^n$. Thus, the series sum over n represents a wave equation multipole expansion. Wu and Talmadge have shown that the residual upwash and thus the incremental potential is everywhere small. The variation with x is given as:

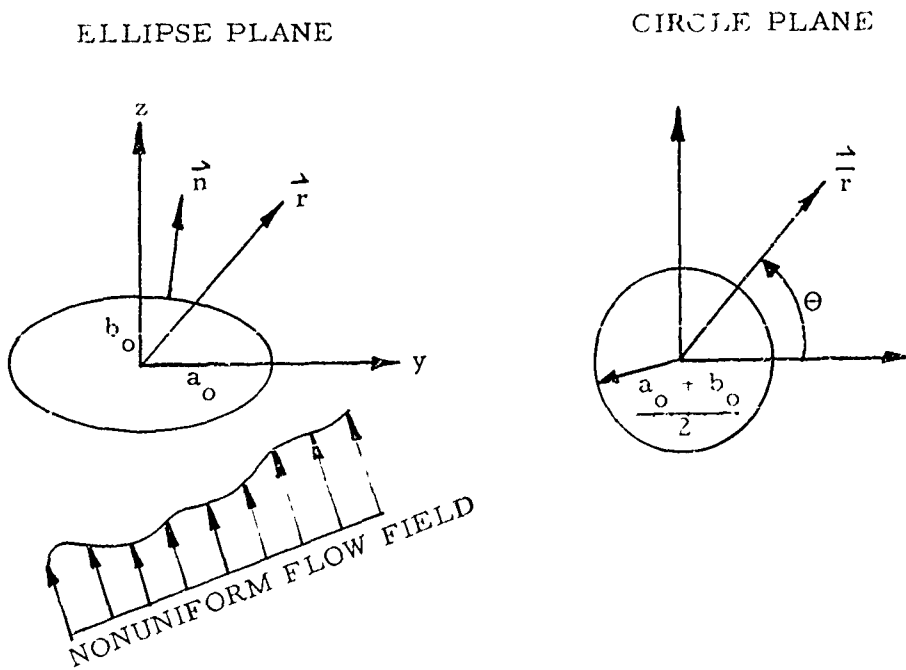
$$\lim_{x \rightarrow 0} \phi_2 \rightarrow 0(x)$$

$$\lim_{x \rightarrow \infty} \phi_2 \rightarrow 0(x^{-2})$$

*Wu and Talmadge actually consider a jet and not a body. However, the basic solution for the jet and body are very similar.

Although the image system makes the major contribution towards satisfying the body boundary condition, there are still some effects not accounted for. These effects can be classified loosely as follows: 1) effects of bound vorticity, 2) effects of noncircular cross sections, and 3) effects of unsteadiness.

These effects produce residual velocities normal to the body surface. These residual velocities, however, are free from singularities since it was one of the main requirements of the image system to eliminate such singularities. Since no singularities exist, a solution of the axial singularity type may be used. Again, slender body theory will be used to find the strength of the axial singularity required to eliminate the residual velocity normal to the body surface. In order to use the axial singularity system, an effective up-or sidewash velocity must be determined from the nonuniform residual onset flow obtained from the lifting surface and its image surface. Slender body theory allows two-dimensional quasi-steady methods to be employed to find this effective velocity. The basic problem is shown in Sketch 2.5-5.



Sketch 2.5-5

The basic steps in the solution are outlined as follows:

1. Transform the normal velocity boundary conditions, which are caused by nonuniform residual onset flow, to the circle plane;
2. Solve the potential flow problem in the circle plane;
3. Transform the solution back to the ellipse plane;
4. Knowing the doublet strength, find the effective velocity necessary to produce it.

The normal component of the residual velocity, w , is

$$w = \vec{n} \cdot \{ j w_R(y) + k w_R(z) \} \quad (2.5-15)$$

where w_R is the residual onset flow. This residual onset flow is caused by the lifting surface elements plus their images inside the body (or bodies). That is

$$w_R = w_S + w_I$$

For an ellipse

$$\vec{n} = \frac{j b \cos \theta + k a \sin \theta}{\sqrt{b^2 \cos^2 \theta + a^2 \sin^2 \theta}}$$

The normal velocity transformed into the circle plane, \bar{w} , is

$$\bar{w} = w \frac{2}{1 + b/a} \sqrt{1 - [1 - (b/a)^2] \cos^2 \theta} \quad (2.5-16)$$

In the circle plane this normal velocity may be negated by a multipole expansion centered on the body axis. In the circle plane the multipoles are designated by $\frac{\mu}{v}$.

$$-\bar{w} = -\frac{1}{2\pi} \sum_{v=1}^{\infty} v \left[\frac{\frac{\mu}{v}(y) \cos v\theta}{r^{v+1}} + \frac{\frac{\mu}{v}(z) \sin v\theta}{r^{v+1}} \right] \quad (2.5-17)$$

where the subscript v indicates the order of the singularity considered. For example, $v = 1$ indicates a doublet, etc. If both sides of Eq. (2.5-17)

are multiplied by $\cos \bar{v}\theta$ and integrated from $\theta = 0 \rightarrow 2\pi$ the result is:

$$\int_0^{2\pi} \bar{w} \cos \bar{v}\theta d\theta = \frac{1}{2} \sum_{v=1}^{\infty} \frac{\tilde{\mu}_v(y)}{r^{\bar{v}+1}} \quad (2.5-18)$$

Similarly, if $\cos \bar{v}\theta$ is replaced with $\sin \bar{v}\theta$, the result is

$$\int_0^{2\pi} \bar{w} \sin \bar{v}\theta d\theta = \frac{1}{2} \sum_{v=1}^{\infty} \frac{\tilde{\mu}_v(z)}{r^{\bar{v}+1}} \quad (2.5-19)$$

Eqs. (2.5-18,-19) give the values of the doublet, quadrupole, etc., strengths to satisfy the normal velocity boundary conditions. These singularity strengths may be transformed back to give the appropriate singularities in the ellipse plane. Formulas developed previously (Section 2.4) for the far field properly represent the multipole expansion through the second term $\bar{v} = 2$. The distance d is selected such that the proper quadripole strength is generated. In Section 2.4 the distance d was a function of the cross section only, i.e., b/a , however, here d is a function of both cross section and nonuniformity in the residual onset flow field. It is impractical to use an influence formula that is a function of onset flow, thus the effect of nonuniformity on the value of d will be ignored. Only the cross-sectional shape will be used to determine d . Since d has been determined previously, only the doublets need be considered in Eqs. (2.5-18, -19). The doublet transforms unchanged from the circle plane to the ellipse plane. After substituting m for \bar{w} (Eq. (2.5-16)), the expressions for $\tilde{\mu}(y)$ and $\tilde{\mu}(z)$ (remember $\mu = 2\tilde{\mu}$) become:

$$\tilde{\mu}(y) = 2a^2(1 + b/a) \int_0^{2\pi} w \cos \theta \sqrt{1 - [1 - (b/a)^2] \cos^2 \theta} d\theta \quad (2.5-20)$$

$$\tilde{\mu}(z) = 2a^2(1 + b/a) \int_0^{2\pi} w \sin \theta \sqrt{1 - [1 - (b/a)^2] \cos^2 \theta} d\theta \quad (2.5-21)$$

Numerically, the integrals are replaced by sums in the present method. These integrals may be translated into an equivalent velocity as follows:

$$w(y) = D_{2D}(y) w(y) \quad (2.5-22)$$

$$w(z) = D_{2D}(z) w(z) \quad (2.5-23)$$

where $w(y)$ is simply the right-hand-side of Eq. (2.5-20) divided by $D_{2D}(y)$. The term $w(z)$ may be found in a similar manner. The superscripts (y) and (z) on the term D_{2D} are to indicate that there is a difference between them for noncircular cross sections.

$$D_{2D}(z) = 2\pi a_0(a_0 + b_0) \quad (2.5-24)$$

$$D_{2D}(y) = 2\pi b_0(a_0 + b_0) \quad (2.5-25)$$

In Eqs. (2.5-20) and (2.5-21) the terms a and b are those used for the image calculation. That is, they are constant for the entire cross section. Thus, the velocity normal to the surface is calculated on the constant section tube used for the images. The values of a_0 and b_0 found in Eqs. (2.5-24) and (2.5-25) vary along the length of the body. When Eqs. (2.5-24) and (2.5-25) are placed into Eqs. (2.5-22, -23) and then into (2.5-20, -21), the results are:

$$w(y) = \frac{1}{\pi} \frac{a(a+b)}{a_0(a_0 + b_0)} \int_0^{2\pi} f w \cos \theta d\theta \quad (2.5-26)$$

$$w(z) = \frac{1}{\pi} \frac{a(a+b)}{a_0(a_0 + b_0)} \int_0^{2\pi} f w \sin \theta d\theta \quad (2.5-27)$$

$$f = \sqrt{1 - [1 - (b/a)^2] \cos^2 \theta}$$

The assumption that is made for the calculation is that the image cross section approximates the actual one. In order to more closely transfer this onset flow to the actual surface, the value of $a(a+b)/a_0(a_0 + b_0)$ is set to unity. The velocity normal to the surface of the ellipse due to lifting surface elements and images is calculated using D and D_I . If the sending element is located along a body axis and not on a lifting surface, then, $E^{(y)}$ and $E^{(z)}$ are used. The dihedral angle at the receiving point to be used is the

local surface slope on the elliptic cross section. The integrals are evaluated by calculating w at various points around the circumference of the cross section

$$w(y) = \frac{1}{\pi} \sum_{v=1}^{N\theta} w_v \cos \theta_v f_v \Delta \theta_v \quad (2.5-28)$$

A similar expression exists for $w(z)$. The subscript v indicates that the receiving point is located at θ_v as follows:

$$\begin{aligned} y &= n_a + a \cos \theta_v \\ z &= \xi_a + b \sin \theta_v \\ \cos \gamma_{r_v} &= \frac{a}{\rho} \sin \theta_v \\ \sin \gamma_{r_v} &= \frac{-b}{\rho} \cos \theta_v \\ \rho &= \sqrt{b^2 \cos^2 \theta + a^2 \sin^2 \theta} \end{aligned} \quad (2.5-29)$$

Eqs. (2.5-26, -27), are applied to the influence matrix relating the normalwash due to a lifting surface element and its image at the body surface.

As it stands in Eq. (2.5-14) $\{w_R\}$ is partitioned into two parts: 1) the normalwash at the lifting surface elements, w_R , and 2) the normalwash at the body surface at various meridian angles (θ_v) , $w_R^{(\theta)}$

$$\{w_R\} = \left\{ \begin{array}{l} w_R \\ w_R^{(\theta)} \end{array} \right\} = \left[\begin{array}{c} \bar{D} \\ \bar{D}(\theta) \end{array} \right] \{\Delta C_p\} \quad (2.5-30)$$

In order to obtain the average z - and y -velocities at the bodies Eqs. (2.5-26, -27) must be applied

$$\bar{D}(z) = \frac{1}{\pi} \int_0^{2\pi} \bar{D}_\theta f \cos \theta d\theta \quad (2.5-31)$$

$$\bar{D}(y) = \frac{1}{\pi} \int_0^{2\pi} \bar{D}_\theta f \sin \theta d\theta \quad (2.5-32)$$

Then the matrix $\{w_s\}$ becomes:

$$\{w_R\} = \begin{Bmatrix} w_R \\ -w_R(z) \\ -w_R(y) \\ w_R \end{Bmatrix} = \begin{Bmatrix} \bar{D} \\ -\bar{D}(z) \\ -\bar{D}(y) \end{Bmatrix} \left\{ \Delta C_p \right\} \quad (2.5-33)$$

It is important to notice that the cross-sectional shape (and size) used in the determination of the effective up- and sidewash (Eqs. (2.5-31, -32)) must be the same as that used to determine the images. This cross section is constant for the entire body length. The effective velocity obtained from these calculations, however, is applied to the actual body cross-sectional shape and size through the use of the local influence function $D2D$ and the setting of the term $a(a + b)/a_0(a_0 + b_0)$ to unity.

Thus far the effect of lifting surface elements and their images on bodies has been considered. Attention is now turned to the interference effects of bodies on all parts of the configuration, i.e., other bodies and lifting surfaces.

The residual interference flow is to be generated using the same singularities as those used for the isolated body (section 2.4, Eqs. (2.4-16, -17)). The only differences are: 1) that the distribution of elements will be different, 2) the normalwash is determined at points on the cross-sectional surface rather than at the body axis (even though the results are applied to the exact surface).

The distribution of elements for interference could be identical to that for the isolated body for simplicity. However, this is inefficient. The singularity strengths for the isolated body are known and do not add to the number of unknowns in the problem as do the interference elements. For this reason a generous number of elements may be allocated, for the isolated body, to properly describe the body radius distribution, the greatest variation of which is near the leading and trailing edges. The greatest variation in the residual flow may be elsewhere, specifically near the body/lifting-surface intersection.

The body radius must equal the constant value used in the image calculation. The reason is that the image singularity surfaces exist within this constant section tube. Thus, two idealizations for the body are used: 1) to generate the flow field of the isolated body, the exact radius distribution is used, and 2) to account for interference, a tube of constant cross section is used along with the exact body shape.

The residual flow field due to lifting surfaces and images has nonuniformities across the body surface. Thus, the averaging of this nonuniform velocity, given by Eqs. (2.5-26, -27) is required. For the effect of bodies on other bodies, however, the nonuniformities are small and the normalwash may be evaluated on the axis.

The influence matrix relating the normalwash at a field point due to an interference body element is formally the same as that for an isolated body except that the values of $\mu_n^{(y)}$, $\mu_n^{(z)}$ are not known.

$$\{w_n\} = [E^{(z)}] \{\mu_n^{(z)}\} + [E^{(y)}] \{\mu_n^{(y)}\} \quad (2.5-34)$$

$E_{rs}^{(z)} = E_{rs}^{(y)} = 0$ when the receiving element lies on the sending body
except when $r = s$

$$\begin{aligned} E_{rs}^{(z)} &= D2D(z) \text{ when } r = s \\ E_{rs}^{(y)} &= D2D(y) \text{ when } r = s \end{aligned} \quad (2.5-35)$$

$$b/a \geq 1$$

$$\begin{aligned} E_{rs}^{(z)} &= \text{Eq. (2.4-16) with } \gamma_s = 0 \\ E_{rs}^{(y)} &= \text{Eq. (2.4-17) with } \gamma_s = -90^\circ \end{aligned} \quad (2.5-36)$$

$$b/a < 1$$

$$\begin{aligned} E_{rs}^{(z)} &= \text{Eq. (2.4-17) with } \gamma_s = 0 \\ E_{rs}^{(y)} &= \text{Eq. (2.4-16) with } \gamma_s = -90^\circ \end{aligned} \quad (2.5-37)$$

The receiving points for the lifting surface elements are the 3/4-chord points. The receiving points for the bodies are on the body axis at $y_r = n_{a_r}$, $z_r = \xi_{a_r}$ and centered longitudinally on the element.

In summary then, the residual interference is handled in the following manner:

1. The up- or sidewash at bodies due to lifting surfaces and their images is determined using an averaging technique on the normalwash at the body surface. The body surface used for this purpose is a constant cross-section tube.
2. Interference body elements are used to negate the up- and sidewash given in (1) and also the up- and sidewash generated by other bodies. The interference body elements are distributed differently from isolated or slender body elements. This is done to reduce the number of unknowns in the problem and to place interference elements where they are most needed.

2.5.7 The Use of Surface Singularities for the Residual Interference Flow

In the last section axial singularities were used for the determination of the residual potential. An alternate method is presented here. Specifically, the normalwash boundary condition can be satisfied using a distribution of either unsteady horseshoe vortices or quadrilateral vortices on the body surface. In Part I of this report, unsteady horseshoe vortices were used on the body surface to account for all of the body/lifting-surface interference. (Slender body elements were used to determine Δw .) For the present method, however, surface singularities on the body surface may be used to account only for the well-behaved residual flow. Thus, both an image system and surface singularities can be used. The number of elements on the body surface need not be as large as for the method of Part I since the residual flow is well behaved. However, the introduction of surface singularities greatly increases the number of unknowns in the problem and the computational effort. It is anticipated that this method will be used only for difficult configurations or if a very high degree of accuracy is required. It may also be desirable to have such an approach for cross-checking purposes.

The normalwash, w_T , to lifting surface elements lying on body surfaces is determined in the same manner as the w_T for axial interference elements. The only difference is that the velocity normal to the surface elements is determined instead of z- and y-wash at the body axis. For a single body, w_T at these surfaces is zero since it is assumed that the slender body axial distribution has diverted the onset flow around the body surface (except for interference flow). If two or more bodies exist (including symmetry and ground effect bodies), then one body may induce a nonzero w_T on another body.

Eventually it may be desirable to use quadrilateral vortices that are inclined to the flow field so that more details of the body surfaces may be treated. In such a case it is necessary to use a more general formula than the one developed in Appendix B. An expression for a pressure doublet inclined to the flow was developed by Berman⁴⁹. Such an expression integrated over an element would give an inclined horseshoe vortex. This type of singularity is unsatisfactory for the body surface since a wake trails back from each point on the surface. Such wakes would then thread in and out of the body surface. A similar expression for a velocity potential doublet would be desirable to produce an inclined quadrilateral vortex without a wake. If any wake did exist it could be added at the end of the body using unsteady horseshoe vortices.

2.5.8 The Image System for Wing-Tail Configurations

The method of images requires a body of constant cross section. The image system trails back on the inside of the body without any changes in lateral position. The application of the image system concept to bodies of variable cross section with special reference to the wing-tail problem is the subject of this subsection.

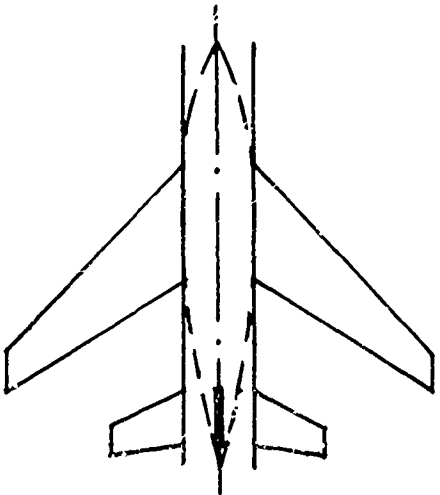
If a lifting surface system is attached to a body at only one location, then a fairly simple solution to this problem exists. At the intersection of the body lifting-surface system an average body cross section is selected for use with the image system. The effects of the lifting surface on the actual body can be determined on this average surface. In other words, the normalwash to the actual body surface generated by the lifting surface and image

system can be calculated on the average surface. The results calculated on the average surface are then applied to the actual surface as if they were calculated on the actual surface. If the residual flow field is reasonably uniform (laterally), then very little error should be introduced with this method.

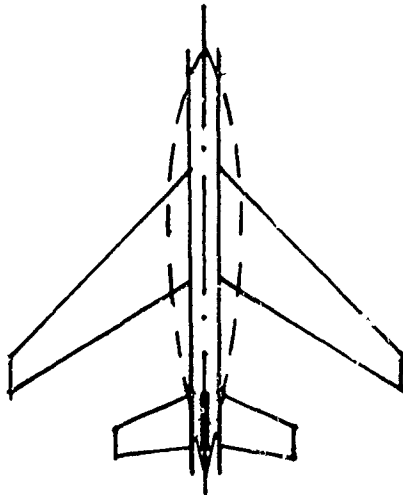
This approach is very similar to that of Woodward for steady flow. His basic approach is to use slender body theory for the exact body shape in a uniform flow to determine the axial doublet and source distribution. These singularities are then used to calculate an offset flow to the lifting surfaces on the wing. Lifting surface elements are then placed on an idealized body shape of constant cross section to account for the rest of the interference. If a wing-tail configuration is considered, then the tail must be attached to the idealized body shape. This idealized shape usually takes on the radius of the body as it is at the wing-body intersection. This may cause errors in the tail loads for two reasons: 1) the relative positions of the left and right horizontal stabilizers as well as the fin may be changed considerably to accommodate the idealized fuselage shape, and 2) the loads in the presence of a very large diameter fuselage are different from those in the presence of a small diameter fuselage. Reference 21 gives examples of the Woodward approach for the B-58 and other aircraft configurations.

A possible solution for the wing-tail problem is to use one idealization for wing-body interference and second idealization for the tail-body interference. This cannot be done with the Woodward approach, but it may be possible with the present approach. For instance, the body idealization suitable for the wing-body intersection could be used to determine wing-on-wing, wing-on-body, and wing-on-tail interference. The body idealization suitable for the tail-body intersection could be used to determine tail-on-tail, tail-on-body and tail-on-wing interference. Sketch 2.5-6 gives a graphical example of this approach.

The relative positions of the left and right lifting surface systems are now correct for the local influence of these surfaces on themselves. The effect of the wing on the wing is very accurate as well as the effect of the tail on the tail. The effect of the wing on the tail deserves some special consideration. The approach outlined accounts, in a crude way, for the fact that the wake follows the flow field around the body. Consider, for instance,



IDEALIZATION FOR DETERMINING
THE EFFECT OF THE WING ON
ITSELF AND OTHER PARTS OF THE
AIRCRAFT



IDEALIZATION FOR DETERMINING
THE EFFECT OF THE TAIL ON
ITSELF AND OTHER PARTS OF
THE AIRCRAFT

Sketch 2.5-6

the trailing vortex at the wing root. This vortex follows the fuselage and crosses the tail plane at the fuselage-tail intersection, i.e., at the horizontal tail root. With the approach just outlined, the same effect is achieved by placing the wing and tail-root sections at the same points laterally. If more information is known about the wake location, either laterally or vertically, the tail position could be adjusted to more accurately reflect the relative geometries of the wing wake and tail. The idea is to select an idealization that places the wing wake properly relative to the tail since it is the wake that generates the strong wing-tail coupling.

Adams and Sears³³ presented a fairly simple formula for calculating the lateral streamline displacement about a body of revolution neglecting vortex sheet roll-up. It is

$$r^2(\xi) = r^2(\xi_1) - a_0^2(\xi_1) + a_0^2(\xi) \quad (2.5-38)$$

Here $r(\xi)$ is the lateral position of a streamline (where the radius is $a_0(\xi)$) that had its origin at $r(\xi_1)$ (where the radius is $a_0(\xi_1)$). Such a formula could be used to determine where wing trailing vortices emanating at $r(\xi_1)$

will strike the tail plane. The use of this approach would cause practical difficulties for the lattice method*. In the lattice method the trailing vorticity is idealized in discrete vortex lines. These vortices must impinge on the tail plane at strip edges (if wing and tail are coplanar or near coplanar). The strips at the horizontal tail must then be adjusted so that they align with the wing edges after the transformation (2.5-38) is applied.

By far, the largest factor in determining the position of the wing wake at the tail is the vortex sheet convection and roll-up. Although the present method does not determine this effect, there is no fundamental reason why it could not be included at a later date. It seems appropriate, at the present time, to delay the inclusion of the second-order wing-tail idealization improvements (outlined in this section) until a full study of all of the second-order effects can be made.

2.6 Body Force and Moment Distributions

Heretofore this report has concerned itself with the determination of the singularity system that has been substituted in place of the aircraft. This section deals with the loading obtained from the singularity distribution and subsequently the generalized forces from the loading.

On all lifting surfaces the loading is equal to the singularity strength and thus no further discussion is needed. However, for the bodies involved, the situation is much more complicated.

The objective is to develop a simple set of expressions for the load distribution on a body, in the presence of a singularity distribution. Both the singularity distributions interior to the body (axial doublets, vortex quadrilaterals and images) and those exterior to the body (lifting surface elements and axial singularities on other bodies) generate lifting forces on bodies. Unlike lifting surfaces, bodies have nonzero thickness. A change in potential, say from the bottom to the top side of a body, causes a net

*Such a method would be fairly easy to apply to loading function methods. The spanwise distribution of vorticity would simply be modified by Eq. (2.5-38).

force. The flow fields of all singularity distributions give rise to a variation in $\phi_x + i\omega\phi$ across the body and thus generate a force on the body. Such a variation is not experienced by lifting surfaces since they are of zero thickness. The only variation is caused by the local potential jump, $\Delta\phi$, which generates the local ΔC_p . The contribution to the loading from the slender body singularities is easily obtained using the theory of Miles. The contributions due to the rest of the singularities will be determined numerically.

All of the singularities used to model the aircraft can be expressed in terms of unsteady pressure doublets. It is sufficient, then, to develop an expression for the force and moment on a body due to a point pressure doublet. This expression is then applied to the equivalent pressure doublet distribution that has been substituted for the actual singularity distribution.

2.6.1 Reduction of All Singularity Distributions to Pressure Doublet Distributions

The reduction of the unsteady horseshoe vortices to doublets is straightforward since the horseshoe vortex is simply an integration of the pressure doublet in the spanwise direction over a short element. The unsteady horseshoe vortex is simply replaced by one or more point doublets depending on the accuracy required and the distance between the horseshoe vortex and body. Currently, in the present method, only one point pressure doublet is used. The total doublet strength of an unsteady horseshoe vortex of strength ΔC_p is $\Delta C_p \cdot A$ where A is the area of the element associated with the horseshoe vortex. In the analysis of Appendix D it is assumed that all point pressure doublet strengths are given by $C_p \cdot A$ even though the doublet may be due to an axial element and not a lifting surface element.

Consider now the axial doublet of strength $\tilde{\mu}$ associated with the modified acceleration potential (Appendix A, Eqs. (A-19, -20)). The points of concentrated pressure (delta functions), which correspond to the origin of an equivalent pressure doublet, are obtained from Eqs. (A-21) and (A-27) as

$$\Delta C_p = \frac{1}{\pi} \left\{ \tilde{\mu} e^{i \omega \xi_c / U_\infty} \right\} e^{-i \omega \xi / U_\infty} \quad (2.6-1)$$

where

$$\Delta \bar{Q} = \delta(n - n_a, \xi - \xi_a) \hat{\mu}(\xi) \quad (2.6-2)$$

Here δ is a two-dimensional Dirac delta function, and

$$\xi_c = \frac{\xi_2 + \xi_1}{2}, \quad \xi_1 \leq \xi \leq \xi_2$$

Thus ξ_c is the center of a doublet element running from ξ_1 to ξ_2 . When ξ is outside of the range shown, ξ_c jumps to the center of the next element. Thus, $\xi_c(\xi)$ is a step function at $\xi = \xi_1$ and ξ_2 . For an isolated element

$$\xi_c = 0 \quad \xi < \xi_1 \text{ or } \xi > \xi_2$$

Also for an isolated element

$$\Delta \bar{Q} = 0 \quad \xi < \xi_1 \text{ or } \xi > \xi_2$$

that is, the doublet strength drops to zero off of the element as a step function in ξ .

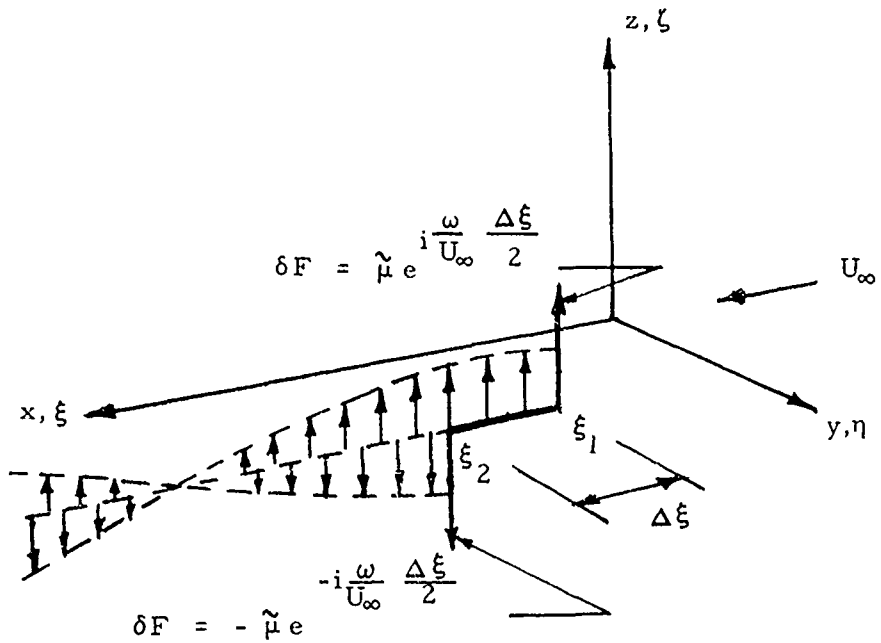
The product $\Delta \bar{Q} e^{i\omega\xi_c/U_\infty}$ then is also a step function at $\xi = \xi_1$ and ξ_2 . The derivative of this step function is zero everywhere except at $\xi = \xi_1$ and ξ_2 at which point it is infinite. The results are two delta functions.

$$\begin{aligned} \Delta \bar{C}_p \delta A &= \delta(n - n_a, \xi - \xi_a) \delta(\xi - \xi_1) \hat{\mu} e^{i\omega\Delta\xi/2U_\infty} \\ &\quad - \delta(n - n_a, \xi - \xi_a) \delta(\xi - \xi_2) \hat{\mu} e^{-i\omega\Delta\xi/2U_\infty} \end{aligned} \quad (2.6-3)$$

where

$$\frac{\Delta\xi}{2} = \xi_c - \xi_1 = \xi_2 - \xi_c$$

These expressions represent two-point pressure doublets: one at $\xi = \xi_1$ of strength $\hat{\mu}_n e^{i\omega\Delta\xi/2U_\infty}$ and one at $\xi = \xi_2$ of strength $\hat{\mu}_n e^{-i\omega\Delta\xi/2U_\infty}$. Sketch 2.6-i presents a graphical illustration of the singularity (the imaginary part is omitted for clarity).



Sketch 2.6-1

Usually the doublet elements are not isolated but are linked end-to-end down the center of a body. In this case each end point possesses two point pressure doublets whose strengths may be summed.

$$\Delta \bar{C}_p \delta A = \mu_T = \tilde{\mu}_s e^{i \frac{\omega \Delta \xi_s}{2 U_\infty}} - \tilde{\mu}_{s-1} e^{-i \frac{\omega \Delta \xi_{s-1}}{2 U_\infty}} \quad (2.6-4)$$

where s indicates the element subscript, i.e., element s lies directly aft of element $(s-1)$ on the same body.

The same analysis is valid for quadrilateral vortex rings except that horseshoe vortices are used in place of pressure doublets. At a particular end point of an element there exist two horseshoe vortices: one emanating from the element upstream of the point and one from the downstream element. These two horseshoe vortices are each replaced by one or more pressure doublets just as the lifting surface horseshoe vortices were replaced by pressure doublets. The fact that the upstream element may be larger in span than the downstream element poses no problem. The element width only enters in the determination of the element area. The expression for the equivalent pressure doublet strength for quadrilateral vortices is,

$$\Delta C_p \delta A = \Delta \bar{Q}_s 2d_s e^{i \omega \Delta \xi_s / 2U_\infty} - \Delta \bar{Q}_{s-1} 2d_{s-1} e^{-i \omega \Delta \xi_{s-1} / 2U_\infty} \quad (2.6-5)$$

where $\Delta \bar{Q} 2d$ may be considered a doublet strength, $\tilde{\mu}$, since $2d$ is the width of the trapezoidal vortex. In fact, for use with bodies, the doublet strength μ_n is used instead of $\Delta \bar{Q}$. Thus, Eq. (2.6-3) may be used for both doublets and trapezoidal elements.

The loads due to slender body elements can be obtained directly using Miles' slender body theory.

$$\Delta c_z = w_z L + \frac{\partial w_z}{\partial x} M \quad (2.6-6)$$

$$\Delta c_y = w_y L \frac{b}{a} + \frac{\partial w_y}{\partial x} M \frac{b}{a} \quad (2.6-7)$$

$$L = \pi (2 \frac{\partial a_0}{\partial x} + i 2k_r a_0 / \bar{c})$$

$$M = \pi a_c / \bar{c} \quad (2.6-8)$$

where a_0 is the local body width and b/a is the ratio of the semi-minor to semimajor axis. The terms w_z and w_y indicate upwash and sidewash, respectively. The relation between the axial loading $\partial F / \partial x$, and the pressure, Δc_z , Δc_y is:

$$\frac{\partial F_z / q}{\partial x} = \Delta c_z 2a_0 \quad (2.6-9)$$

$$\frac{\partial F_y / q}{\partial x} = \Delta c_y 2a_0 \frac{b}{a} \quad (2.6-10)$$

To simplify the logic of the computer program, these loads are converted to point pressure doublets and treated like all of the other pressure doublets.

$$(\Delta C_p \delta A)_z = \tilde{\mu}_{s_z} = \frac{\partial F_z / q}{\partial x} \Delta x (1 + b/a) \quad (2.6-11)$$

$$(\Delta C_p \delta A)_y = \tilde{\mu}_s y = \frac{\partial F}{\partial x} \frac{y/q}{\delta x} \Delta x (1 + a/b) \quad (2.6-12)$$

The term Δx is the slender body element length. The factors $(1 + b/a)$ for $\tilde{\mu}_s$ and $(1 + a/b)$ for y/q are applied because of the cross-sectional effectivity. For example, a circle ($a/b = b/a = 1$) transmits only half the point pressure doublet strength to the body; thus, the doublet strength has to be multiplied by $(1 + a/b) = (1 + b/a) = 2$.

2.6.2 Calculation of Force and Moment on a Body in the Presence of a Point Pressure Doublet

The expression for the pressure at all points in a flow field due to a point pressure doublet is given in Appendix D as:

$$C_p(x, y, z) = \frac{\Delta C_p(\xi, n, \zeta) \delta A}{4\pi} e^{i\lambda M(x-\xi)} \frac{\partial}{\partial N} \left\{ \frac{e^{-i\lambda R}}{R} \right\} \quad (2.6-13)$$

where $\Delta C_p \delta A$ is the strength of the point pressure doublet. Lawrence and Flax⁴⁷ have integrated the steady version of this equation making use of the following assumptions. 1) doublet lies at a large distance from body, 2) body is circular, 3) the pressure doublet is oriented in the z-direction and also lies in the $z = 0$ plane, and 4) only the force in the z-direction is desired. The basic idea of the Lawrence and Flax method is to integrate the steady version of Eq. (2.6-13) around the cross section for an arbitrary value of x thus producing a distribution of force along the body axis. A second method to be discussed later, integrates first in the x-direction (analytically) and then integrates numerically around the cross section to produce the total force (and moment). This method does not produce a distribution for a single doublet since the total force and moment are lumped at the same x-direction as that of the doublet.

A generalization of the steady flow method of Lawrence and Flax is derived in Appendix G. Specifically, the force distribution in both the y- and z-directions is derived for a doublet located at any point in the flow field which has an arbitrary orientation. If \vec{N} is a unit vector in the direction of the doublet, and if n and ζ are the coordinates of the doublet, then:

$$\partial(\vec{F}/q)/\partial x = \frac{\Delta C_p \delta A}{4} \frac{\beta^2 a_0^2}{R_a^3} \left\{ \mu_\theta \vec{i}_\theta + \mu_r \left(1 - \frac{3r_a^2 \beta^2}{R_a^2} \right) \vec{i}_r \right\} \quad r_a > a_0 \quad (2.6-14)$$

where

$$R_a^2 = (x - \xi)^2 + \beta^2 r_a^2$$

$$\vec{N} = \mu_\theta \vec{i}_\theta + \mu_r \vec{i}_r$$

$$r_a^2 = (y - n_a)^2 + (z - \zeta_a)^2$$

and where r_a is the radial distance from the circle origin to the doublet, and \vec{i}_θ and \vec{i}_r are unit vectors in the θ - and r_a -directions, respectively. If this result is integrated to obtain the total lift on a body of constant cross section, then

$$\vec{F}/q = \frac{\Delta C_p \delta A}{2} \frac{a_0^2}{r_a^2} (\mu_\theta \vec{i}_\theta - \mu_r \vec{i}_r) \quad r_a > a_0 \quad (2.6-15)$$

The total moment on the body is zero since the distribution is symmetrical in x for the steady case. An amazing result is observed from Eq. (2.6-15). The total force obtained by integrating the approximate formula of Eq. (2.6-14) is exactly correct as seen by comparison with equation F-13 of Appendix F. Equation (2.6-14) was derived for values of R_a which are large, however the integrated value is exact for all values of R_a where $r_a > a_0$.

A similar expansion for small r_a/a gives the following result for doublets that lie within the body:

$$\partial(\vec{F}/q)/\partial x = \frac{\Delta C_p \delta A}{4} \frac{\beta^2 a_0^2}{R_a^3} (\mu_\theta \vec{i}_\theta + \mu_r \vec{i}_r) \quad r_a < a_0 \quad (2.6-16)$$

where

$$\bar{R}_a^2 = (x - \xi)^2 + \beta^2 a_0^2$$

Again if this equation is integrated over a constant cross-sectional body, then:

$$\vec{F}/q = \frac{\Delta C_p \delta A}{2} (\mu_\theta \vec{i}_\theta + \mu_r \vec{i}_r) \quad r_a < a_0 \quad (2.6-17)$$

This result corresponds to the exact values obtained in Appendix F.

Such encouraging results for the steady case (body of circular cross section) indicate that a similar approximate analysis might work for both the unsteady case and the case of noncircular cross sections. A derivation for the unsteady case (circular body) is given in Appendix G. For the case where the doublet lies outside of the body, i.e., $r_a > a_0$, the result is:

$$\partial(\vec{F}/q)/\partial x = \frac{\Delta C_p \delta A}{4} \beta^2 a_0^2 e^{i\lambda[M(x-\xi)-R_a]} (\vec{T}_\theta T_\theta + \vec{T}_r T_r) \quad r_a > a_0 \quad (2.6-18)$$

where

$$T_\theta = \left\{ \frac{1}{R_a^3} + \frac{i\lambda}{R_a^2} \right\}$$

$$T_r = T_\theta \left\{ 1 - \frac{i\lambda r_a^2 \beta^2}{R_a} - \frac{3\beta^2 r_a^2}{R_a^2} \right\} + \frac{i\lambda \beta^2 r_a^2}{R_a^4}$$

Here

$$\lambda = \omega M / \beta^2 U_\infty = 2k_r \frac{M}{\beta^2} \frac{1}{c} \quad (2.6-19)$$

For the case where the doublet lies on or inside the body, i.e., $r_a \leq a_0$, the result is:

$$\partial(\vec{F}/q)/\partial x = \frac{\Delta C_p \delta A}{4} \beta^2 a_0^2 e^{i\lambda[M(x-\xi)-R_a]} \left\{ \frac{1}{R_a^3} + \frac{i\lambda}{R_a^2} \right\} \left\{ \vec{T}_\theta \mu_\theta + \vec{T}_r \mu_r \right\} \quad (2.6-20)$$

$$r_a \leq a_0$$

These results can be integrated over a constant cross-sectional body to give the total force. The term $\vec{F}/q \cdot \vec{T}_\theta$ can be integrated analytically to give

$$F_\theta/q = \frac{\Delta C_p \delta A}{2} \frac{a_0^2}{r_a^2} K \left(\frac{i\pi}{2} \right) H_j^{(2)}(\bar{k}) \quad (2.6-21)$$

where $\bar{k} = \omega r_a M / U_\infty$ and where $H_j^{(2)}$ is the Hankel function of the second kind and zeroth order. The result for F_r/q must be integrated numerically.

Just as in the steady case the total forces integrated over a body of constant cross section are exact. The results of (2.6-21) and the results of numerically integrating F_r/q are plotted in Sketch 2.6-2. The exact results are obtained by the method presented in Appendices D and E (for the total force).

The results for $\partial(\vec{F}/q)/\partial x$ are given above in terms of $u_\theta \vec{i}_\theta$, and $u_r \vec{i}_r$. A conversion to the y-z plane gives:

$$\frac{\partial(F_z/q)}{\partial x} = N_z \frac{\partial(F_z^{(z)}/q)}{\partial x} + N_y \frac{\partial(F_z^{(y)}/q)}{\partial x} \quad (2.6-22a)$$

$$\frac{\partial(F_y/q)}{\partial x} = N_y \frac{\partial(F_y^{(y)}/q)}{\partial x} + N_z \frac{\partial(F_y^{(z)}/q)}{\partial x} \quad (2.6-22b)$$

where

$$\frac{\partial(F_z^{(z)}/q)}{\partial x} = \cos^2 \theta_1 \frac{\partial(F_\theta/q)}{\partial x} + \sin^2 \theta_1 \frac{\partial(F_r/q)}{\partial x}$$

$$\frac{\partial(F_y^{(y)}/q)}{\partial x} = \sin^2 \theta_1 \frac{\partial(F_\theta/q)}{\partial x} + \cos^2 \theta_1 \frac{\partial(F_r/q)}{\partial x}$$

$$\frac{\partial(F_z^{(y)}/q)}{\partial x} = \cos \theta_1 \sin \theta_1 \left(\frac{\partial(F_r/q)}{\partial x} - \frac{\partial(F_\theta/q)}{\partial x} \right)$$

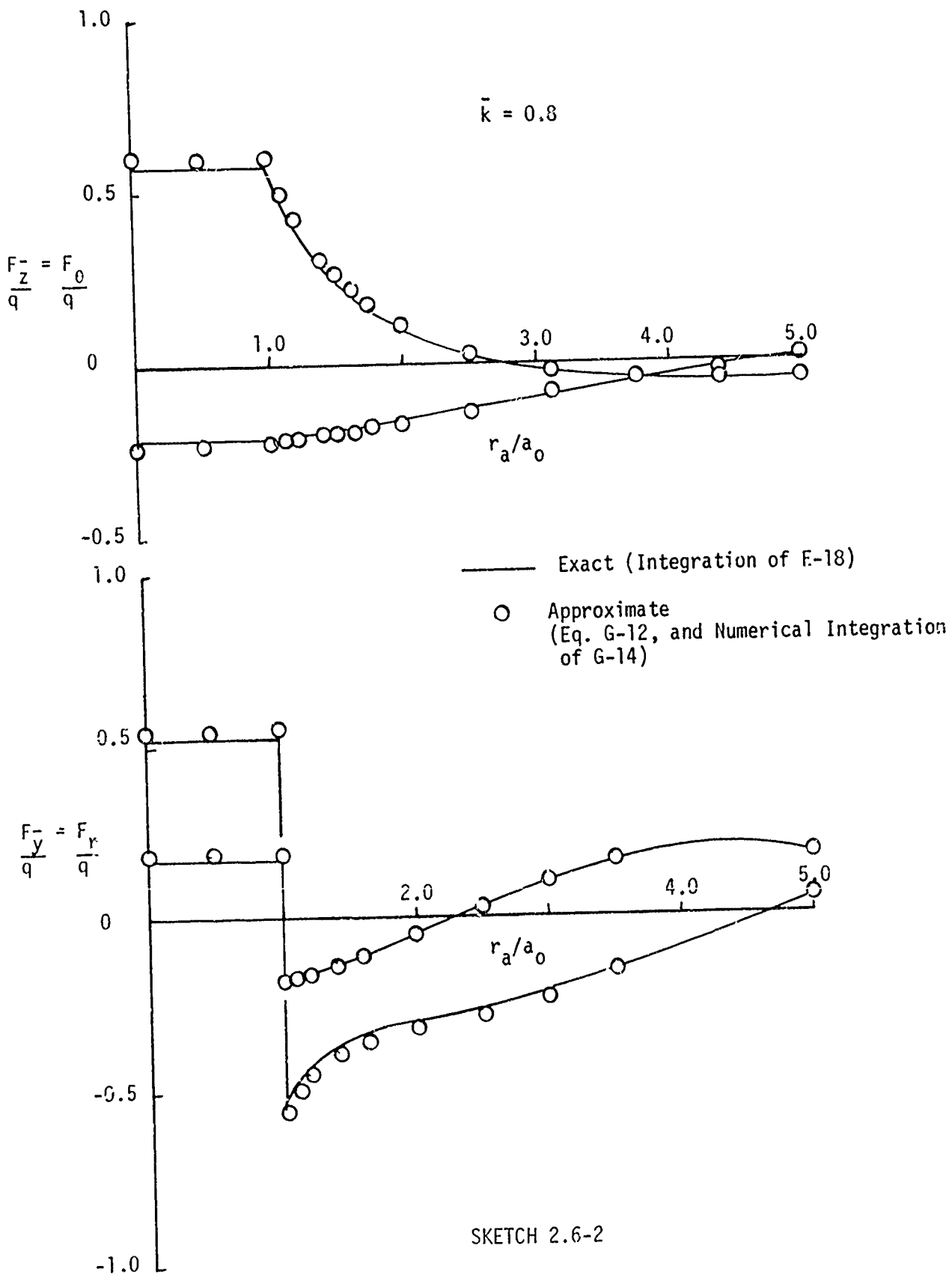
and where

$$\vec{N} = \vec{j}N_y + \vec{k}N_z$$

$$\tan \theta_1 = \left(\frac{z_a - z}{y_a - y} \right)$$

$$\frac{\partial(F_\theta/q)}{\partial x} = - \frac{\partial(\vec{F}/q)}{\partial x} \cdot \vec{i}_\theta$$

$$\frac{\partial(F_r/q)}{\partial x} = \frac{\partial(\vec{F}/q)}{\partial x} \cdot \vec{i}_r$$



The circumferential integration for a circular cross section has been performed. In the present method the force distribution is given, not at every value of x , but at a set of points which correspond to the midpoints of a set of body elements (the slender body elements). The value of the circumferential integration, $\partial(\vec{F}/q)/\partial x$, must be averaged over these elements. If not, then errors could be introduced due to local variations over the elements. The average of $\partial(\vec{F}/q)/\partial x$ over an element is obtained by integrating it and dividing by Δx . Ultimately the total force, \vec{F}/q on the element is required, thus the division by Δx can be left out.

$$\vec{F}/q = \int_{x_A - (\Delta x/2)}^{x_A + (\Delta x/2)} \frac{\partial(\vec{F}/q)}{\partial x} dx$$

where x_A and Δx are the element center and length, respectively. In equation (2.6-22) the elements that go to make up $\partial(\vec{F}/q)/\partial x$ are $\partial(F_z^{(z)}/q)/\partial x$, $\partial(F_y^{(y)}/q)/\partial x$, and $\partial(F_z^{(y)}/q)/\partial x$. These are all integrated in the same manner as is $\partial(\vec{F}/q)/\partial x$ producing:

$$\frac{F_z^{(z)}}{q} = \int_{x_A - (\Delta x/2)}^{x_A + (\Delta x/2)} \frac{\partial(F_z^{(z)}/q)}{\partial x} dx \quad (2.6-23a)$$

$$\frac{F_y^{(y)}}{q} = \int_{x_A - (\Delta x/2)}^{x_A + (\Delta x/2)} \frac{\partial(F_y^{(y)}/q)}{\partial x} dx \quad (2.6-23b)$$

$$\frac{F_z^{(y)}}{q} = \int_{x_A - (\Delta x/2)}^{x_A + (\Delta x/2)} \frac{\partial(F_z^{(y)}/q)}{\partial x} dx \quad (2.6-23c)$$

Also, required for future analysis is $F_y^{(z)}/q$. This case is

$$F_y^{(z)}/q = F_z^{(y)}/q \quad (2.6-23d)$$

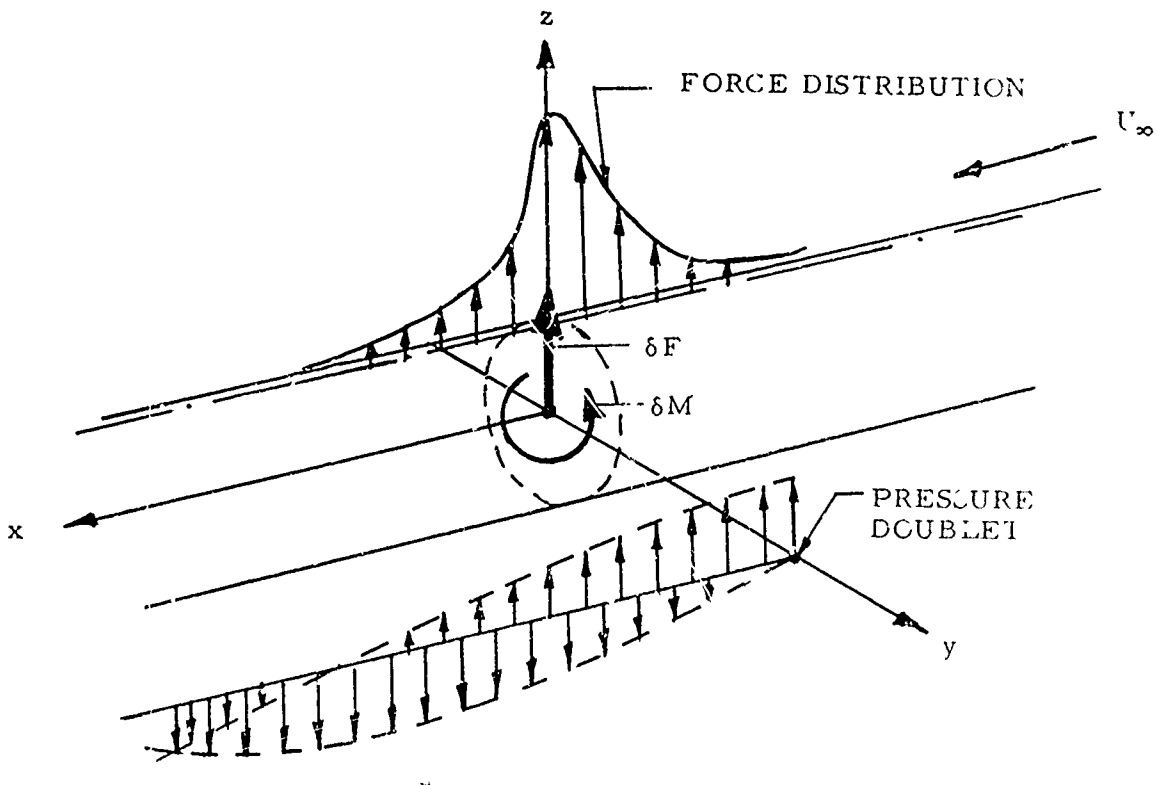
In addition, future calculation will require moments on the elements. For this method (circular bodies) the moments are zero.

The above simplified approaches for the steady and unsteady cases (which will be called Approach I) are based on expansions in terms of a_0/R_a or r_a/R_a . As such they are approximate even though the total forces are exact (the total moment is correct for the steady case also).

For the case of an elliptic cross section, the simple expansion techniques used above and derived in Appendix G (Approach I) fail to converge to sufficient accuracy for the total integrated values. Therefore, these results are not presented. A different approach (Approach II) will have to be taken for the case of noncircular cross sections .

The basic idea of the second approach is to reverse the order of integration in finding the total force on the body. That is, Eq. (2.6-13) is integrated in the x-direction first and then integrated around the cross section. The advantages of this method are that: 1) unsteady flow can be considered for bodies of arbitrary cross section since Eq. (2.6-13) can be integrated analytically along the body, and 2) only a single term arises from the expression and not an entire distribution for each pressure doublet. The disadvantage of this method is that although the force and moment are correct, the detailed distribution is not given. (See Sketch 2.6-3 for a graphical representation of approach II.) In a practical problem there are many pressure doublets and approach II produces a distribution since there is a distribution of pressure doublets. The distribution, however, is more abrupt than the actual since the force and moment are concentrated at one point.

The integration of Eq. (2.6-13) to obtain the total force and moment is carried out in Appendix D. The integration in the x-direction is performed analytically in terms of two Hankel functions. The results are:



Sketch 2.6-3

$$F = \frac{\Delta C_p \delta A}{2\pi} \oint f(\bar{k}) \frac{\vec{r}_r \cdot \vec{N}}{r} \vec{n} \cdot \vec{i}_F ds \quad (2.6-24)$$

$$M = \frac{\Delta C_p \delta A}{2\pi} \oint r p(\bar{k}) \frac{\vec{r}_r \cdot \vec{N}}{r} \vec{n} \cdot \vec{i}_F ds \quad (2.6-25)$$

where

$$f(\bar{k}) = -i \frac{\pi}{2} \bar{k} H_1^{(2)}(\bar{k})$$

$$p(\bar{k}) = M \frac{\pi}{2} \bar{k} H_0^{(2)}(\bar{k})$$

$H_r^{(2)}(\bar{k})$ = Hankel function of second kind

$$\bar{k} = 2k_r M r/c$$

$$k_r = \omega c / 2U_\infty$$

\vec{N} = direction of pressure doublet

\vec{i}_F = direction of force \vec{F}

\vec{i}_r = direction of radius \vec{r}

$$\vec{r} = \vec{i}_r \sqrt{(y - n)^2 + (z - \zeta)^2} = \vec{j}(y - n) + \vec{k}(z - \zeta)$$

$$q = \frac{1}{2} \rho U_\infty^2 = \text{dynamic pressure}$$

and where the contour integral is to be taken around the cross section. The cross-sectional shape under consideration is the one possessed by the body at the longitudinal location of the point pressure doublet. Currently, for simplicity, the constant cross section designated by a and b is used instead of the local values, a_0 and b_0 . Appendix D shows that higher-order moments diverge and thus cannot be used.

The integrals found in Eqs. (2.6-24, -25) can be evaluated analytically for only the simplest cases. One such case is the one considered earlier in this section, i.e., a circle in steady flow. Appendix F gives the details of this integration. The results are:

$$\frac{F}{q} = \Delta C_p \delta A I \quad (2.6-26)$$

$$I = \begin{cases} \frac{1}{2} \vec{i}_F \cdot \vec{N} & \text{Pressure doublet inside body} \\ \frac{1}{2} \vec{i}_F \cdot \vec{N}_1 (a/r_a)^2 & \text{Pressure doublet outside body} \end{cases} \quad (2.6-27)$$

where a is the circle radius, r_a is the radial distance from the pressure point to the circle center, and

$$\vec{N}_1 = \vec{k} \sin(\phi - 2\bar{\theta}) - \vec{j} \cos(\phi - 2\bar{\theta})$$

where ϕ and $\bar{\theta}$ are defined implicitly as follows:

$$N = \vec{k} \sin \phi + \vec{j} \cos \phi$$

$$\vec{r}_0 = |\vec{r}_0| (\vec{k} \sin \bar{\theta} + \vec{j} \cos \bar{\theta})$$

For other cross-sections the integrals in Eqs. (2.6-24, -25) must be done numerically. Appendix E gives the details of a successful numerical scheme for evaluating these integrals.

The basic idea is to break up the contour integrals into a sum of integrals over short surface segments. On each of these elements the values of $f(\vec{k})$ and $p(\vec{k})$ may accurately be held constant. The integrals then become:

$$F/q = \frac{\Delta C_p \delta A}{2\pi} \sum_{j=1}^N f(\vec{k}_j) \int_{-e_j}^{e_j} \frac{\vec{t}_r \cdot \vec{N} \vec{n} \cdot \vec{t}_F}{r} ds \quad (2.6-28)$$

$$M/q = \frac{\Delta C_p \delta A}{2\pi} \sum_{j=1}^N p(\vec{k}_j) \int_{-e_j}^{e_j} \vec{t}_r \cdot \vec{N} \vec{n} \cdot \vec{t}_F ds \quad (2.6-29)$$

The integral over the small element extending from $-e$ to $+e$ in the moment equation (2.6-29) is very simple since no singularities exist. However, the $1/r$ singularity in the force integral requires special treatment and its accurate evaluation is difficult. Several procedures were tried which ignored the curvature effect. These proved to be inaccurate and had to be abandoned. The major part of Appendix E is devoted to the evaluation of the element integral in Eq. (2.6-11). It is convenient to break F/q and M/q into their component parts

$$\begin{aligned} \frac{F(z)}{q} &= \frac{F}{q} (\vec{N} = \vec{k}, \vec{t}_F = \vec{i}) \\ \frac{F(v)}{q} &= \frac{F}{q} (\vec{N} = \vec{j}, \vec{t}_F = k) \\ \frac{F(y)}{q} &= \frac{F}{q} (\vec{N} = \vec{k}, \vec{t}_F = \vec{s}) \\ F(y) &= \frac{F}{q} (\vec{N} = \vec{j}, \vec{t}_F = \vec{s}) \end{aligned} \quad (2.6-30)$$

Similar expressions may be written for M/q .

To test the accuracy of the formulas in Appendix E, comparison is made to the analytic solution for a circle given in Eqs. (2.6-26, -27). Figure 4 presents results for the cases

$$(a) \quad \vec{i}_F = \vec{N} = \vec{k}$$

$$(b) \quad \vec{i}_F = \vec{N} = \vec{j}$$

(In Figure 4 as well as Figures 5, 6, 7 and 8, $\Delta C_p \delta A$ is assumed to be unity.) The numerical results are accurate even near the body surface. It is near the surface, both inside and outside, where greatest difficulty is encountered in obtaining accurate solutions. There is a tendency for the internal solution to drop below its correct constant value near the surface. Similar calculations were carried out for elliptic cross sections. One such calculation is given in Figure 5. The internal values stay constant except near the surface where a slight variation is noticed. In Figure 5 the pressure doublet is located in the $z = 0$ plane. In Figure 6 a similar plot is shown. Here, however, the doublet lies in the $y = 0$ plane. No irregularities are observed. The reason for the difference in accuracy between Figures 5 and 6 is the fact that near the surface the curvature is higher in Figure 5. Figure 7 is presented to furnish a check on the unsteady case. The pressure doublet is located on the axis of a circle. In this case the integrals of Eqs. (2.6-24, -25) are easily performed since r is not a function of the surface coordinate s and can be taken out of the integral. The results are:

$$\frac{F}{q} = \frac{\Delta C_p \delta A}{2} f(\bar{k}) T$$

$$\frac{M}{q} = \frac{\Delta C_p \delta A}{2} p(\bar{k}) a T$$

where

$$T = N_y i_{F_y} + N_z i_{F_z}$$

In Figure 7, T and $\Delta C_p \delta A$ are assumed to be unity. The comparison of the analytic and calculated results is essentially perfect. Notice that for the steady case, the pressure doublet of strength $\Delta C_p \delta A$ produces a lift on the body of strength $\Delta C_p \delta A/2$. For other cross-sectional shapes, this

factor changes. For an ellipse in steady flow with a z-oriented pressure doublet located inside the cross section, the variation of the force with b/a is

$$\frac{F}{q} = \Delta C_p \delta A \left(\frac{a}{a+b} \right)$$

As the cross section becomes flat ($b \rightarrow 0$), the body becomes more effective until $b = 0$ at which point the body becomes like a lifting surface and the force is equal to the pressure doublet strength, $\Delta C_p \delta A$. Figure 8 presents a comparison of this formula with calculated numerical results. The agreement is very good even for very small values of b/a or a/b .

2.6.3 Effects of Symmetry, Ground Effect and Images

The method outlined so far considers only a single point pressure doublet. In actuality for every pressure doublet located on a lifting surface, there may be: 1) one for symmetry, 2) one for ground effect, 3) one for the interaction of symmetry and ground effect, 4) images in bodies associated with the lifting surface, and 5) images due to symmetry and ground effect. The z-force on body, b , due to pressure doublet located at ξ, η, ζ oriented normal to a surface of dihedral γ is:

$$F_z(b) = \cos \gamma \bar{F}_z(z)(\xi, \eta, \zeta) - \sin \gamma \bar{F}_z(y)(\xi, \eta, \zeta)$$

$$+ \sum_{b=1}^{NAB} [\hat{\mu}_z \bar{F}_z(z)(\xi, \eta_I^{(b)}, \zeta_I^{(b)}) + \hat{\mu}_y \bar{F}_z(y)(\xi, \eta_I^{(b)}, \zeta_I^{(b)})]$$

$$+ \delta \left\{ \begin{aligned} & \cos \gamma \bar{F}_z(z)(\xi, -\eta, \zeta) + \sin \gamma \bar{F}_z(y)(\xi, -\eta, \zeta) \\ & + \sum_{b=1}^{NAB} [\hat{\mu}_z \bar{F}_z(z)(\xi, -\eta_I^{(b)}, \zeta_I^{(b)}) + \hat{\mu}_y \bar{F}_z(y)(\xi, -\eta_I^{(b)}, \zeta_I^{(b)})] \end{aligned} \right\}$$

$$+ \epsilon \left\{ \begin{aligned} & \cos \gamma \bar{F}_z(z)(\xi, \eta, -\zeta) + \sin \gamma \bar{F}_z(y)(\xi, \eta, -\zeta) \\ & + \sum_{b=1}^{NAB} [\hat{\mu}_z \bar{F}_z(z)(\xi, \eta_I, -\zeta_I) + \hat{\mu}_y \bar{F}_z(y)(\xi, \eta_I, -\zeta_I)] \end{aligned} \right\}$$

$$+ \delta \epsilon \left\{ \begin{aligned} & \cos \gamma \bar{F}_z^{(z)}(\xi, -\eta, -\zeta) - \sin \gamma \bar{F}_z^{(y)}(\xi, -\eta, -\zeta) \\ & + \sum_{b=1}^{\text{NAB}} [\hat{u}_z^{(b)} \bar{F}_z^{(z)}(\xi, -\eta_I, -\zeta_I) + \hat{u}_y^{(b)} \bar{F}_z^{(y)}(\xi, -\eta_I, -\zeta_I)] \end{aligned} \right\} \quad (2.6-31)$$

where

$$\bar{F}_z^{(z)} = \frac{r_z^{(z)}/q}{iC_p A} \quad (2.6-32)$$

and a similar result holds for $\bar{F}_y^{(y)}$, $\bar{F}_z^{(z)}$, etc. The term NAB indicates the bodies associated with the pressure doublet, i.e., those bodies that have an image of the pressure doublet within them. The terms $\hat{u}_z^{(b)}$ and $\hat{u}_y^{(b)}$ arise from the fact that the image point pressure doublet has a modified strength as shown in Appendix C, Eq. (C-5). If this equation is rewritten in terms of real variables and the circle radius a is replaced with the radius of curvature a , η_a , ζ_a ,

$$\begin{aligned} \bar{F}_z^{(z)} &= \frac{r_z^{(z)}/q}{iC_p A} \{ (\xi - \bar{y}_a)^2 + (\zeta - \bar{z}_a)^2 + \delta \epsilon [(\eta - \bar{y}_a)^2 + (\zeta - \bar{z}_a)^2] \} \\ &= \frac{r_z^{(z)}/q}{iC_p A} \{ (\xi - \bar{y}_a)^2 + (\zeta - \bar{z}_a)^2 + \delta \epsilon [(\eta - \bar{y}_a)^2 + (\zeta - \bar{z}_a)^2] \} \end{aligned} \quad (2.6-33)$$

where

$$r_z^{(z)} = (\xi - \bar{y}_a)^2 + (\zeta - \bar{z}_a)^2$$

and where \bar{y}_a , \bar{z}_a are the coordinates of the local center of curvature (for a circle these are the coordinates of the body axis).

An expression similar to Eq. (2.6-31) may be written for the force in the y -direction, i.e., $F_y^{(y)}$. The only changes to be made are that $\bar{F}_z^{(z)}$ is replaced by $\bar{F}_y^{(y)}$ and $\bar{F}_z^{(z)}$ is replaced by $\bar{F}_y^{(y)}$. For the moment calculation, simply replace all F 's with M 's. Eq. (2.6-31) may be made to hold for point pressure doublets originating on body axes by: 1) omitting all images, 2) setting $\theta = 0$ for z -oriented doublets and $\theta = -90^\circ$ for y -oriented doublets.

So far, two basically different methods have been described; one for bodies of circular cross section and one for all other bodies. The first of these methods produces a distribution of forces on all elements of the body due to a single doublet. If we characterize all doublet strengths as $\Delta C_p \delta A$, then the total force at an element is:

$$FZ_T^{(b)} = \sum FZ_{rs}^{(b)} (\Delta C_p \delta A)_s \quad (2.6-34)$$

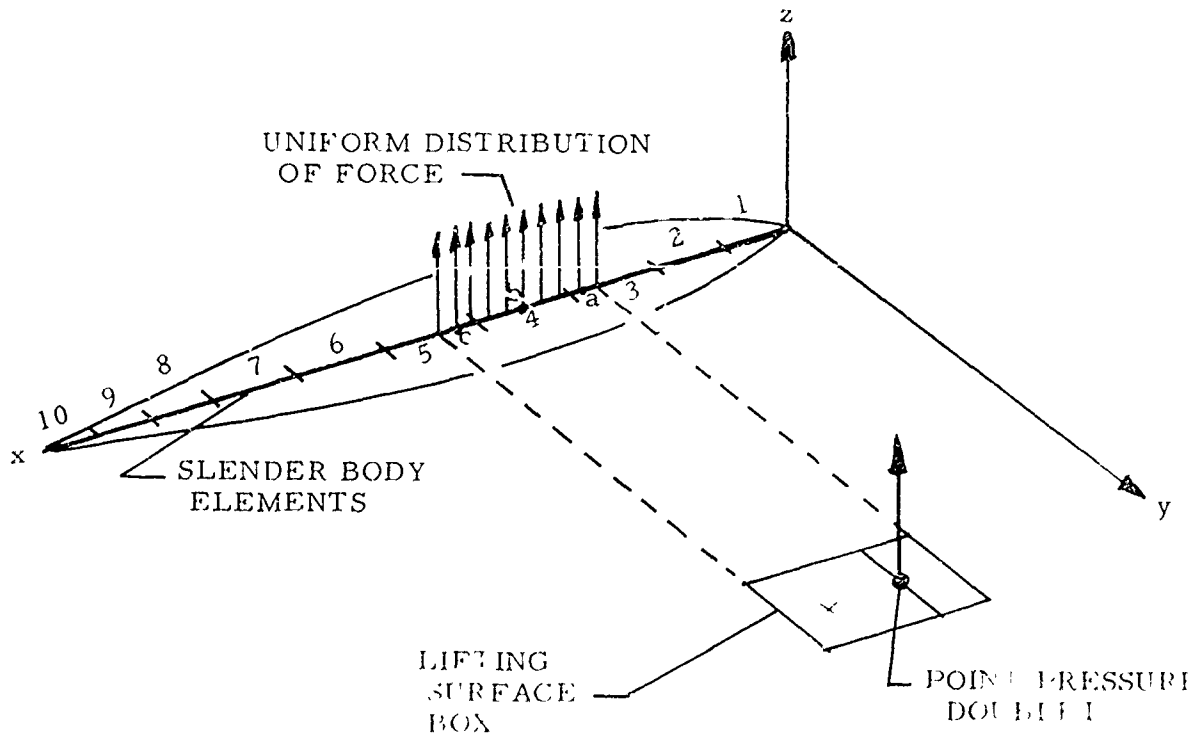
where r represents the receiving element and s represents the sending doublet. A similar expression exists for $FY_T^{(b)}$. In matrix notation

$$\{FZ_T^{(b)}\} = [FZ^{(b)}] \{\Delta C_p \delta A\} \quad (2.6-35a)$$

$$\{FY_T^{(b)}\} = [FY^{(b)}] \{\Delta C_p \delta A\} \quad (2.6-35b)$$

The superscript b stands for body. There is a column matrix $FZ_T^{(b)}$ and $FY_T^{(b)}$ for each body.

For the second method, each doublet produces a point force and moment on the body. As illustrated in Sketch 2.6-4, the longitudinal location of the



Sketch 2.6-4

center of force is at the location of the point pressure doublet. Again the slender body element system is used to keep track of the loads on the bodies. If the longitudinal location of a point pressure doublet lies between the leading and trailing edges of a slender body element, the force and moment are added to the load on that element. To smooth out this bookkeeping procedure, it is assumed that the force is uniformly distributed over a short segment, on the axis of the receiving body, whose length is equal to the length of the element upon which the point pressure doublet lies. Thus, the force and moment due to one particular pressure doublet may be spread out over several slender body elements. Sketch 2.6-4 gives a graphical example. The load and moment due to the pressure doublet is distributed over slender body elements 3, 4 and 5. The center of load on these three elements lies at a, b, and c, respectively. The fact that the load is off center contributes to the moment on the slender body elements.

2.6.4 Redistribution of Body Loads for Alternate II

The previous sections have described the two methods of determining the force and moment distributions for bodies. For alternate II (general body cross section) the contribution of each point pressure doublet emanating from each singularity and image, etc., is allocated to the proper slender body element. The final result for a body, then, is a distribution of forces among its slender body elements. The distribution thus obtained approaches the exact distribution as the body radius becomes small. For thick bodies, however, the resulting distribution is somewhat distorted even though the total force and moment are correct. The only way to avoid this distortion is to consider that each point pressure doublet contributes to all slender body elements as the result of its longitudinal distribution. To do this, however, Eq. (2.6-13) would have to be integrated first around the contour. Such an integration has been done for circular cross sections but has not been done for elliptic cross sections. Until such time as this integration can be performed, alternate II will be used for such cases. There is a way to alleviate some of the distortion of alternate II and that is by redistribution. After the effects of all point pressure doublets have been allocated among the slender body elements, assume that these forces have arisen solely from an axial point pressure doublet distribution within that body. Only a relatively small number of point pressure doublets are now considered. It is

assumed that Eq. (2.6-20) gives a good approximation to the shape of the longitudinal distribution of the force along the body, even though it only holds for circular cross sections. The body radius used is $(a_0 + b_0)/2$, i.e., the average of semi-major and semi-minor axes. The redistribution thus outlined will not, then, affect the total lift of the distribution. This redistribution is then applied to each of the slender body elements. Even though the results obtained using this method show good agreement with experimental data, it is not proposed here as the final answer to the distribution problem. Further work is required to integrate Eq. (2.6-13) around arbitrary cross sections.

2.7 Generalized Forces and Aerodynamic Parameters

2.7.1 Generalized Forces

The pressures, forces and moments obtained on lifting surfaces and bodies along with their appropriate displacements are outlined as follows:

1. $\Delta C_p, h$, (normal to lifting surfaces)
2. $\partial(F_z/q)/\partial x, h_z$ (z-direction on bodies)
3. $\partial(F_y/q)/\partial x, h_y$ (y-direction on bodies)
4. $\partial(M_z/q)/\partial x, dh_z/dx$ (z-direction on bodies)
5. $\partial(M_y/q)/\partial x, dh_y/dx$ (y-direction on bodies)

The virtual work, δW_j , done by these pressure forces and moments during a virtual displacement is:

$$\frac{\delta W_j}{q} = G \iint_{R.S.} \Delta C_{p_j} \delta h \, ds + g \left\{ \int_B \frac{\partial(F_z/q)_j}{\partial \xi} \delta h_z \, d\xi + \int_B \frac{\partial(F_y/q)_j}{\partial \xi} \delta h_y \, d\xi + \int_B \frac{\partial(M_z/q)_j}{\partial \xi} \delta \left(\frac{dh_z}{d\xi} \right) \, d\xi + \int_B \frac{\partial(M_y/q)_j}{\partial \xi} \delta \left(\frac{dh_y}{d\xi} \right) \, d\xi \right\} \quad (2.7-1)$$

where q is the dynamic pressure. The integration limit R.S. indicates that only the lifting surfaces on the right-hand-side of the aircraft are considered.

$$G = \begin{cases} 1 & \text{if lifting surface lies in plane of symmetry (e.g., vertical fin)} \\ 2 & \text{otherwise} \end{cases}$$

The integration limit B. indicates all bodies lying on the right-hand side of the aircraft.

$$g = \begin{cases} 1 & \text{if body lies on plane of symmetry (e.g., a fuselage)} \\ 2 & \text{otherwise (e.g., a nacelle)} \end{cases}$$

The integral over the lifting surface L.S. represents a series of integrals over each of the lifting surfaces which go to make up the total configuration. The value of G for each of these surfaces may be different. A similar argument is valid for the integral over the bodies B., thus the value of g may vary from body to body.

The values of $\partial(F/q)/\partial x$ and $\partial(M/q)/\partial x$ are the original values obtained before redistribution.

Two definitions for the generalized force will be introduced, i.e., Q_{ij} and \bar{Q}_{ij} .

$$\frac{\delta W_j}{q} = \bar{c}A \sum Q_{ij} \delta \bar{q}_i \quad (2.7-2)$$

$$\frac{\delta \bar{W}_j}{q} = -2s^3 \sum \bar{Q}_{ij} \delta \bar{q}_i \quad (2.7-3)$$

Here \bar{q}_i is the i -th generalized coordinate, \bar{c} the reference chord length, A the total reference area and s the reference semispan. With the introduction of generalized coordinates, the displacements may be written:

$$h = \bar{c} \sum \bar{q}_i f_i$$

$$h_z = \bar{c} \sum \bar{q}_i f_{z_i}$$

$$h_y = \bar{c} \sum \bar{q}_i f_{y_i} \quad (2.7-4)$$

Introducing the virtual displacements of Eq. (2.7-4) (and its derivative) into Eq. (2.7-1), and equating (2.7-1) to (2.7-2, -3) gives the results for the generalized forces Q_{ij} and \bar{Q}_{ij} .

$$Q_{ij} = \frac{1}{A} \left[G \iint_{L.S.} \Delta C_{p_j} f_i ds + g \left\{ \int_{B.} \frac{\partial (F_z/q)_j}{\partial \xi} f_{z_i} d\xi + \int_{B.} \frac{\partial (F_y/q)_j}{\partial \xi} f_{y_i} d\xi \right. \right. \\ \left. \left. + \int_{B.} \frac{\partial (M_z/q)_j}{\partial \xi} \frac{df_{z_i}}{d\xi} d\xi + \int_{B.} \frac{\partial (M_y/q)_j}{\partial \xi} \frac{df_{y_i}}{d\xi} d\xi \right\} \right] \quad (2.7-5)$$

$$\bar{Q}_{ij} = Q_{ij} \left(\frac{Ac}{-2s^3} \right) \quad (2.7-6)$$

2.7.2 Aerodynamic Parameters

It is desirable and sometimes necessary to generate conventional aerodynamic data. Such data, in addition to being useful in itself, provide an excellent check for the computer program and/or specific cases to be run by it.

The local normal force coefficient and pitching moment coefficient about the local 1/4-chord point are:

$$c_n = \frac{1}{c} \int_{\text{chord}} \Delta c_p d\xi \quad (2.7-7)$$

$$c_m = -\frac{1}{c^2} \int \Delta c_p (\xi - \xi_{1/4}) d\xi \quad (\text{nose up}) \quad (2.7-8)$$

where c is the local chord length. The local center of pressure is:

$$\begin{aligned} c.p.\text{Re} &= \frac{-\text{Re}(c_m)}{\text{Re}(c_n)} + 0.25 \\ c.p.\text{Im} &= \frac{-\text{Im}(c_m)}{\text{Im}(c_n)} + 0.25 \end{aligned} \quad (2.7-9)$$

The total vertical and side-force coefficients on lifting surfaces are

$$C_z = \frac{(1 + \delta)}{A} \int_{\text{R.S.}} c c_n d\eta \quad (2.7-10)$$

$$C_y = \frac{(1 - \delta)}{A} \left(\frac{G}{Z} \right) \int_{\text{R.S.}} c c_n d\xi \quad (2.7-11)$$

The total vertical and side-force coefficients on bodies are

$$C_{z_b} = \frac{(1 + \delta)}{A} g \int_{\text{B.}} \frac{\partial (F_z/q)}{\partial \xi} d\xi \quad (2.7-12)$$

$$C_{y_b} = \frac{(1 - \delta)}{A} g \int_{\text{B.}} \frac{\partial (F_y/q)}{\partial \xi} d\xi \quad (2.7-13)$$

The pitching and yawing moment coefficients on lifting surfaces taken about the point XM are:

$$C_M = \frac{(1 + \delta)}{A\bar{c}} \int_{R.S.} \{ c^2 c_m - cc_n (\xi_{1/4} - XM) \} d\eta \quad (\text{nose up}) \quad (2.7-14)$$

$$C_N = \frac{(1 - \delta)}{A\bar{c}} \left(\frac{G}{2}\right) \int_{R.S.} \{ c^2 c_m - cc_n (\xi_{1/4} - XM) \} d\xi \quad (\text{nose right}) \quad (2.7-15)$$

For bouies

$$C_{M_b} = \frac{(1 + \delta)}{A\bar{c}} g \int_{B.} \left\{ \frac{\partial(M_z/q)}{\partial\xi} - (\xi - XM) \frac{\partial(F_z/q)}{\partial\xi} \right\} d\xi \quad (\text{nose up}) \quad (2.7-16)$$

$$C_{N_b} = \frac{(1 - \delta)}{A\bar{c}} g \int_{B.} \left\{ \frac{\partial(M_y/q)}{\partial\xi} - (\xi - XM) \frac{\partial(F_y/q)}{\partial\xi} \right\} d\xi \quad (\text{nose right}) \quad (2.7-17)$$

The total rolling moment for the aircraft is:

$$C_l = -\frac{(1 - \delta)}{2sA} \left\{ \int_{R.S.} cc_n n d\eta + \frac{G}{2} \int_{R.S.} cc_n \zeta d\xi + \int_{B.} \frac{\partial(F_z/\partial\xi)}{\partial\xi} n_a d\xi \right. \\ \left. + g \int_{B.} \frac{\partial(F_y/\partial\xi)}{\partial\xi} \zeta_a d\xi \right\} \quad (\text{right wing down}) \quad (2.7-18)$$

3.0 CALCULATED RESULTS

3.1 Parameter Variation Studies

Before discussing the correlations of the present method with other theories and experimental data, a series of studies will be made to determine the effect of varying some of the important parameters of the problem. These studies not only show how results are changed by changing a parameter but also indicate the range of validity of the present method.

3.1.1 The Effect of Body Radius

Figure 9 presents a comparison of spanwise lift distribution on a wing (exposed portion only) that is attached to a circular fuselage whose radius has been varied. The exposed wing is the same in all cases — it is attached to the fuselage center — and is oscillating in pitch at a reduced frequency of unity. The fuselage is at zero incidence and thus the upwash generated by the fuselage is not present. Thus, this figure gives only the interference effect of the fuselage. The effects of zero radius and infinite radius are the same. Consider the lift coefficient at the wing root. When the diameter-to-chord ratio is increased from zero to 0.125, then the lift drops. A further increase to 0.50 produces an increase in lift coefficient over the zero value case. Further increases eventually bring the fuselage effect back to the zero diameter case.

The effect of the fuselage when it too is given an angle of attack is much different. The effect is monotonic in fuselage diameter-to-chord ratio and in the limit of infinite radius the lift coefficient is twice the zero diameter value.

3.1.2 The Effect of Cross-Sectional Shape

The effect of fuselage ellipticity is illustrated in Figure 10. Specifically, the distribution of lift coefficient for a wing-fuselage combination is presented for the aspect ratio b/a ranging from zero to infinity. The semi-width a is constant and equal to 0.25 for all calculations. The case $b/a = 0.0$ is special and is obtained by replacing the body by a flat-lifting surface. The case $b/a = \infty$ is also special and is obtained by placing a plane of

symmetry at the wing root (this case is given the designation of "wing alone"). All of the intermediate cases which are not special should lie within the envelope formed by the two special cases described above. The curve corresponding to the lowest value of b/a ($=0.25$) does not fall within the envelope. The curve corresponding to the highest value of b/a ($=2.0$) still lies inside the envelope but comes very close to passing outside of it. The upper bound of validity, for b/a , of the present method, is then somewhere near or below 2.0. The lower bound of validity for b/a is somewhere between 0.5 and 0.25. If configurations are to be analyzed that fall outside of this range, then it is recommended that either the body be replaced by a lifting surface ($b/a < 0.5$) or a plane wall for ($b/a > 2.0$). An additional alternate is to place lifting surface singularities on the body surface in addition to, or in place of, the image system.

The use of lifting surface singularities on the body surface, as described in Part I of this report, does not always increase the accuracy of the solution. Figure 11 presents a comparison of the present method with the method of Part I for the wing-fuselage combination ($b/a = 2.0$) of Figure 10. Two separate idealizations are used to describe the fuselage. The first idealization uses three panels or strips to describe a quarter of the fuselage. The resulting calculation falls below that of the present method. When the number of fuselage elements is doubled, the agreement is improved. The actual spanwise distribution of lift coefficient probably lies between the present method and the six strip idealization since Figure 10 indicates that the present method may be high by a slight amount and Figure 11 indicates that the method of Part I may be low.

A third calculation which has not yet been discussed is the use of lifting surface panels and images in the present method. This calculation has not been done for the steady case of Figure 11; however, Figure 14 shows such a calculation for the unsteady case, and is discussed below.

3.1.3 The Effects of Frequency

A comparison of the lift coefficient, as calculated by the present method and the method of Part I for a wing-fuselage combination, is given in Figure 12. The motion of the wing may be described as a modified pitch where the normalwash

corresponds to that of steady pitch. The effects of frequency enter through the influence matrix $[D_T]$. The fuselage has a circular cross section and is not in motion. Agreement between the two methods is good for the two common frequencies ($k_r = 0.0$ and 1.0). Intermediate frequencies, $k_r = 0.1$ and 0.5 are also plotted to show the variation with frequency.

3.1.4 A High-Wing Configuration

A comparison between the results of the present method and the method of Part I is shown in Figure 13. The wing-fuselage combination associated with Figures 10 through 12 is used except for a small extension of the exposed area of the wing at the root section. The total semispan is held constant and in order to join the wing to the fuselage; a small extension to the wing surface is required at the wing root. The comparison between the two methods shows the same trends observed in Figure 11, i.e., that the results of the method of Part I lie below those of the present method.

Also shown in Figure 12 are results obtained for the midwing case. These results lie below those for the high-wing case.

Figure 14 presents a similar comparison except that the frequency is 1.0 instead of 0.0 as in Figure 13. The wing is pitching about its root leading edge. The body is at rest. In this case the real parts are in good agreement. The imaginary parts, however, differ near the wing-fuselage juncture. The imaginary lift coefficients for the present method lie below that calculated by the method of Part I. This seems to be contrary to what is expected since the results of the present method have been greater than the results of the method of Part I in Figures 11 and 13. A third calculation is presented to help decide which solution is most accurate. Specifically, the third solution consists of placing lifting surface elements on the body surface in addition to the images of the present method. The results agree almost perfectly with the present method near the wing-fuselage intersection. However, over the outboard half of the wing this calculation agrees best with the method of Part I. However, it may be observed that the difference among any of the solutions is fairly small over the outboard half of the span. This figure indicates that the image method is most accurate for this case.

3.1.5 End Plating Effects

In all of the calculations presented thus far, the configurations have been symmetrical about the $y = 0$ plane. If the left-hand wing half is omitted from the calculation, then the effect of body end-plating can be ascertained. Such a calculation is presented in Figure 15. Again the same midwing configuration, as found in Figures 10 through 12, is used except for the missing left wing half. It is expected that the end-plating effects, as obtained by the present method, are slightly smaller than they should be. Two reasons are offered for this: 1) the image within the ellipse is cut off once it crosses the $y = 0$ plane, and 2) the interference singularities cannot account for a flow that is antisymmetric across the body. If the body were circular, then the image would fully account for the end-plating effect and the onset flow to the body would be symmetric across the body thus allowing the axial singularities to properly account for interference. However, for the elliptical case, some of the end-plating effect may be lost due to the approximated and abbreviated image system. The resulting residual flow should make up for this loss in end-plating. However, flows that are antisymmetric to the body surface cannot be accounted for because of the truncation of the multipole series. If one further term were added to this series, then this effect could be accounted for even for highly elliptic cases ($b/a > 1.0$).

A comparison of lift coefficient distribution as calculated by the present method and the method of Part I, is presented in Figure 15. The wing is given an angle-of-attack of 1.0 radians. The body incidence is zero. The two methods appear to be in very close agreement. Figure 11 presents the identical case except for symmetry. In Figure 11 the calculated results of the present method lie everywhere above those of the method of Part I. However, in Figure 15 the lift distribution as calculated by the present method falls below that of the method of Part I over most of the span. This shows that, relative to the method of Part I, the present method has lost some of its end-plating effect.

The end-plating effect of a body whose ellipticity b/a falls below unity ($b/a < 1.0$) is a different matter. In this case the important component of the residual flow to the body is symmetric. As the body becomes flatter, the residual flow may lose some accuracy, as already illustrated in Figure 10, but

the ability to furnish an end-plating effect remains intact even for very small b/a ratios. Of course, if b/a becomes small enough, the body can be replaced by a lifting surface.

3.1.6 The Effect of Pickup Point Location

The averaging process (applied to the residual onset flow) outlined in Section 2.5.6 involves finding the flow normal to the body surface at various points around the cross section. These points are input quantities to the computer program of the Present Method. Figure 16 illustrates the effect of increasing the number of these points. In the lower curve, μ_z/μ^* represents the z-component of the interference doublet strength normalized by the doublet strength that would exist in the fuselage if it were pitched up at the same angle-of-attack as the wing. In this case the wing alone is pitched up to one degree and the value of μ^* is 0.001095. The upper curve gives the value of μ_y/μ^* . Of course, for this symmetric case, this quantity should be zero. If the values of α_i were chosen symmetrically (say $\alpha = 45^\circ, 135^\circ, 225^\circ, 315^\circ$) then the fictitious μ_y/μ^* would not appear. As the values of α_i are rotated away from the symmetric position, the fictitious μ_y/μ^* appears. At 15° of rotation it is at its worst (upper curve given by circles). At this worst possible point the number of points is doubled. The result is a two-thirds reduction of the error. Thus, as the number of integration points increases, the accuracy increases. However, a judicious choice of these points will allow fewer of them to be considered for the same accuracy.

3.2 Correlation of the Present Method with Other Methods and Experimental Data

3.2.1 Wing-Fuselage Combinations (Emphasis on Wing Loads)

A wing-fuselage comparison presented in Reference 8 is represented in Figure 17. In addition, calculations using the Present Method are shown. The span load for a wing (at 4.7° angle-of-attack) attached to a circular fuselage (at 0.7° angle-of-attack) is given in this figure. The agreement between the Present Method and the method of Reference 8 is excellent as is the correlation with the experimental data⁵⁰. Since this is a steady case, the agreement between the two methods should be perfect; however, a change in the number of spanwise strips near the tip has caused a slight disparity.

A second wing-fuselage comparison presented originally in Reference 18 and in Part I of this report, is reproduced in Figure 18. Shown in this figure are span loads for two modes of motion;

$$\text{Body Pitch, } h_z = \bar{c} \left(\frac{x}{\bar{c}} - \frac{x_c}{\bar{c}} \right) e^{i\omega t}$$

$$\text{Body Camber, } h_z = \bar{c} \frac{R_{\max}}{L} \left(\frac{x}{\bar{c}} - \frac{x_c}{\bar{c}} \right)^2 e^{i\omega t}$$

The first of these is pitching (of the body only) about the point x_c which is the coordinate of the center of the body. The second mode is a cambering of the body only. The nodal point is at x_c . The maximum amplitude of oscillation occurs at the body leading and trailing edges and is equal to the maximum body radius at its center. The body length is L .

The original version of Figure 18 contained a comparison of three different methods. To this list the Present Method is added. Again the Present Method agrees with the method of Reference 8. (Actually, for this figure, the method of Reference 8 has been modified to account for the doublet distribution on a body of varying radius.) The other methods referred to are those of Woodward¹⁹ and the method of Part I of this report. There are no volume effects for this problem since axial sources will not affect the wing as it is placed on the fuselage for this case. Actually, the nonlifting (source) effects of volume are not large in most cases and can usually be ignored. Also, in unsteady flow there are no nonlifting (source) volume effects since the volume is not changing with time. Currently, no volume effects are contained in the Present Method.

The results presented in Figure 18 are for steady flow. The method of Reference 8 and Woodward's method are restricted to steady flow; however, the method of Part I is not. Figure 19 presents a comparison of the Present Method with the method of Part I for the same configuration considered in Figure 18 but oscillating at a frequency of 1.0. This figure is a duplication of one found in Reference 18 and Part I of this report, with the results of the Present Method added. The real part of the span load due to body camber was plotted with the wrong sign in the original figures but is corrected here. Also, in Reference 18 there appears an error in the labeling of the ordinate.

The agreement between the two results is good for the body pitch mode but is only fair for the body camber mode. The results of the Present Method look more realistic, especially for the imaginary part of the span loads due to body camber. The probable reason for the disparity is the idealization of the body for the method of Part I. If more panels were placed on the body, an increase in accuracy would probably result (refer to Figure 11).

3.2.2 Wing-Fuselage Combination (Emphasis on Fuselage Loads)

The four methods compared in Figure 18 are again compared in Figure 20. The original version of this figure appeared in Reference 13. To this figure the results of the Present Method have been added. The configuration consists of a simple swept wing attached to a very large diameter circular fuselage. The wing is at 1.0 radian angle of attack while the fuselage is held to zero incidence. All methods are in good agreement. However, the Present Method is in better agreement with the method of Reference 8 while the Woodward method is in better agreement with the method of Part I. Again, the method of Part I predicts a lift coefficient distribution that lies below that of the Present Method.

Special attention should be paid to the fuselage span load. The usual output of the Present Method is a longitudinal loading along the fuselage length (see Figure 21). Also the total lift is known for each body. If this total lift is normalized by the root-chord length and the span over which it acts, then an average span load is the result. This average is shown as a horizontal dashed line across the fuselage. The area under the horizontal dashed line seems to be low compared with the areas produced by the other methods; however, this is deceptive and requires an explanation.

For steady flow and circular fuselages, it can be shown that an excellent approximation to the fuselage span load is made up of a constant load minus an elliptic one. The constant has the value of the lift coefficient at the root and this constant value extends from the fuselage center to the wing root and no further. The lift loss due to the elliptic distribution extends from the fuselage center to the edge of the fuselage. As in this case (Figure 20), the fuselage edge extends out beyond the wing root position and thus there is a region between the wing root and fuselage edge where there exists only the

negative elliptic distribution. Combining these two loadings gives the dashed curve across the fuselage in Figure 20. Notice that the two curves combine to give a positive span load across that part of the fuselage that does not overlap the wing. Over the overlapping part, the lift is negative. The areas under the two dashed curves (one constant) are equal. The agreement between the method of Reference 8 and the Present Method is excellent over that part of the fuselage not overlapping the wing. It is conventional to take the negative lift distribution that exists in the overlapping region and add it to the wing span load. If this is done, all curves are in close agreement. The deceptive aspect of this plot is the fact that the span load in the overlapping region of the fuselage and wing is attributed to the fuselage alone. The fact is, however, that the span load on the fuselage in this region is actually negative. This explains why the area under the dashed horizontal curve (which applies only to the fuselage) is equal to that under the curved dashed line.

The spanwise distribution of fuselage load is given in Figure 20. Figure 21 presents the longitudinal variation of the same fuselage lift. Four curves are shown: one due to the method of Part I and three due to the Present Method. The loading on the fuselage is due entirely to the wing (lift carryover) since the fuselage is at zero incidence. As expected, the Present Method Alternate II does not compare very well since the body has a large diameter compared to the wing dimensions. As noted in Figure 20, however, the total lift is in excellent agreement with the other methods. The moment (not shown) is also very good; however, the distribution of force is skewed due to the assumptions made in alternate II. Some of this skewness can be eliminated if the approximate redistribution technique, described in Section 2.6.4, is employed. The curve marked Present Method Alternate II (redistributed) is in closer agreement with the method of Part I. Since the body is circular, Alternate I may also be used. The curve marked Present Method Alternate I shows excellent agreement with the results of Part I. The results of the Present Method Alternate I lie slightly above the results of Part I but this is expected since the wing loading shows the same trend.

Figures 22 through 32 present a correlation of the Present Method with the experimental data of Körner⁵¹ and the theory of Labrujere²⁰ et al. There are a total of four configurations considered: 1) a swept wing alone (see Figure 23), 2) a swept wing and a fuselage ($D/c = 1.0$) (see Figure 24),

3) a swept wing and a fuselage ($D/c = 0.68$) (see Figure 26), 4) and a straight wing-fuselage combination ($D/c = 1.0$) (see Figure 30). The swept wings in all of the configurations are similar. Each has a constant chord and is swept 45° . The span is the same for all configurations and the only changes to the wings are those necessary to extend the wing root to the fuselage surface. In the case of the wing alone, the wing is extended to the $y = 0$ plane. Figure 22 presents the idealization of configuration 2, i.e., swept wing with $D/c = 1.0$. This idealization is typical of all the others. The solid lines represent lifting surface or body interference element boundaries. The dashed lines represent slender body element boundaries.

The experimental data of Reference 51 are given for various angles of attack. The value of $c_{L\alpha}$ (per degree) may be obtained from this data. Figure 23 presents a comparison of the distribution of lift-curve-slope as calculated for a wing alone using the Present Method and as obtained from experimental data. Experimentally, there is an obvious loss of lift due to viscosity. Notice that $c_{L\alpha}$ is lower at $\alpha = 6^\circ$ than at 3° . This is a clear indication of a nonlinear viscous effect in the data.

Figure 24 presents a similar comparison except that the configuration consists of a wing and fuselage. The fuselage is at zero incidence while the wing is pitched up. Again $c_{L\alpha}$ across both the wing and fuselage shows the characteristic loss of lift due to viscosity.

This loss of lift due to viscosity is accentuated when the fuselage is given the same angle of attack as the wing. Figure 25 presents such a comparison.

Figures 26 and 27 show comparisons similar to those given in Figures 24 and 25. The configuration is almost identical except for the fact that the fuselage is smaller ($D/c = 0.68$). The span load behaves in an interesting manner in Figure 27. The comparison seems to be very good over the outboard half semispan. The agreement then deteriorates toward the wing-fuselage intersection. This could be due to the thickening of the boundary layer in the region of the wing-fuselage intersection.

The longitudinal loading, as calculated by the Present Method, is compared to that determined experimentally in Figures 28 and 29. The fuselage

incidence is zero in Figure 28 and equal to that of the wing in Figure 9. In the region near the wing Alternate I and the redistributed Alternate II are in good agreement with the experimental data. A large disagreement between Alternate I and Alternate II appears at the leading and trailing edges of the body in Figure 29. The basic reason for this is the fact that the total lift of a slender body element is lumped at that element in the method of Alternate II whereas it is distributed over the body for Alternate I and Alternate II (redistributed).

Labrujere et al.¹⁰ compared their steady flow theory with Körner's data for an unswept-wing/fuselage combination. Figures 30 and 31 present comparisons of the spanwise lift coefficient distribution for a wing at 6° angle of attack. The fuselage is at zero degrees incidence in Figure 30 and at 6° in Figure 31. For the case of zero fuselage incidence the Present Method is in closer agreement with the method of Labrujere et al. than with the experimental data. However, for the case where the wing and fuselage are at the same incidence, the distribution calculated by the Present Method lies almost equidistant between the data and the method of Labrujere et al. The discontinuity in the span load apparent in the theory of Labrujere et al. is caused by the fact that the fuselage does not close, due to the wind tunnel sing, and thus there exists a resultant slender body lift.

Figure 32 presents a comparison of experimental and calculated longitudinal loading for the zero incidence fuselage case. The redistribute loading (Alternate II) is in very good agreement with the experimental data as is Alternate I. The original distribution, also now shown, however, shows large variations. The straight wing case exaggerates these variations because the contribution of every wing lifting surface element occurs on the body surface in that short space lying between the root chord leading and trailing edges. There is a negative drop in the longitudinal loading which is due to the fuselage interference elements. These interference elements react to the upwash generated at the body due to the bound vortices on the wing.

The last two correlations of this section are found in Figures 33 and 34. The experimental and calculated longitudinal loading on a transport aircraft

are compared for two values of Mach number. In both cases the redistributed loadings are used for alternate II. The agreement is good especially for the $M = 0.6$ case. At the higher Mach number it may be that shock waves have interferred with the flow at the point near the wing root trailing edge, where the experimental data takes a sharp jump.

3.3 T-Tail Fuselage Combination

Zwaan^{52,53} has developed a kernel function technique for T-tails. Of particular interest are the span load plots of Reference 52 for a T-tail tested with both a ground plane and a fuselage. Figure 35 presents a comparison of spanwise loading as calculated by the Present Method, by Zwaan and as determined experimentally for a T-tail in yaw. Results for the Present Method are given both for the T-tail with ground plane and fuselage. The experimental data are given only for the T-tail with ground plane. Difficulty was experienced in interpreting Zwaan's results. In Reference 52 a symbol $|k|$ was given as the absolute value of the loading. This symbol was not defined in this reference. Integration of experimental pressure data indicates that $|k|$ is $(cc_x)/(\bar{c}C_y)$, where C_y is based on the total area of the vertical fin. Using this definition, the correlation of the data with the Present Method for the vertical stabilizer is good. (Refer to the calculation of the Present Method marked "Ground Effect.") Both the absolute magnitude and phase angle compare well. If the same definition of $|k|$ holds for the horizontal stabilizer, ther there is an inconsistency in Zwaan's calculation as presented in Reference 52, Figure 8. The jump in $|k|$ on the vertical fin at the intersection of the horizontal stabilizer should be twice the value of k at this intersection on the horizontal stabilizer. If the area of the horizontal stabilizer is used in the definition of C_y then Zwaan's calculated results become consistent. (The value of $|k|$ on the horizontal at the root then becomes approximately 0.415 while half the jump on the vertical is about 0.425.) The new definition for both Zwaan's calculation and the experimental data are used to give the results of Figure 35 for the stabilizer. The agreement is good.

The effects of using a ground plane in place of the fuselage are shown in Figure 35. The two calculations, done using the Present Method, show that the ground plane increases the loading substantially, both on the vertical fin and horizontal stabilizer.

Experimental data have also been obtained for the T-tail and fuselage in steady flow (yaw). The shape of the fuselage was taken from a small sketch given in Reference 52, Figure 12. This sketch is reproduced in Figure 35. Figure 36 shows a similar sketch with the addition of the idealized fuselage that is used with the Present Method. The results correlate well except near the fuselage.

3.4 Wing and Tip Mounted Nacelle Combination

The only experimental data that have been found for a wing/body configuration in oscillatory motion is that reported by Cazemier and Bergh^{54,55,56}. A wooden model of a low-aspect-ratio wing, fitted with a large wing-tip nacelle was tested over a wide range of frequencies. The wind tunnel Reynolds number was low, $Re = 4.7 \times 10^6/\text{meter}$, and the model was about one meter in semispan. The test was set up to read the lifting pressure $[C_p(\text{lower}) - C_p(\text{upper})]$ directly. The pressures were transmitted from the model through calibrated tubes. The tubes were calibrated to eliminate the phase shift caused by the transmission time required to communicate the pressure from the model to the pick-up point.

An extensive correlation of the Present Method with this experimental data is presented — since it is the only data of its kind available. Figures 38 through 57 are devoted to this correlation.

Figure 37 illustrates the idealization of the two configurations considered, a wing alone and a wing/nacelle. The wings in the two configurations are slightly different. The first wing strip, in the wing/nacelle configuration, is missing on the wing-alone configuration. The last strip on the aileron is filled in for the wing alone configuration. The interference elements are shown on the nacelle; however, the slender body elements are not. On the wing the inboard control surface is called the flap and the outboard control surface is called the aileron. The pitch and roll axes are presented in Figure 37, as are the stations at which experimental pressures were taken.

A comparison of lifting pressure for the wing alone in steady pitch is given in Figure 38. The experimental data lies above the calculated results for all stations presented. This is very extraordinary since experimental data usually lies below the calculated results. Normally the wing will be less effective as a lifting surface due to the action of viscosity. The

reason for this peculiar behavior is not known. A similar comparison for a deflected flap is shown in Figure 39. The correlation is good and shows the correct relationship between calculated results and experimental data. A further comparison for a deflected aileron is given in Figure 40. The correlation is not quite as good as for the flap.

In all of the comparisons the pressures are normalized as follows:

$$\Delta C_p = \frac{\Delta P}{qB}$$

$$B = \begin{cases} s &= 1.097m, \text{ plunge} \\ \alpha &, \text{ pitch} \\ \delta_f &, \text{ flap} \\ \delta_a &, \text{ aileron} \\ \phi &, \text{ roll} \end{cases}$$

where α , δ_f , δ_a , and ϕ are the angle-of-attack, flap angle, aileron angle and roll angle. The reduced frequency is based on $\bar{c} = 1.097m$ for both the wing alone and wing/nacelle cases. The reduced frequency as defined in References 54, 55 and 56 is $\omega\bar{c}/U_\infty$, which is twice as large as that defined in this report, $\omega\bar{c}/2U_\infty$. Thus, reduced frequencies of 0.5 and 1.0 listed in the figures of this report represent frequencies of 1.0 and 2.0 in the notation of References 54, 55 and 56.

A comparison of lifting pressures for the wing alone oscillating at a reduced frequency of 0.5 is given in Figure 41. The real part of the lifting pressure for pitching motion is very similar to the steady case. The correlation at this reduced frequency leaves something to be desired, especially for the plunging case. Pressure plots for rolling and aileron motion are given in Figure 42. The case of rolling is very similar to that of plunging, as it should be. The aileron correlation is good. Figure 43 is the same as 41 except the frequency is 1.0 instead of 0.5. Surprisingly, the agreement between data and calculated results is better at this reduced frequency (1.0) than it is at 0.5. The same comment can be made of the plunge case shown in the same figure. An extra station is included for the pitching case to compare Laschka's method⁵⁷ with the Present Method and the experimental data. Laschka's theory (as read from a very small figure) is given for strip number 5. Essentially, the results by Laschka are the same as the Present Method.

A comparison of pressures for rolling and flapping is presented in Figure 44. Again the correlation is somewhat better for the reduced frequency of 1.0 than it is for 0.5.

The above comparisons refer to the wing-alone calculation. These were presented so that the nacelle effects present in the next set of comparisons could be properly assessed.

The lifting pressure distribution for the wing/nacelle at station 2 is presented in Figure 45; both calculated results and experimental data are shown. The comparison is as good as the wing-alone case. A comparison of lifting pressure for pitch, plunge and roll at a reduced frequency of 0.5 is given in Figure 46. Generally, the agreement between the Present Method and experimental data is better than for the wing-alone case. As much cannot be said of the agreement at the reduced frequency of 1.0. Figure 47 presents this comparison. The agreement between calculated results and experimental data for pitch is good, while that for plunge and roll is not as good. In all of the results where the agreement is not as good as it might be, there seems to be a phase shift of the results.

The pressure plots just discussed are presented to compare experimental and calculated chordwise loadings. In many instances, a comparison of these two for the span load or lift coefficient distribution is more enlightening. For this reason, the experimental lifting pressure data available in References 55 and 56 has been integrated to give lift coefficient. The method of integration was to connect the experimental data by straight lines and integrate by planimeter.

The first of the lift coefficient distribution comparisons is given in Figure 48 for the steady case. The upper curve gives a comparison of lift coefficient, as calculated by the Present Method, and as determined experimentally for the wing alone case. The agreement is generally good except for the strange property that the experimental data lies above the calculated results. The lower curve presents a similar comparison for the wing/nacelle case. There are two curves marked "Present Method." The lower curve is the result of using the usual method where axial elements in conjunction with images are used to model the flow. The upper curve results were obtained

after lifting surface elements were placed on the body surface (in conjunction with images). This upper curve is in better agreement with the data. The results of the upper curve are obtained at the cost of doubling the number of unknowns in the problem. Thus, accuracy and efficiency must be balanced by the user of the Present Method. Also shown on the wing/nacelle (lower) plot is the wing-alone case. There is a very large difference between the wing-alone and wing/nacelle lift coefficient distributions. The Present Method goes a long way toward predicting the full effect of the nacelle even when lifting surface elements are not placed on the body surface.

At a reduced frequency of 0.5, the comparison between calculated results and experimental data shows good agreement for the real part and poor agreement for the imaginary part. Figure 49 presents such a comparison for plunging and pitching. A comparison for aileron motion is given in Figure 50. This figure shows that the aileron is not as effective as predicted, especially for the imaginary part. The comparison of lift coefficient distribution for a reduced frequency of 1.0 is given in Figure 51 for roll and pitch. The agreement between calculated and experimental data is worse for the real part and better for the imaginary part when compared with the results at the reduced frequency of 0.5. The results presented in Figure 52 are of interest when compared with those of Figure 50. In Figure 50 the experimental data lay below the calculated results for both real and imaginary parts. In Figure 51 the real part of the data lies above the calculated results while the imaginary part lies below.

The next set of comparisons is for the lift coefficient distribution for the wing/nacelle combination. One peculiarity of these plots is that there are discontinuities in the distributions at the root and tip of the wing. These are caused by a discontinuous chord length at these locations. Reference back to Figure 37 will show immediately these planform peculiarities.

The agreement between calculated and experimental spanwise distribution of lift coefficient for the wing/nacelle combination is about the same as that for the wing alone. Figure 53 presents these results for plunge and pitch motions. Except for some scatter (station 2) the real parts are in close agreement while the experimental data lies below the calculated results for the imaginary part. The comparison at a reduced frequency of 1.0 is shown in

Figure 54 for rolling and pitching. Again the comparison is about the same as the wing-alone case.

In all of the comparisons presented for the wing-alone and wing/nacelle there seems to be a phase shift between the calculated results and the experimental data. The phase shift seems to increase as the frequency increases. The reason for this is not known. It is felt that the agreement should be better, especially for the wing-alone calculation, since similar comparisons have been made in References 10, 12 and 13 and show good agreement.

Further analysis of the lift coefficient data has been done in an attempt to isolate the nacelle effect on the wing. Specifically, the wing-alone distributions have been subtracted from the wing/nacelle distributions both for the calculated results and the experimental data. Some irregularities are introduced when this is done since the wing without the nacelle is not exactly the same as that with the nacelle. Some of the effects, then, will be due to this difference and not due to the nacelle.

The steady flow results for pitch are given in Figure 55. The experimental data lies generally between the two approaches of the Present Method (one with axial body elements, one with surface elements, both with images). The same type of comparison is given in Figure 56 for a reduced frequency of 0.5. The data shows scatter for the real part both for plunge and pitch although the agreement is excellent near the wing/nacelle intersection. The agreement for the imaginary parts for plunge and pitch is not very good. When the reduced frequency is increased to 1.0, the correlation for the real part improves, generally, as shown in Figure 57. The imaginary part, however, is not as good, especially for pitch. Also shown in Figure 57 are results obtained from Part I of this report (also, Reference 18) for the wing in pitch. The effect of the nacelle in these results is very large. This discrepancy may be due to the fact that a slightly different wing planform was used in Part I. Specifically, the gaps at the wing root and tip are not present in the calculation presented in Part I. Also, the nacelle cross section was represented by a rectangle. This rectangle was large enough to envelope the nacelle. Thus, the end-plating effect was larger.

3.5 Wing-Nacelle-Fuselage Combination

A good example of a complex wing-nacelle-fuselage combination is found in the B-58 bomber. Data were made available from General Dynamics, Fort Worth Division, through Dr. R. G. Bradley. The data are for configurations with and without nacelles. A detailed description of the configuration is found in Reference 58. The idealization of this configuration for calculations by the Present Method is given in Figure 58. The fuselage was cambered as well as the wing. The wing camber was restricted to a conical region at the leading edge. This region is easily identified in Figure 58 as the one containing the conical rays emanating from a point on the x-axis. The camber is approximated by three constant slope conical wedges. A more conventional idealization is developed for that region of the wing without camber and for the pylon. The outboard pylon is omitted since it was thought to be too small to effect the calculations. There is a gap between the wing and outboard nacelle. The outboard nacelle is at a negative incidence and therefore the leading edge is considerably lower than the trailing edge where it attaches to the wing. The average gap at the center of the nacelle is the one shown in the figure. The small arrows on the fuselage and nacelle axes indicate the directions of force (and doublet orientation) that are allowed for the calculation. The interference elements are shown on the fuselage and nacelles. Shown on the fuselage alone are the slender body elements indicated by tick marks on the actual fuselage shape.

A comparison of the Present Method with experimental data for the configuration with nacelles is presented in Figure 59. Specifically, the span load for the wing at 4 degrees angle-of-attack (in addition to the conical camber) is presented. The experimental data lie above the calculated values. Similar results were obtained by Bradley and Miller²¹ for the B-58 bomber. The cause of this is found in the very high sweep of the leading edge. As is well known, wings with large leading edge sweep angles develop a leading edge vortex which causes an increase in the lift. Figure 60 presents a similar comparison for the case of the wing without the nacelles. Again the leading edge vortex increases the lift over the calculated value.

To determine the effect of the nacelles on the wing span-loading, the calculated results of Figures 59 and 60 are replotted on a single curve

in Figure 61. A calculation was made in which the nacelle diameters were doubled. The results of this calculation are also shown in Figure 61. The obvious conclusion that is drawn from this figure is that as the nacelle diameter is increased, the lift on the wing is increased. The nacelles as well as the pylon tend to prevent spanwise flow and in this way increase the lift.

The span load on the B-58 wing in oscillatory motion is given in Figure 62. Specifically, the aircraft was made to pitch about the wing "apex" (determined by an extension of the wing leading edge to the center of the fuselage) at a reduced frequency of 0.5 ($\bar{c} = 19.15$ in.). The normalizing chord length used for the span load is c_R which is the root-chord length (34.7 in.). These dimensions are for the wind tunnel model. One further calculation is presented in Figure 62. The aircraft is made to operate in ground effect, at a height of 10 in. above the ground. The height/root chord ratio is 0.288. The effect of the ground is appreciable especially for the real part of the span loading inboard of the pylon. There the load is nearly doubled. Also, nearly doubled for the ground effect case is the computing time. The reason for this is that the kernel is evaluated twice as many times in the ground effect case. Each sending point on the aircraft has a counterpart in its ground effect image.

The span load calculations presented in Figure 62 are for unit angle of attack, no cambering modes are present. For this case a simple idealization of the wing is used.

The fuselage loading associated with the unsteady case (out of ground effect) is presented in Figure 63. The original loading for Alternate II is presented. In this case the original loading and the redistributed loading should be very close because of the slenderness of the fuselage. The major contribution to the fuselage lift is obtained in the region of the wing (indicated in Figure 63 by a heavy line lying on the x-axis). It is interesting to note that the point of maximum loading for the imaginary part lies a considerable distance aft of the point of maximum loading for the real part.

The loading on the nacelle is considerably less than that on the fuselage. Figure 64 shows that the maximum lift (or side force) coefficient is about 6.0, while Figure 63 shows the maximum for the fuselage is about 30. Figure 64 presents the vertical loading on the inboard nacelle and the horizontal loading on the outboard nacelle. The load distributions given in Figure 64 have not been redistributed and are the original ones of Alternate II.

4.0 CONCLUSIONS AND RECOMMENDATIONS

4.1 Conclusions

A method for predicting oscillatory loads on very general configurations has been developed. Configurations may include a combination of any or all of the following components: 1) lifting surfaces such as wings, pylons, stabilizer, fin, etc., with arbitrary dihedral, 2) partial or full span control surfaces and, 3) bodies such as fuselages, nacelles, stores, etc. with elliptic cross-sectional shapes. The operating conditions are also very general: 1) all frequencies of practical interest and all subsonic Mach numbers, 2) symmetry and ground effect, 3) mutual interference of lifting surfaces, and 4) multiple modes of oscillation (described by polynomials).

One of the main features of the Present Method is the efficiency with which these configurations and conditions are handled. With the kernel function techniques even simple plane wings present time consuming numerical difficulties. If it were possible to extend the kernel function method to the status of the present method the computational effort might be excessively large.

The effects of varying some of the important parameters involved have been studied. Specifically the effects considered are those of: 1) body radius, 2) cross-sectional aspect ratio, 3) frequency, 4) wing position on the fuselage, and 5) end plating effects of a body. The conclusions drawn from these studies are outlined below:

- 1) The body radius has two distinct effects: one is due to the flow field associated with a body at angle of attack and the other is associated with interference. The fuselage angle of attack effect increases the wing loading as the ratio of fuselage diameter to wing span is increased. The fuselage interference effect shows variations as the radius ranges from zero to infinity but is the same at the two extremes.
- 2) The interference effect of fuselage cross-sectional aspect ratio (ratio of b/a where b = semi-height, a = semi-width) is monotonic, reaching its greatest value when the fuselage is a vertical slit $b/a = \infty$.

The angle of attack effect is just the opposite reaching a minimum when $b/a = \infty$. The image system for elliptic cross sections starts to fail when b/a is greater than 2.0 or less than 0.5.

3) The effects of frequency for wing-body combinations are very similar to the wing alone case.

4) Placing a wing high on a fuselage of elliptic cross section tends to bring the left and right wing halves closer together. This increases the interference effect of the body. The angle of attack effect, however, is reduced.

5) The Present Method predicts the end plating effect of a body very accurately for a circular cross section ($b/a = 1$). However, when the ratio of b/a is near the value of 2.0 (or greater) the predicted end plating effect starts to fall below the correct value. There are two reasons for this behavior. The first is the fact that the image within the ellipse is terminated at its centerline. The second reason is that the interference elements cannot account for an anti-symmetric flow across the body cross section.

If conditions or configurations are simplified, then other methods may be used to compare with the present method. Cases which involve only lifting surfaces may be handled by the methods of Laschka⁵⁷ and Zwan⁵². Comparisons of these methods with the Present Method show good agreement. For the steady case the theories of Woodward¹³ and Labrujere²⁰ may be used for comparison. Loads predicted by the Present Method fall slightly below the thick wing theory of Labrujere but lie slightly above those of Woodward.

The Present Method is also compared with the method of Part I of this report. The method of Part I employs lifting surface elements on the body surface to account for the body interference effects. The results are highly dependent on the idealization. If the cross section is represented by only a few defining elements then the results can be inaccurate especially for unsteady flow.

Several general conclusions can be made about the comparison of the

Present Method and the method of Part I. In steady flow the loading, as calculated by the method of Part I, usually falls slightly below that calculated by the Present Method. As the number of body surface elements is increased (for the method of Part I) the agreement between the two methods improves. For unsteady flow the situation is more complicated. There exist differences between the two methods especially near the wing-fuselage intersection. If the representation, in the method of Part I, is crude then variations in the results occur that do not exist in the results of the Present Method. In some instances a third calculation was done in which both images and lifting surface elements were used. This calculation confirmed the results of the Present Method in most cases. The exceptions to this were cases involving bodies placed at wing tips.

The total loads and moments on bodies, as calculated by the Present Method, are very accurate. The spanwise variation of lift coefficient agrees very well with the method of Part I, Woodward's¹⁹ method and the method of Reference 8. The longitudinal distribution of load along the body surface is not as accurate for Alternate II. The reason for this is that the total load on the body due to one lifting surface element is found and lumped at the same longitudinal location as the lifting surface element for this method. The longitudinal distribution on the body arises then only from the longitudinal distribution of lifting surface elements. A redistribution of the load, based on an approximate procedure, increases the accuracy under most conditions.

Many comparisons of the results of the Present Method with experimental data are presented in this report. Some of the results are apparently contradictory. For this reason the results will be discussed for each of the experiments.

The data of Martina⁵⁰ for a wing-fuselage combination agrees very well with the results of the Present Method. Similar data were obtained by Körner⁵¹ for low Reynolds Number and low Mach Number. The data show

a characteristic loss of effectiveness relative to the calculated results which is the direct result of the boundary layer. Specifically the boundary layer is much thicker on the upper surface and effectively produces an "uncambering" of the wing. The boundary layer is also very thick at the wing-fuselage intersection and thus it is not surprising that the loss of lift is found to be greatest there. The redistributed longitudinal loading on the fuselage is in good agreement with the experimental data.

The only experimental data found for a wing/body combination in oscillatory flow were reported by Cazemier and Bergh^{54, 55, 56} who considered a wing with a tip-mounted engine nacelle. These data were obtained at low Reynolds Number and low Mach Number. For reference purposes some of the data were obtained for the wing alone case. The experiment for the wing alone in steady flow was found to lie slightly above the calculated results. This is a very strange result for this configuration and casts some doubt on all of the comparisons. Usually the data are below the calculated results. For the unsteady cases there seemed to be a phase shift between the data and calculated results. Also plots are presented to isolate the effects of the nacelle. In general, the real or in-phase components of the calculated results and experimental data agreed well but the imaginary parts did not agree as well. Generally speaking, the comparisons of calculated and experimental chordwise loading showed good to fair agreement. The functional shapes of the pressure as determined experimentally and as calculated are in good to fair agreement even though the integrated value of lift may, in some instances, not be.

Finally, a comparison is made between calculated and experimental span loading for the B-58 bomber. The leading edge sweep of the B-58 is 60°. Because of this a leading edge vortex is formed. This causes the experimental data to lie above the calculated results. The Present Method does not account for this nonlinear effect.

4.2 Recommendations for Further Work

The recommendations for future work fall into three categories:
1) improved efficiency, 2) improved modal representation and, 3) improved body representation.

A large amount of time is expended in calculating the kernel function. The kernel is evaluated at three points on each lifting surface element*. For each element there may be several images, a symmetry plane and a ground effects plane. Efficiency would be improved if appropriate far field formulas are used for receiving points that lie at a large lateral distance from the element. A second and more radical method of improving the efficiency is to cover the lifting surfaces with trapezoidal vortices. The trapezoidal vortex developed in the Present Method is simple but not very efficient. A new formula could be developed for the trapezoidal vortex that does not require the evaluation of the complicated kernel. It would be simpler because the trapezoidal vortex possesses no wake and thus the expression contains one less integration. The only place where a wake is required is at the wing trailing edge.

The second recommendation pertains to an improvement of the aircraft modal representation. The polynomial approach lends itself to scientific investigation where modes are simple. When the modes become complicated however it may be desirable to incorporate other more practical modal input methods. Several other methods have been outlined in Section 2.2 and will be repeated here. One possibility is to input a set of modal deflections at various spanwise stations along the wing and use a spline fitting technique to interpolate for intermediate values of deflections and slopes in both the span and chordwise directions. A second method would be to generate an aerodynamic influence coefficient matrix [AIC] for such a set of structural deflection points.

The third recommendation deals with a series of improvements of the body representation. The longitudinal distribution of load on the body surface could be improved. Currently the unsteady pressure equation

*The value of the kernel at the outboard edge of an element is the same as the kernel at the inboard edge of the element on the next strip outboard. This fact is taken into account requiring that the kernel be evaluated only twice per element.

is integrated first longitudinally and then around the cross section for Alternate II. If possible, this integration procedure should be reversed for elliptical cross sections so that more accurate distributions could be obtained. The computational effort would be increased but it may be worth the effort. The theory for circular cross sections has not been automated. It is anticipated that it will furnish more accurate results for bodies with circular cross sections.

Currently, the flow field due to a body is generated by one or two singularities placed near the body axis. The resulting cross-sectional shapes may not represent the actual body shape accurately. The flow field close to the body is highly dependent on the details of the shape of the cross section. It may be worth while to investigate the possibility of improving upon the current idealization. A more refined method of accounting for the end plating effects of a body would be appropriate. Specifically, a more complicated singularity should be developed to account for an anti-symmetric flow to the body surface.

The entire problem of wing-tail interference should be reconsidered. The recommendations of Section 2.5.8 could be implemented along with a method of accounting for wing wake convection and roll up. One of the recommendations of Section 2.5.8 is to use two different average fuselage diameters. A diameter appropriate for the wing is used for wing-on-wing and tail-on-wing interactions. A diameter appropriate for the tail would be used for wing-on-tail and tail-on-tail interaction.

REFERENCES

1. Watkins, C.E., Runyan, H.L., and Cunningham, H.J., "A Systematic Kernel Function Procedure for Determining Aerodynamic Forces on Oscillating or Steady Finite Wings at Subsonic Speeds," R-48, 1959, NASA.
2. Ashley, H., Widnall, S., and Landahl, M.T., "New Directions in Lifting Surface Theory," AIAA Journal, Vol. 3, No. 1, 1965, pp. 3-16.
3. Falkner, V.M., "The Calculation of Aerodynamic Loading on Surfaces of Any Shape," R&M 1910, 1943, British Aeronautical Research Council.
4. Rubbert, P.E., "Theoretical Characteristics of Arbitrary Wings by a Non-Planar Vortex Lattice Method," Report D6-9244, 1964, Boeing Company, Seattle, Washington.
5. Dulmovits, J., "A Lifting Surface Method for Calculating Load Distributions and the Aerodynamic Influence Coefficient Matrix for Wings in Subsonic Flow," Report ADR 01-02, 64.1, 1964, Grumman Aircraft Engineering Corp., Bethpage, New York.
6. Hedman, S.G., "Vortex Lattice Method for Calculation of Quasi Steady State Loadings on Elastic Wings in Subsonic Flow," Report FFA 105, Oct. 1965, Aeronautical Research Institute of Sweden, Stockholm.
7. Belotserkovskii, S.M., The Theory of Thin Wings in Subsonic Flow, Plenum Press, New York, 1967.
8. Giesing, J.P., "Lifting Surface Theory for Wing-Fuselage Combinations," Report DAC-67212, Aug. 1, 1968, McDonnell Douglas Corp. Long Beach, California.
9. James, R.M., "On the Remarkable Accuracy of the Vortex Lattice Discretization in Thin Wing Theory," Report DAC-67211, Feb. 1969. McDonnell Douglas Corp. Long Beach, California.
10. Albano, E., and Rodden, W.P., "A Doublet-Lattice Method for Calculating Lift Distributions on Oscillating Surfaces in Subsonic Flows," AIAA Journal, Vol. 7, No. 2, Feb. 1969, pp. 279-285; errata, AIAA Journal, Vol. 7, No. 11, Nov. 1969, p. 2192.
11. Stark, V.J.E., "Aerodynamic Forces on a Combination of a Wing and Fin Oscillating in Subsonic Flow," Report TN-54, 1964, Saab Aircraft Co., Linkoping, Sweden.
12. Stahl, B., Kalman, T.P., Giesing, J.P., and Rodden, W.P., "Aerodynamic Influence Coefficients for Oscillating Planar Lifting Surfaces by the Doublet Lattice Method for Subsonic Flows Including Quasi-Steady Fuselage Interference," Report DAC-67201, Oct. 1968, McDonnell Douglas Corp., Long Beach, California.

13. Kalman, T.P., Rodden, W.P., and Giesing, J.P., "Application of the Doublet-Lattice Method to Nonplanar Configurations in Subsonic Flow," Journal of Aircraft, Vol. 8, No. 6, June 1971, pp. 406-413.
14. Rodden, W.P., Giesing, J.P., and Kalman, T.P., "Refinement of the Non-planar Aspects of the Subsonic Doublet Lattice Lifting Surface Method," Douglas Paper No. 5819, June 1970. (To be published in the Journal of Aircraft.)
15. Rodden, W.P., and Giesing, J.P., "Application of Oscillatory Aerodynamic Theory to Estimation of Dynamic Stability Derivatives," Journal of Aircraft, Vol. 7, No. 3, May-June 1970, pp. 272-275.
16. Giesing, J.P., and Rodden, W.P., "Sears Function and Lifting Surface Theory for Harmonic Gust Fields," Journal of Aircraft, Vol. 7, No. 3, May-June 1970, pp. 252-255.
17. Kalman, T.P., Giesing, J.P., and Rodden, W.P., "Spanwise Distribution of Induced Drag in Subsonic Flow by the Vortex Lattice Method," Journal of Aircraft, Vol. 7, No. 6, Nov.-Dec. 1970, pp. 574-576.
18. Rodden, W.P., Giesing, J.P., and Kalman, T.P., "New Developments and Applications of the Subsonic Doublet-Lattice Method for Nonplanar Configurations," AGARD Symposium on Unsteady Aerodynamics for Aeroelastic Analyses of Interferring Surfaces, Paper No. 4, presented in Sonsberg, Osisofjorden, Norway, 3-4 November 1970, AGARD-CP-80-71.
19. Woodward, F.A., "Analysis and Design of Wing-Body Combinations at Subsonic and Supersonic Speeds," Journal of Aircraft, Vol. 5, No. 6, Nov.-Dec. 1968, pp. 528-534.
20. Labrujere, Th.E., Loeve, W., Slooff, J.W., "An Approximate Method for the Calculation of the Pressure Distribution on Wing-Body Combinations at Subcritical Speeds," NLR MP 70014U. Also presented at the AGARD Specialist Meeting on Aerodynamic Interference, Silver Spring, Maryland, 28-30 September 1970, AGARD Conference Proceedings No. 71.
21. Bradley, R.G., and Miller, B.D., "Application of Finite-Element Theory to Airplane Configurations," Journal of Aircraft, Vol. 8, No. 6, June 1971, pp. 400-405.
22. Spangler, S.B., and Menderhall, M.R., "Theoretical Investigation of Ducted Fan Interference for Transport-Type Aircraft," NASA Symposium on Analytic Methods in Aircraft Aerodynamics, 28-30 October 1969. Published in NASA SP-228, Paper No. 30, pp. 703-719.
23. Borland, C.J., "Methods of Calculating Aerodynamic Loads on Aircraft Structures: Part 1 - Wing-Body Interference Effects," AFFDL-TR-66-37, Part 1, Aug. 1966, Air Force Flight Dynamics Laboratory, Wright-Patterson Air Force Base, Ohio.

24. Chou, D.C., "Methods of Calculating Aerodynamic Loads on Aircraft Structures: Part III - Effects of Engines, Stores and Wing-Tail Interference," AFFDL-TR-66-37, Part 3, May 1966, Air Force Flight Dynamics Laboratory, Wright-Patterson Air Force Base, Ohio.
25. Harder, R.L., MacNeal, R.H., and Rodden, W.P., "A Design Study for the Incorporation of Aeroelastic Capability into NASTRAN," NASA CR-111, 1971.
26. Revell, J.D., "Second-Order Theory for Steady or Unsteady Subsonic Flow Past Slender Lifting Bodies of Finite Thickness," AIAA Journal, Vol. 6, No. 6, June 1969, pp.
27. Munk, M.M., "The Aerodynamic Forces on Airship Hulls," NACA Report 184, 1924.
28. Von Kármán, T., "Calculation of Pressure Distribution on Airship Hulls," NACA Report 574, July 1930.
29. Lighthill, M.J., "Supersonic Flow Past Slender Bodies," A.R.C. R&M No. 2003, 1945.
30. Jones, R.T. "Properties of Low-Aspect-Ratio Pointed Wings at Speeds Below and Above the Speed of Sound," NACA Report No. 835, 1946; also NACA TN No. 1032, 1946.
31. Miles, J.W., "On Non-Steady Motion of Slender Bodies," Aeronautical Quarterly, Vol. II, Nov. 1950.
32. Ward, G.N., "Supersonic Flow Past Slender Pointed Bodies," Quarterly Journal Mach. & Appl. Math., Vol. 2, pp. 75-97, 1940.
33. Adams, M.C., and Sears, W.R., "Slender Body Theory-Review and Extension," J. Aeronautical Sciences, Vol. 20, No. 2, pp. 85-98, Feb. 1953.
34. Van Dyke, M.D., "First- and Second-Order Theory of Supersonic Flow Past Bodies of Revolution," J. Aeronautical Sciences, March 1951.
35. Hess, J.L., and Smith, A.M.O., "Calculation of Potential Flow About Arbitrary Bodies," Progress in Aeronautical Sciences, Vol. 8, Pergamon Press, Oxford, New York, 1966.
36. Landweber, L., "Potential Flow About Bodies of Revolution and Symmetric Two-Dimensional Forms," Iowa Institute of Hydraulic Research, December 1959, State University of Iowa, Iowa City, Iowa.
37. Von Kármán, T., and Moore, N.B., "The Resistance of Slender Bodies Moving with Supersonic Velocities with Special Reference to Projectiles," Trans. A.S.M.E., Vol. 54, pp. 303-310, 1932.
38. Tsien, Hsue-Shen, "Supersonic Flow Over the Inclined Body of Revolution," J. Aeronautical Sciences, Vol. 5, No. 12, pp. 480-483, 1938.

39. Lennertz, J., "On the Mutual Reaction of Wings and Body," NACA TM 400, 1927.
40. Durand, W.F., "Influence of the Propeller on Other Parts of the Airplane Structure," Aerodynamic Theory (Durand, F.W., Editor) Vol. 4, Div. M. Julius Springer, Berlin, 1935.
41. Rehorst, S., "Aerodynamics of Nonuniform Flows as Related to an Airfoil Extending Through a Circular Jet," J. Aeronautical Sciences, Vol. 25, No. 1, pp. 11-28, 1958.
42. Wu, T., Yao-tsu, and Talmadge, R.B., "A Lifting Surface Theory for Wings Extending Through Multiple Jets," Vehicle Research Corporation, Report No. 3, Aug, 1961.
43. Zlotnick, M., and Robinson, S.W., "A Simplified Mathematical Model for Calculating Aerodynamic Loading and Downwash for Wing-Fuselage Combinations with Wings of Arbitrary Plan Form," NACA TN 3057, Jan. 1954.
44. Gray, W.L., and Schenk, K.M., "A Method for Calculating the Subsonic Steady-State Loading on an Airplane with a Wing of Arbitrary Plan Form and Stiffness," NACA TN 3030, 1953.
45. Multhopp, H., "Zur Aerodynamik des Flugzeugrumpfes (Or. the Aerodynamics of the Fuselage)," Luftfahrtforschung, 18, pp. 52-66, 1945.
46. Weber, J. Kirby, D.A., and Kettle, D.A., "An Extension of Multhopp's Method of Calculating the Spanwise Loading of Wing Fuselage Combinations," British R&M 2872, 1956.
47. Lawrence, H.R., and Flax, A.A., "Wing-Body Interference at Subsonic and Supersonic Speeds-Survey and New Developments," Journal of Aeronautical Sciences, Vol. 21, No. 5, May 1954.
48. Laschka, B., "Interfering Lifting Surfaces in Subsonic Flow," AGARD Structures and Material Panel Meeting, Istanbul, Turkey, 28 Sept.-8 Oct. 1969.
49. berman, J.H., Shpyrykevich, P., and Smedfjeld, J.B., "A Subsonic Non-planar Kernel Function for Surfaces Inclines to the Freestream," Journal of Aircraft, Vol. 7, No. 2, Mar.-Apr. 1970, pp. 188-190.
50. Martina, A.P., "The Interference Effect of a Body on the Spanwise Load Distribution of Two 45° Sweptback Wings of Aspect Ratio 8.02 from Low-Speed Tests," NACA TN 3730, Aug. 1956.
51. Körner, H., "Untersuchungen zur Bestimmung der Druckverteilung an Flügel-Rumpf-Kombinationen, Teil I: Messergebnisse für Mitteldeckeraanordnung aus dem 1.3m - Windkanal," DFVLR - Rept. No. 0562. June 1969.
52. Zwaan, R.J., "Calculated Results for Oscillating T-Tails in Subsonic Flow and Comparison with Experiments," NLR Rept. MP 253, Aug. 1967.

53. Zwaan, R.J., "Application of a Method for Estimating Experimental Pressure Distributions to an Oscillating T-Tail," NLR TR 68048L, May 1968.
54. Cazemier, P.G., and Bergh, H., "Messungen Instationärer Druckverteilungen am Flügelhalbmodell der V.J. 101-C," NLR Rept. F.232, Oct. 1964.
55. Bergh, H., and Cazemier, P.G., "Ergebnisse der Instationären Druckmessungen am Flügelhalbmodell der V.J. 101-C mit Triebwerksgondel," NLR F.233, May 1963.
56. Bergh, H., Cazemier, P.G., "Ergebnisse der Instationären Druckmessungen am Flügelhalbmodell der V.J. 101-C ohne Triebwerksgondel," NLR F.234, May 1963.
57. Laschka, B., "The Pressure, Lift and Moment Distributions on a Harmonically Oscillating Sweptback Wing of Low Aspect Ratio at Low Subsonic Speeds. Comparison Between Theory and Measurements," Proceedings of the International Council of the Aeronautical Sciences. Fourth Congress, Paris, pp. 259-313, 1964. Also, Royal Aircraft Establishment Library Translation 1223, April 1967.
58. Phelps, E.R., "Pressure Distribution at Mach Numbers of 1.6 and 1.9 of a Conically Cambered Wing of Triangular Plan Form with and without Pylon Mounted Engine Nacelles," NACA RM A56B03.
59. Walker, C., "Summary Report of Wind Tunnel Tests on a 1/17-scale Pressure Model of the Project MX-1964 Airplane at the 10-foot Transonic Tunnel of WADC," Convair-Fort Worth, Report FZT-4-102, 22 September 1955.
60. Hess, J. L., and Riddell, T. M., "Direct Solution of a Square Matrix Whose Size Greatly Exceeds High-Speed Storage," Douglas Aircraft Company Report DAC-70000, July 1969.

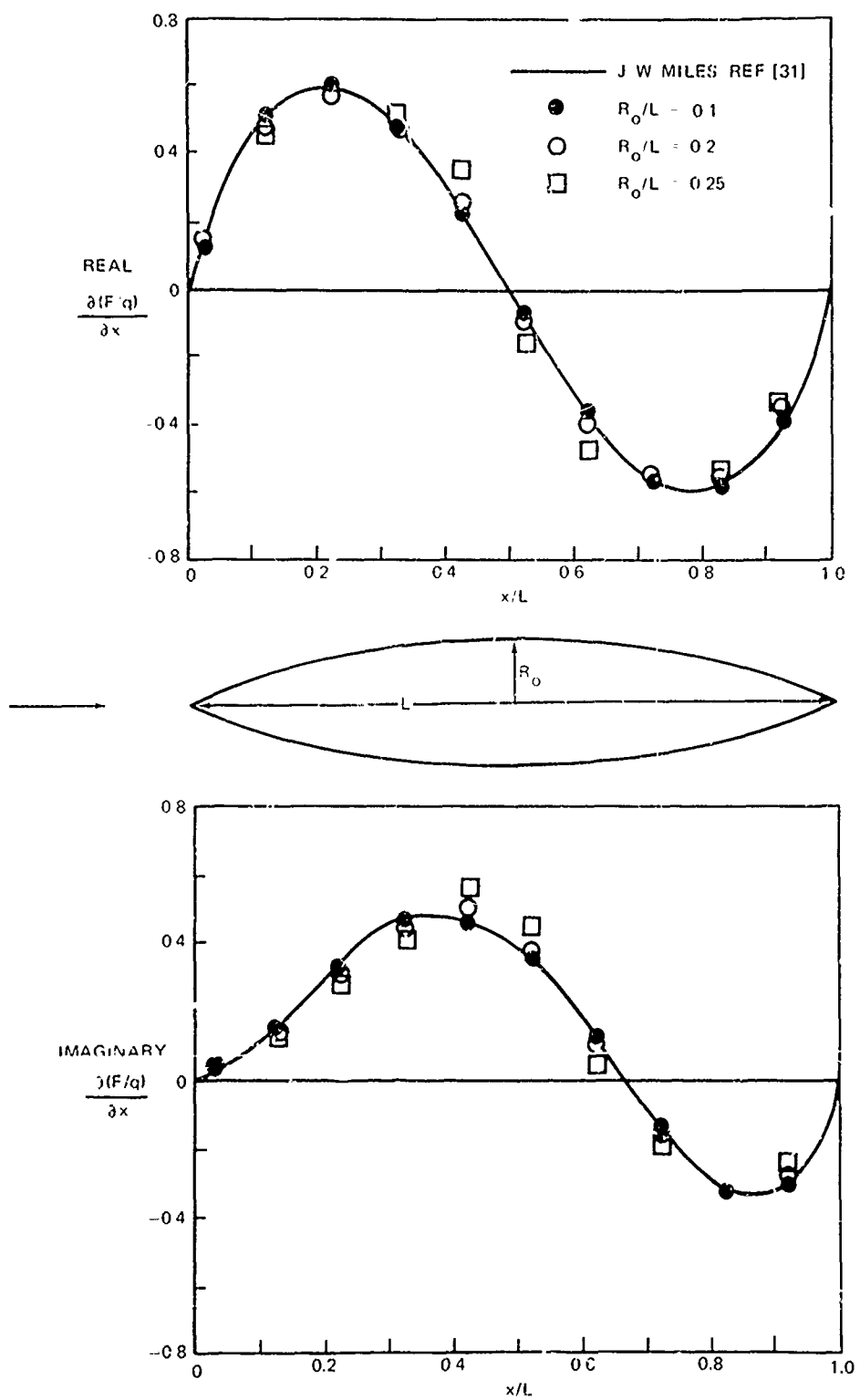


Figure 1. Axial Load Distribution on a Parabolic Pointed Body of Revolution Oscillating in Pitch about its Leading Edge. ($\omega L/U_\infty = 0.1$)

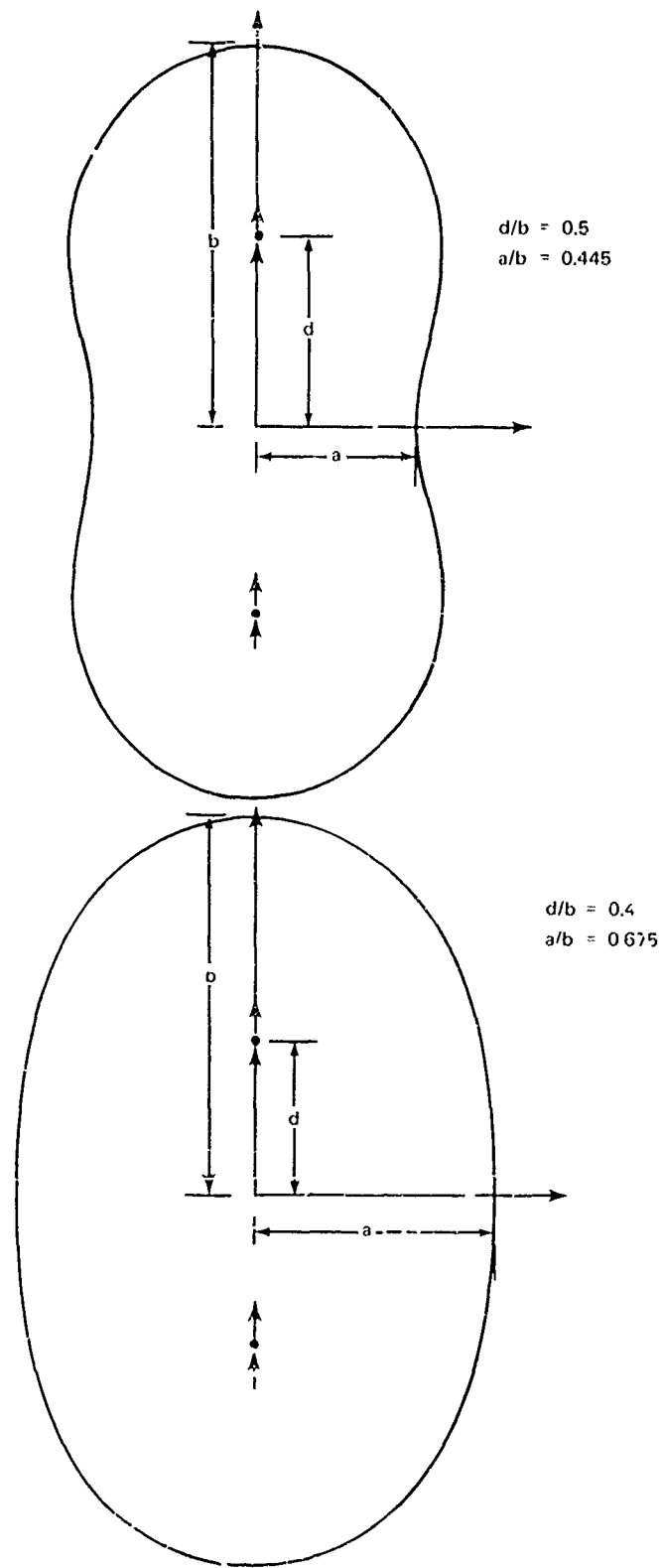


Figure 2. Cross-Sectional Shapes Generated by Two Doublets Placed in a Crossflow.

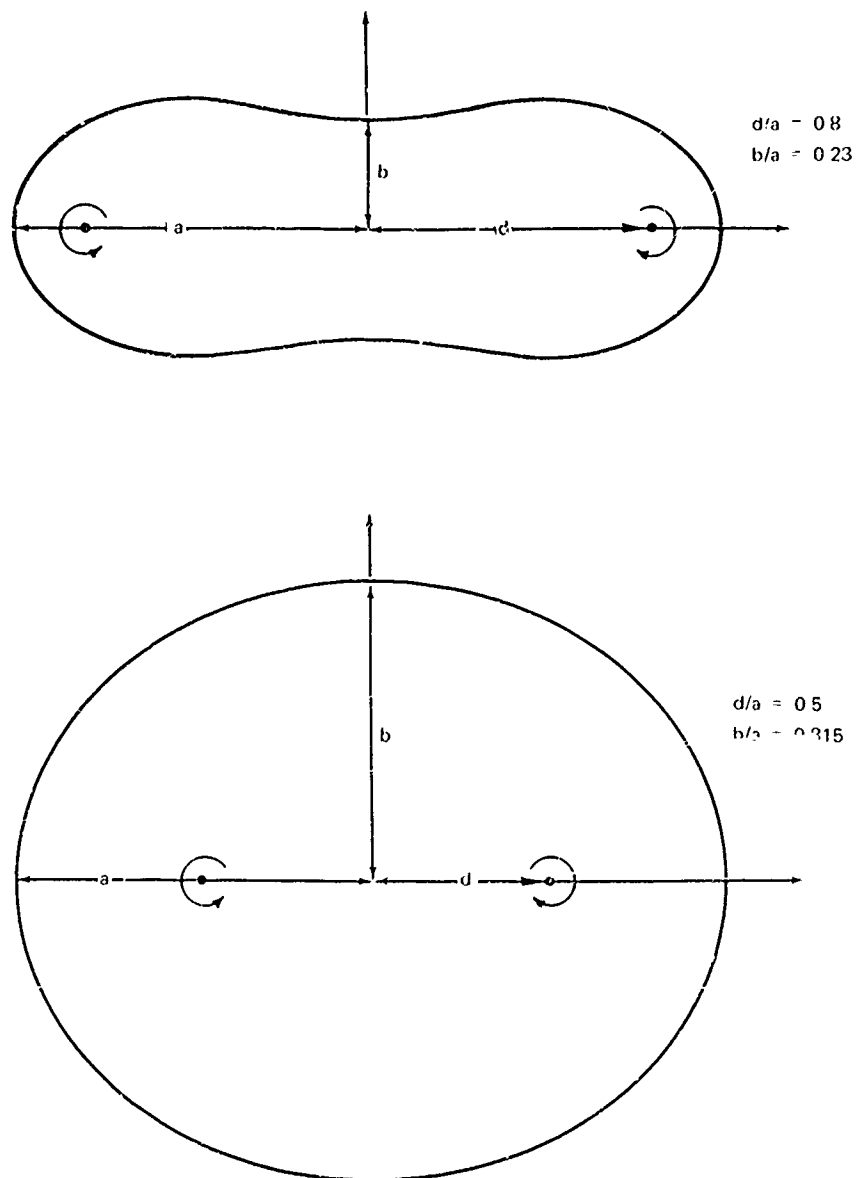


Figure 3. Cross-Sectional Shapes Generated by Two Vortices Placed in Crossflow.

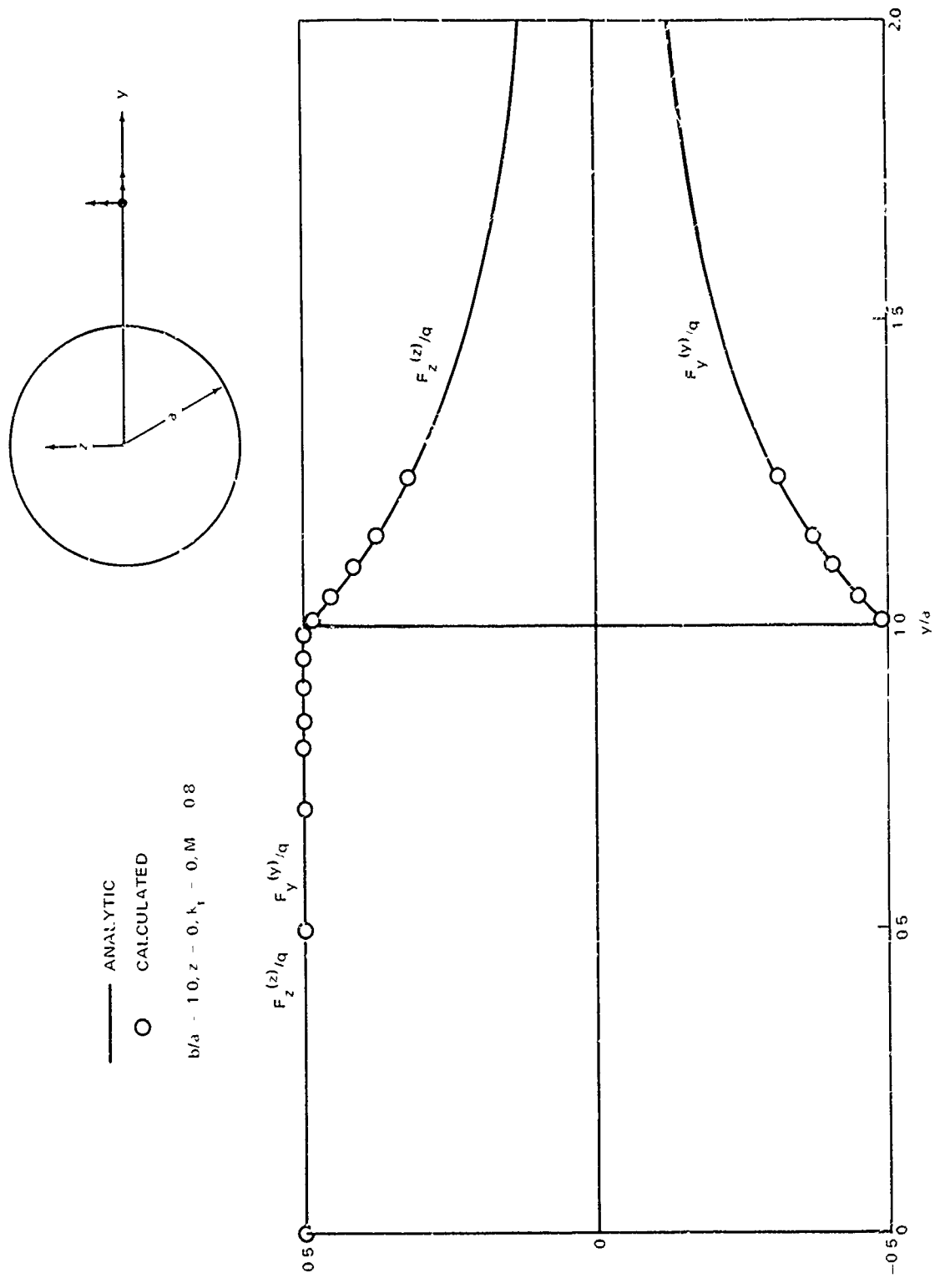


Figure 4. Total Force on a Body of Circular Cross Section due to a Pressure Doublet Located on the y-Axis.

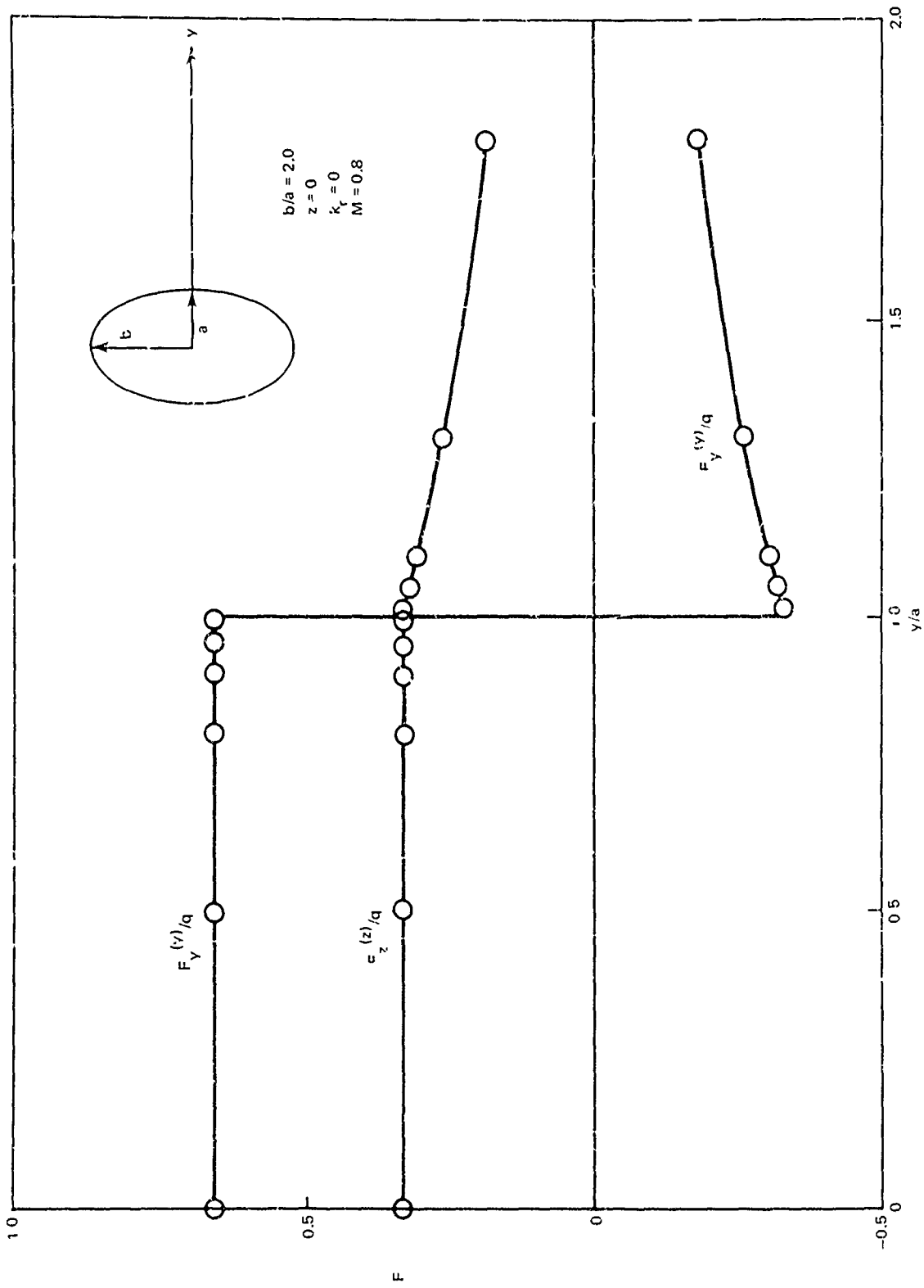


Figure 5. Total Force on a Body of Elliptic Cross Section ($b/a = 2.0$) due to a Pressure Doublet Located on the y -Axis.

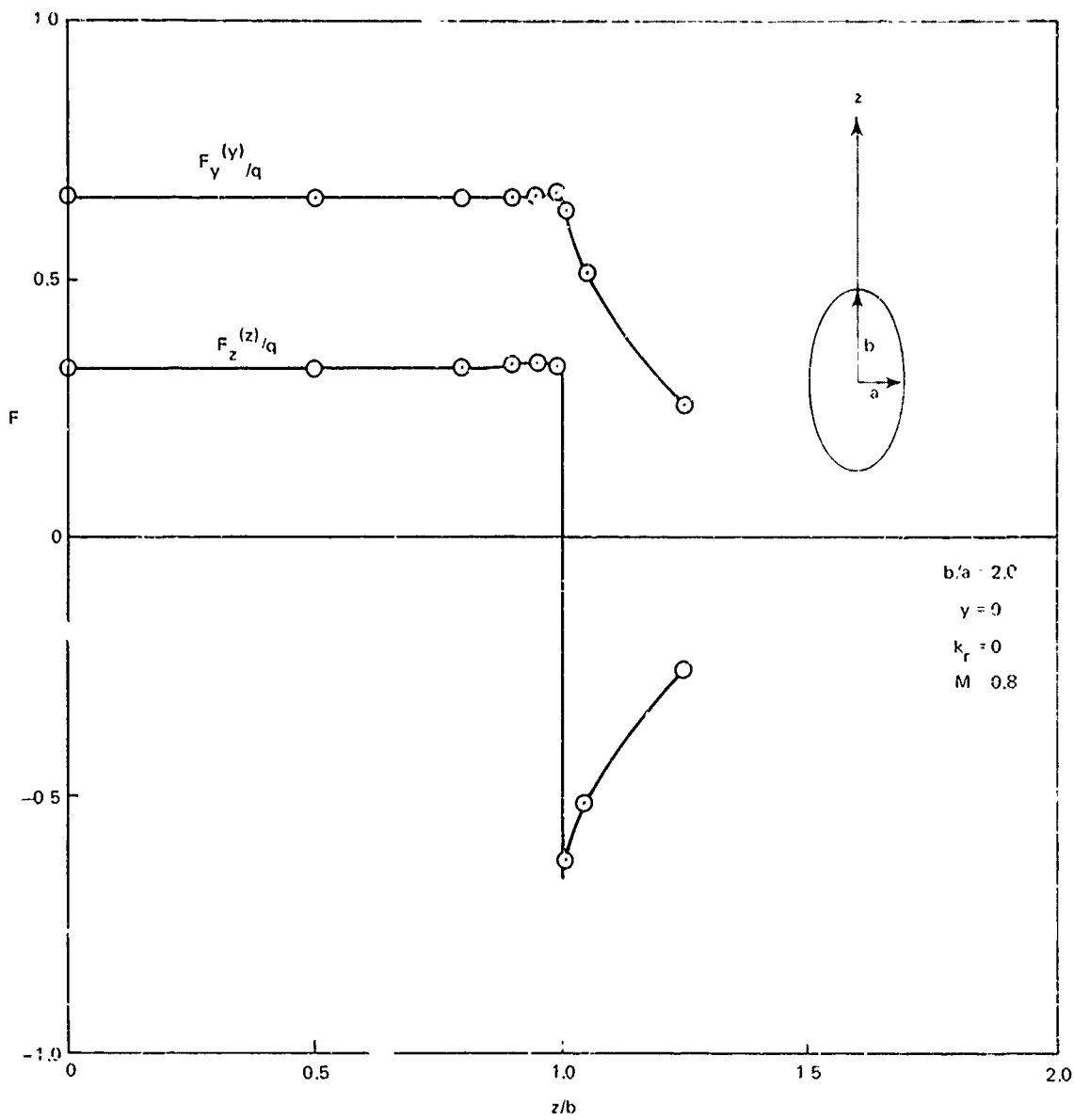


Figure 6. Total Force on a Body of Elliptic Cross Section ($b/a = 2.0$) due to a Pressure Doublet Located on the z -Axis.

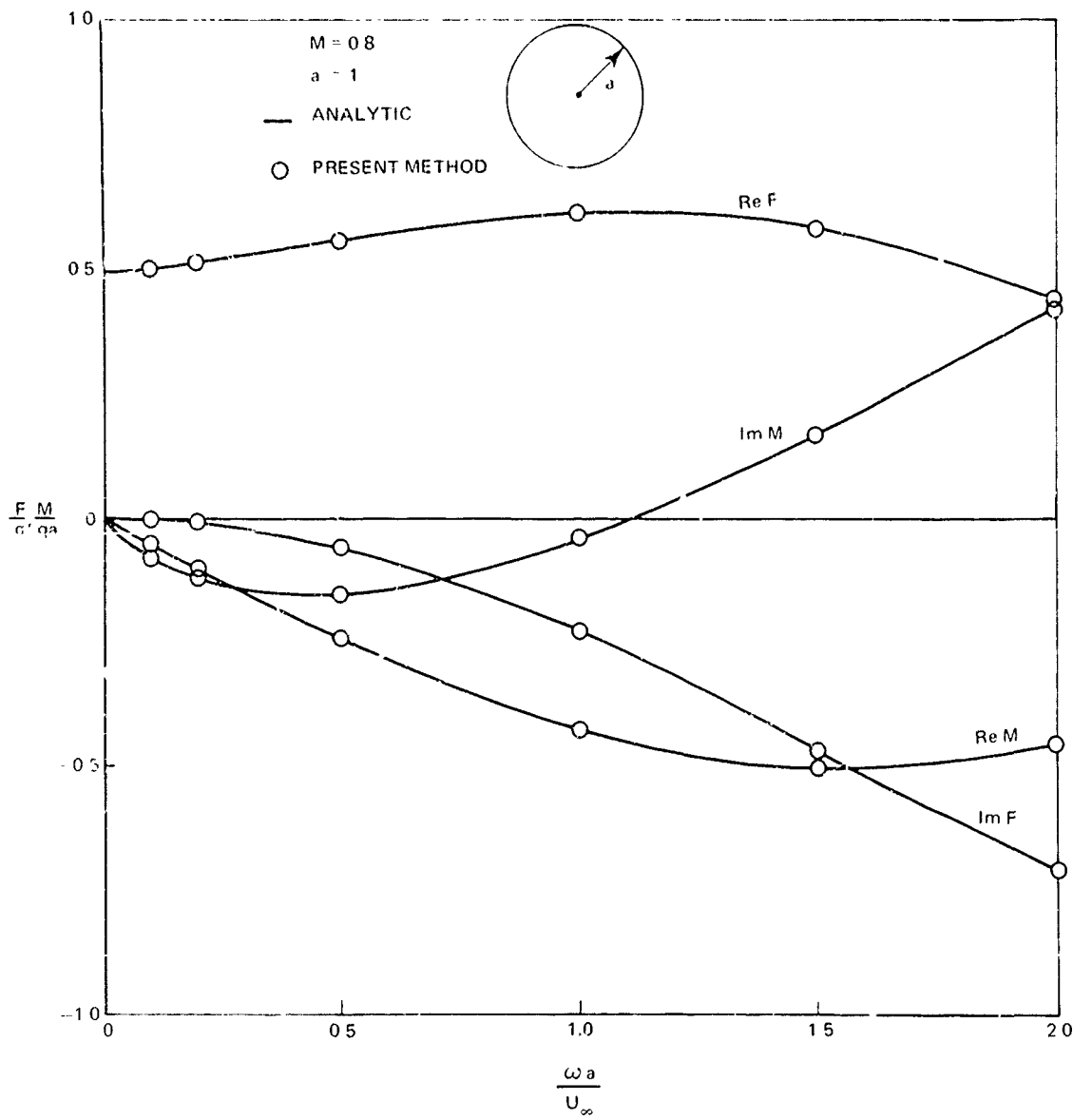


Figure 7. Total Force and Moment on a Body of Circular Cross Section due to a Pressure Doublet Located on the Body Axis.

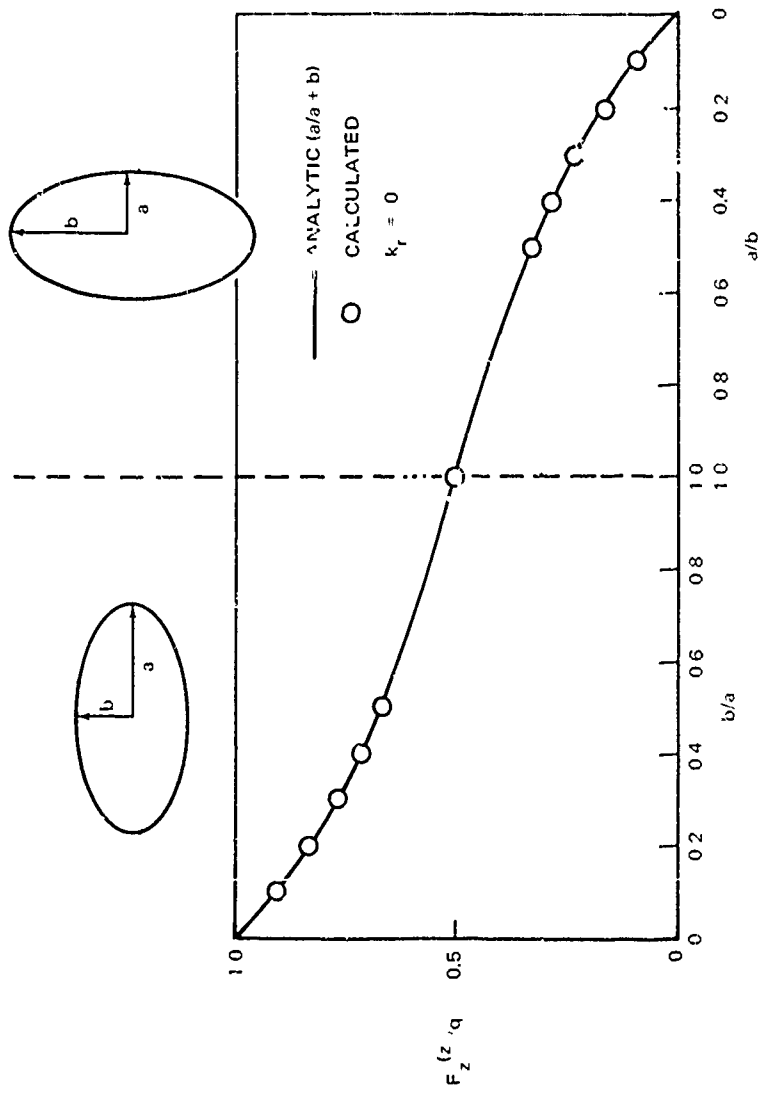


Figure 8. Total Force on Cross Sections of Various Shapes due to a Pressure Doublet Located on the Body Axis.

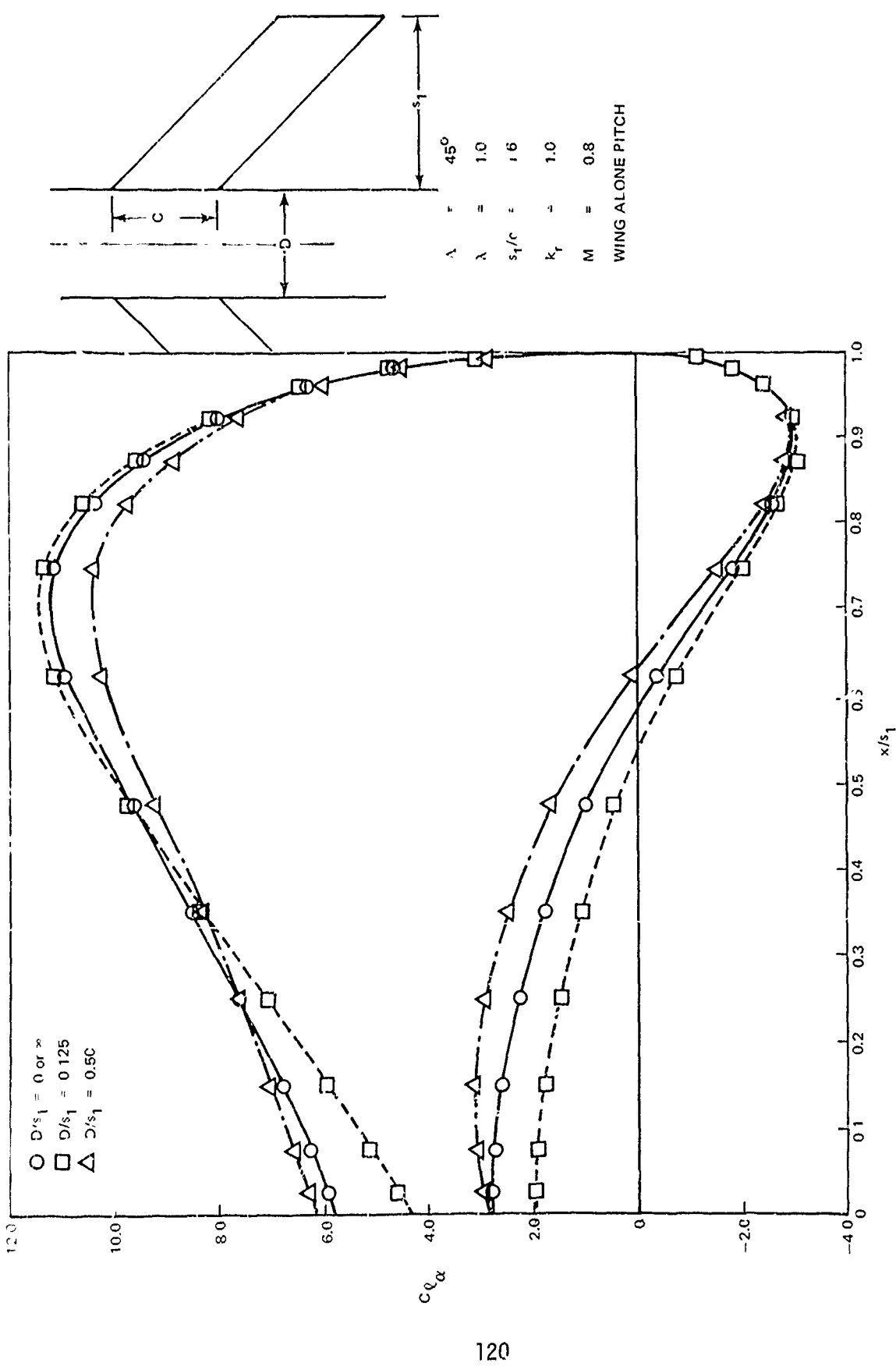


Figure 9. Effect of Fuselage Diameter on the Lift Coefficient Distribution of the Wing.

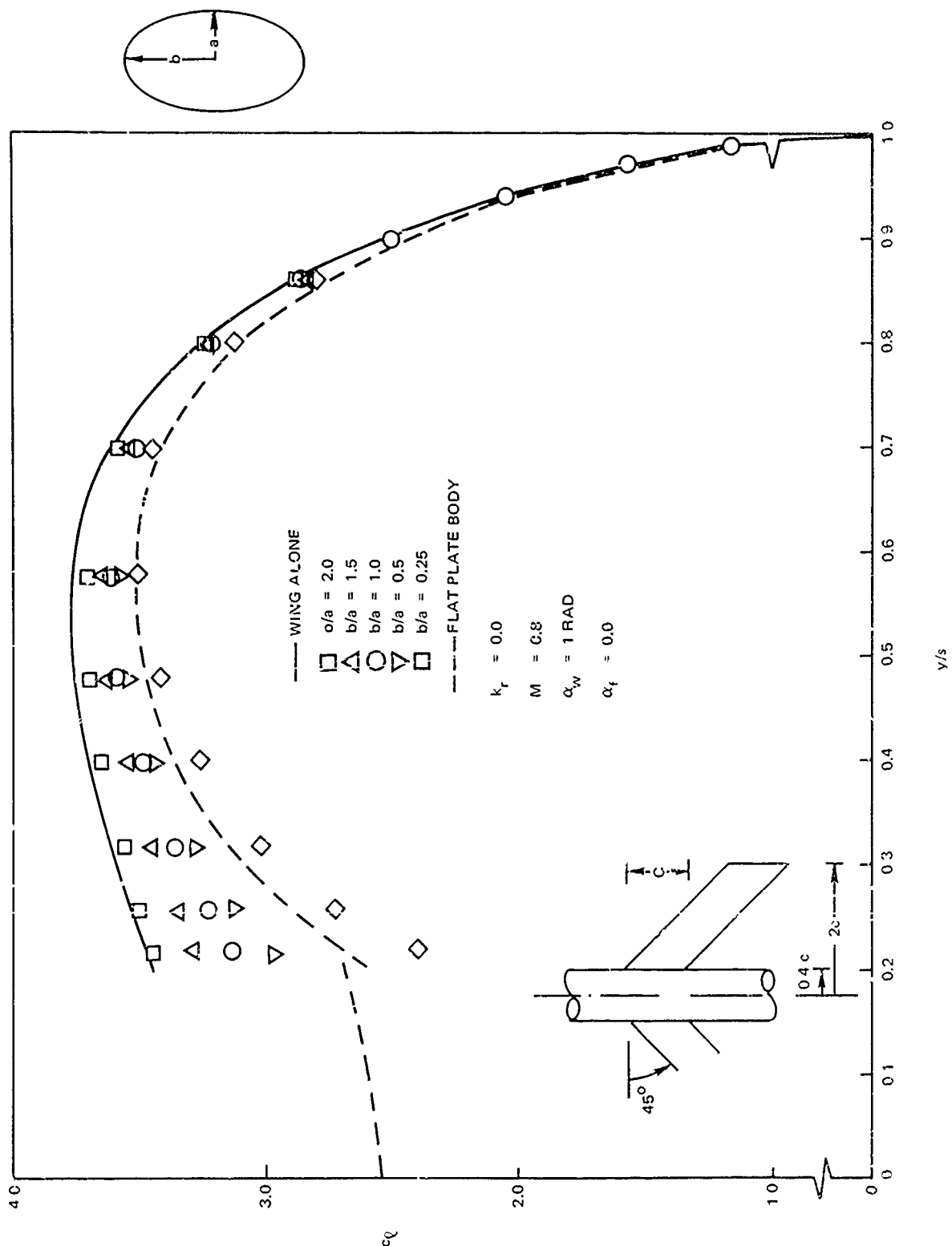


Figure 10. Effect of fuselage Cross-Sectional Aspect Ratio (b/a) on the Lift Coefficient: Distribution of the wing.

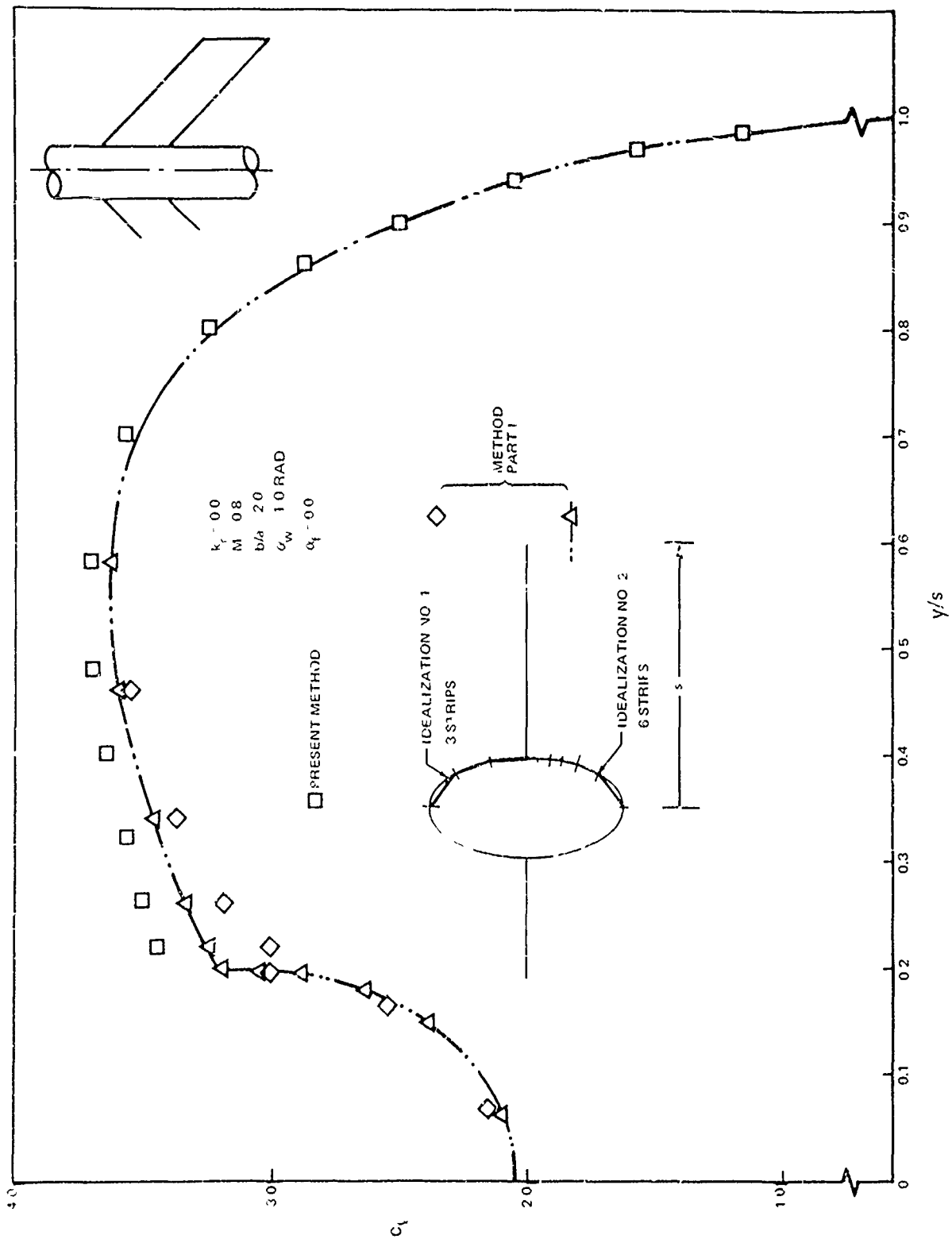


Figure 11. Comparison of the Lift Coefficient Distribution as Calculated by the Method of Part I and the Present Method for a Wing-Fuselage Combination. (Midwing, Elliptic Cross Section)

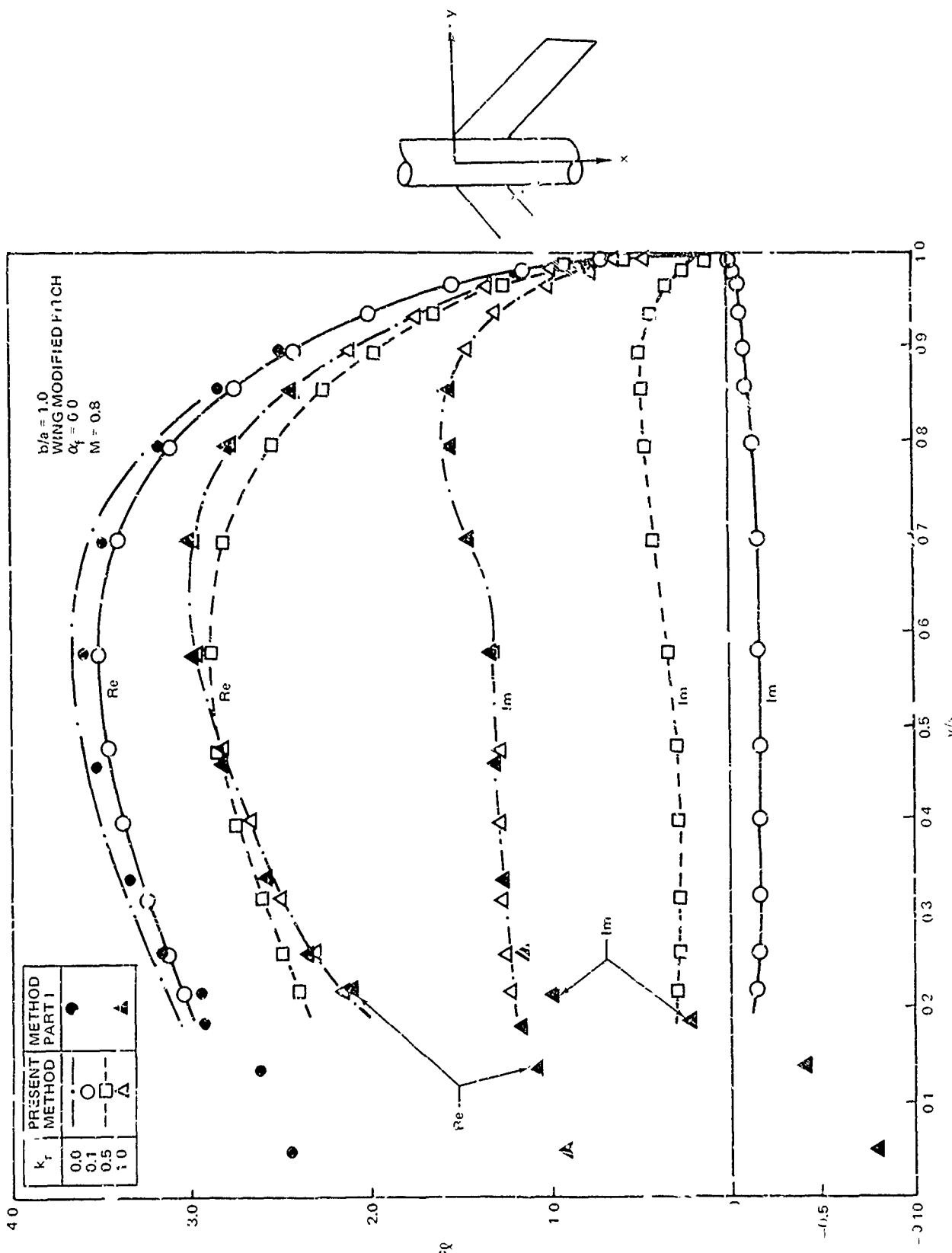


Figure 12. Effect α_f Reduced Frequency on the Lift Coefficient Distribution for a Wing-Fuselage Combination.

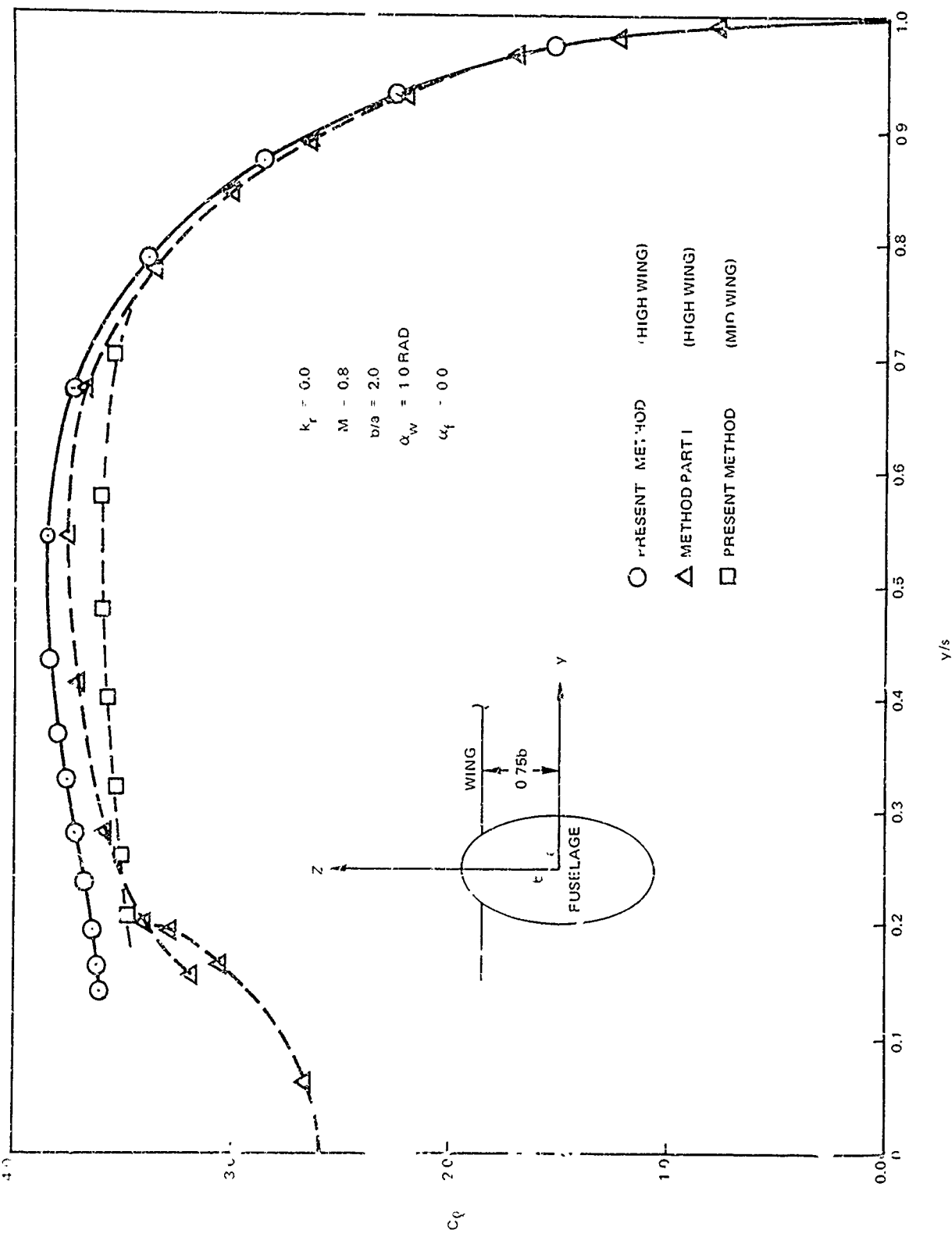


Figure 13. Effect of Wing Height Above the Fuselage Axis on the Lift Coefficient Distribution.

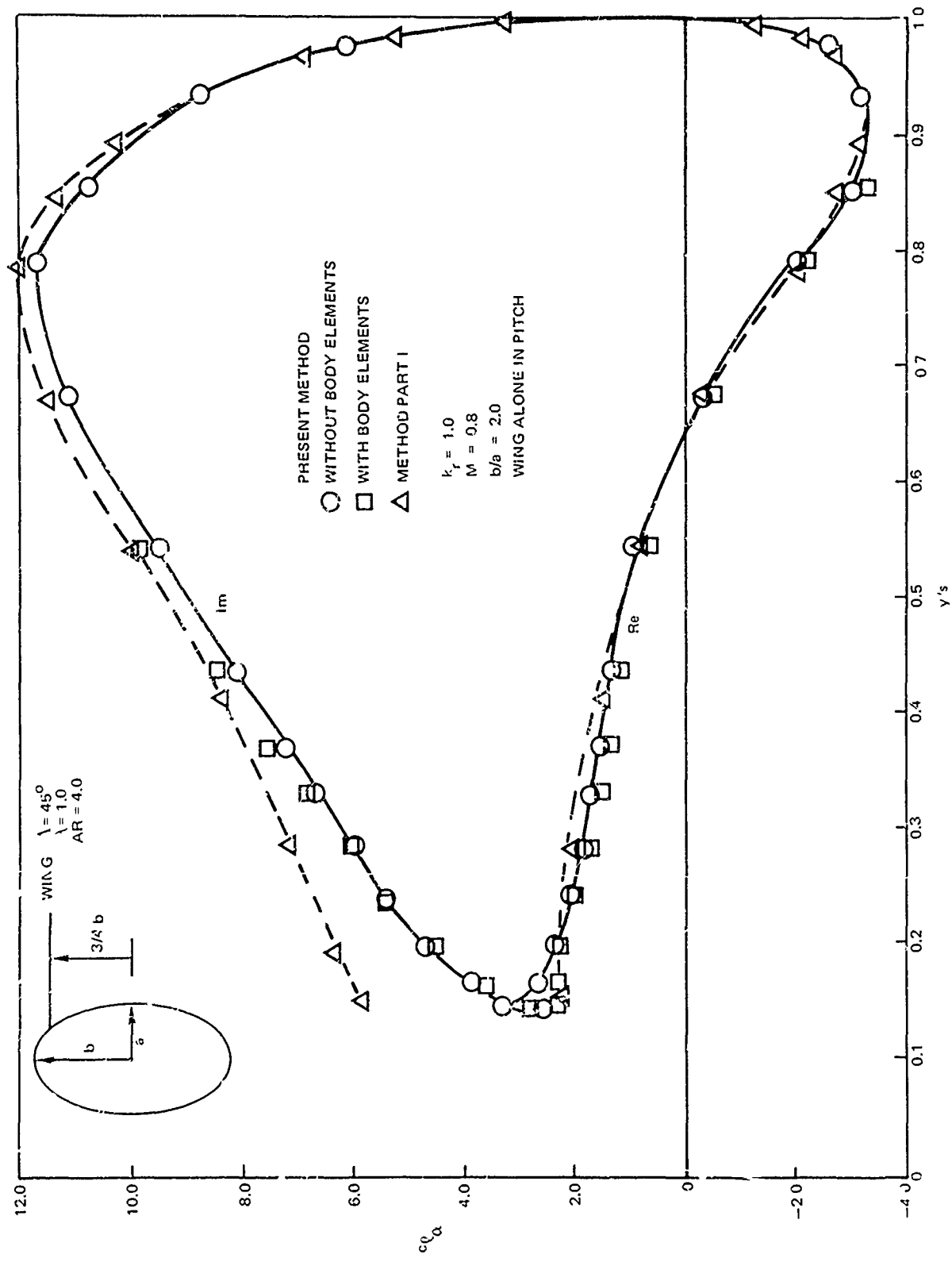


Figure 14. Comparison of the Lift Coefficient Distribution as Calculated by the Method of Part I and the Present Method for a Wing-Fuselage Combination in Unsteady Flow. (High-Wing, Elliptic Cross Section)

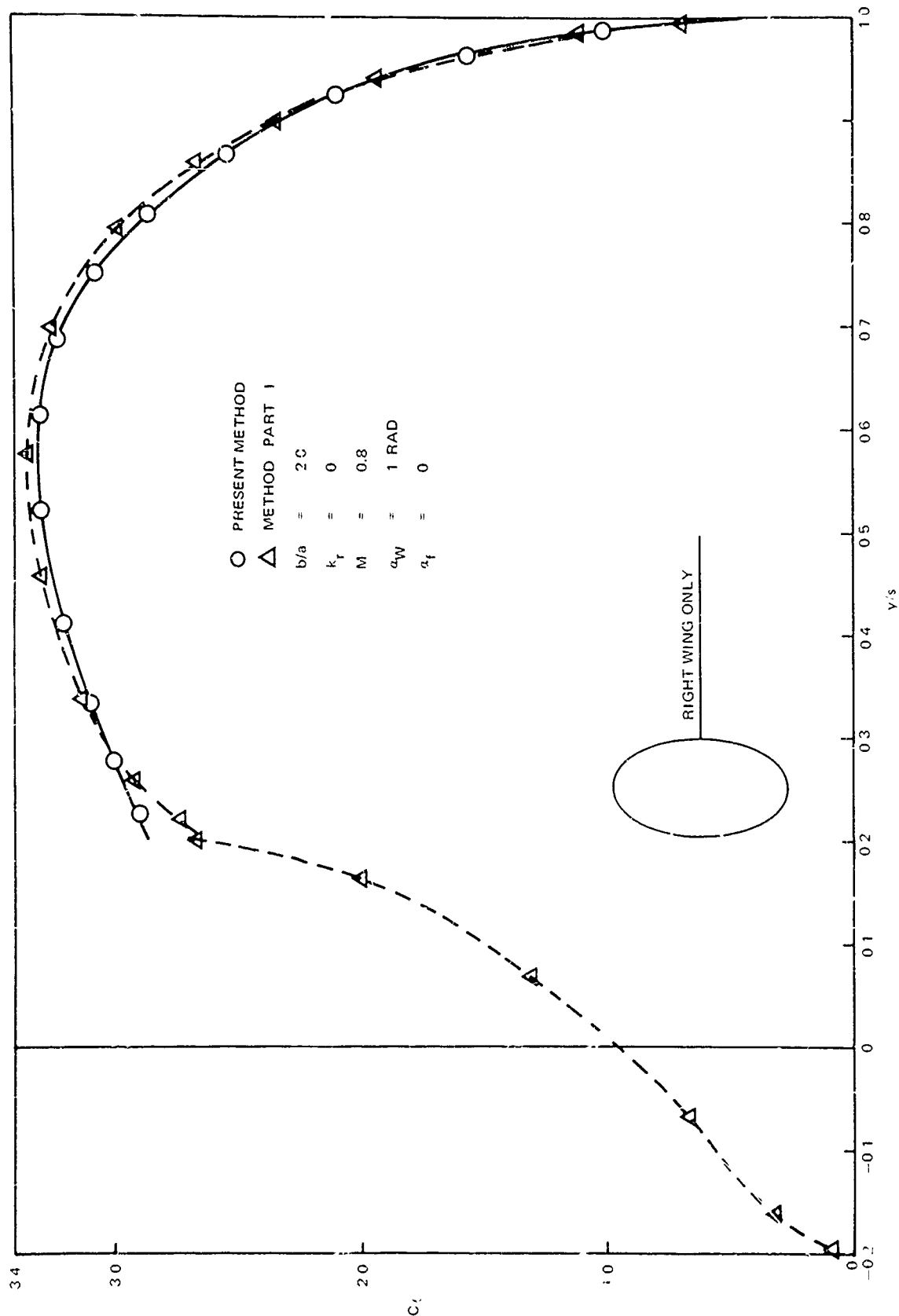


Figure 15. The End-Plating Effect of a Body of Elliptic Cross Section.

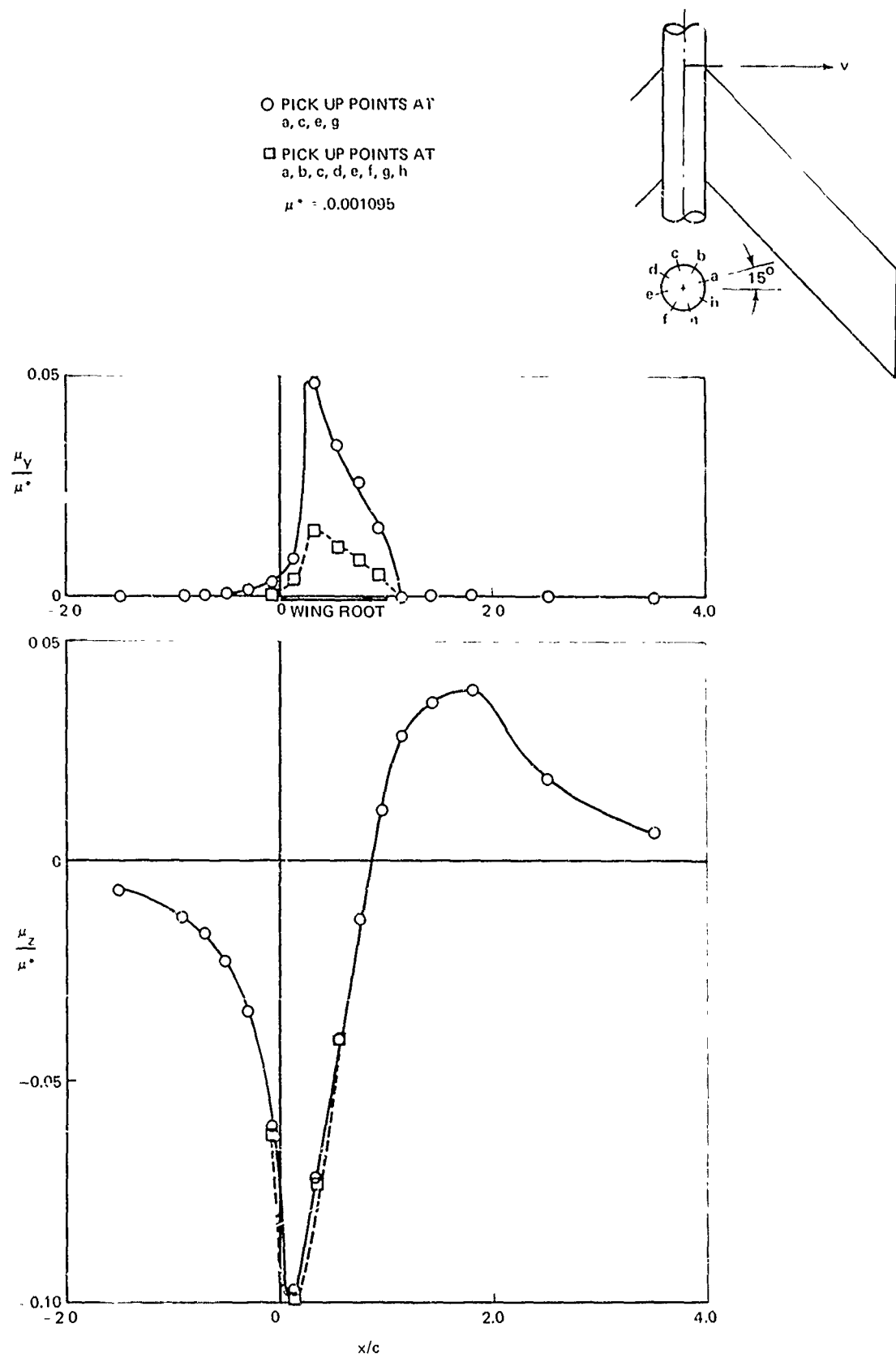


Figure 16. The Effect of Pickup Points on the Fuselage Axial Interference Doublet Strength Distribution.

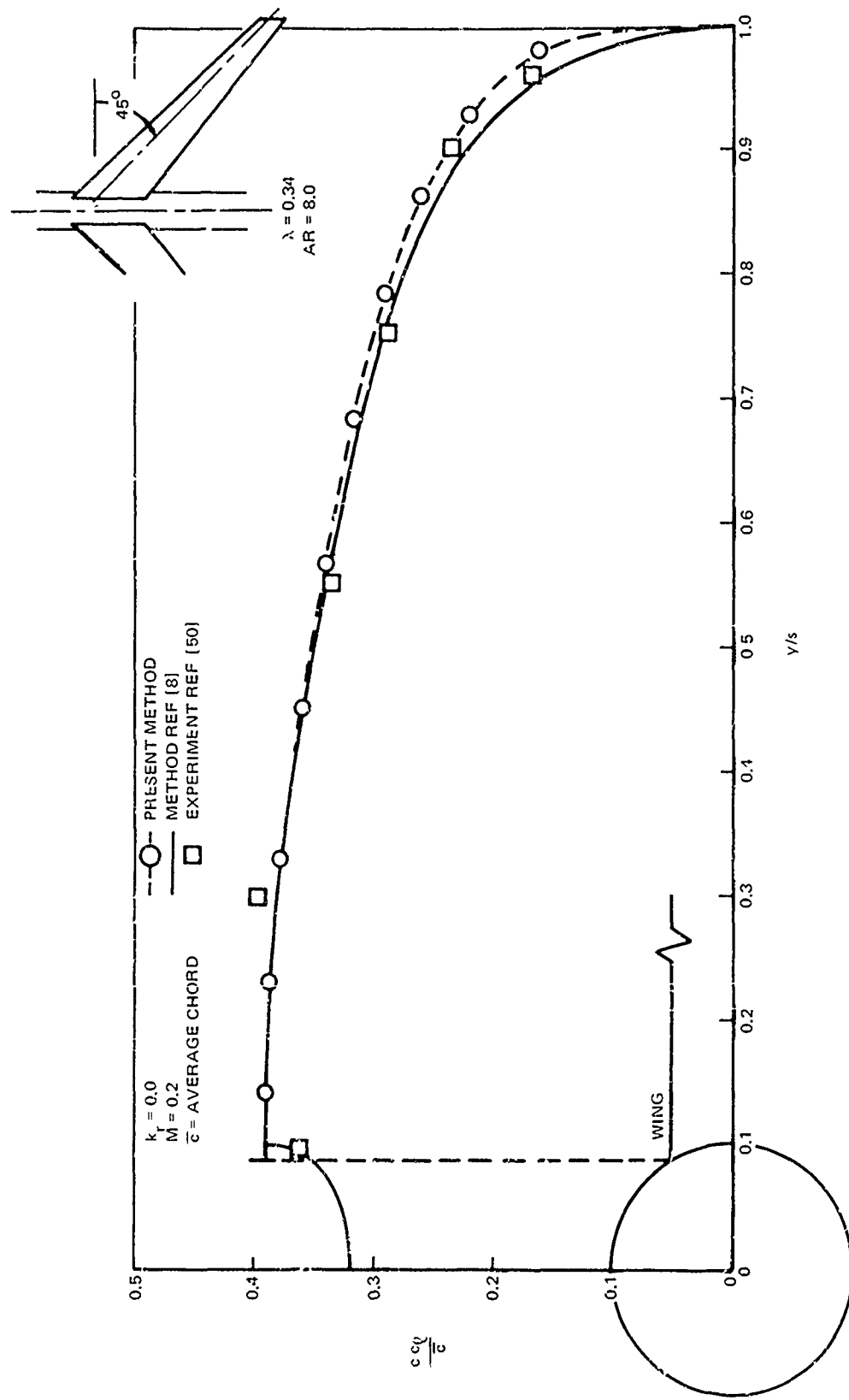


Figure 17. Comparison of Experimental and Calculated Span Load for a Wing-fuselage Combination.

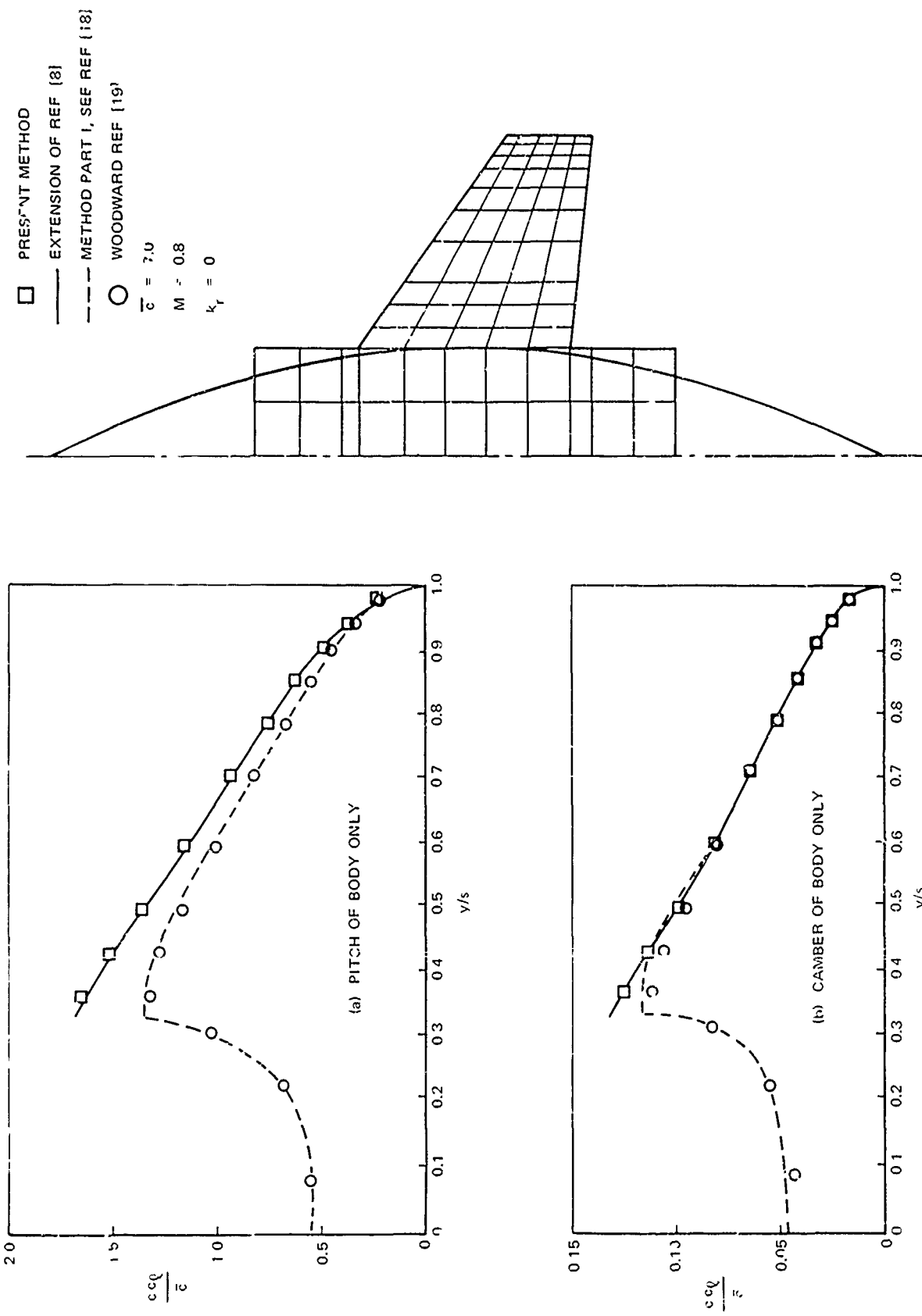


Figure 18. Span Load Distribution for a Wing-Fuselage Combination in Steady Flow. (a) Fuselage Alone in Pitch. (b) Parabolic Camber of Fuselage Alone.

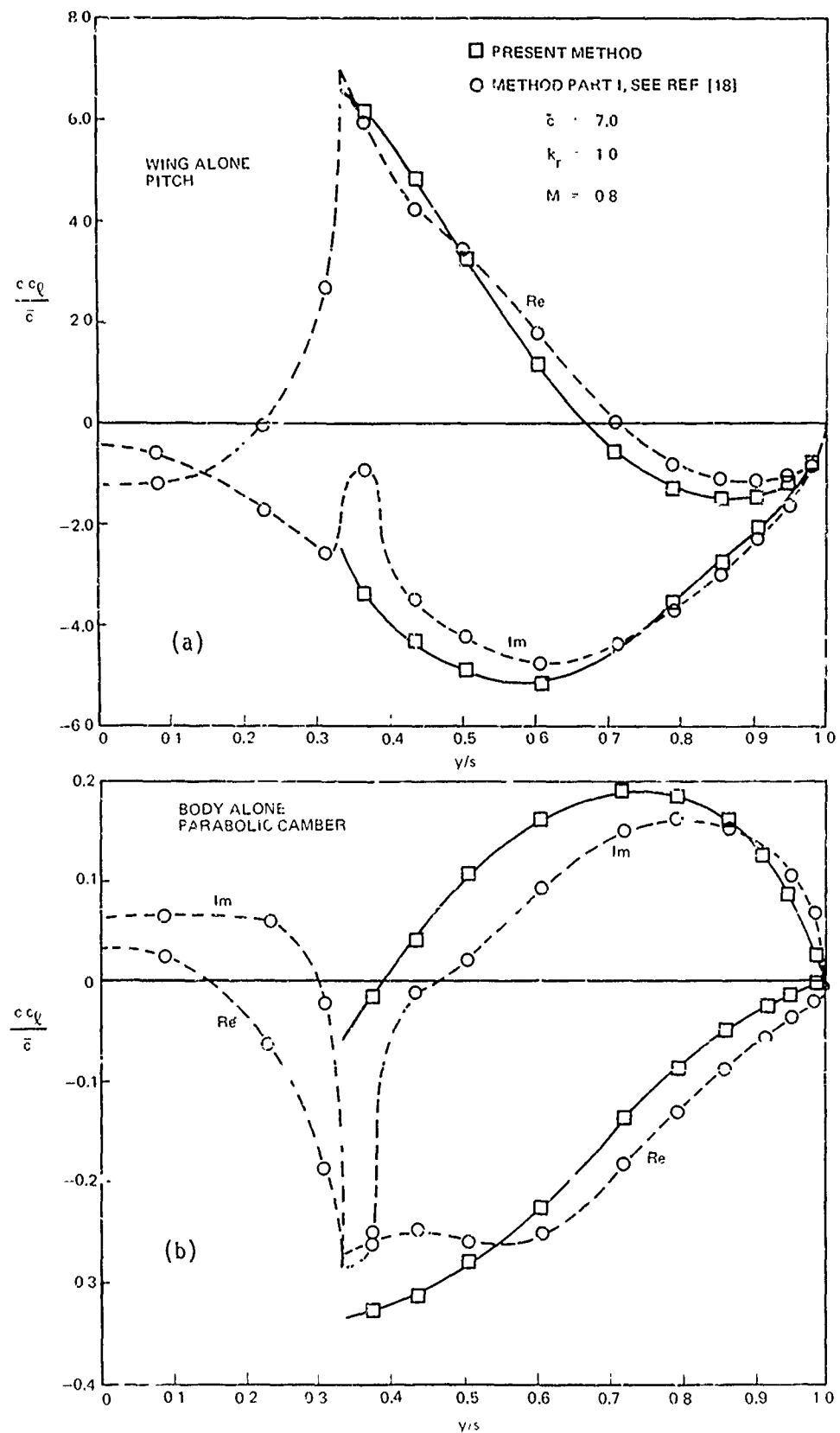


Figure 19. Span Load Distribution for a Wing-Fuselage Combination in Unsteady Flow. (a) Fuselage Alone in Pitch. (b) Parabolic Camber of Fuselage Alone.

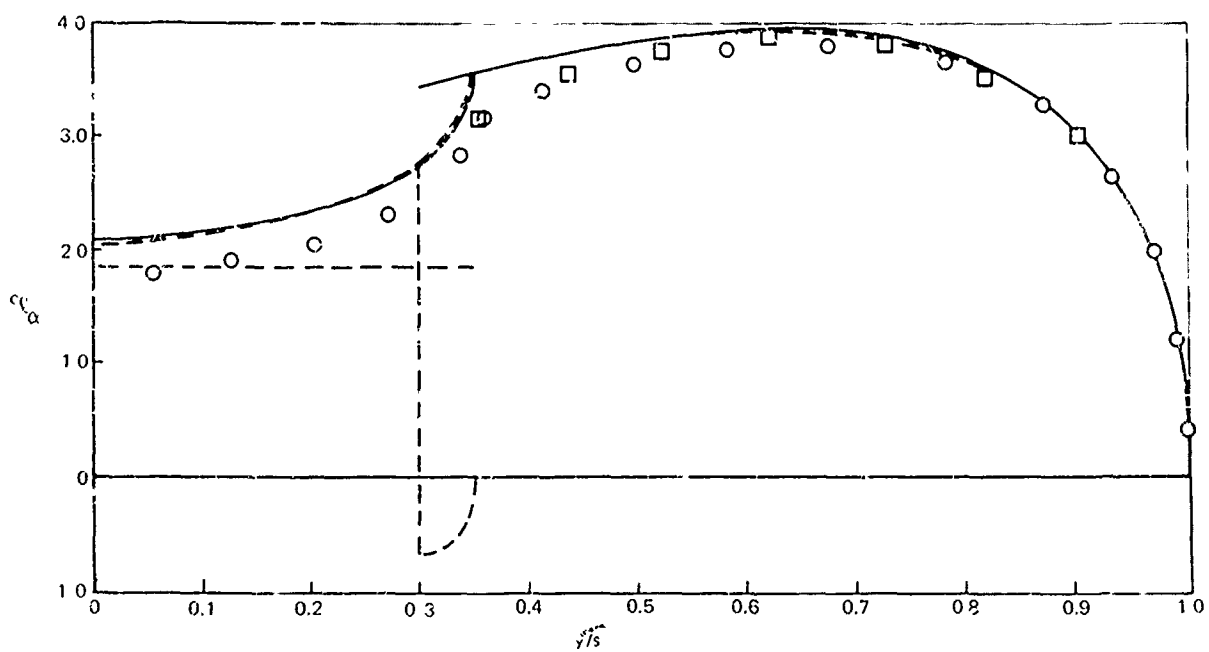
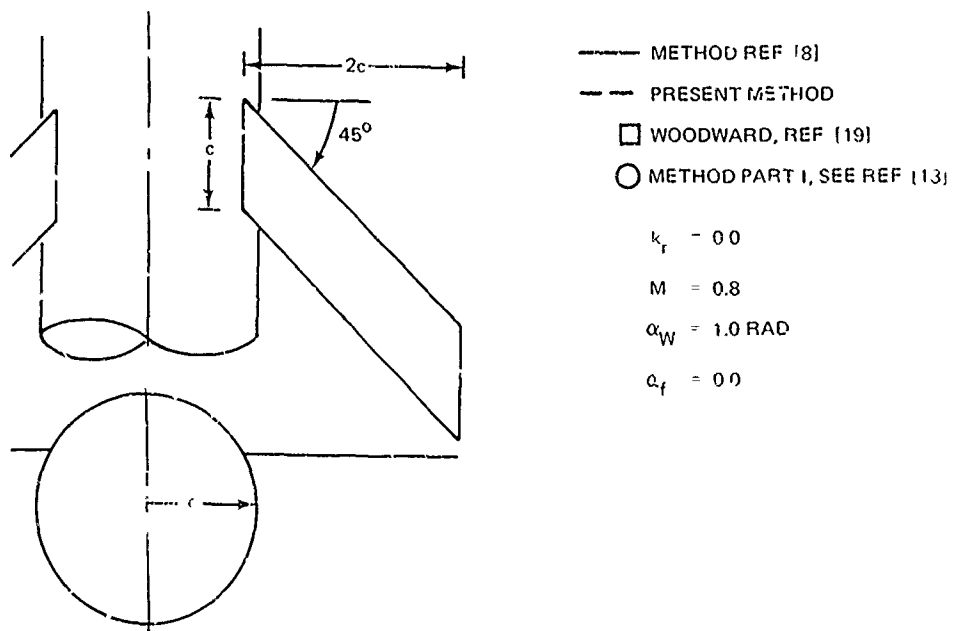


Figure 20. Comparison of the Lift-Curve-Slope Distribution as Calculated by the Present Method and Various Other Methods for a Wing-Fuselage Combination.

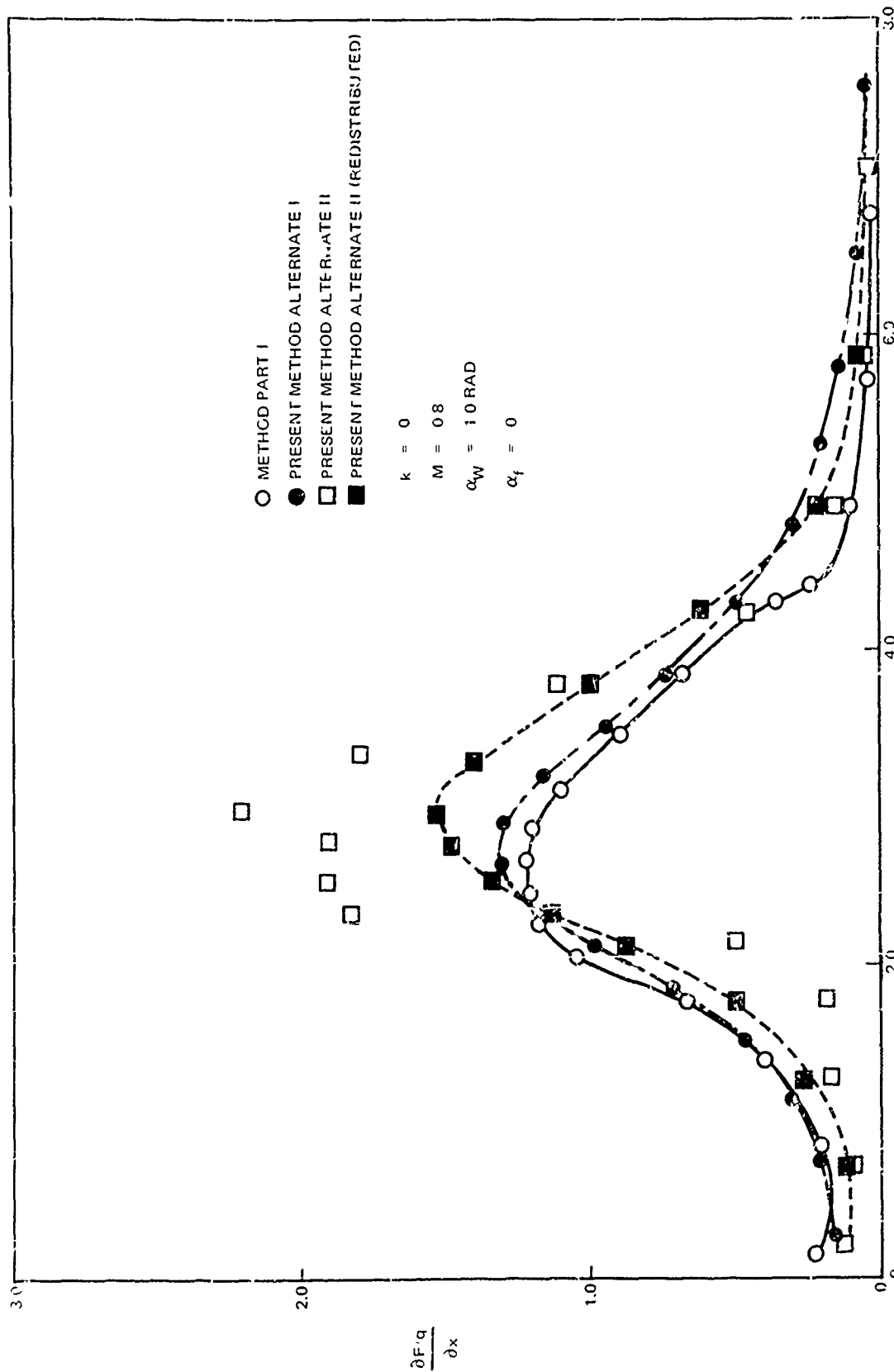


Figure 21. Comparison of the Fuselage Axial Load Distribution as Calculated by the Present Method and the Method of Part I.

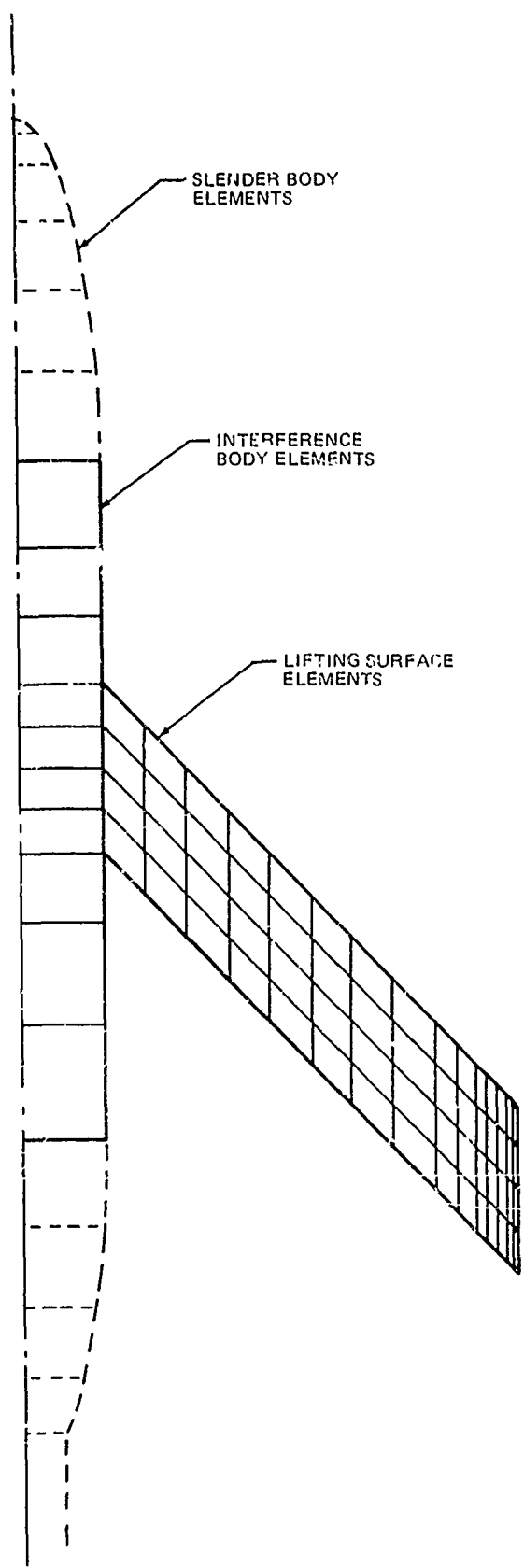


Figure 22. Idealization of a Wing-Fuselage Combination.

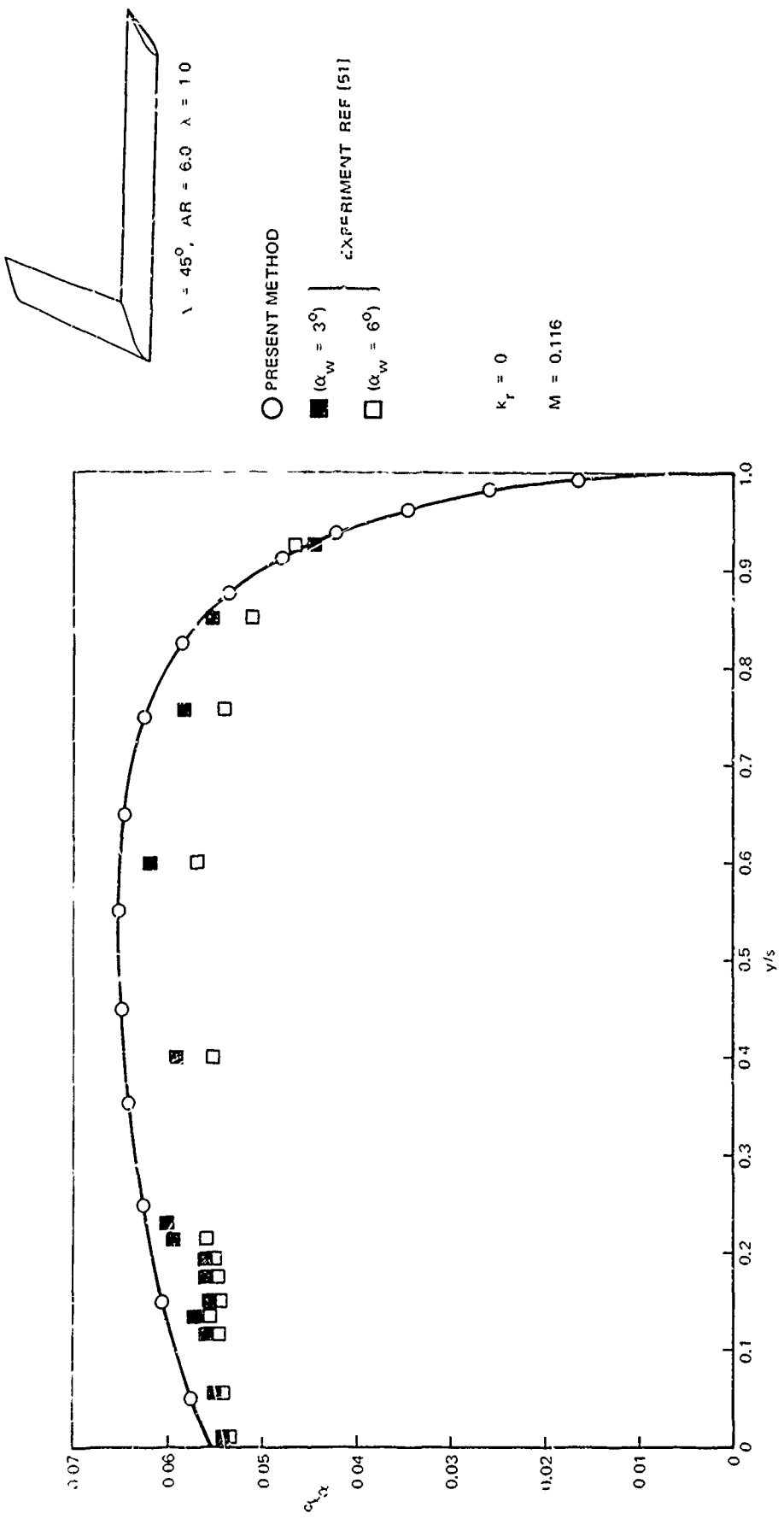


Figure 23. Comparison of Experimental and Calculated Lift-Curve-Slope Distribution for a Swept Wing.

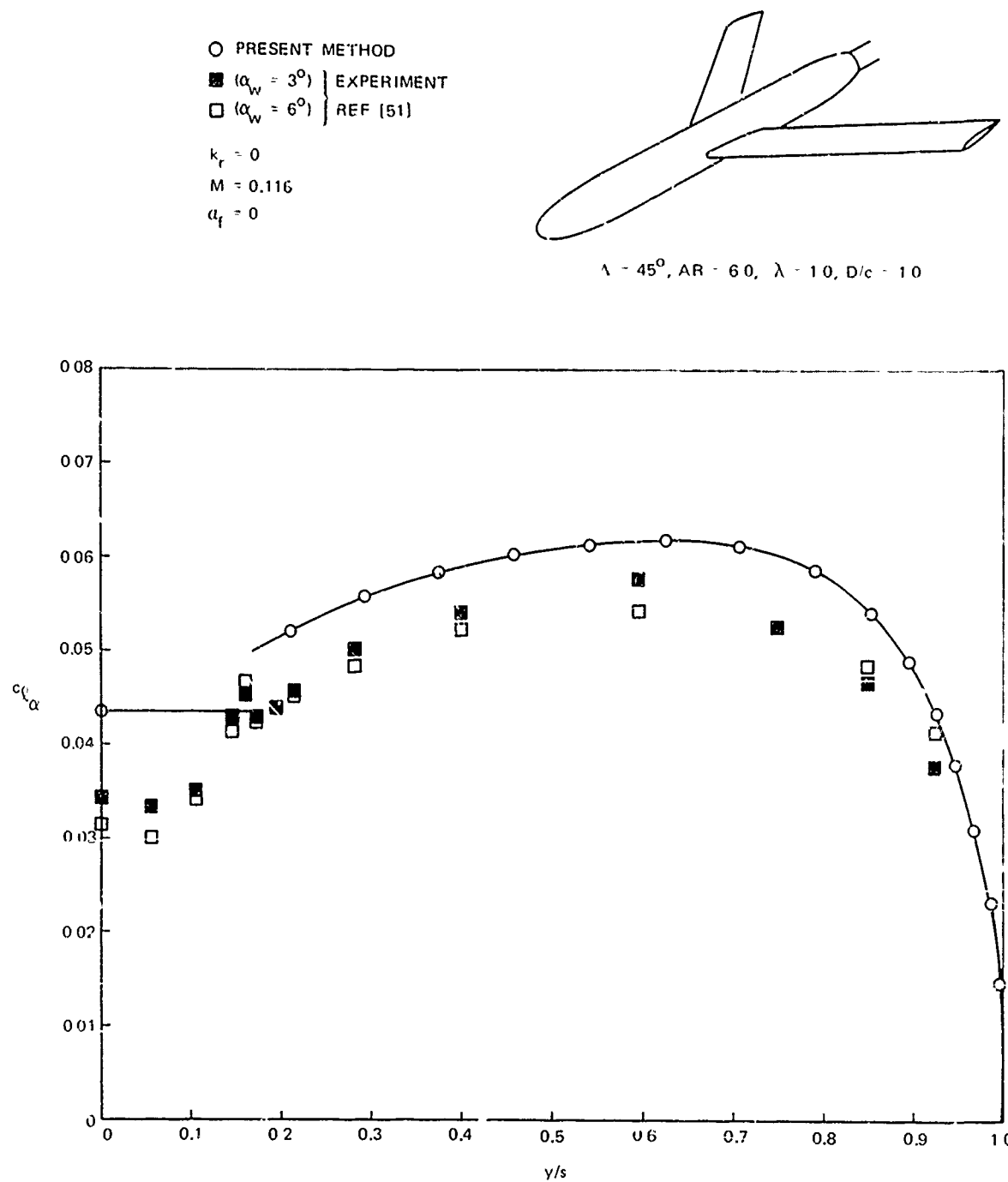


Figure 24. Comparison of Experimental and Calculated Lift-Curve-Slope Distribution for a Swept-Wing/Fuselage Combination. (Fuselage at Zero Incidence)

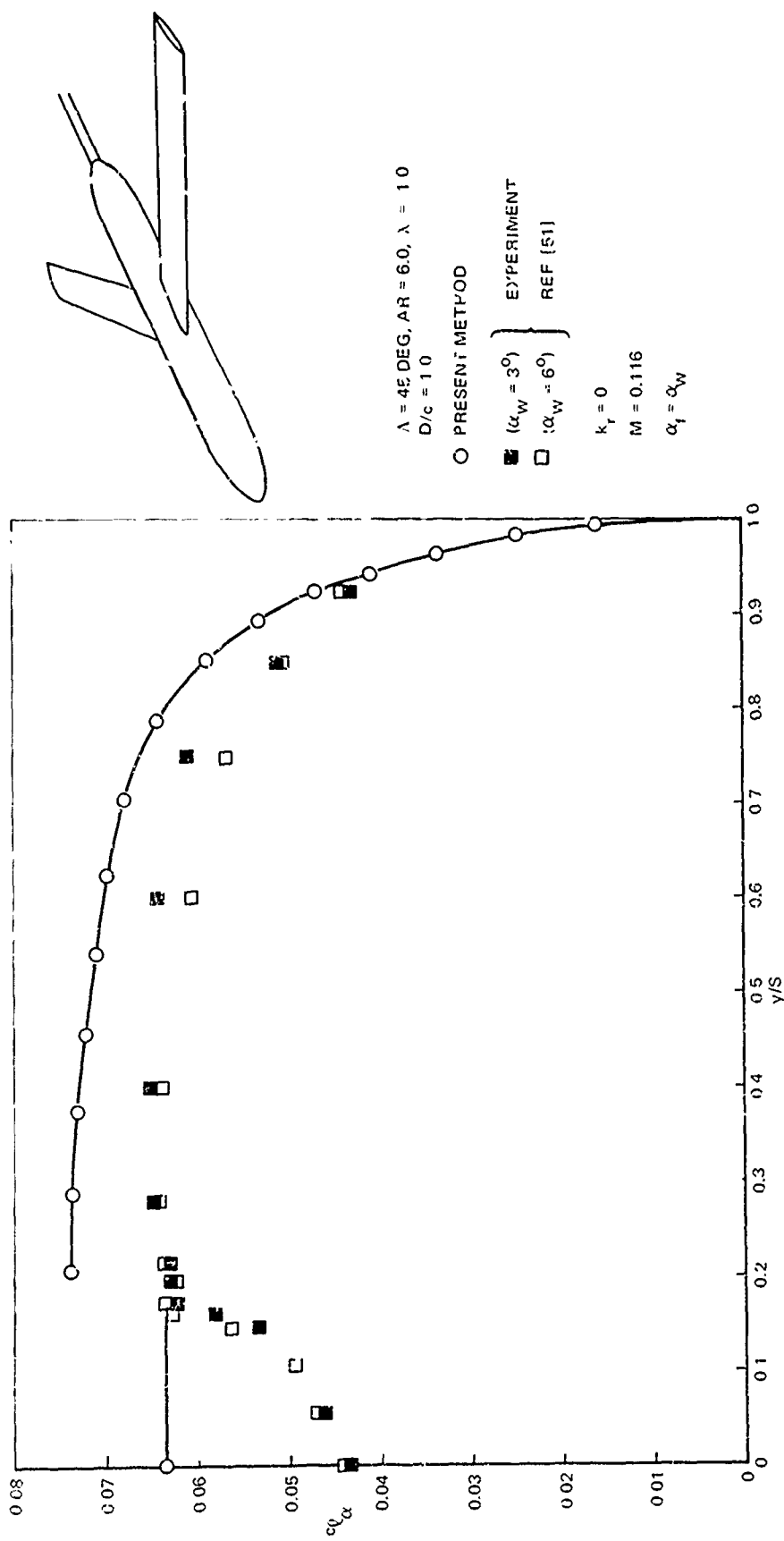


Figure 25. Comparison of Experimental and Calculated Lift-Curve-Slope Distribution for a Swept-Wing/Fuselage Combination.

○ PRESENT METHOD
■ $\alpha_w = 3^\circ$ | EXPERIMENT
□ $(\alpha_w = 6^\circ)$ REF [7]

$k_r \approx 0$

$M = 0.116$

$D/c = 0.68$

$\alpha_f = 0$

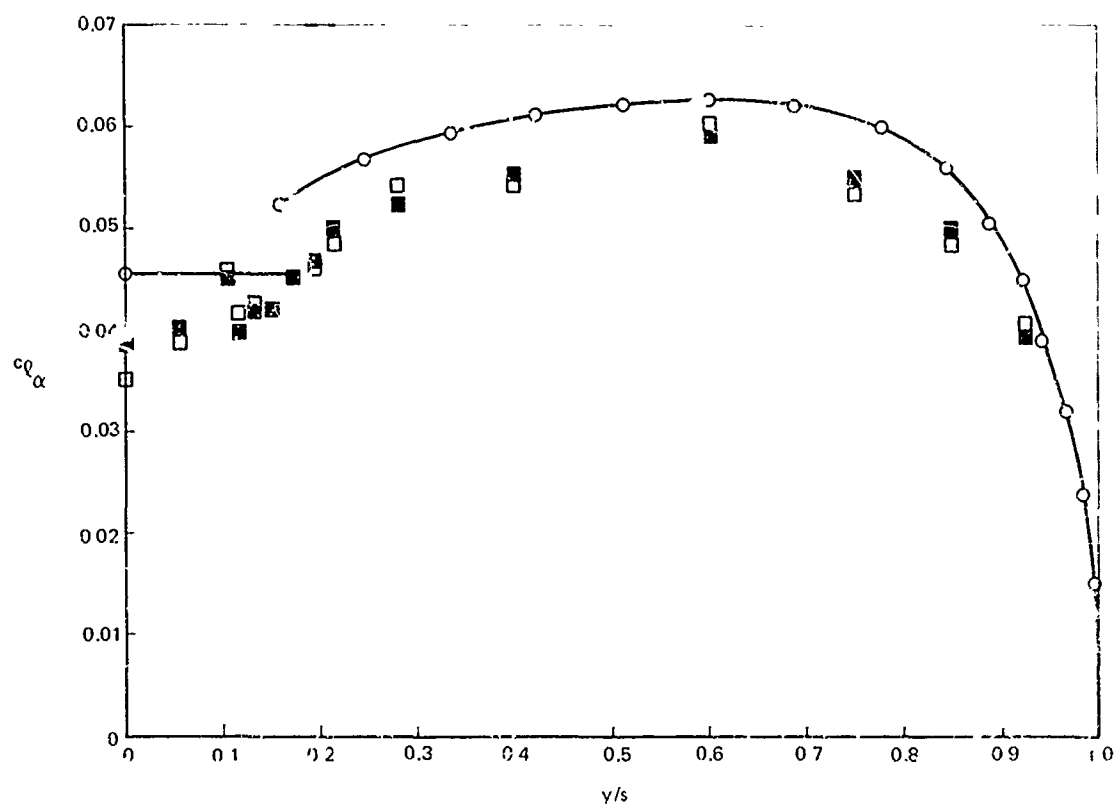
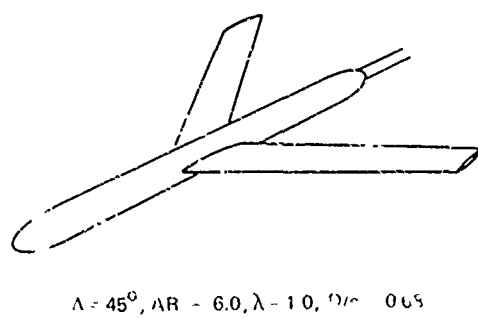


Figure 26. Comparison of Experimental and Calculated Lift-Curve-Slope Distribution for a Swept-Wing/Fuselage Combination. (Fuselage at Zero Incidence)

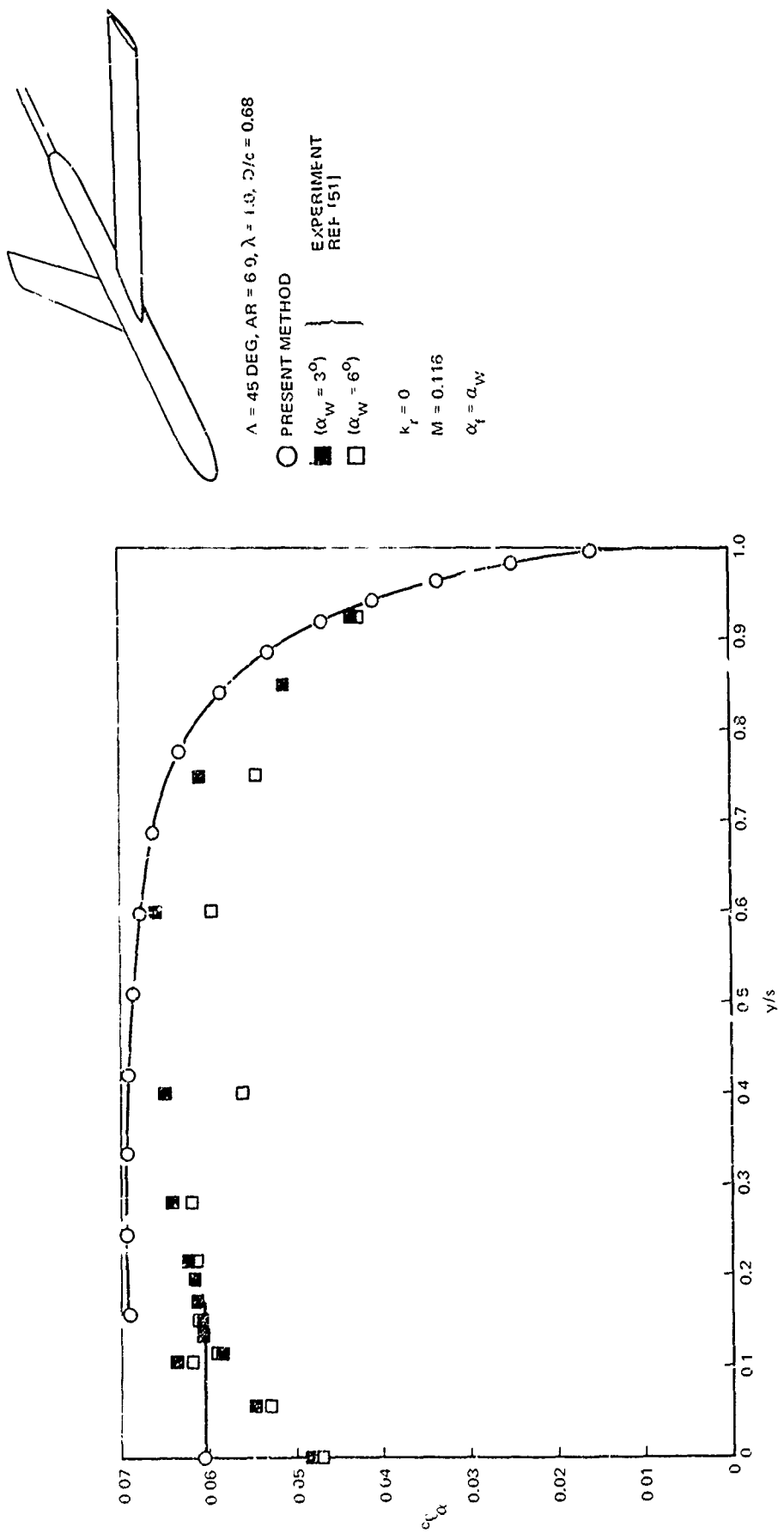


Figure 27. Comparison of Experimental and Calculated Lift-Curve-Slope Distribution for a Swept-Wing/Fuselage Combination.

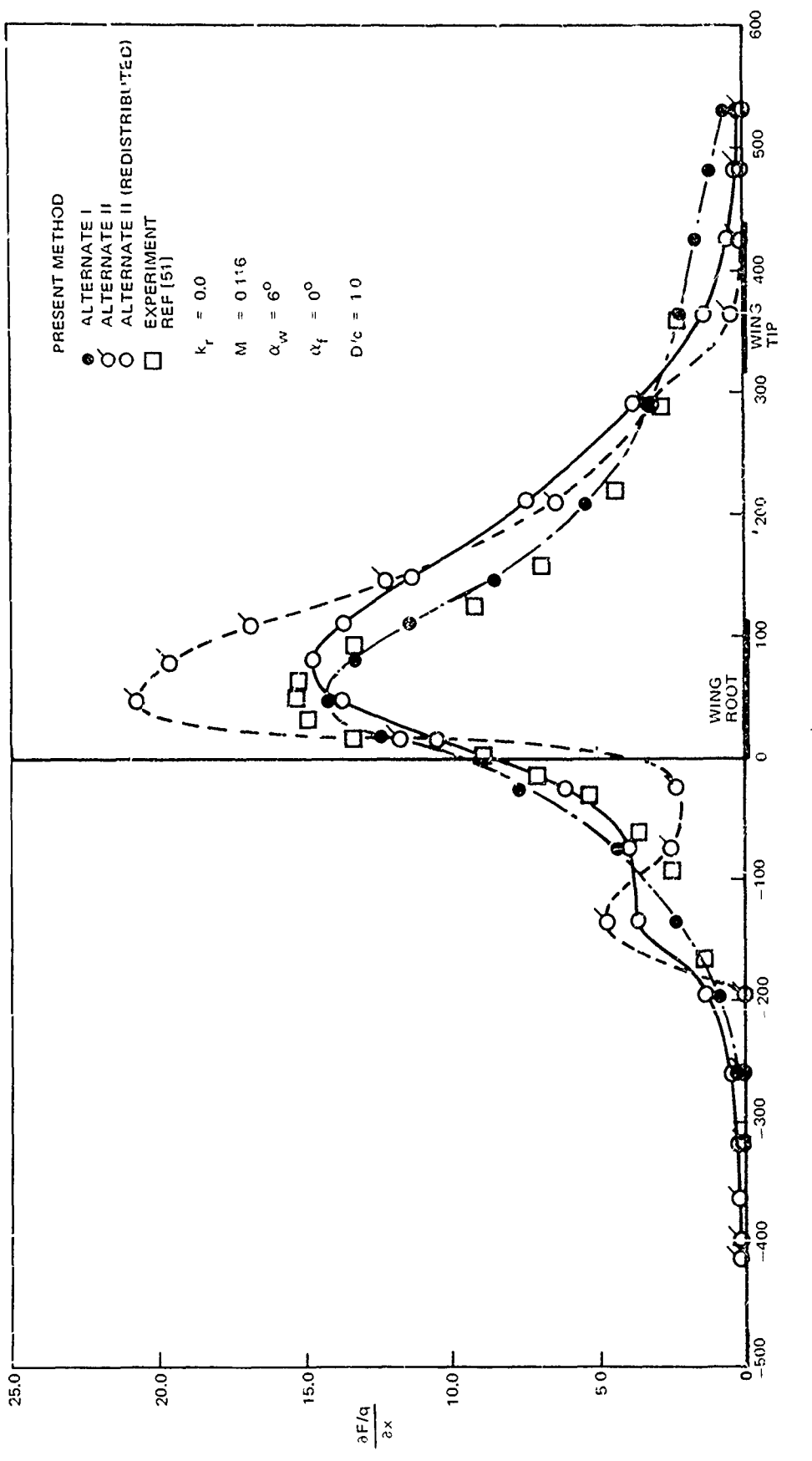


Figure 28. Comparison of Experimental and Calculated Fuselage Axial Load Distribution. (Fuselage at Zero Incidence)

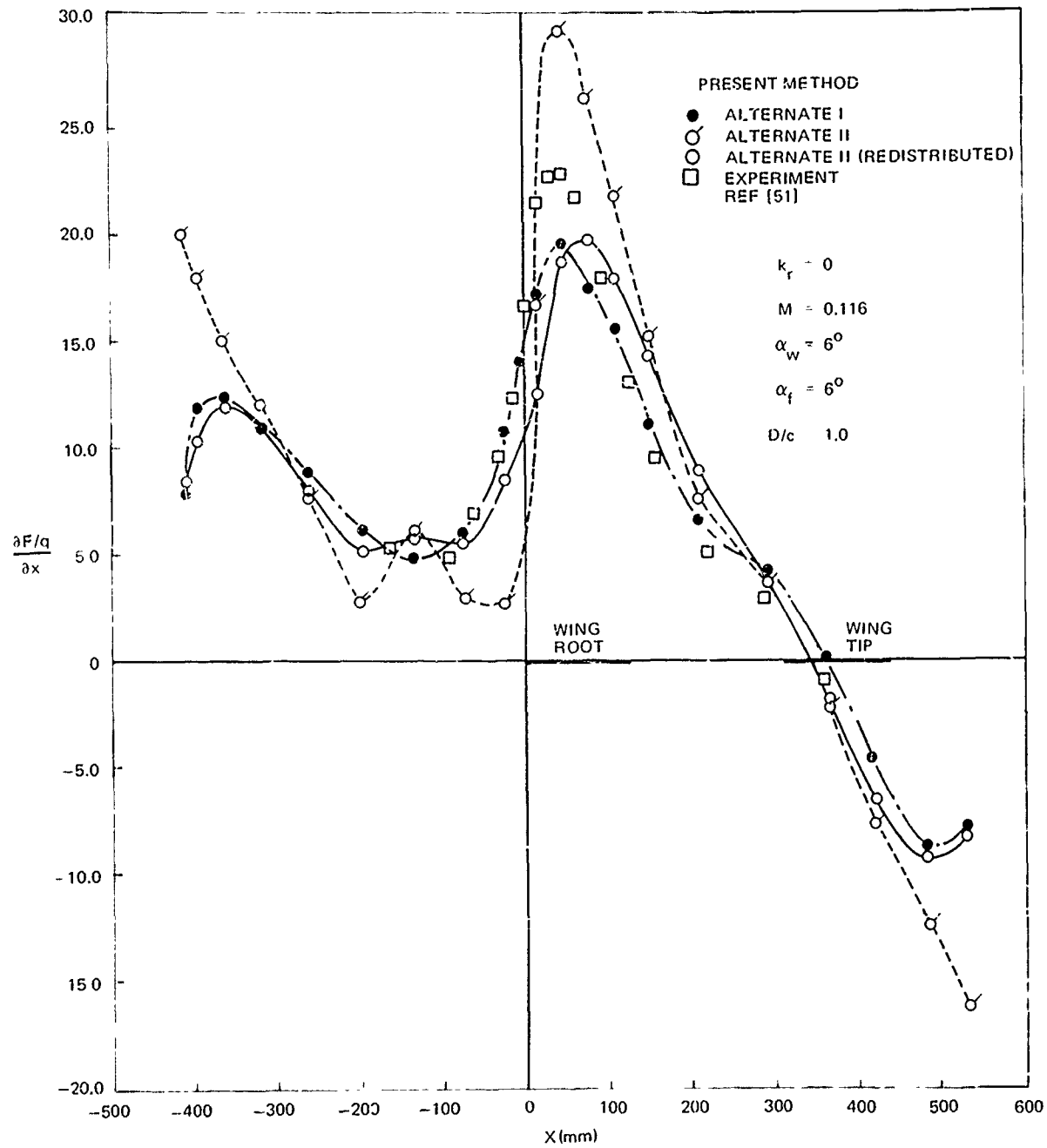


Figure 29. Comparison of Experimental and Calculated Fuselage Axial Load Distribution. (Fuselage at Incidence)

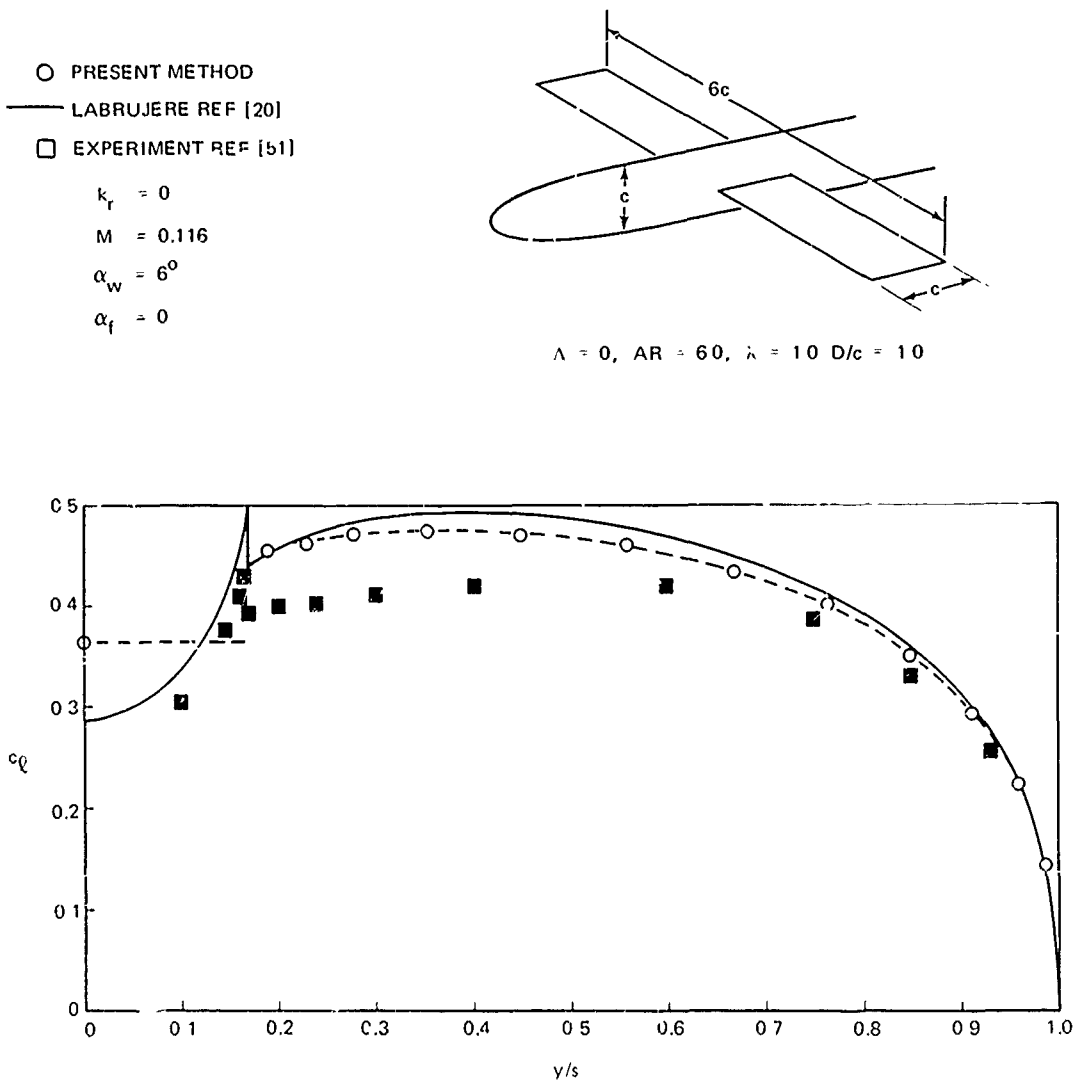


Figure 30. Comparison of Experimental and Calculated Lift Coefficient Distribution for a Straight-Wing/Fuselage Combination. (Fuselage at Zero Incidence)

○ PRESENT METHOD
 — LABROUJERE, REF [20]
 ■ EXPERIMENT REF [51]

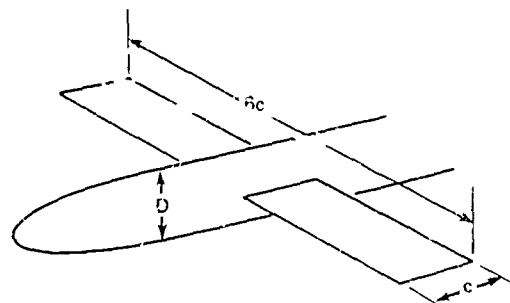
$$k_r = 0$$

$$M = 0.116$$

$$\alpha_w = 6^\circ$$

$$\alpha_f = 6^\circ$$

$$D/c = 1.0$$



$$\Lambda = 0, AR = 6.0, \lambda = 1.0, D/c = 1.0$$

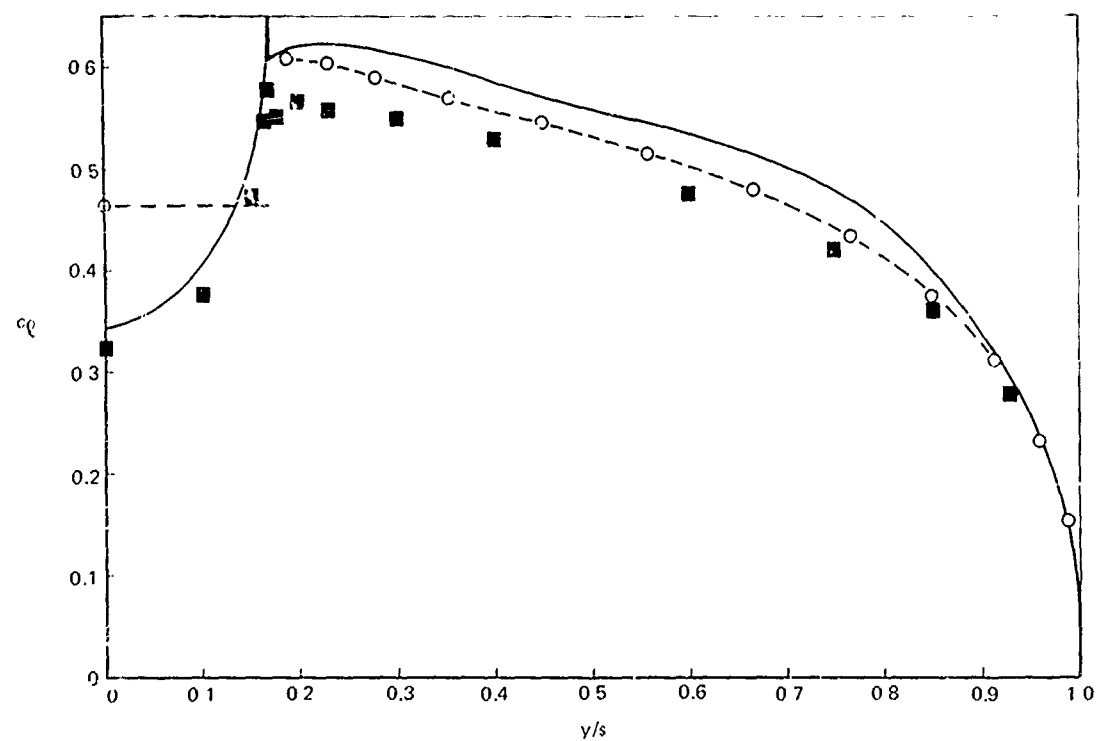


Figure 31. Comparison of Experimental and Calculated Lift Coefficient Distribution for a Straight-Wing/Fuselage Combination.

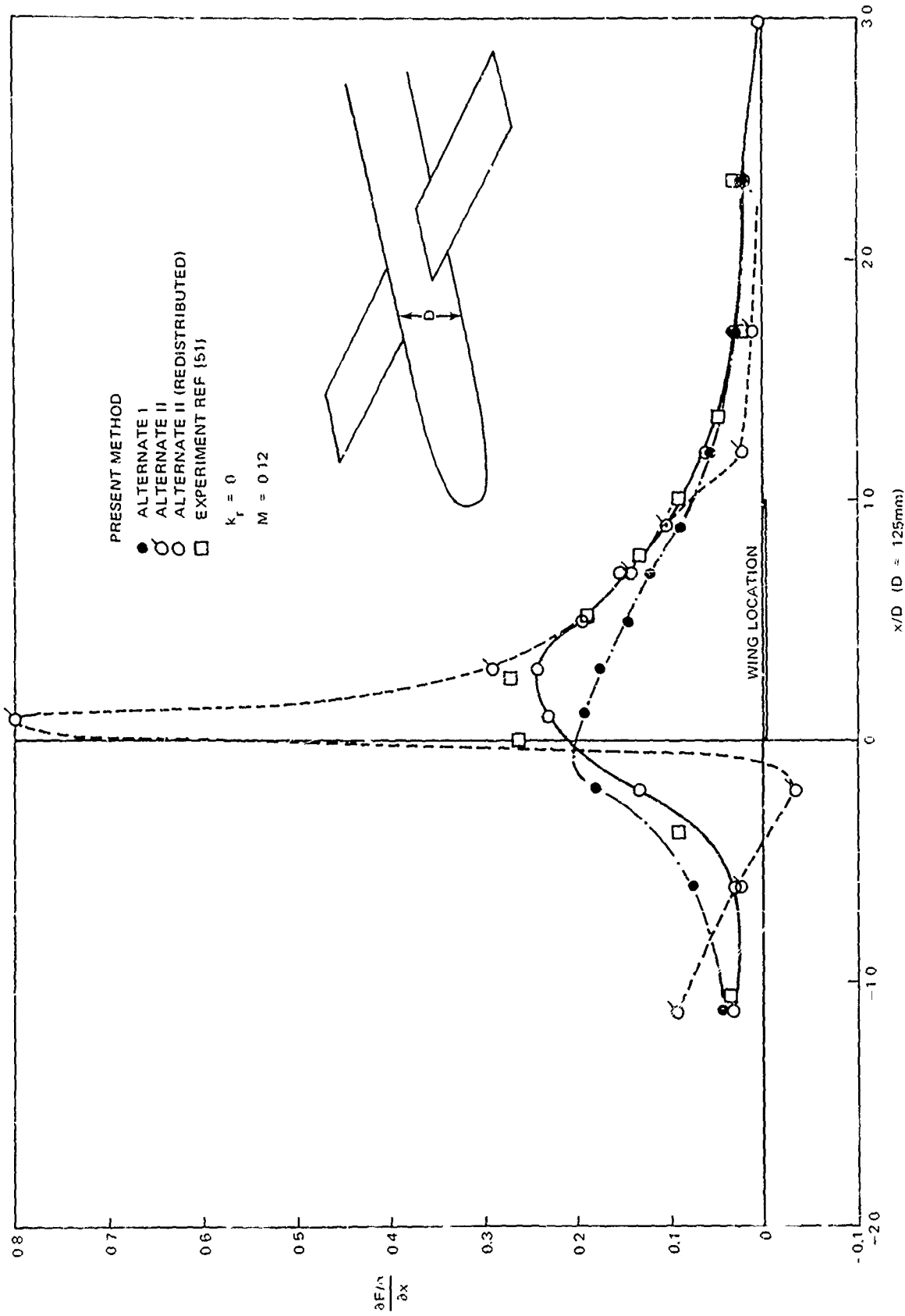


Figure 32. Comparison of Experimental and Calculated Fuselage Axial Load Distribution. (Fuselage at Zero Incidence)

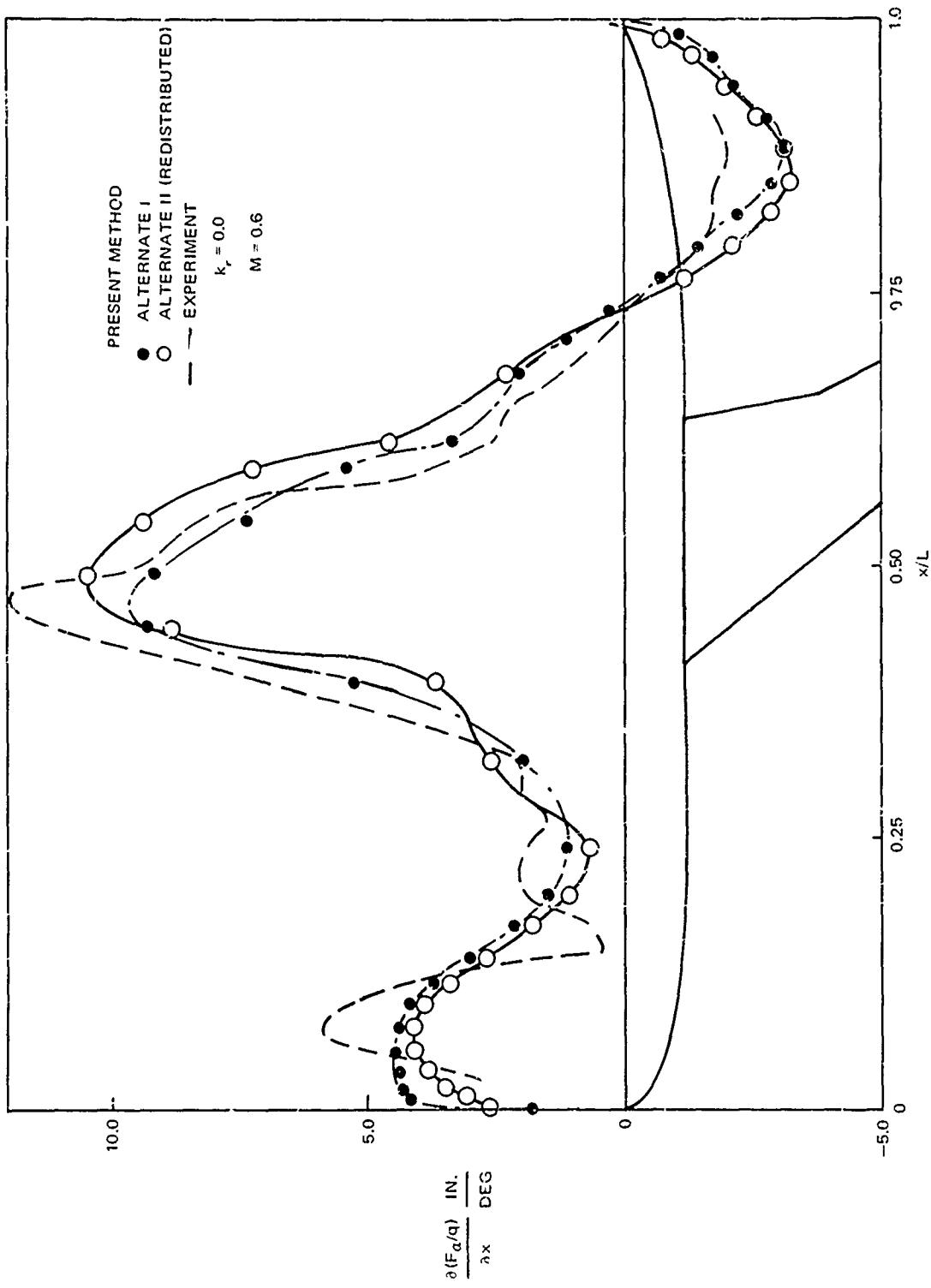


Figure 33. Comparison of Experimental and Calculated Fuselage Axial Load Distribution for a Mach Number of 0.6.

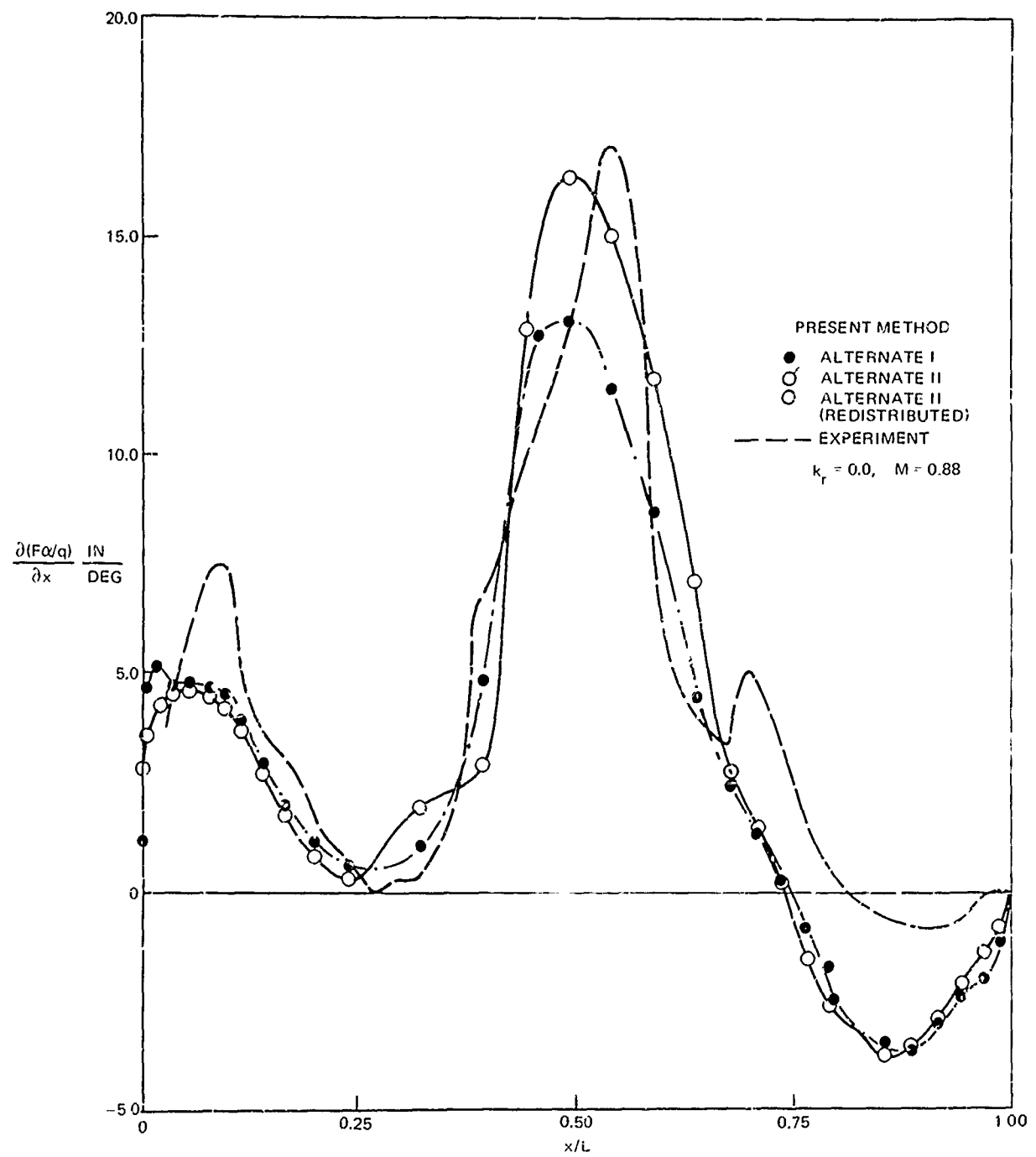


Figure 34. Comparison of Experimental and Calculated Fuselage Axial Load Distribution for a Mach Number of 0.88.

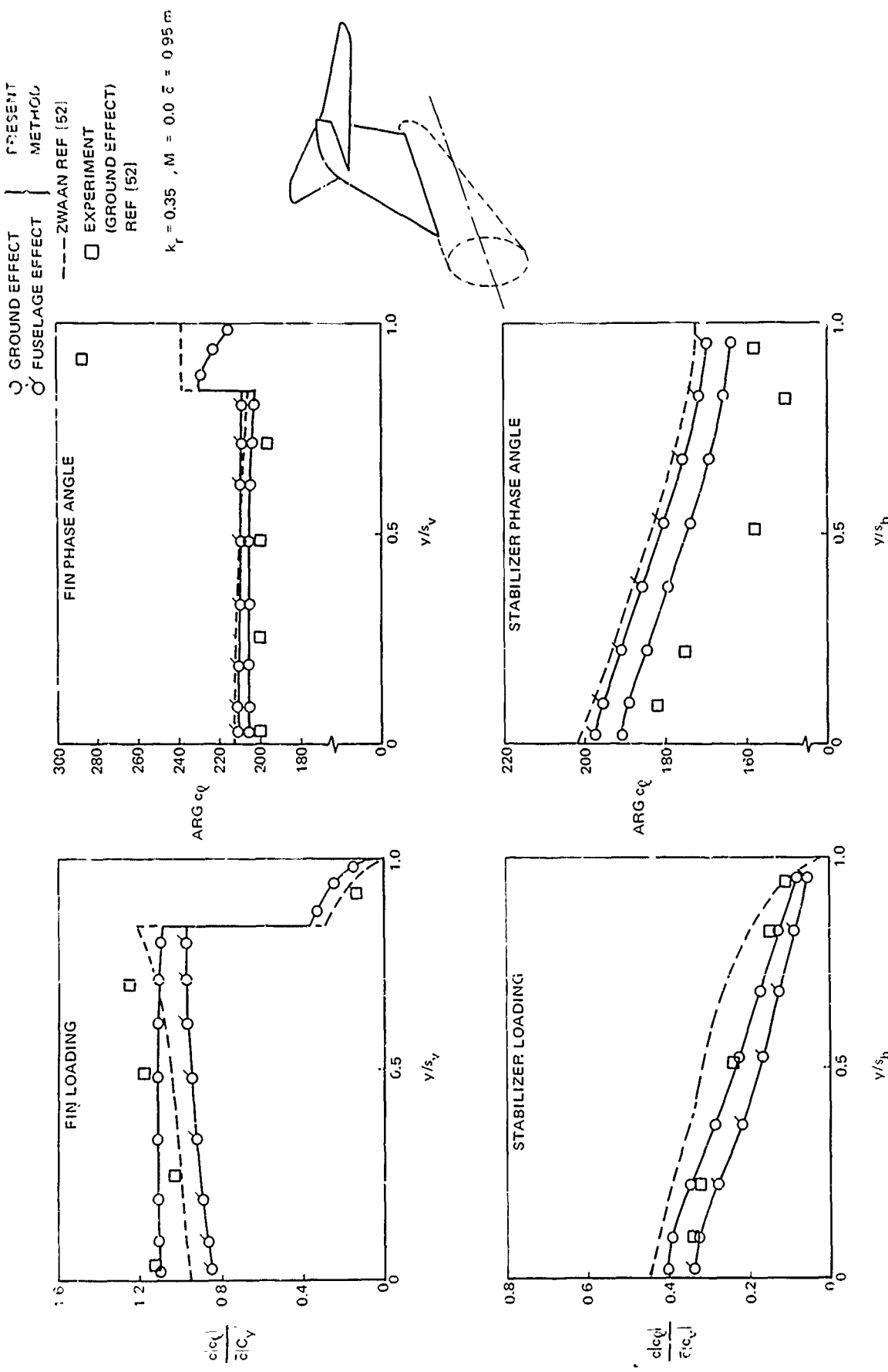


Figure 35. Comparison of Experimental and Calculated Span Load for a T-Tail in Unsteady Flow.

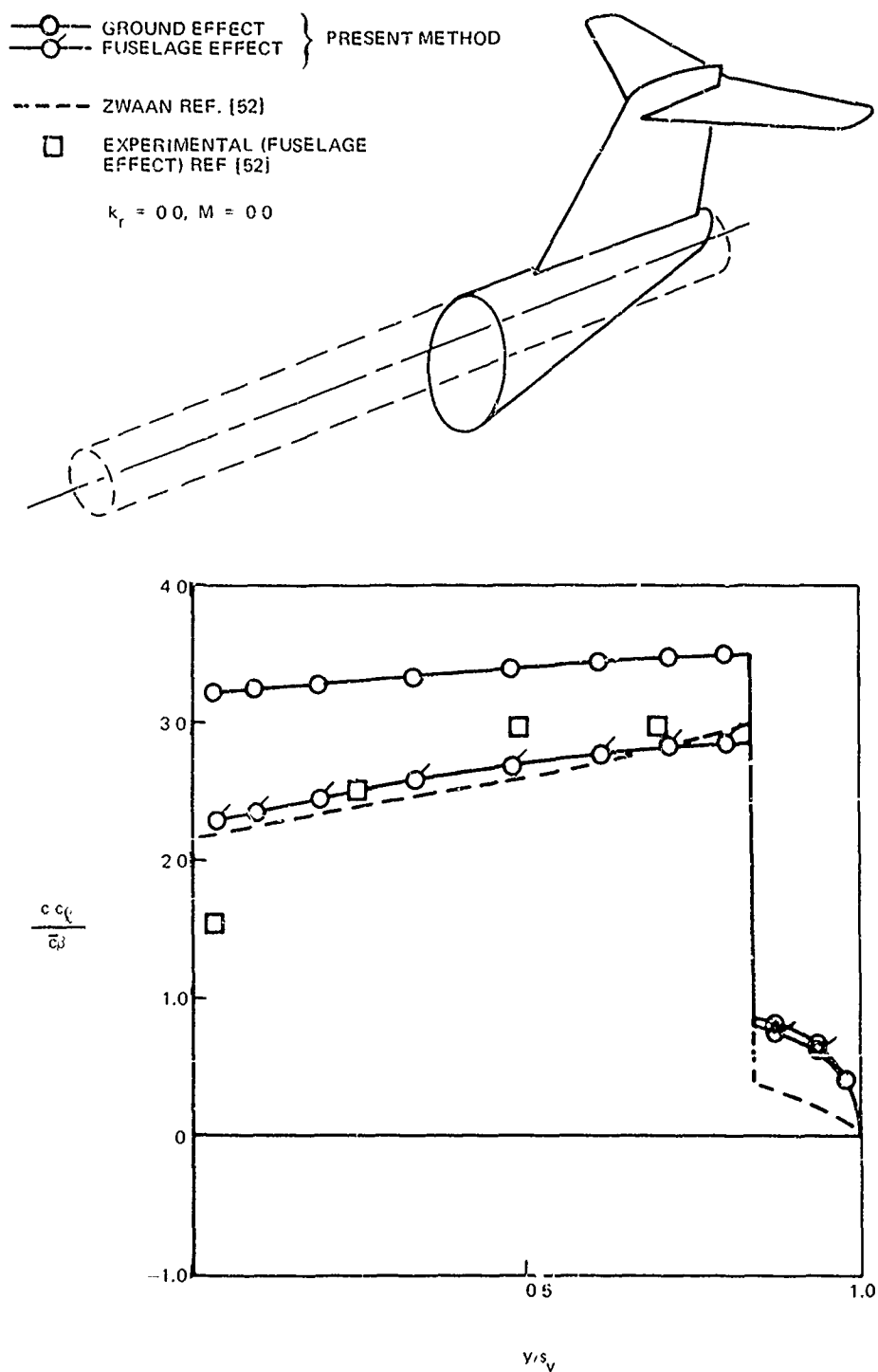


Figure 36. Comparison of Experimental and Calculated Span Load for a T-Tail/Fuselage in Steady Flow.

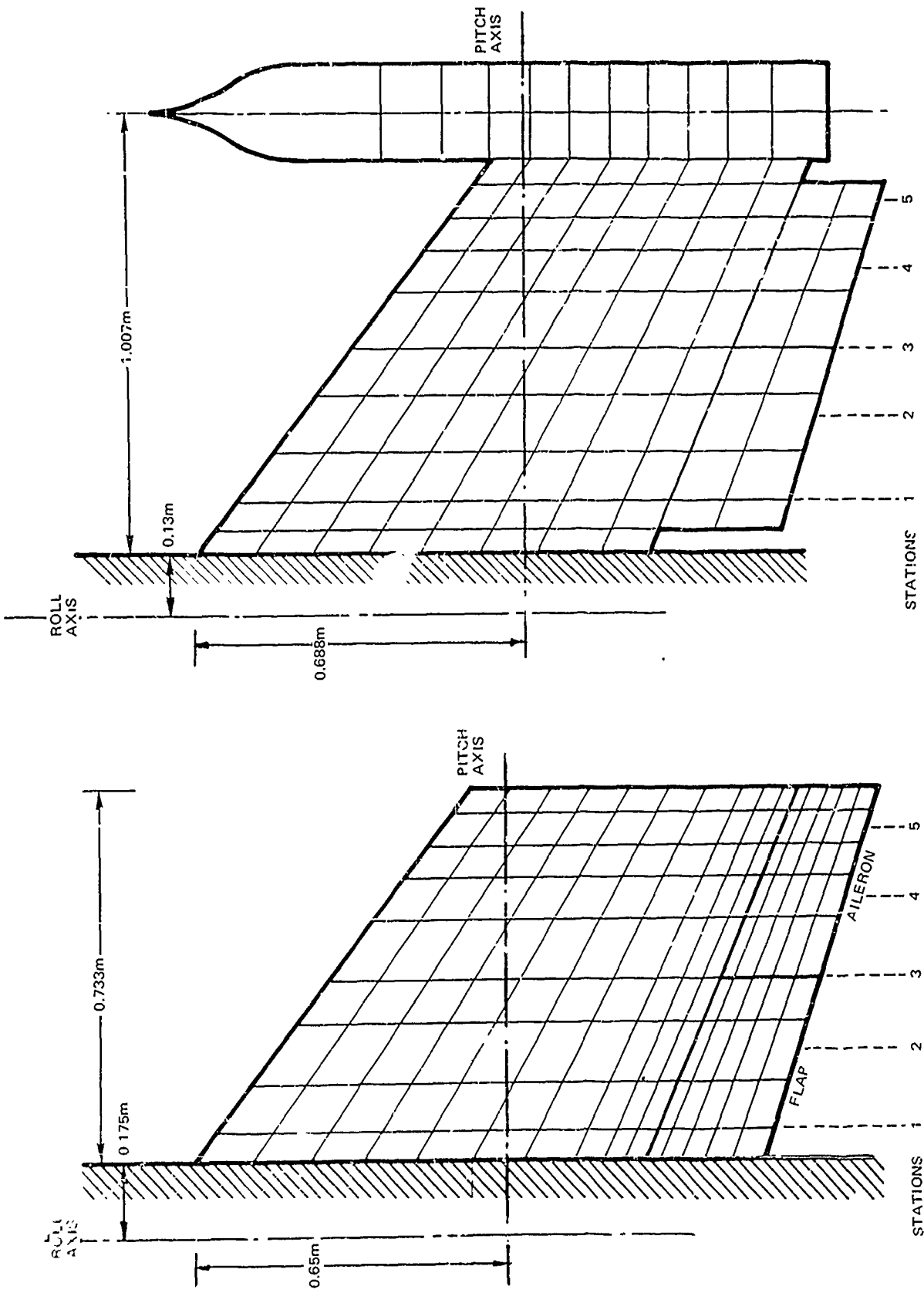


Figure 37. Idealization of the V.J. 101-C Wing Alone and Wing/Nacelle.

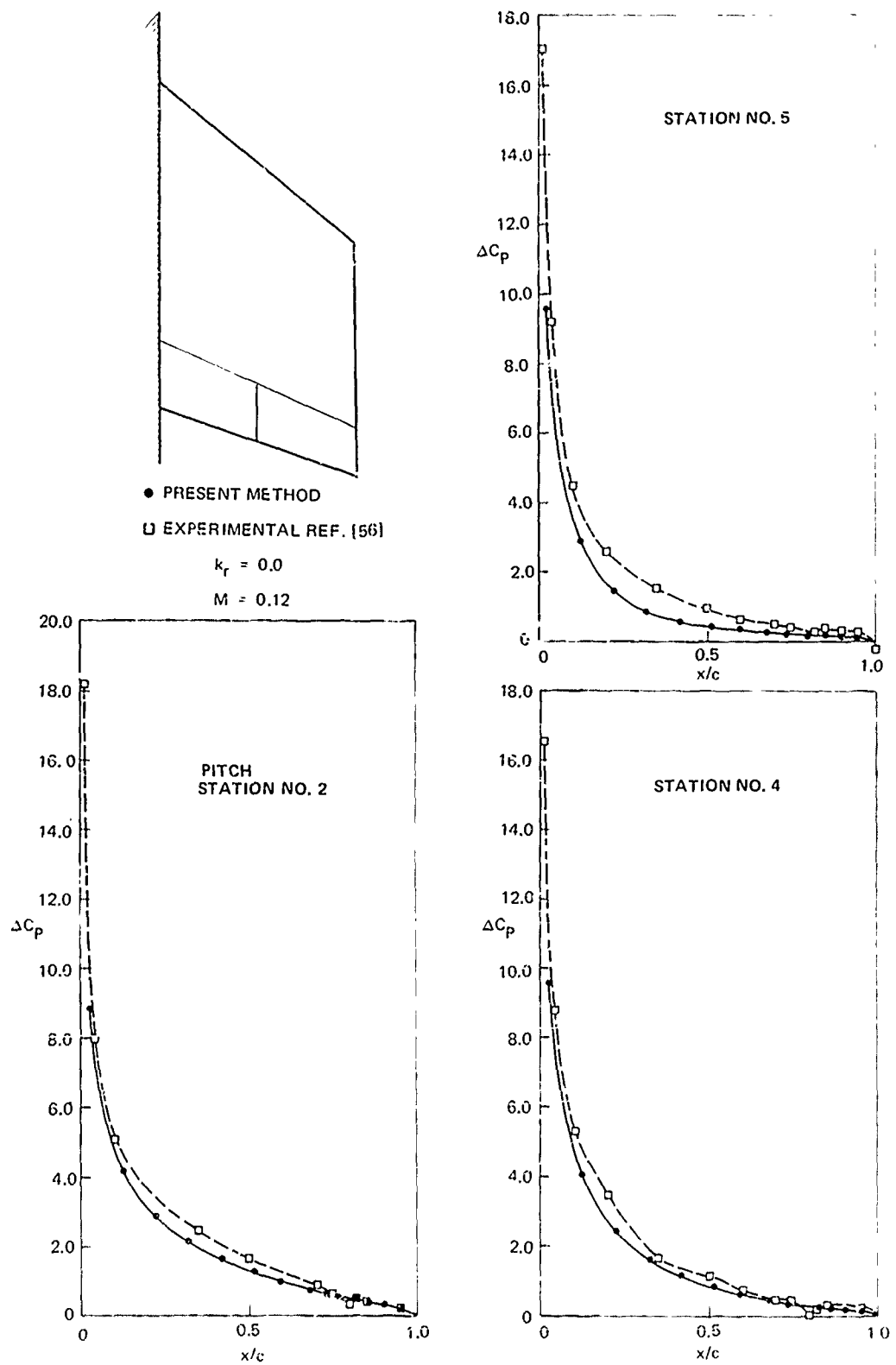


Figure 38. Comparison of Experimental and Calculated Lifting Pressure Distributions for the V.J. 101-C Wing Alone. (Pitch $k_r = 0$).

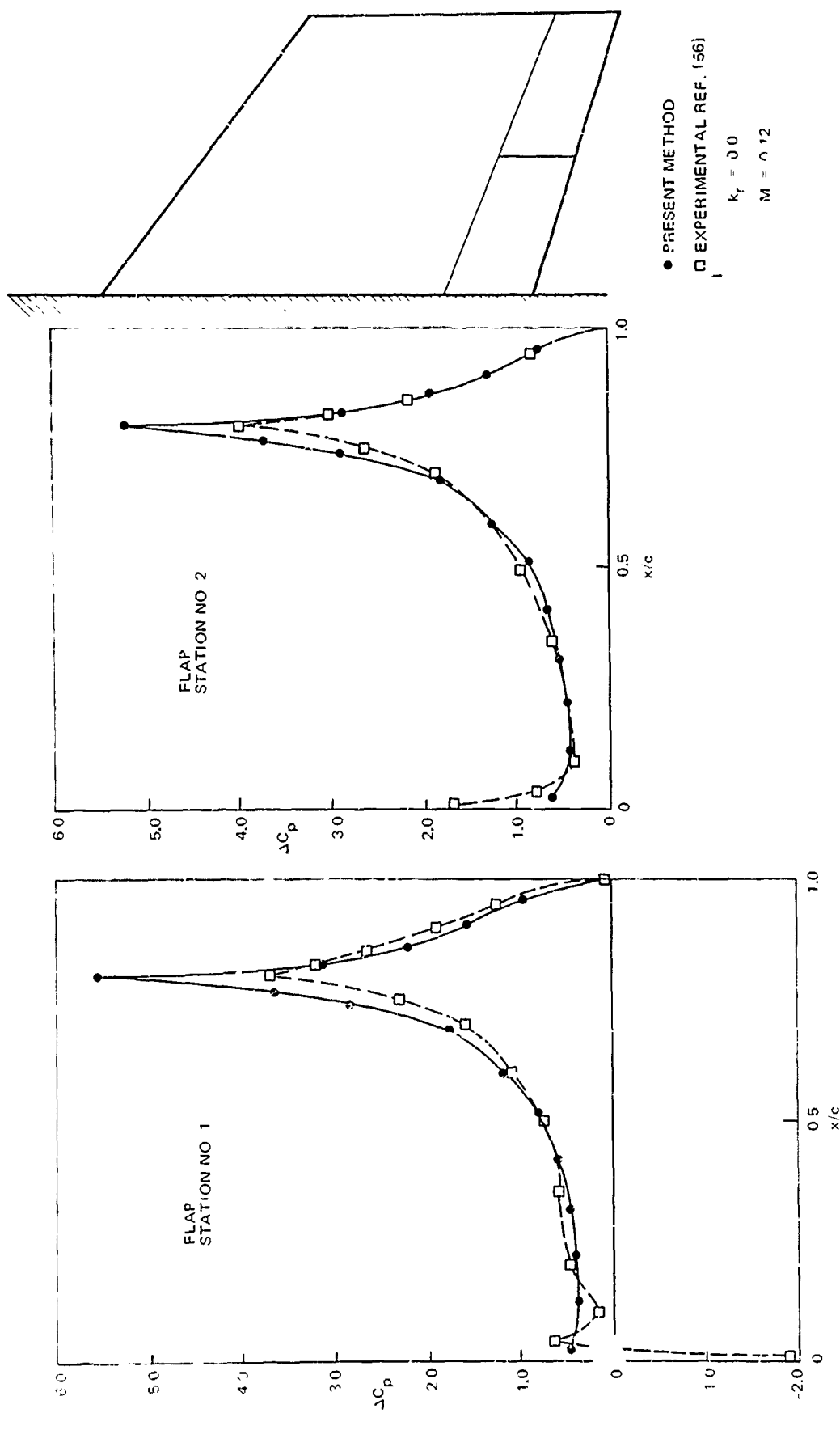


Figure 39. Comparison of Experimental and Calculated Lifting Pressure Distributions for the V.J. 101-C Wing Alone. (Deflected Flap $k_r = 0$)

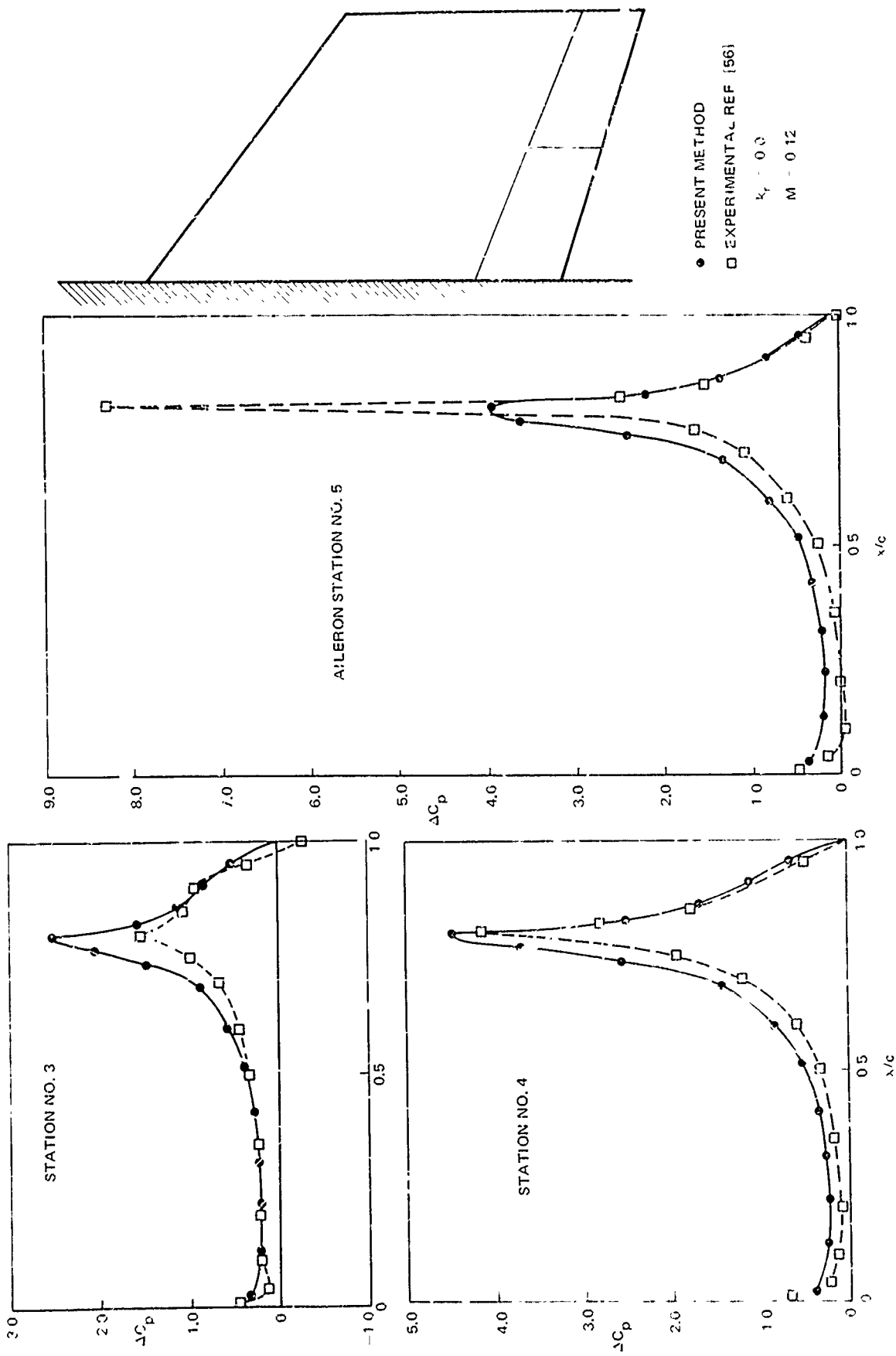


Figure 40. Comparison of Experimental and Calculated Lifting Pressure Distributions for the V.J. 101-C Wing Alone. (Deflected Aileron, $k_r = 0$)

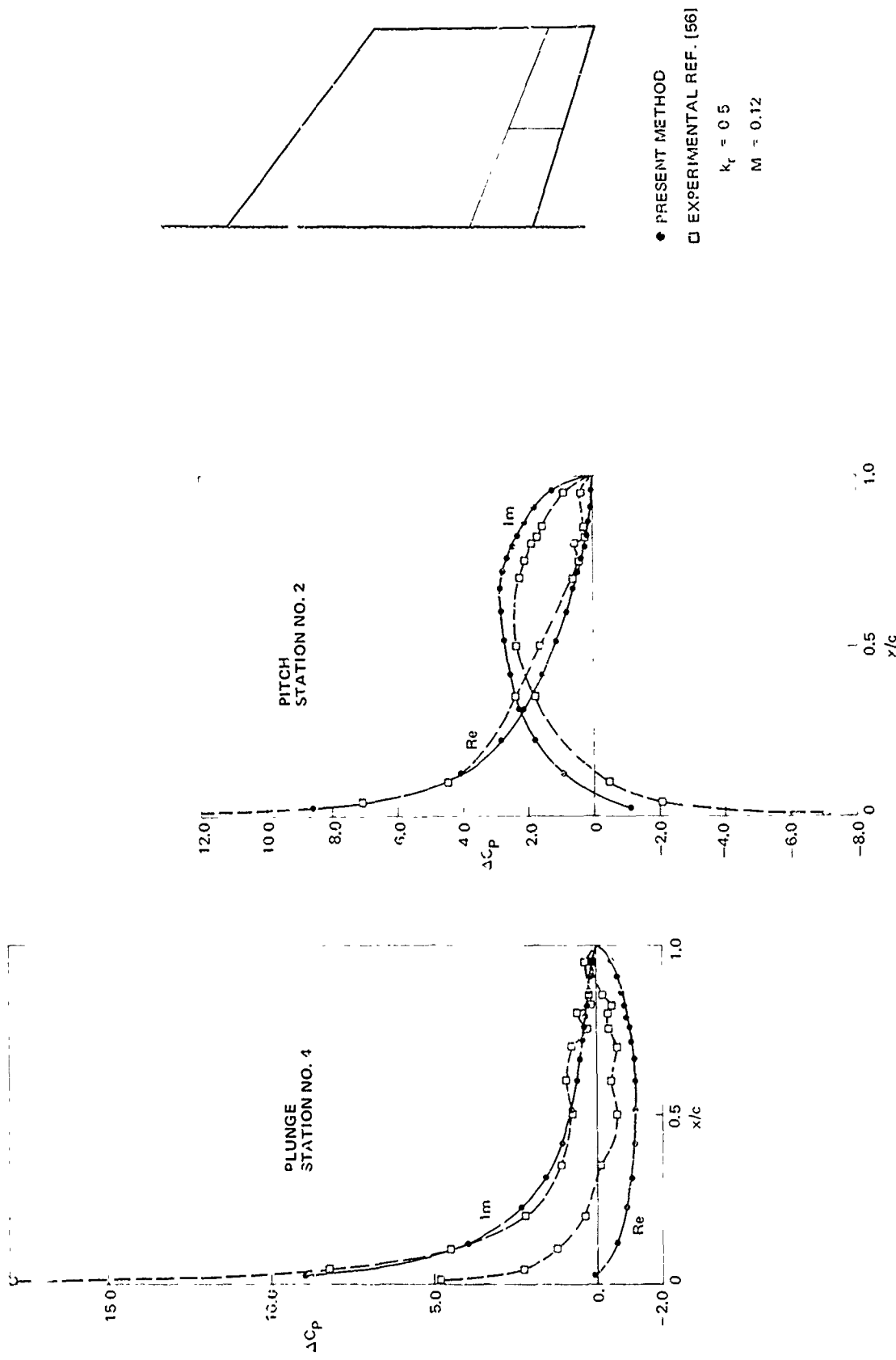


Figure 41. Comparison of Experimental and Calculated Lifting Pressure Distributions for the V.J. 101-C Wing Alone. (Pitch and Plunge, $k_r = 0.5$)

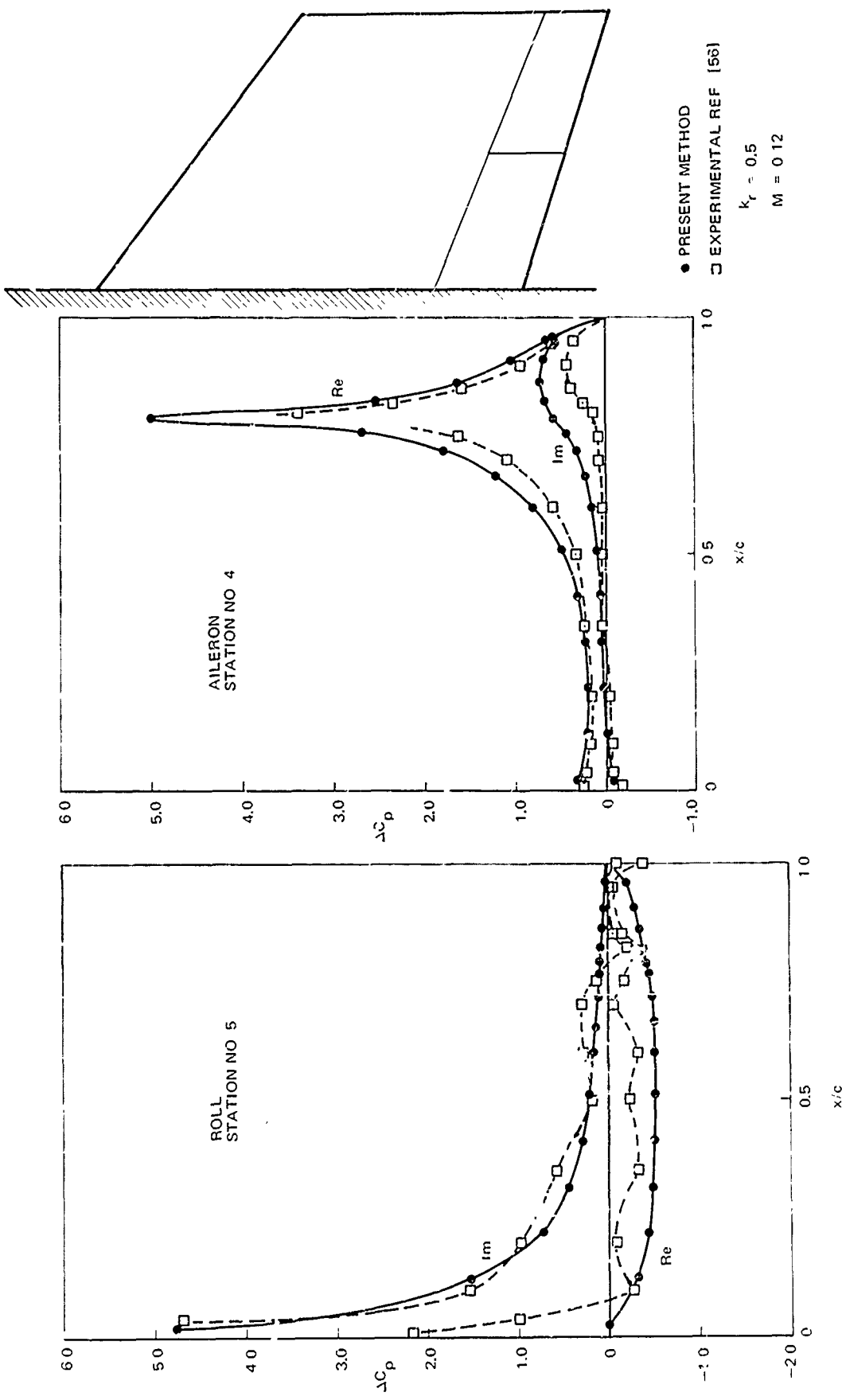


Figure 42. Comparison of Experimental and Calculated Lifting Pressure Distributions for the V.J. 101-C Wing Alone. (Oscillating Aileron and Roll, $k_r = 0.5$)

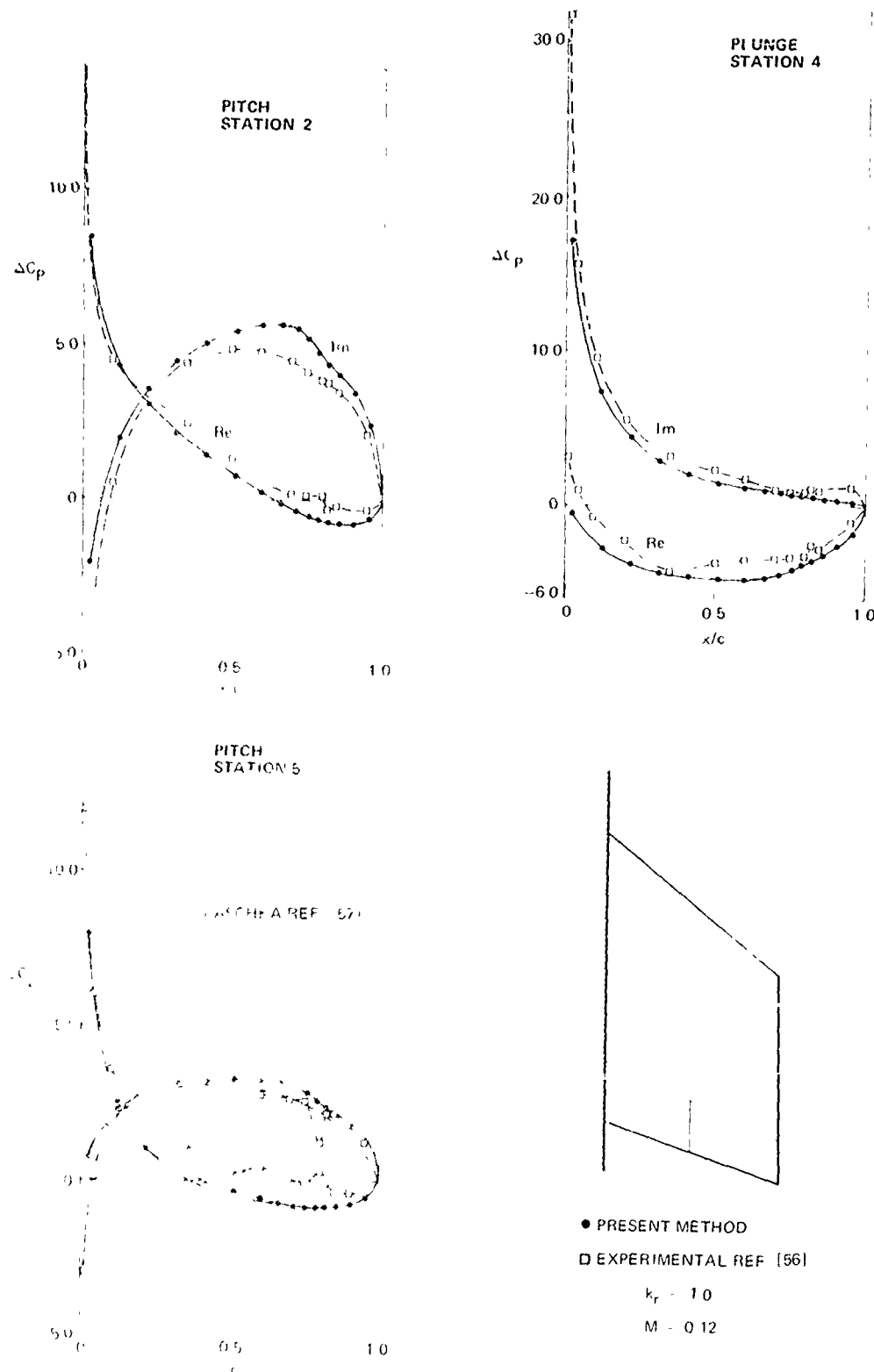


Figure 43. Comparison of Experimental and Calculated Lifting Pressure Distributions for the V.J. 101-C Wing Alone. (Pitch and Plunge, $k_r = 1.0$)

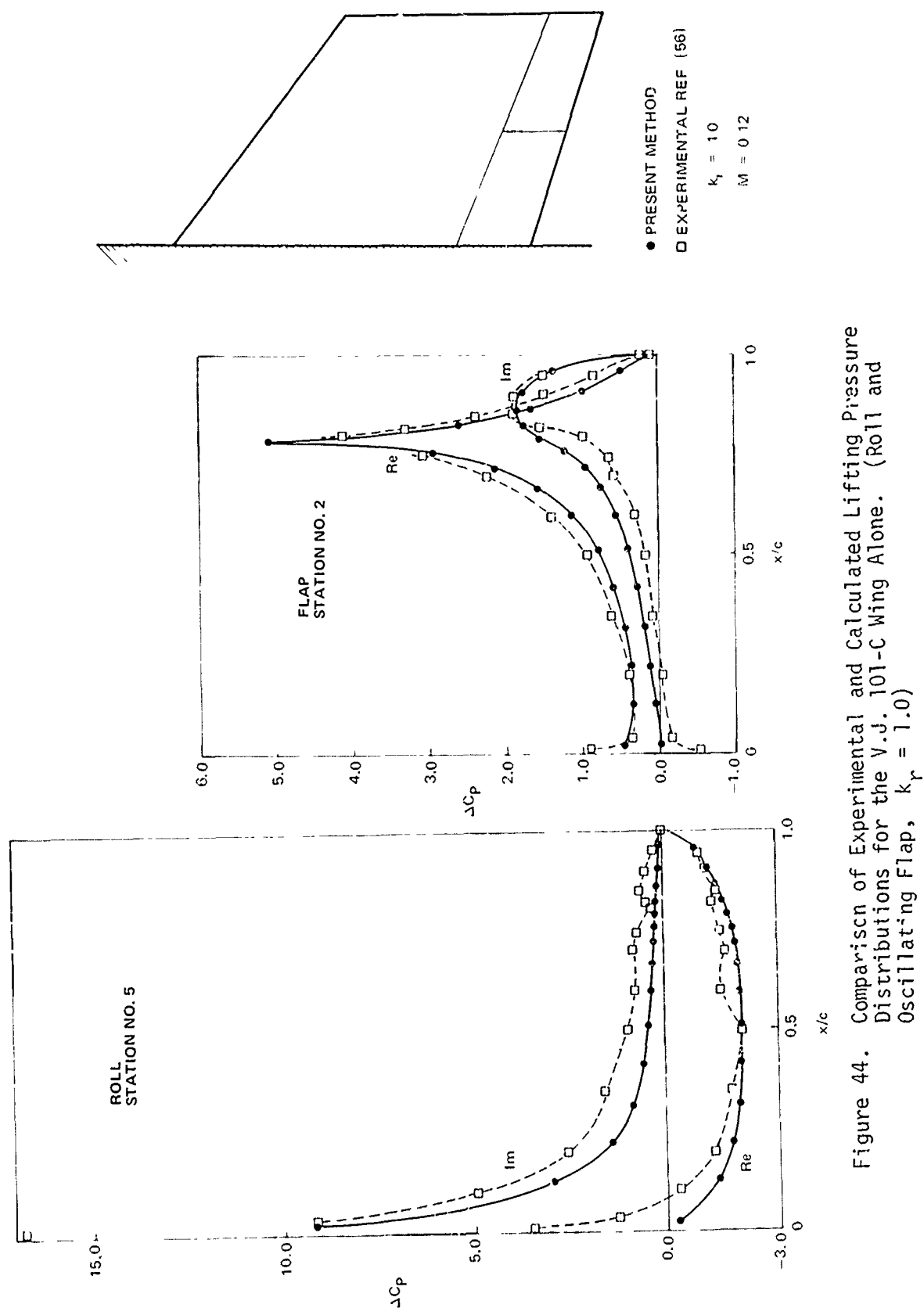


Figure 44. Comparison of Experimental and Calculated Lifting Pressure Distributions for the V.J. 101-C Wing Alone. (Roll and Oscillating Flap, $k_r = 1.0$)

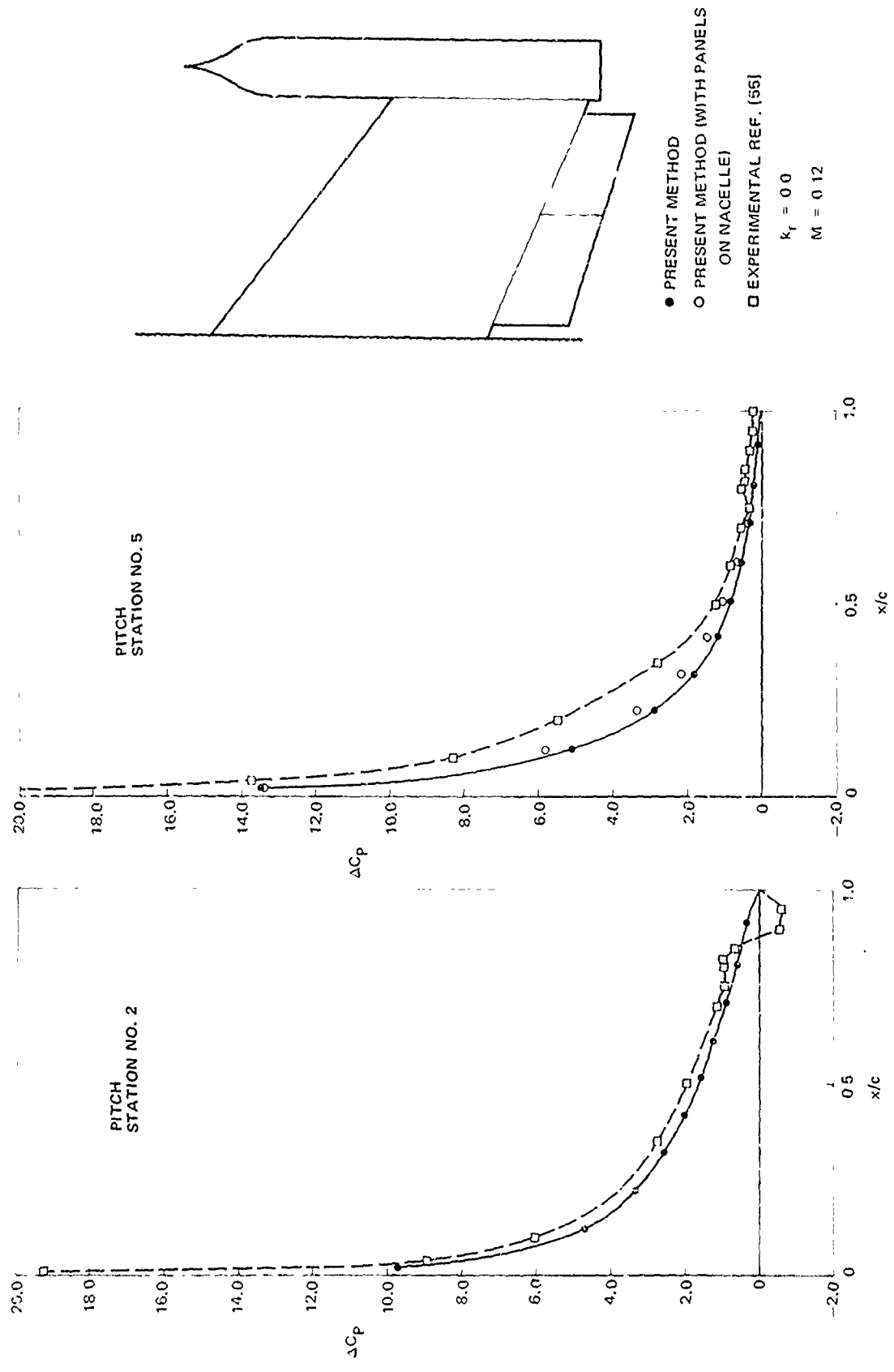


Figure 45. Comparison of Experimental and Calculated Lifting Pressure Distributions for the V.J. 101-C Wing-Nacelle Combination (Pitch, $k_r = 0.0$)

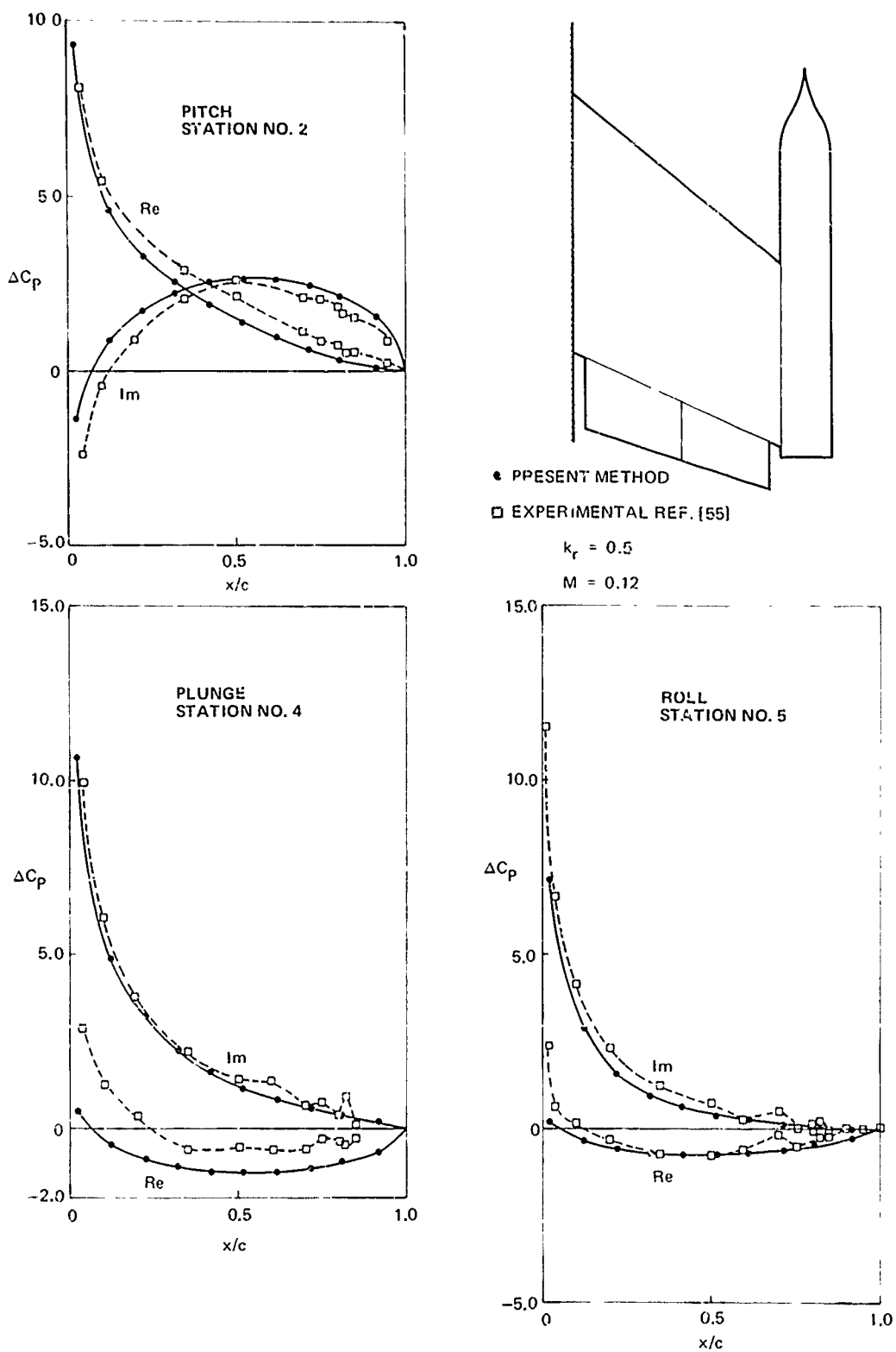


Figure 46. Comparison of Experimental and Calculated Lifting Pressure Distributions for the V.J. 101-C Wing-Nacelle Combination.
(Pitch, Plunge, Roll, $k_r = 0.5$)

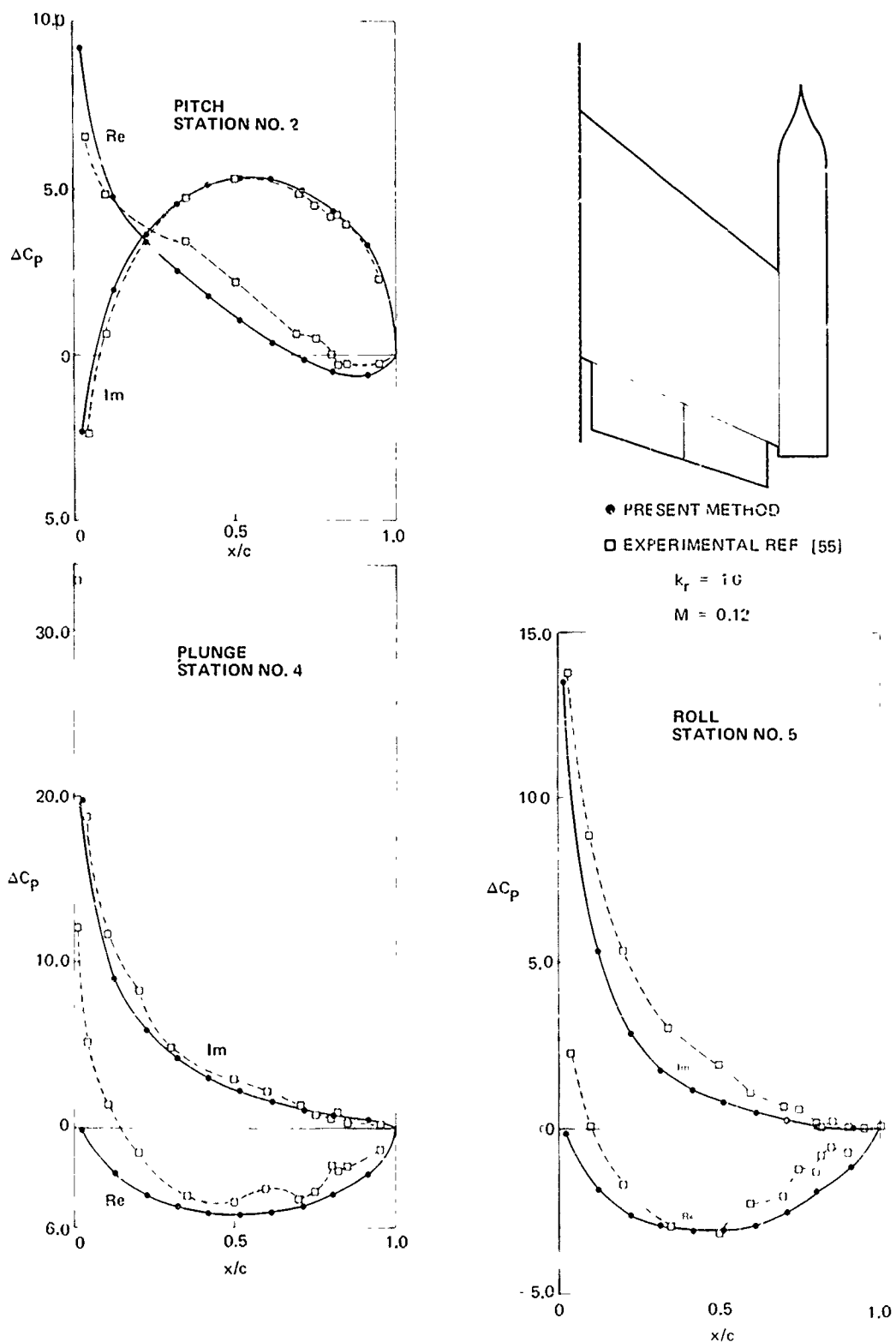


Figure 47. Comparison of Experimental and Calculated Lifting Pressure Distributions for the V.J. 101-C Wing-Nacelle Combination.
(Pitch, Plunge, Roll, $k_r = 1.0$)

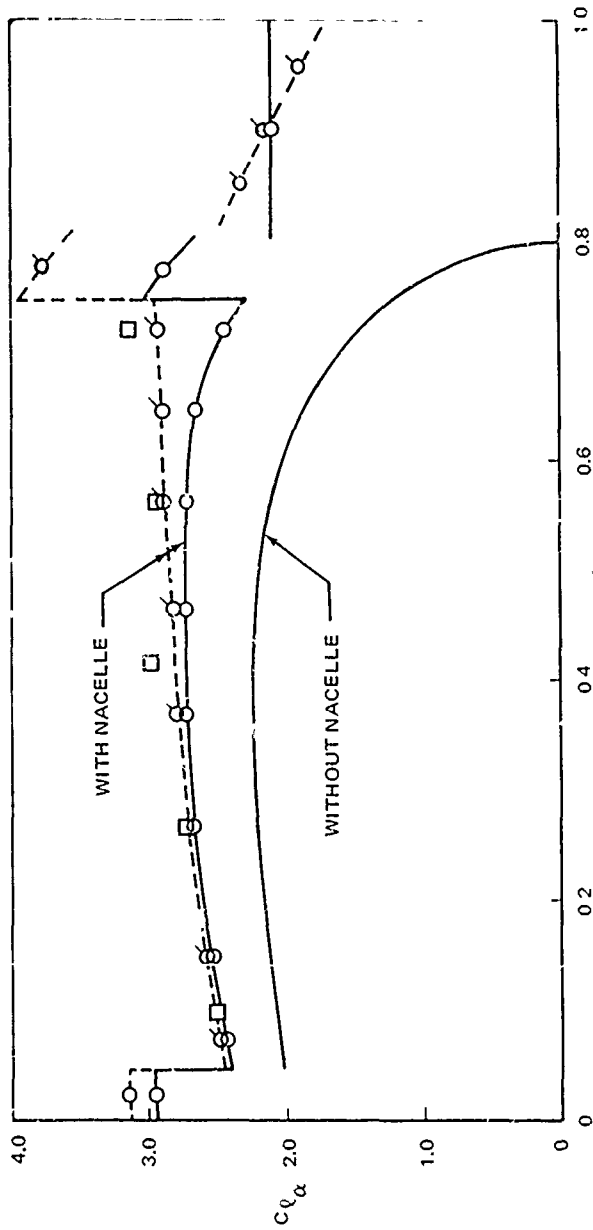
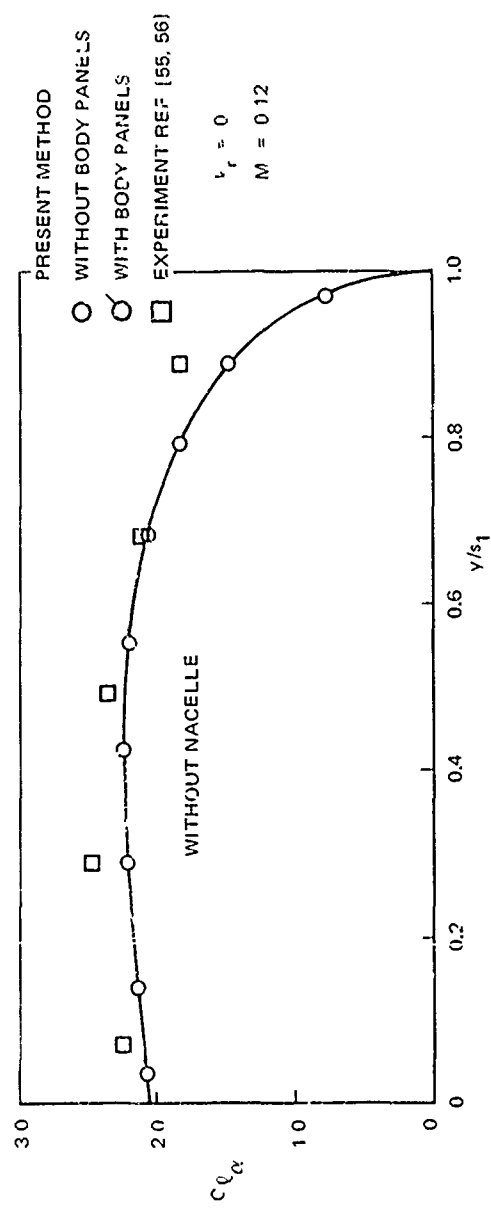


Figure 48. Comparison of Experimental and Calculated Lift-Curve-Slope Distributions for the V.J. 101-C with and without Nacelle in Steady Flow.

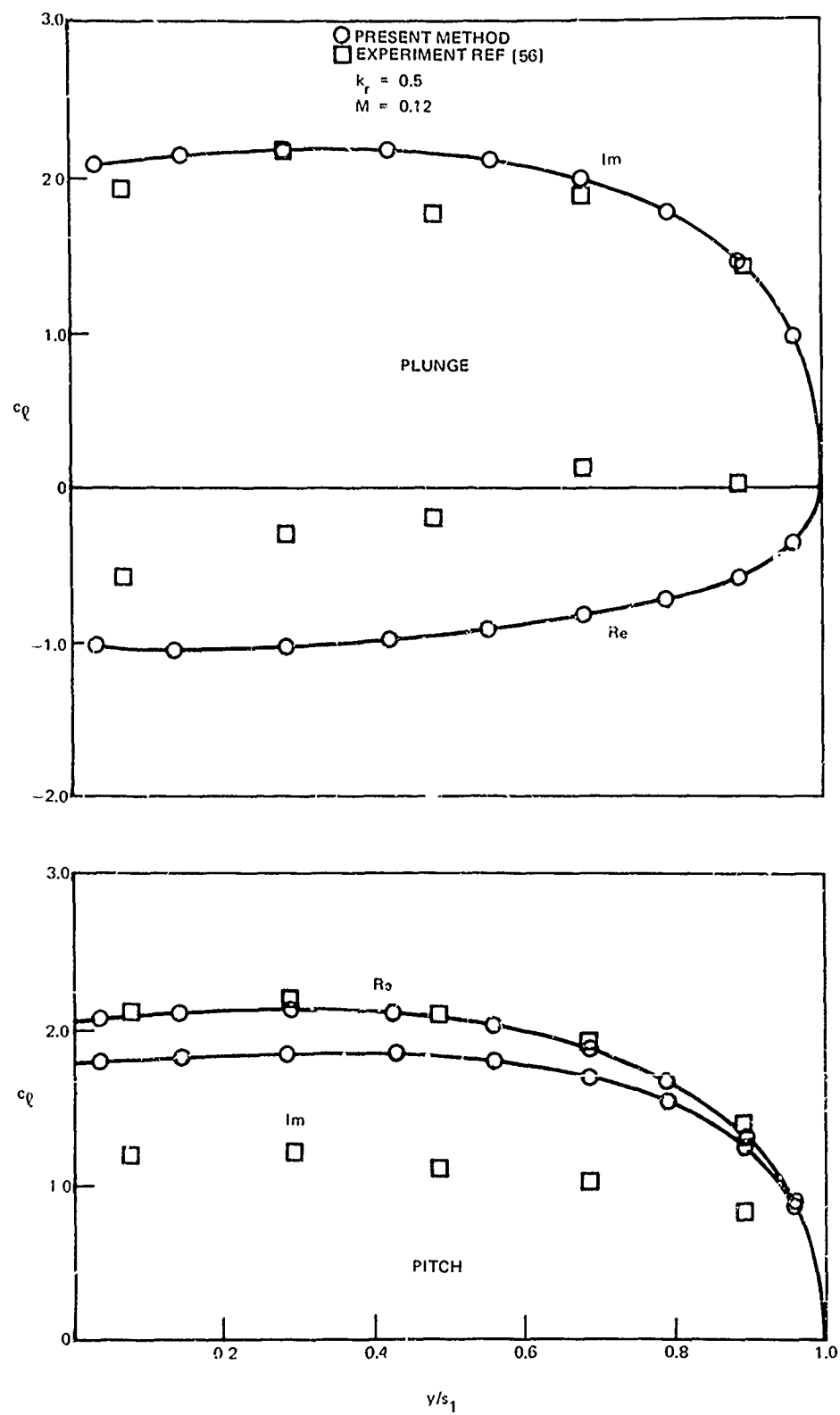


Figure 49. Comparison of Experimental and Calculated Lift Coefficient Distributions for the V.J. 101-C without Nacelle. (Pitch, Plunge, $k_r = 0.5$)

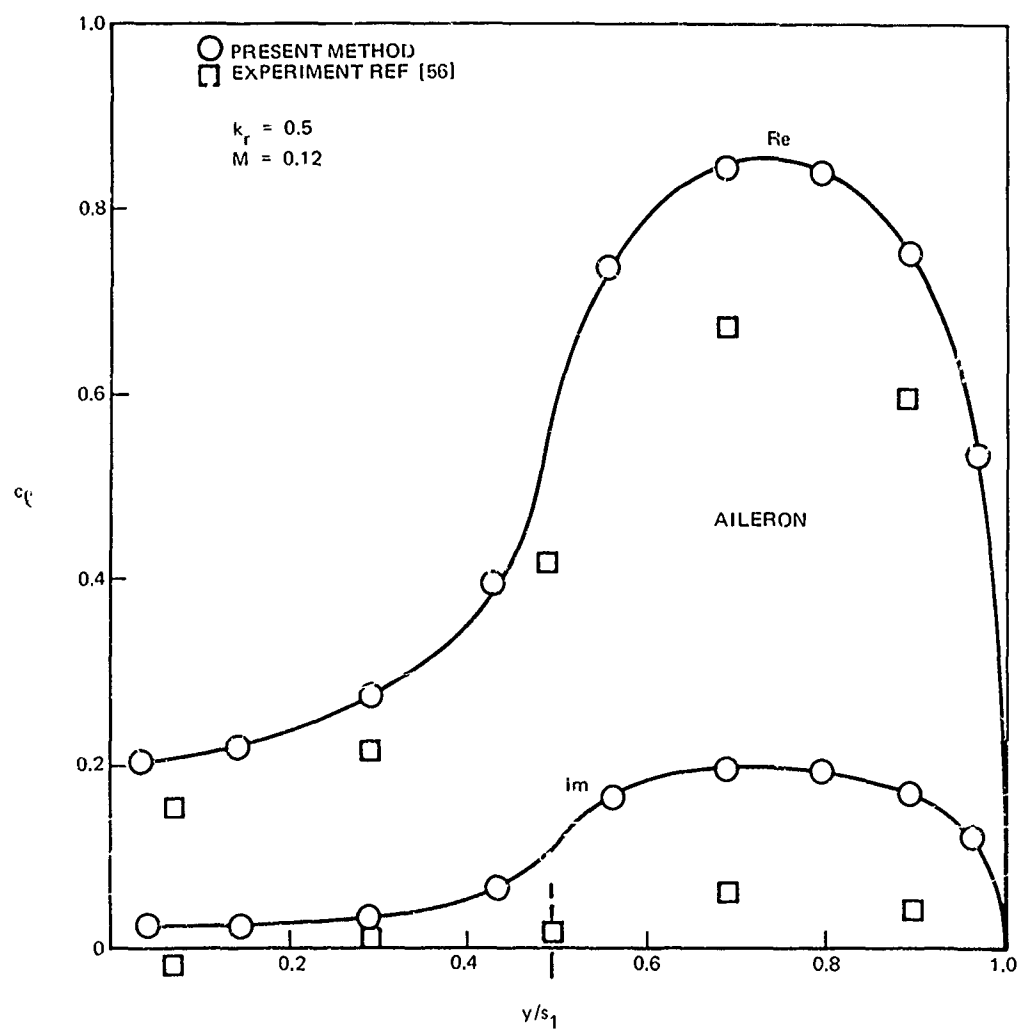


Figure 50. Comparison of Experimental and Calculated Lift Coefficient Distributions for the V.J. 101-C without Nacelle. (Aileron, $k_r = 0.5$)

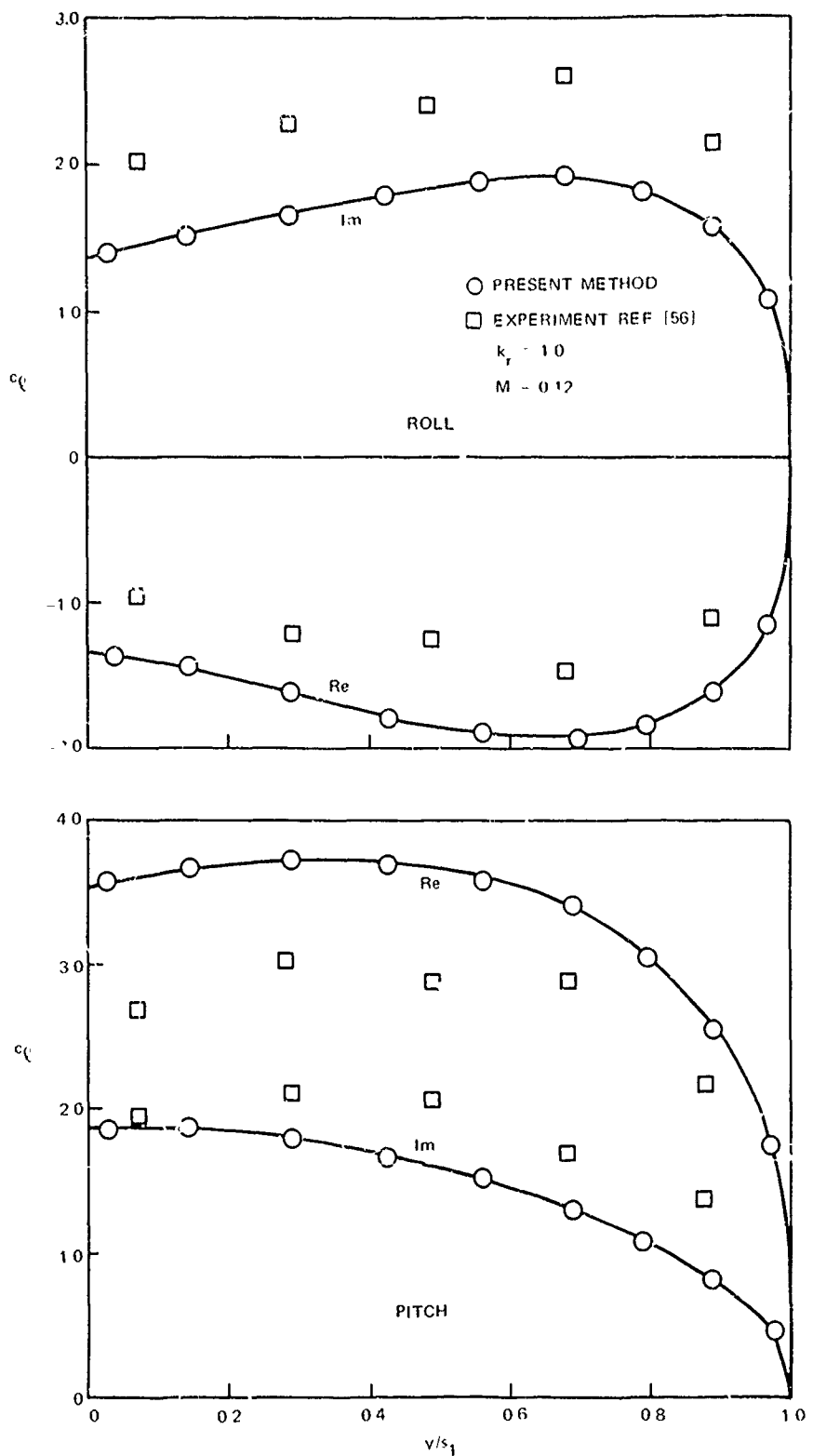


Figure 51. Comparison of Experimental and Calculated Lift Coefficient Distributions for the V.J. 101-C without Nacelle. (Pitch, Roll, $k_r = 1.0$)

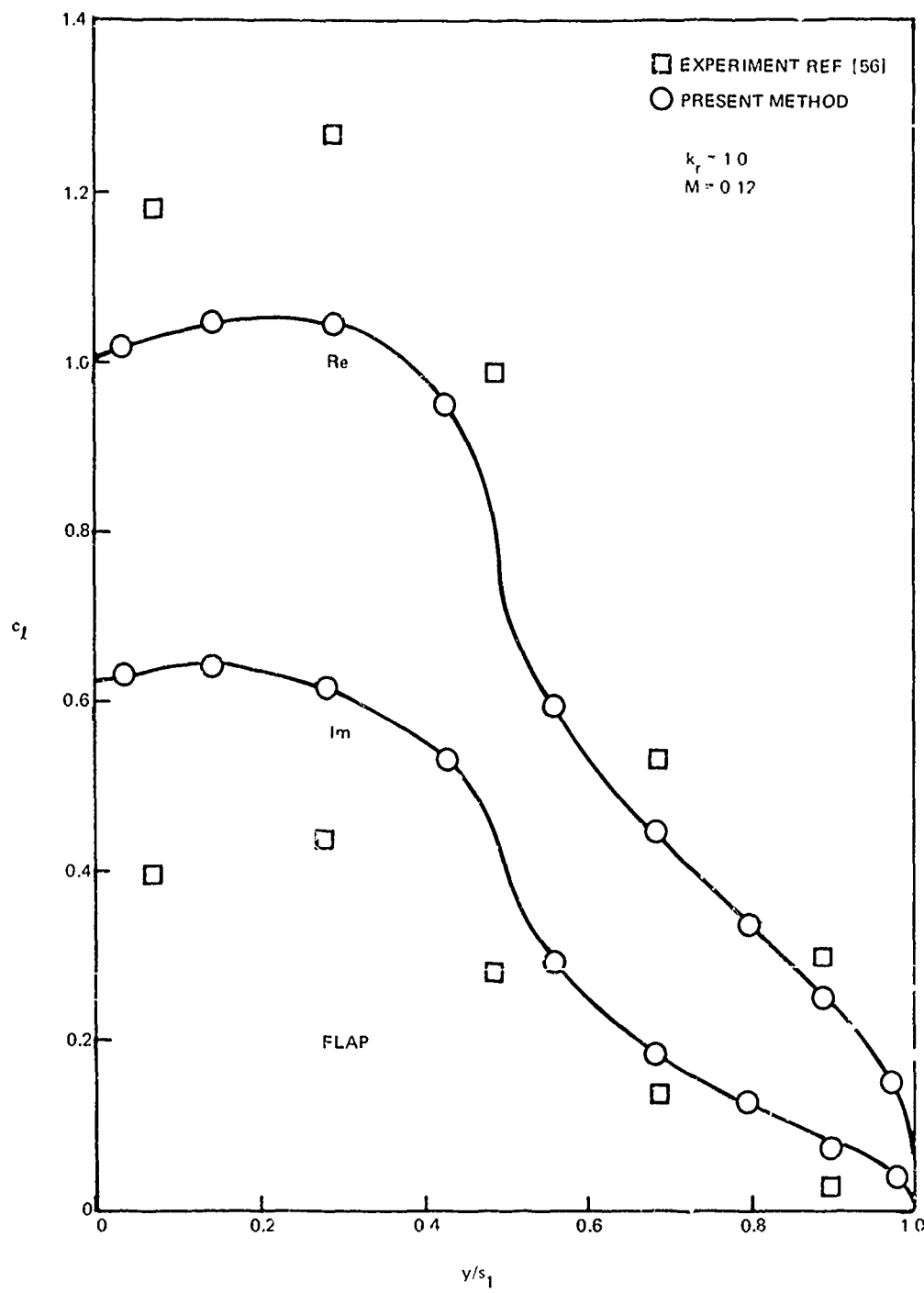


Figure 52. Comparison of Experimental and Calculated Lift Coefficient Distributions for the V.J. 101-C without Nacelle. (Flap, $k_r = 1.0$)

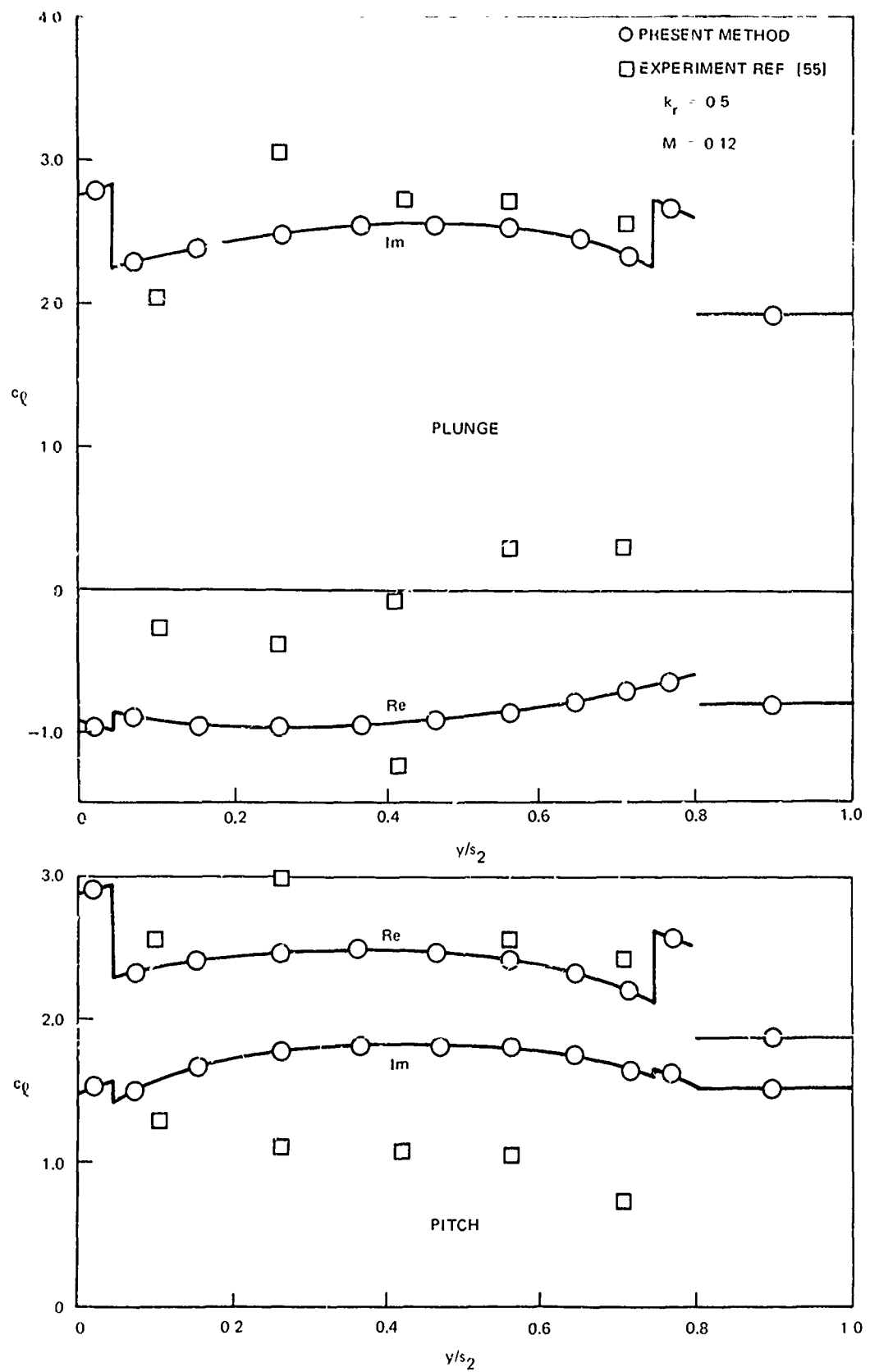


Figure 53. Comparison of Experimental and Calculated Lift Coefficient Distributions for V.J. 101-C with Nacelle. (Pitch, Plunge, $k_r = 0.5$)

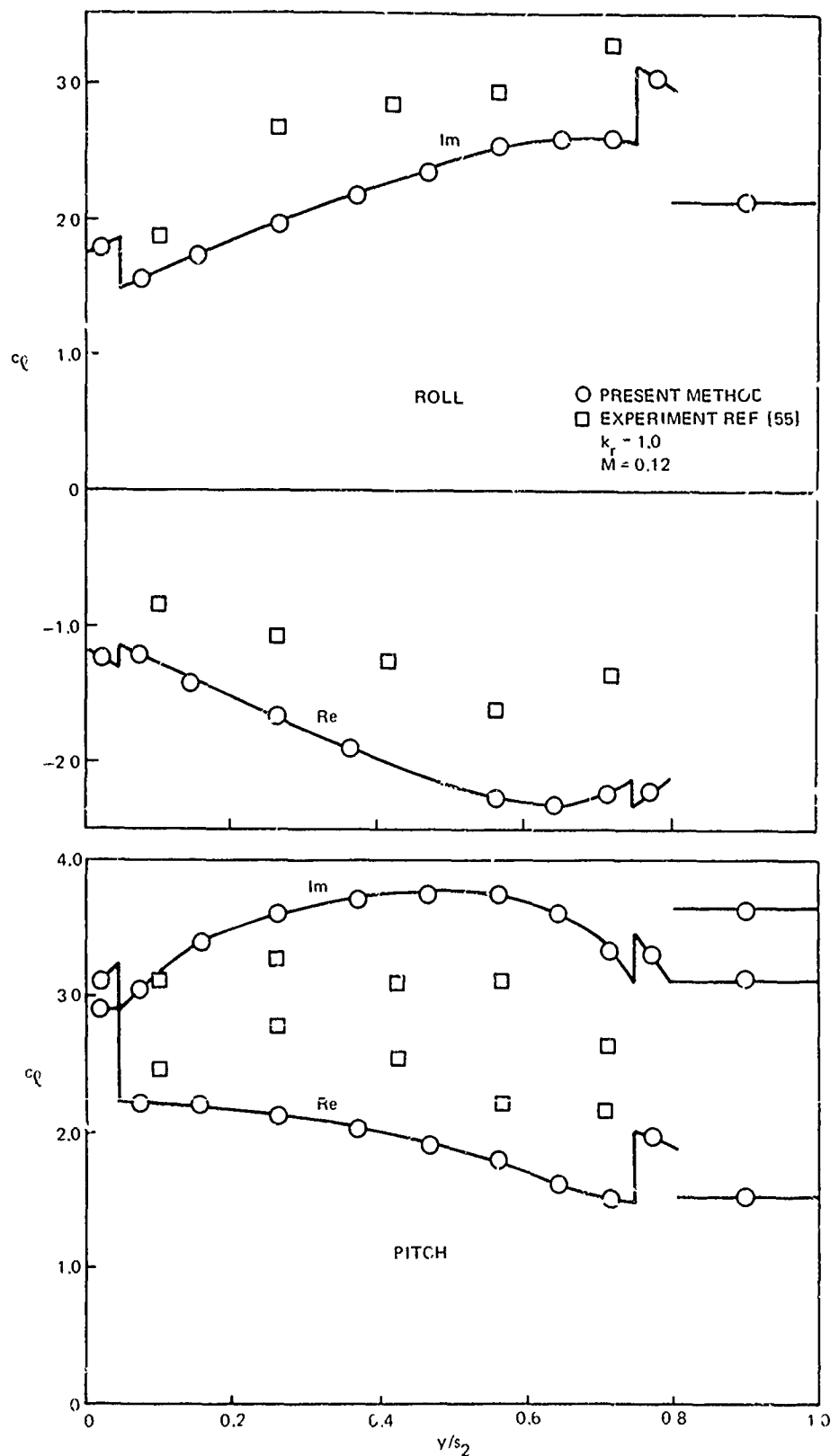


Figure 54. Comparison of Experimental and Calculated Lift Coefficient Distributions for V.J. 101-C with Nacelle. (Pitch, Roll, $k_r = 1.0$)

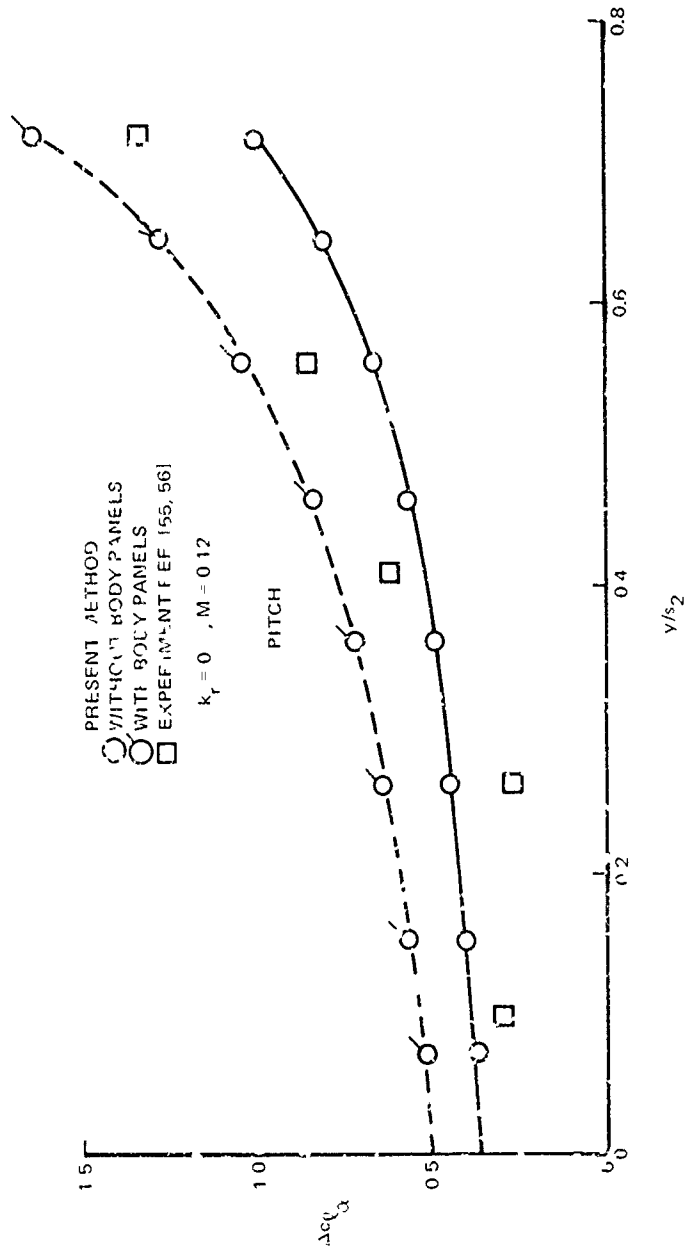


Figure 5b. Comparison of Experimental and Calculated Incremental Lift due to the Nacelle for the J. 101-C. (Pitch, $k_r = 0.0$)

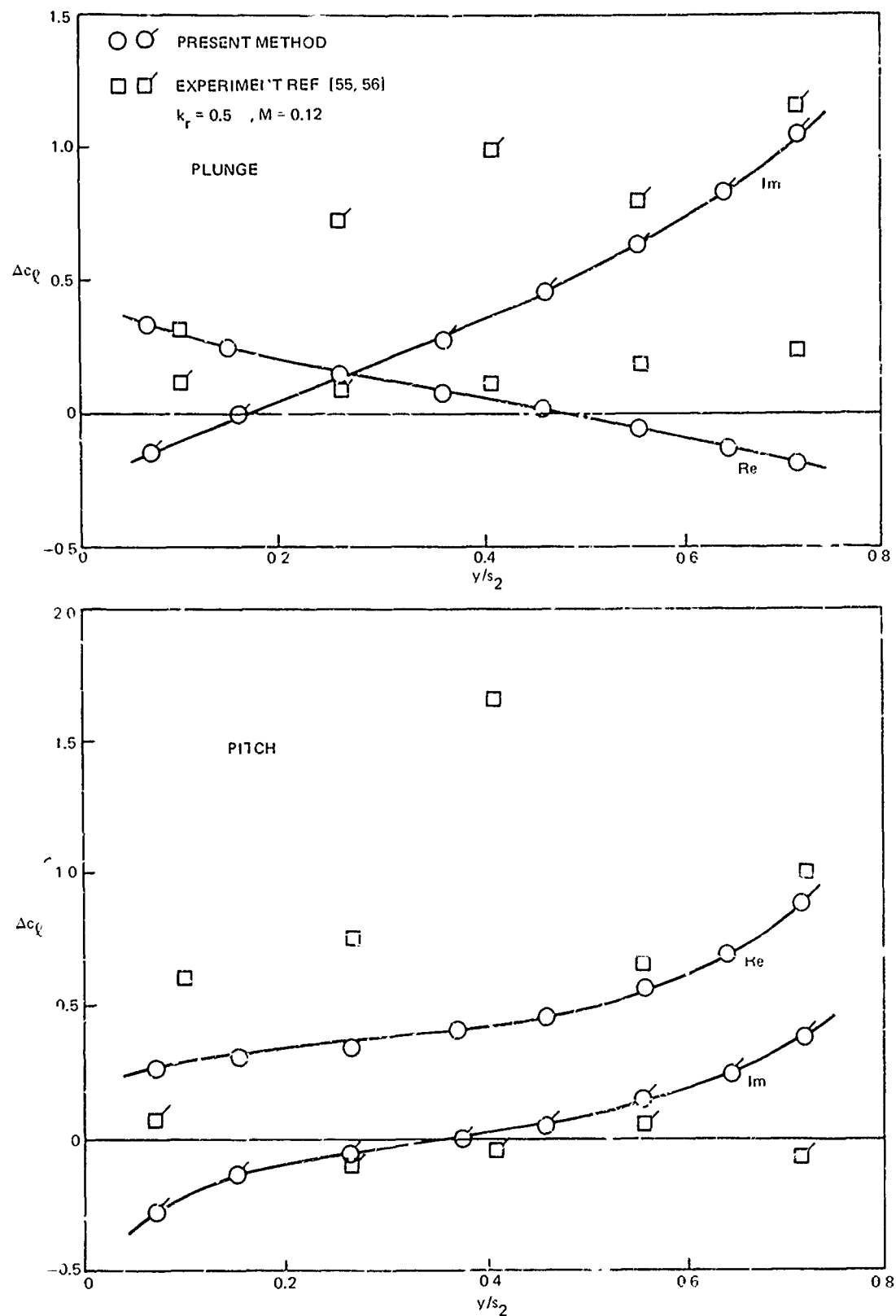


Figure 56. Comparison of Experimental and Calculated Incremental Lift due to the Nacelle for the V.J. 101-C. (Pitch, Plunge, $k_r = 0.5$)

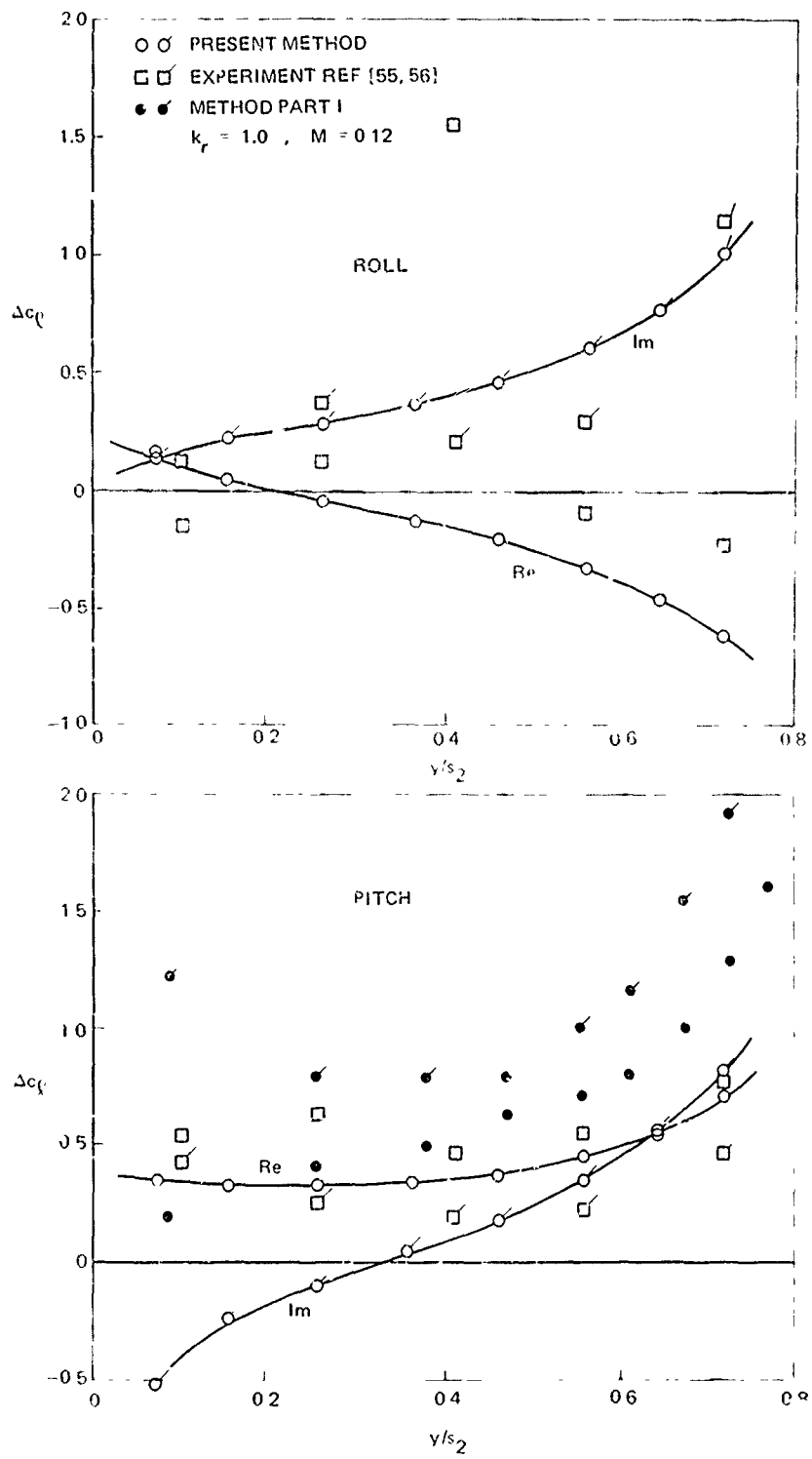


Figure 57. Comparison of Experimental and Calculated Incremental Lift due to the Nacelle for the V.J. 101-C. (Pitch, Roll, $k_r = 1.0$)

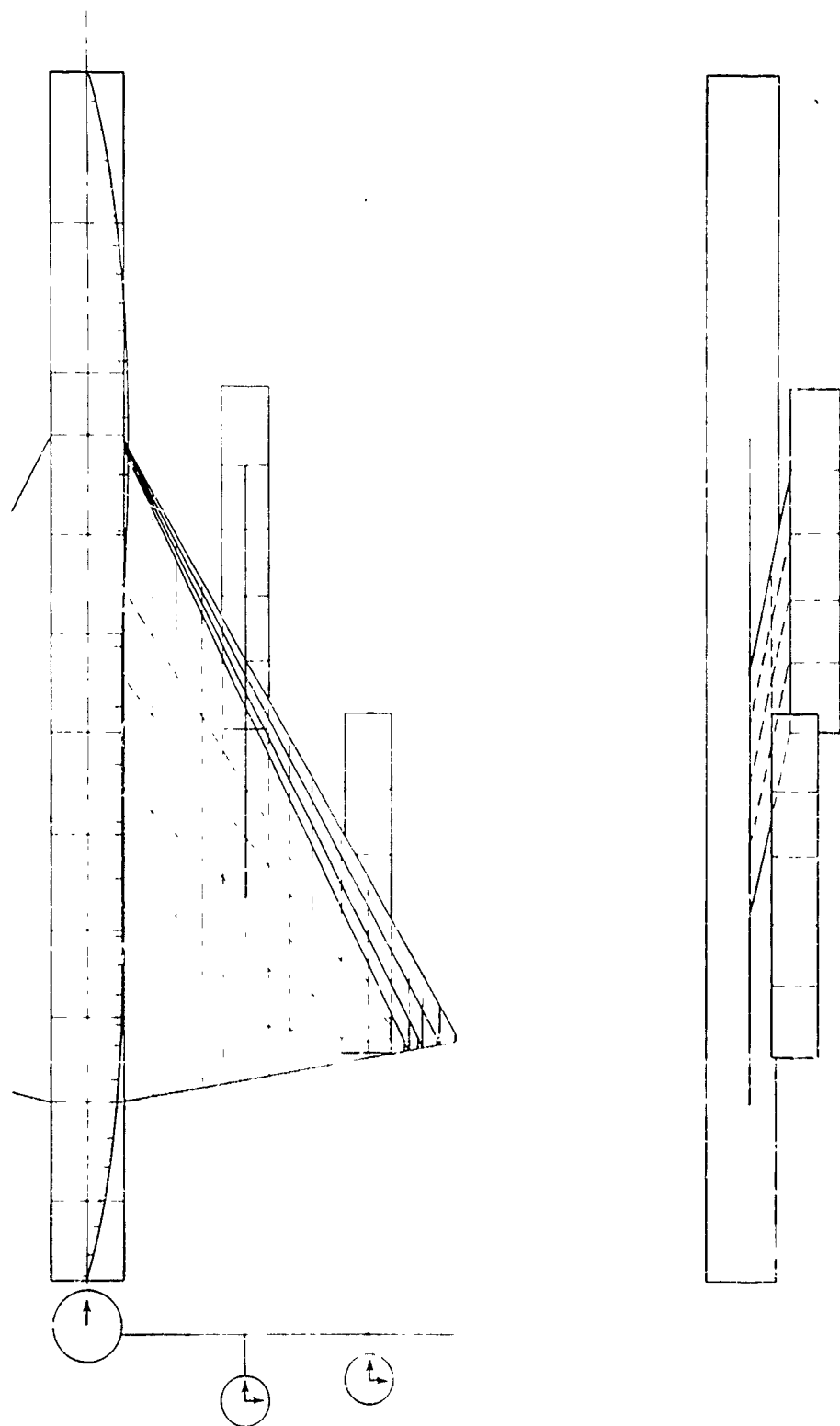


Figure 58. Idealization of the B-58 Bomber.

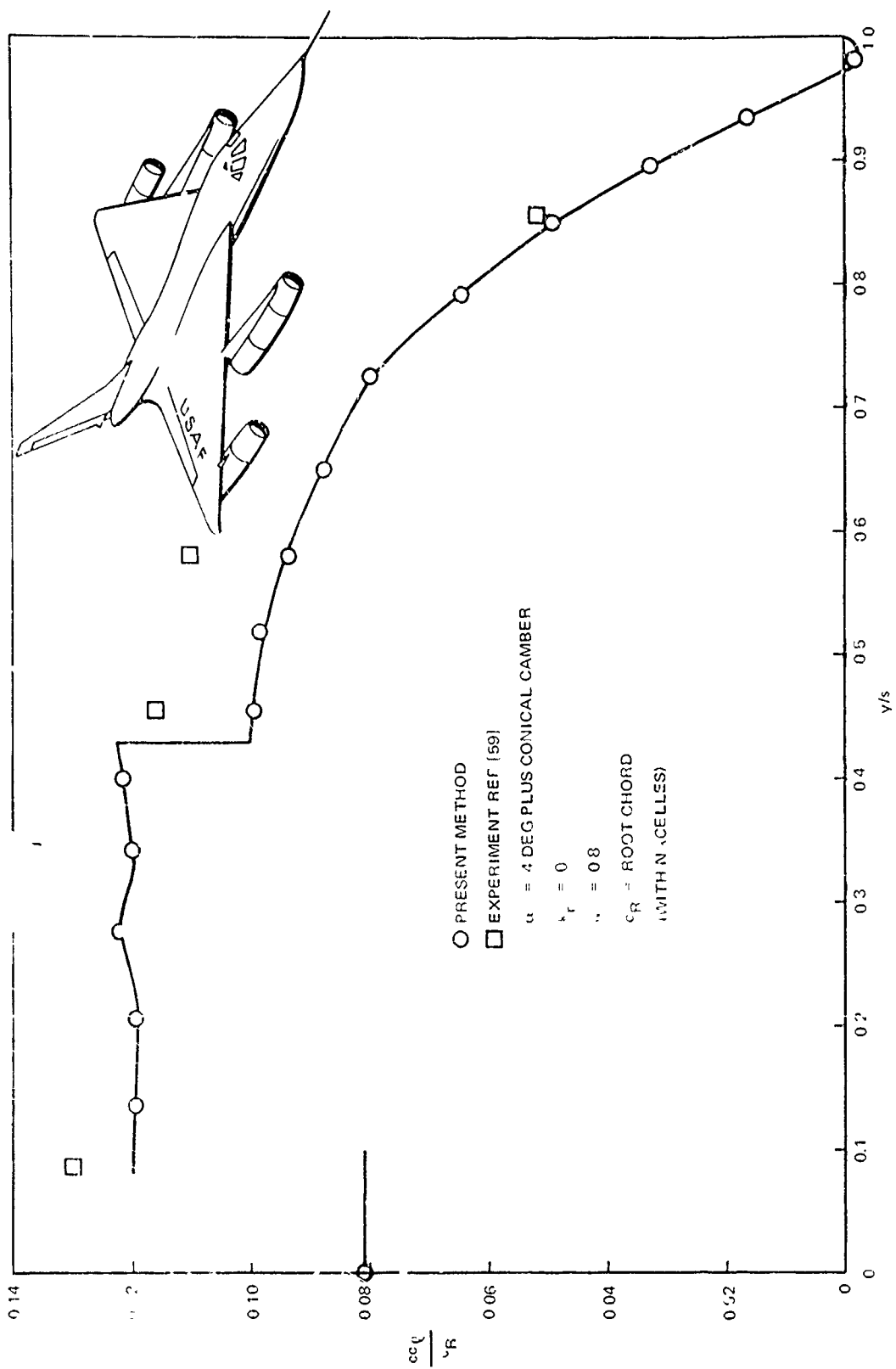


Figure 59. Comparison of Experimental and Calculated Span Loading for the B-58 Aircraft with Nacelles.

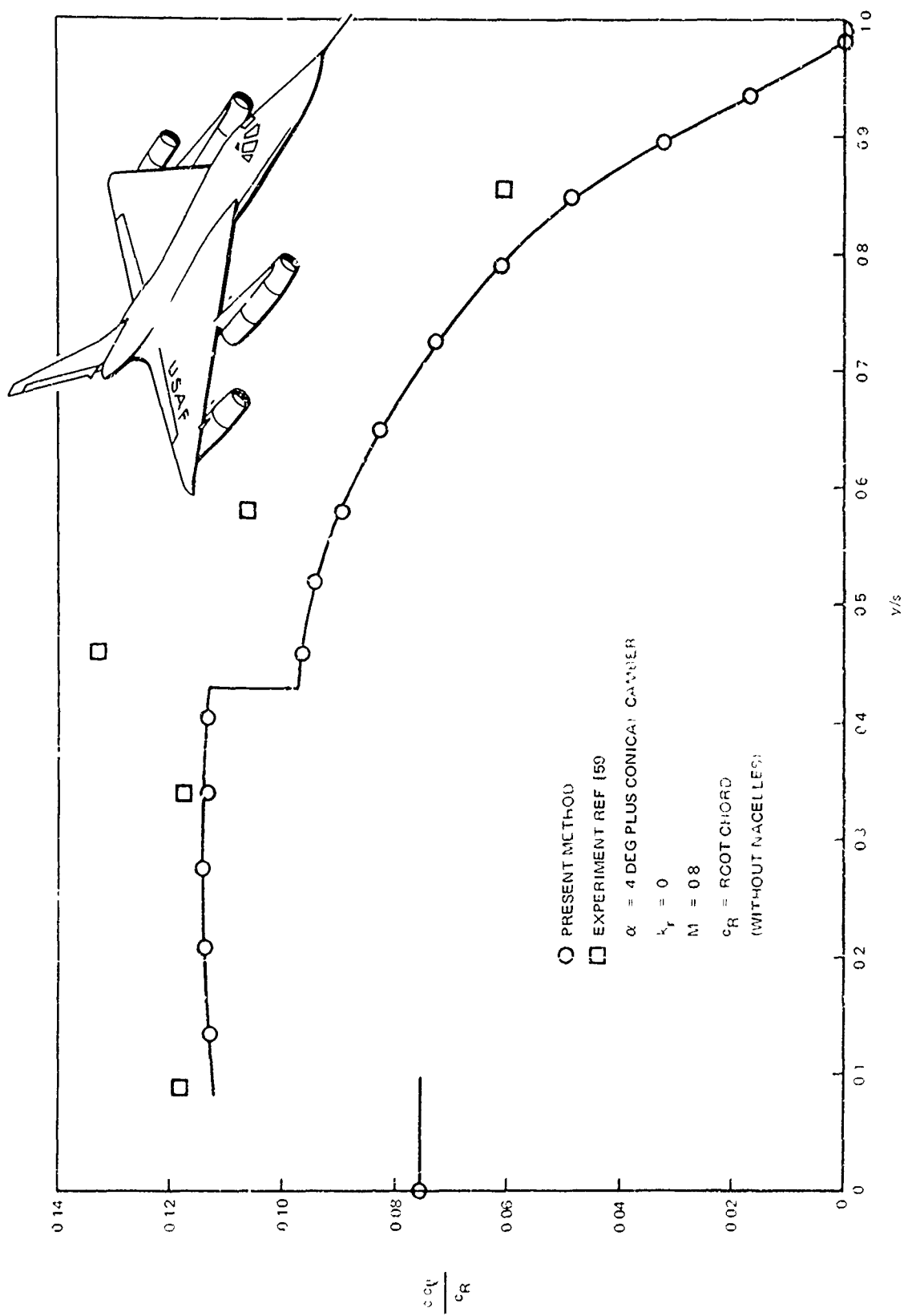


Figure 60. Comparison of Experimental and Calculated Span Loading for the B-58 Aircraft without Nacelles.

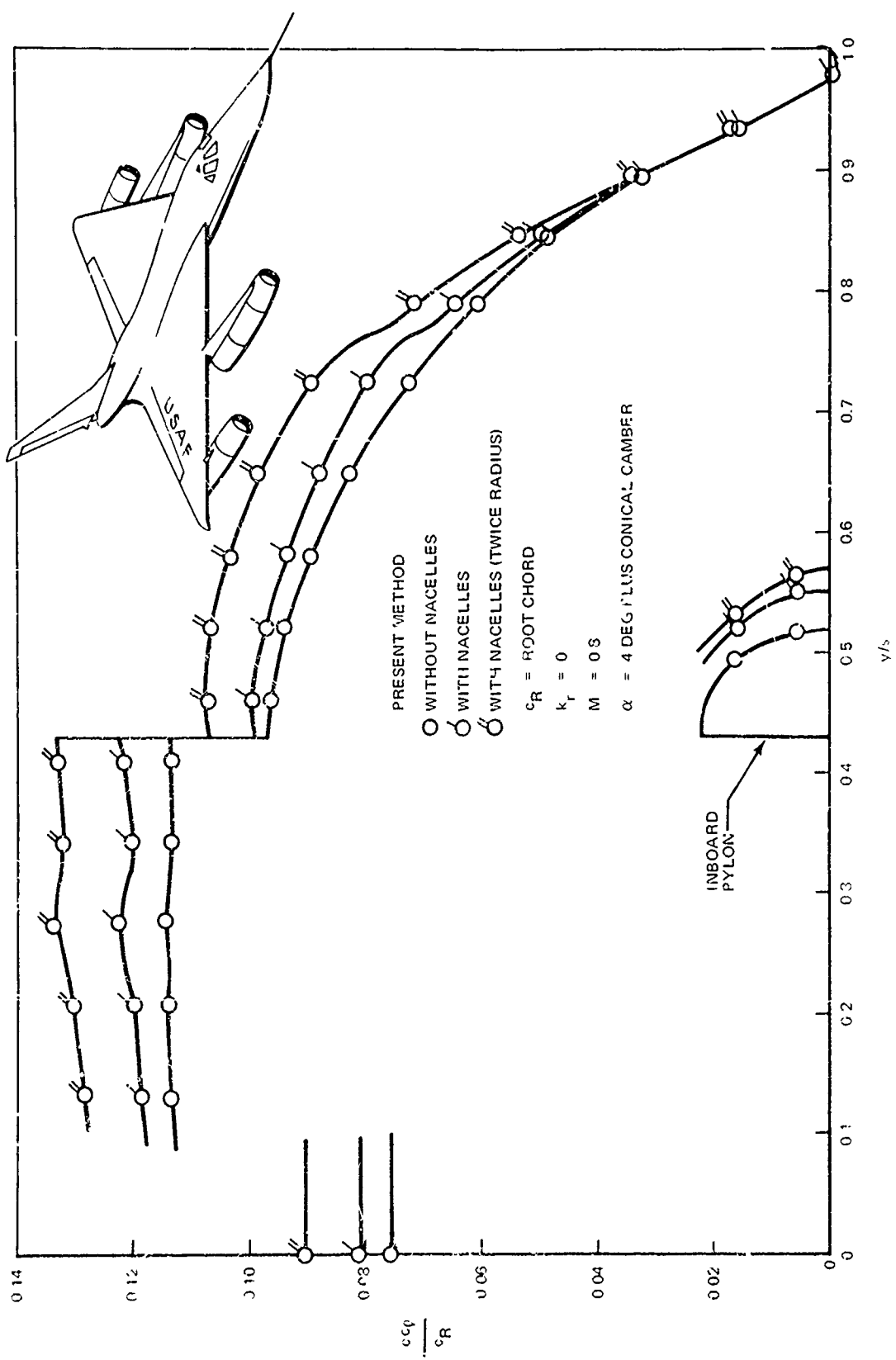


Figure 61. Comparison of The Span Loading on the B-58 Aircraft for Various Nacelle Diameters.

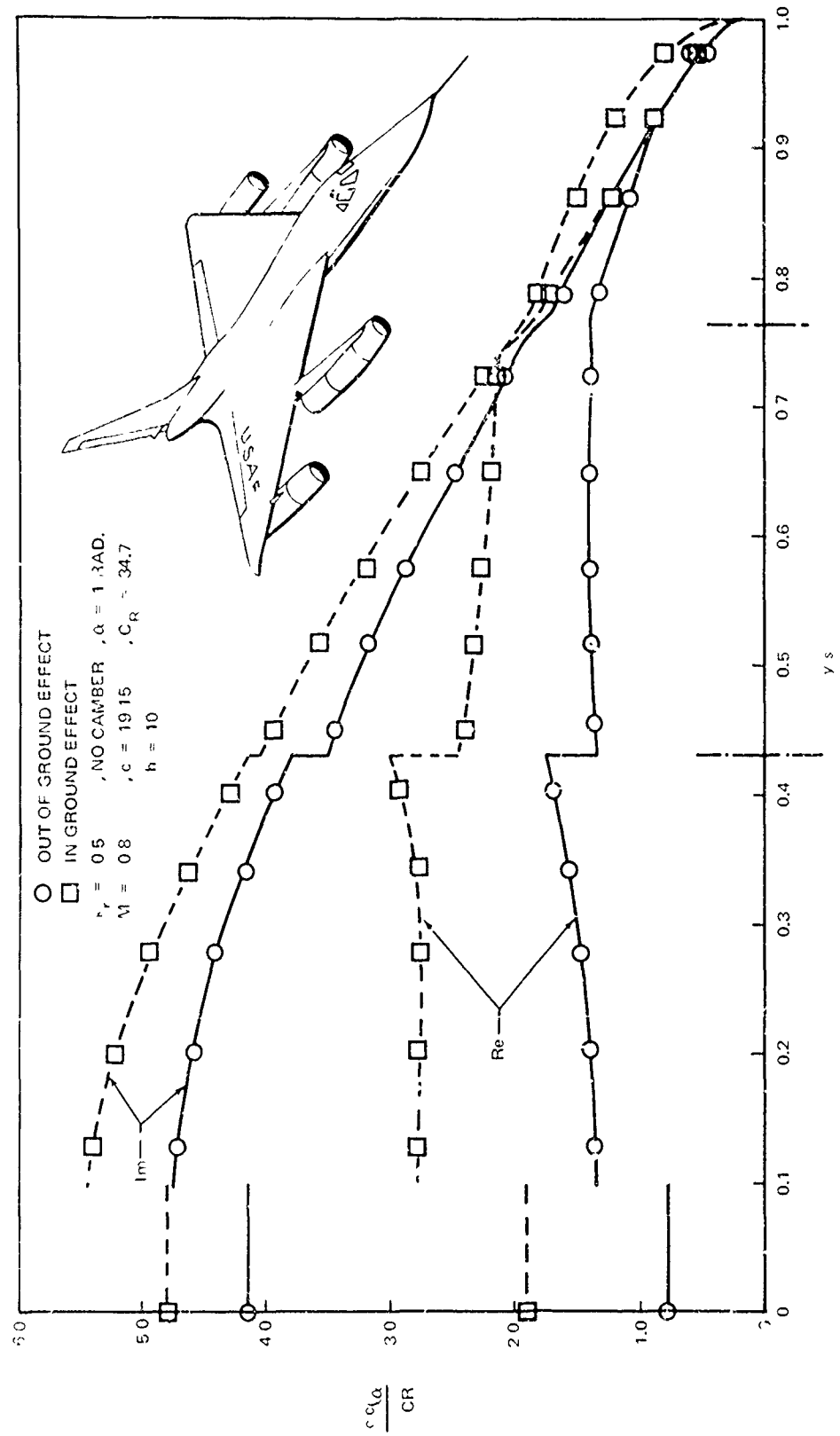


Figure 62. Comparison of the Span Loading on the B-53 Aircraft as Calculated with and without Ground Effect in Unsteady Pitch.

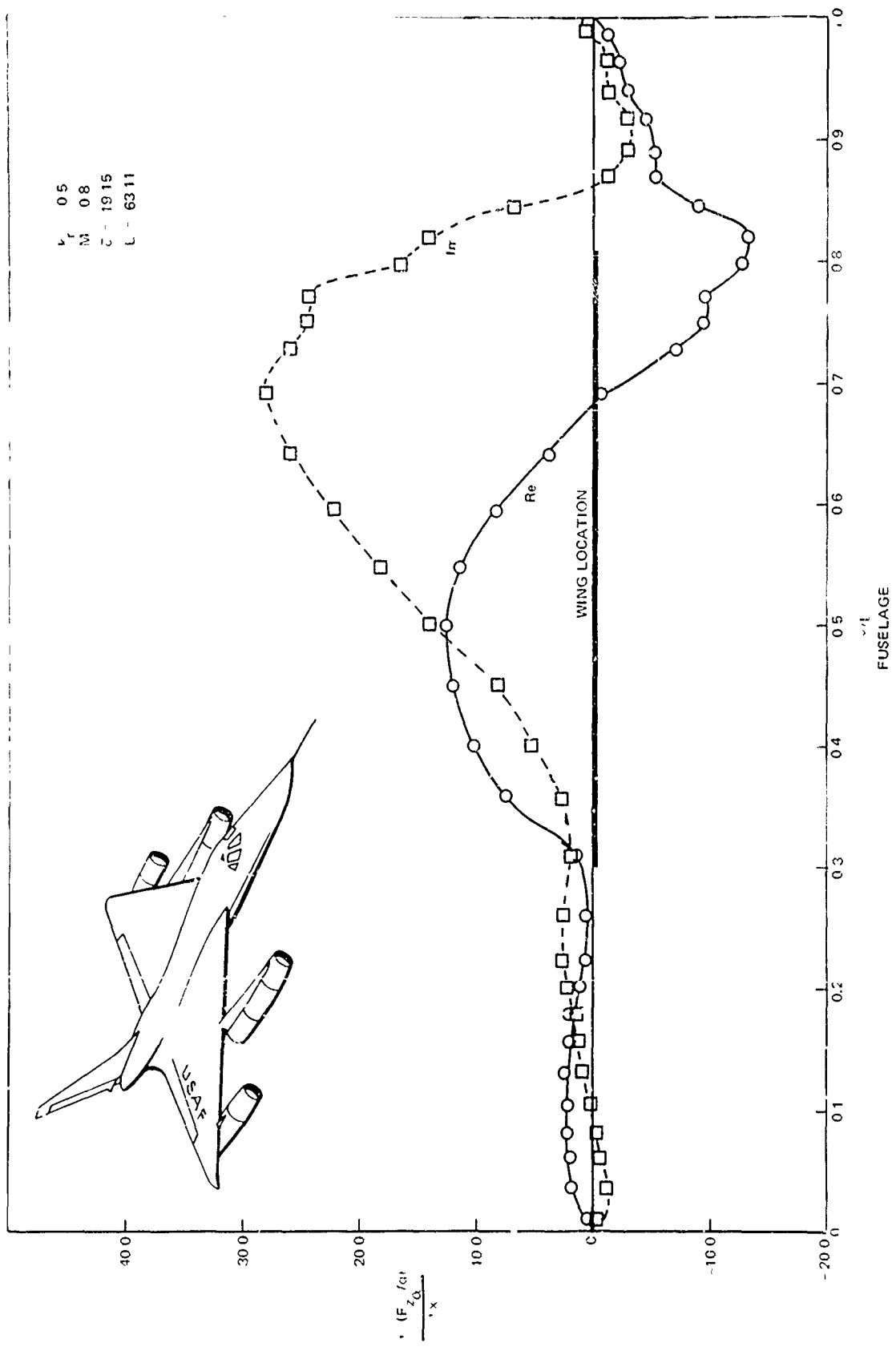


Figure 63. Fuselage Axial Loading for the B-58 Aircraft in Unsteady Pitch.

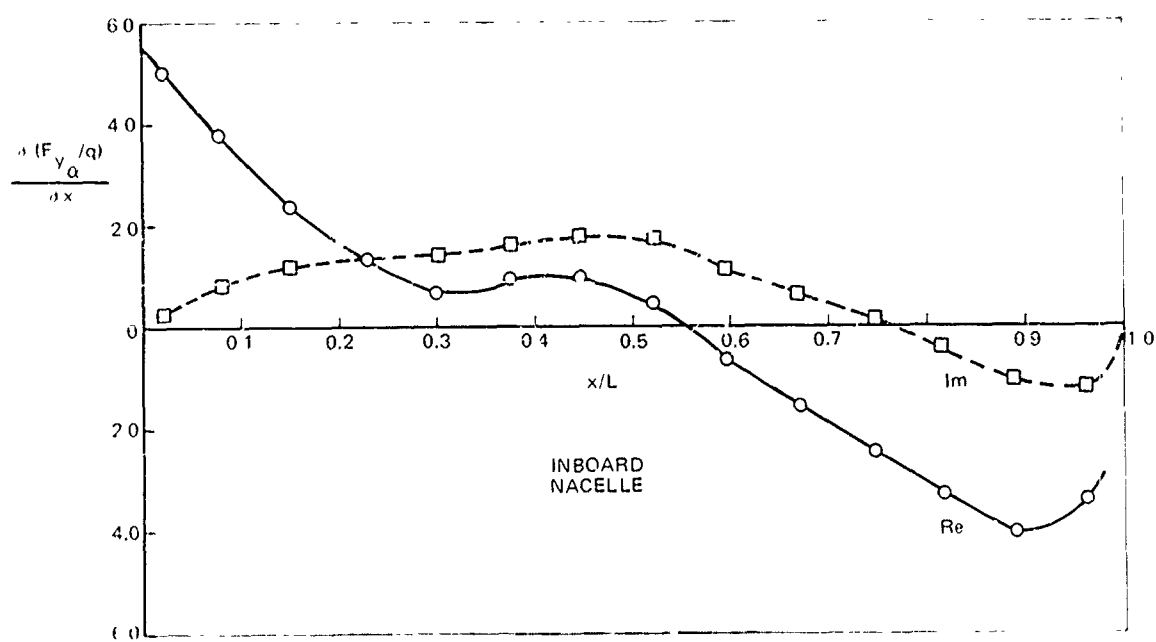
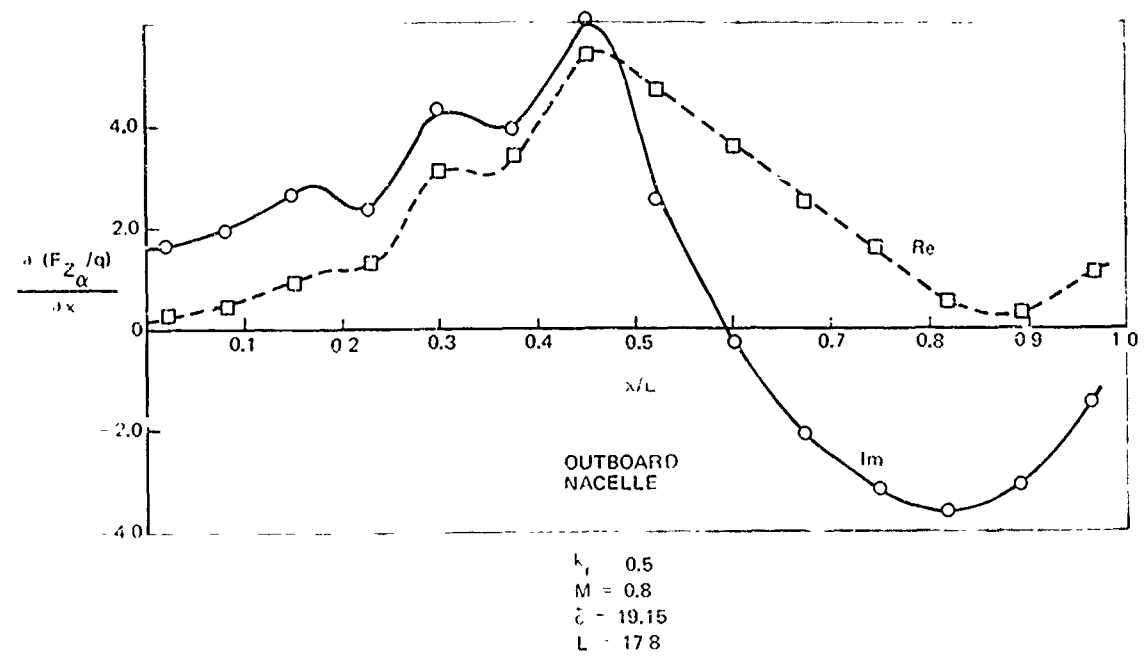


Figure 64. Nacelle Axial Loading for the B-58 Aircraft in Unsteady Pitch.

APPENDIX A. BASIC SINGULARITIES

The basic differential equation governing the potential in compressible isentropic flow is:

$$\beta^2 \bar{\phi}_{xx} + \bar{\phi}_{yy} + \bar{\phi}_{zz} = -\frac{\omega^2}{a^2} \bar{\phi} + \frac{2iM\omega}{a} \bar{\phi}_x \quad (A-1)$$

where $\beta^2 = 1 - M^2$ for subsonic flow and where $\psi = \bar{\phi} e^{-i\omega t}$ for oscillatory flow.

The first step in the solution of (A-1) is to define ψ as follows:

$$\psi = \bar{\phi} e^{-i\lambda M x} \quad (A-2)$$

This equation reduces (A-1) to

$$\psi_{xx} + \frac{1}{\beta^2} (\psi_{yy} + \psi_{zz}) = -\lambda^2 \psi \quad (A-3)$$

$$\text{when } \lambda = \omega M / \beta^2 U_\infty \quad (A-4)$$

An elementary source solution, ψ^* , for (A-3) for outgoing waves is:

$$\psi^* = \frac{e^{-i\lambda R}}{R} \quad (A-5)$$

where

$$R = \sqrt{(x - \xi)^2 + \beta^2 r^2}$$

$$r = \sqrt{(y - \eta)^2 + (z - \zeta)^2}$$

Applying Green's theorem to the lifting surfaces using (A-5) as the elementary solution gives:

$$\psi = \frac{1}{4\pi} \iint_S \Delta \psi(\xi, \eta, \zeta) - \frac{\partial \psi^*}{\partial N} ds \quad (A-6)$$

where S represents a surface over which $\Delta\psi$ is distributed and where $e^{-i\lambda}\partial/\partial N$ represents a point oscillatory compressible doublet oriented normal to the surface (\vec{N}). Using the relation between ψ and $\bar{\phi}$, given in (A-2), in Equation (A-6) gives the final expression for $\bar{\phi}$ in terms of $\Delta\bar{\phi}$.

$$\bar{\phi} = \frac{1}{4\pi} \iint_S \Delta\bar{\phi} e^{i\lambda M(x-\xi)} - \frac{\partial}{\partial N} \left(\frac{e^{-i\lambda R}}{R} \right) ds \quad (A-7)$$

$$\text{Since } i\lambda(M(x-\xi) - R) = -i\frac{\omega}{U_\infty}(x-\xi) + i\frac{\omega}{U_\infty\beta^2}(x-\xi - MR)$$

equation (A-7) can be rewritten as:

$$\bar{\phi}(x, y, z) = \frac{1}{4\pi} \iint_S \Delta\bar{\phi}(\xi, \eta, \zeta) L_\phi ds \quad (A-8)$$

$$\text{where } L_\phi = e^{-i\frac{\omega}{U_\infty}(x-\xi)} - \frac{\partial}{\partial N} \left(\frac{e^{i\frac{\omega}{U_\infty\beta^2}(x-\xi-MR)}}{R} \right)$$

and where $\Delta\bar{\phi} = \bar{\phi}_{\text{upper}} - \bar{\phi}_{\text{lower}}$

This is the final expression for the potential in terms of the potential jump distribution on the surface "S". The term L represents a point doublet, oriented normal to the surface (in the \vec{N} direction).

The expression for the linearized pressure is

$$\bar{c}_p = \frac{-2}{U_\infty} (\bar{\phi}_\infty + i\frac{\omega}{U_\infty} \bar{\phi}) \quad (A-9)$$

$$c_p = \text{Re } \bar{c}_p e^{i\omega t}$$

The terms $\bar{\phi}_x$ and $\bar{\phi}$ each satisfy Equation (A-1). The pressure coefficient $\Delta \bar{C}_p$ then satisfies the equation also. To obtain a solution for \bar{C}_p simply replace $\bar{\phi}$ by \bar{C}_p in Equation (A-3).

$$\bar{C}_p(x, y, z) = \frac{i}{4\pi} \iint -\Delta \bar{C}_p(\xi, \eta, \zeta) e^{-i \frac{\omega}{U_\infty} (x-\xi)} \frac{\partial}{\partial N} \left(\frac{e^{i \frac{\omega}{U_\infty} \beta Z}}{R} \right) ds \quad (A-10)$$

The minus sign in front of $\Delta \bar{C}_p$ indicates a difference in the definition of Δ , i.e., the difference between upper and lower surface quantities. For $\bar{\phi}$

$$\Delta \bar{\phi} = \bar{\phi}_{(\text{upper})} - \bar{\phi}_{(\text{lower})}$$

However for \bar{C}_p

$$\Delta \bar{C}_p = C_p(\text{lower}) - C_p(\text{upper})$$

Thus

$$\Delta \bar{C}_p = \frac{2}{U_\infty} (\Delta \bar{\phi}_x + \frac{i\omega}{U_\infty} \Delta \bar{\phi}) \quad (A-11)$$

Equation (A-10) will give the pressure field anywhere in the fluid due to a pressure loading distribution on the surface "S". Normally $\Delta \bar{C}_p$ is unknown. An integral equation for $\Delta \bar{C}_p$ can be formed if an expression relating potential or velocity to $\Delta \bar{C}_p$ can be found.

Consider the expression for the pressure (A-9). In terms of ψ the pressure is

$$\bar{C}_p = \frac{2}{U_\infty} (-\psi_x + i \frac{\lambda}{M} \omega) e^{i \lambda M x}$$

Define an acceleration potential such that

$$\Omega = \psi e^{i \frac{\lambda}{M} x}$$

The expression for \bar{C}_p is then:

$$\bar{C}_p = -\frac{2}{U_\infty} \Omega_x e^{-i \frac{\omega}{U_\infty} x} \quad (A-12)$$

Placing (A-12) into (A-10), on the right-hand-side gives:

$$\Omega_x = -\frac{U_\infty}{8\pi} \iint_S \Delta \bar{C}_p (\xi \eta \zeta) e^{i \frac{\omega}{U_\infty} \xi} \frac{\partial}{\partial N} \left(\frac{e^{i \frac{\omega}{U_\infty} \beta^2 (x-\xi-MR)}}{P} \right) ds$$

Integrating both sides of this equation with respect to x from $-\infty$ to x gives:

$$\Omega(x, y, z) - \Omega(-\infty) = \frac{U_\infty}{8\pi} \iint_S \Delta \bar{C}_p e^{i \frac{\omega \xi}{U_\infty}} \int_{-\infty}^x \frac{\partial}{\partial N} \left(\frac{e^{i \frac{\omega}{U_\infty} \beta^2 (\bar{x}-\xi-MR)}}{P} \right) d\bar{x} ds$$

where \bar{x} is the dummy integration variable, and $\Omega(-\infty)$ is zero. It can easily be shown that

$$\Omega = \bar{\phi} e^{i \frac{\omega}{U_\infty} x} \quad (A-13)$$

Substituting this equation in the expression for $\Omega - \Omega(-\infty)$ and making the change of variable $t = \bar{x} - \xi$ gives:

$$\bar{\phi} = \frac{U_\infty}{8\pi} \iint_S \Delta \bar{C}_p K \phi ds \quad (A-14)$$

$$K \phi = \left\{ -i \frac{\omega}{U_\infty} (x - \xi) \int_{-\infty}^{x-\xi} \frac{\partial}{\partial N} \left(\frac{i \frac{\omega}{U_\infty} \beta^2 (t - MR)}{R} \right) dt \right\}$$

$$\text{where } R = \sqrt{t^2 + \beta^2 r^2}$$

The boundary conditions on the body surface can usually be given in terms of velocity at the general point x, y, z in the direction normal to the surface

$$\frac{\bar{w}}{U_\infty} = \frac{\nabla \bar{\phi}}{U_\infty} \cdot \vec{n} = \frac{1}{8\pi} \iint \Delta \bar{C}_p K ds \quad (A-15)$$

$$K = \nabla \bar{\phi} \cdot \vec{n}$$

The term K is the usual kernel function.

It is often stated that if the acceleration or pressure potential is used (Equation (A-13) or (A-14)) then the wake need not be considered since the surface, S , over which the integration is performed does not include the wake. The wake, of course, is present. In fact each pressure doublet (of strength $\Delta \bar{C}_p$) contains its own wake. The wake is in actuality a line doublet of strength $e^{-i\frac{\omega}{U_\infty}(\xi - \xi_0)}$ extending downstream from the point ξ_0 , to infinity. This is easily proven using Equation (A-8). The term L is the potential field due to a unit point doublet oriented in \vec{N} direction. The potential due to a continuous distribution of point doublets of strength $e^{-i\frac{\omega}{U_\infty}(\xi - \xi_0)}$ gives:

$$\int_{\xi_0}^{\infty} e^{-i\frac{\omega}{U_\infty}(\xi - \xi_0)} L_\phi(x - \xi, y - \eta, z - \varsigma, M, \omega) d\xi$$

which upon substitution for L becomes

$$e^{-i\frac{\omega}{U_\infty}(x - \xi_0)} \int_{\xi_0}^{\infty} \frac{\partial}{\partial N} \left(\frac{e^{i\frac{\omega}{U_\infty}\beta^2(x - \xi - MR)}}{R} \right) d\xi$$

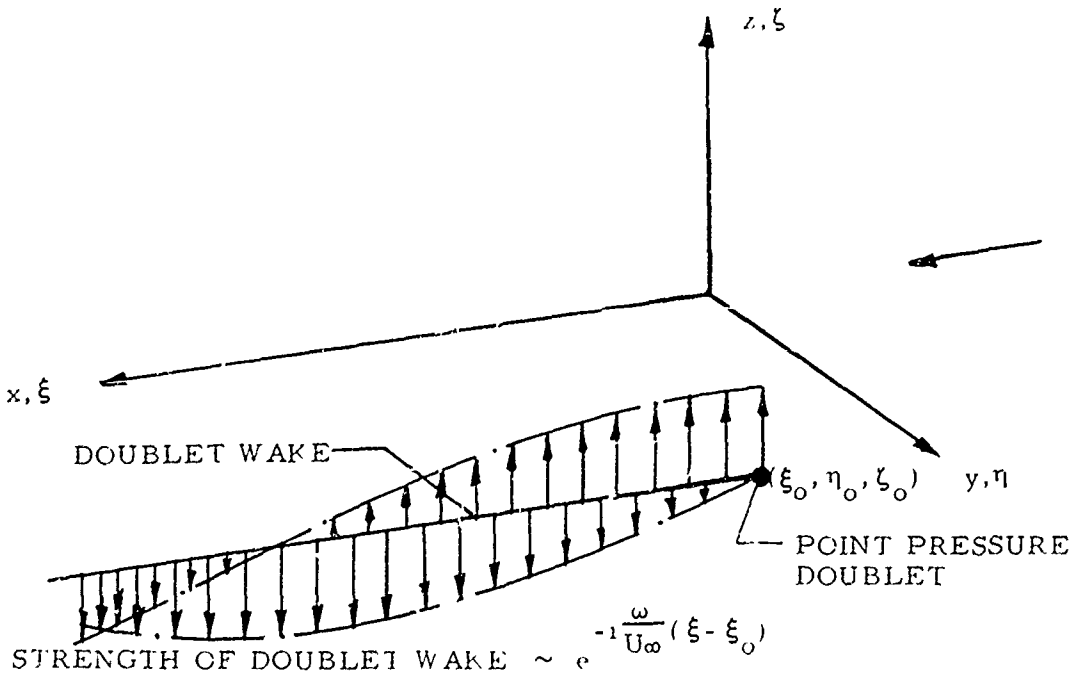
Making the transformation $t = x - \xi$ gives

$$+ e^{-i\frac{\omega}{U_\infty}(x-\xi_0)} \int_{-\infty}^{x-\xi_0} \frac{\partial}{\partial N} \left(\frac{i\frac{\omega}{U_\infty}\beta^2(t-MR)}{R} \right) dt$$

This expression is just $K\phi$ (Equation (A-14)). In summary then

$$\int_{\xi_0}^{\infty} e^{-i\frac{\omega}{U_\infty}(\xi-\xi_0)} L_\phi d\xi = K\phi \quad (A-16)$$

This proves that the point pressure doublet is in actuality a line doublet of varying strength ($e^{-i\frac{\omega}{U_\infty}(\xi-\xi_0)}$) extending from the point ξ_0 to downstream infinity. See Sketch A-1.



SKETCH A-1

Modified Acceleration Potential Approach

One further type of singularity that will be of use is the modified acceleration potential. Equation (A-13) gives

$$\Omega = \bar{\phi} e^{i \frac{\omega}{U_\infty} x}$$

or for surface distributions

$$\Delta\Omega = \Delta\bar{\phi} e^{i \frac{\omega}{U_\infty} \xi}$$

If a modified acceleration potential is introduced, then

$$\Delta\bar{Q} = \frac{2}{U_\infty} \Delta\Omega e^{-i \frac{\omega}{U_\infty} \xi_c} \quad (A-17)$$

where ξ_c is a known function of ξ . Solving for $\Delta\bar{\phi}$ in terms of $\Delta\bar{Q}$ gives:

$$\Delta\bar{\phi} = \frac{U_\infty}{2} \Delta\bar{Q} e^{-i \frac{\omega}{U_\infty} (\xi - \xi_c)} \quad (A-18)$$

Placing this expression into Equation (A-8) gives:

$$\begin{aligned} \bar{\phi} &= \frac{U_\infty}{8\pi} \iint_S \Delta\bar{Q} e^{-i \frac{\omega}{U_\infty} (\xi - \xi_c)} L_\phi ds \\ \bar{\phi} &= \frac{1}{8\pi} \iint \Delta\bar{Q} L_Q ds \end{aligned} \quad (A-19)$$

where

$$L_Q = U_\infty e^{-i \frac{\omega}{U_\infty} (\xi - \xi_c)} L_\phi \quad (A-20)$$

The pressure $\Delta\bar{C}_p$ may be found using $\Delta\bar{Q}$ in Equation (A-12) as follows:

$$\Delta\bar{C}_p = \left(\Delta\bar{Q} e^{i \frac{\omega \xi_c}{U_\infty}} \right)_\xi e^{-i \frac{\omega \xi}{U_\infty}} \quad (A-21)$$

where

$$\Delta\bar{Q} = \bar{Q}_{\text{lower}} - \bar{Q}_{\text{upper}}$$

Axial Distributions

Thus far only surface distributions have been considered. In order to solve body problems axial distributions of singularities must be used. Consider the three types of surface distributions studied so far: velocity potential, pressure and acceleration potential.

$$\bar{\Phi} = \frac{1}{4\pi} \iint \Delta \bar{\Phi} L_\phi ds \quad (A-22)$$

$$\bar{\Phi} = \frac{1}{8\pi} \iint \Delta \bar{C}_p K_\phi ds \quad (A-23)$$

$$\bar{\Phi} = \frac{1}{8\pi} \iint \Delta \bar{Q} L_Q ds \quad (A-24)$$

In order to convert these into axial distributions the surface distributions must be considered as lumped into a line at $\eta = \eta_a$, $\zeta = \zeta_a$. Thus

$$\Delta \bar{\Phi} = \delta(\eta - \eta_a, \zeta - \zeta_a) \mu(\xi) \quad (A-25)$$

$$\Delta \bar{C}_p = \delta(\eta - \eta_a, \zeta - \zeta_a) f(\xi) \quad (A-26)$$

$$\Delta \bar{Q} = \delta(\eta - \eta_a, \zeta - \zeta_a) \tilde{\mu}(\xi) \quad (A-27)$$

where $\delta(\eta - \eta_a, \zeta - \zeta_a)$ is a delta function acting at the body axis η_a, ζ_a with the units of length. Placing these values into the surface integrals above gives:

$$\bar{\Phi} = \frac{1}{4\pi} \int \mu(\xi) L_\phi (\eta - \eta_a, \zeta - \zeta_a) d\xi \quad (A-28)$$

$$\bar{\Phi} = \frac{1}{8\pi} \int f(\xi) K_\phi (\eta - \eta_a, \zeta - \zeta_a) d\xi \quad (A-29)$$

$$\bar{\Phi} = \frac{1}{8\pi} \int \tilde{\mu}(\xi) L_Q (\eta - \eta_a, \zeta - \zeta_a) d\xi \quad (A-30)$$

As the frequency goes to zero $\tilde{\mu}(\xi)$ becomes $\mu(\xi)$.

$$\lim_{\omega \rightarrow 0} \tilde{\mu}(\xi) \rightarrow \mu(\xi)$$

$$L_Q \rightarrow L_\phi$$

APPENDIX B. DISCRETIZATION OF SURFACE AND AXIAL INTEGRALS

Equations (A-22) and (A-25) may be discretized as follows:

$$\bar{\phi} = \frac{1}{4\pi} \sum_{s=1} \Delta\phi_s \iint_{\Delta S_s} L_\phi ds , \quad \text{surface} \quad (B-1)$$

$$\bar{\phi} = \frac{1}{4\pi} \sum_{s=1} \mu_s \int_{\Delta \xi_s} L_\phi (\eta - \eta_a, \zeta - \zeta_a) d\xi , \quad \text{axis} \quad (B-2)$$

The terms ΔS_s and $\Delta \xi_s$ indicate small elements of area and axial length, respectively. In steady flow the integral over the small area ΔS_s produces a vortex quadrilateral, i.e., a vortex that lies along the parameter of the element. This type of element possesses no wake; therefore, for a lifting surface, a wake must be added. The integral over a small axial element produces a line doublet the length of the element.

Equations (A-23) and (A-26) may be discretized as follows:

$$\bar{\phi} = \frac{1}{8\pi} \sum_{s=1} \Delta \bar{C}_p s \Delta \xi \int_{\Delta \bar{\eta}} K_\phi (\xi = \xi_{1/4}) d\bar{\eta} , \quad \text{surface} \quad (B-3)$$

$$\bar{\phi} = \frac{1}{8\pi} \sum_{s=1} f_s \Delta \xi K_\phi (\xi = \xi_{1/4}, \eta = \eta_a, \zeta = \zeta_a) , \quad \text{axis} \quad (B-4)$$

The term $\Delta \bar{\eta}$ indicates the width of the surface element in the plane of the element. The longitudinal integration is performed by lumping the value of the integrand at the 1/4-chord point of the element. The length of the element is $\Delta \xi$ for both the surface and axial line integral. The 1/4-chord line of the element may be swept, therefore,

$$\xi_{1/4} = \xi_{1/4} (\bar{\eta})$$

In steady flow the surface integral produces a horseshoe vortex whose bound portion lies along the 1/4-chord line of each element. This integral is the basis of the Vortex-Lattice Method in steady flow and the Doublet-Lattice Method in unsteady flow. The axial integral produces a semi-infinite line

doublet whose origin lies at the 1/4-chord point of the element. The discretizations given in Equations(B-1), (B-2), (B-3) and (B-4) are consistent with each other even though a simpler technique was employed for Equations (B-3) and (B-4). A system of vortex quadrilaterals covering a surface and wake can be made into a horseshoe vortex system covering only the surface and vice versa. Similarly, a system of finite length axial doublets can be made into a semi-infinite axial doublet system.

Equations (A-24) and (A-27) may be discretized as follows:

$$\bar{\phi} = \frac{1}{8\pi} \sum_{s=1} \Delta \bar{Q}_s \iint_{\Delta S_s} L_Q ds , \quad \text{surface} \quad (B-5)$$

$$\bar{\phi} = \frac{1}{8\pi} \sum_{s=1} \tilde{\mu}_s \int_{\Delta \xi_s} L_Q (\eta = \eta_a, \zeta = \zeta_a) d\xi , \quad \text{axis} \quad (B-6)$$

The integrations over the small area and line segments could be performed as they stand; however, further analysis will show that these integrals can be built up of expressions previously derived. Consider first the axis integral where the actual limits ξ_1 and ξ_2 (leading and trailing edges of the element $\Delta \xi_s$) have been introduced. Define the axial integral as I_{rs} where

$$I_{rs} = \int_{\xi_1 s}^{\xi_2 s} L_{Q_{rs}} d\xi \quad (B-7)$$

Using the expression for L_Q given in Equation (A-20) gives:

$$I_{rs} = \int_{\xi_1 s}^{\xi_2 s} e^{-i\omega U_\infty (\xi - \xi_c)} L_\phi d\xi$$

The term ξ_c is a known function of ξ . Define ξ_c as the center of the element s , where

$$\xi_c = \frac{\xi_1 s + \xi_2 s}{2} , \quad \xi_1 s \leq \xi \leq \xi_2 s \quad (B-8)$$

The function $\xi_c(\xi)$ is then a series of step functions. The integral I_{rs} may be split into two parts:

$$I_{rs} = \int_{\xi_1 s}^{\infty} \left\{ \cdot \cdot \cdot \right\} d\xi - \int_{\xi_2 s}^{\infty} \left\{ \cdot \cdot \cdot \right\} d\xi$$

$$I_{rs} = e^{-i\frac{\omega}{U_\infty}(\xi_1 s - \xi_c s)} \int_{\xi_1 s}^{\infty} e^{-i\frac{\omega}{U_\infty}(\xi - \xi_1 s)} L_\phi d\xi \quad (B-9)$$

$$- e^{-i\frac{\omega}{U_\infty}(\xi_2 s - \xi_c s)} \int_{\xi_2 s}^{\infty} e^{-i\frac{\omega}{U_\infty}(\xi - \xi_2 s)} L_\phi d\xi$$

Reference to Equation (A-16) shows that

$$\left. \begin{aligned} \int_{\xi_1 s}^{\infty} e^{-i\frac{\omega}{U_\infty}(\xi - \xi_1 s)} L_\phi d\xi &= K_\phi(x - \xi_1 s, \dots) \\ \int_{\xi_2 s}^{\infty} e^{-i\frac{\omega}{U_\infty}(\xi - \xi_2 s)} L_\phi d\xi &= K_\phi(x - \xi_2 s, \dots) \end{aligned} \right\} \quad (B-10)$$

Thus

$$I_{rs} = e^{i\frac{\omega}{U_\infty} \frac{\Delta \xi_s}{2}} K_\phi(x - \xi_1 s, \dots) - e^{-i\frac{\omega}{U_\infty} \frac{\Delta \xi_s}{2}} K_\phi(x - \xi_2 s, \dots) \quad (B-11)$$

The K_ϕ terms possess wakes but the integral I must not possess a wake. The wake of the first term in Equation (B-11) is cancelled by the wake of the second term. This equation represents a short segment of doublet strength, which varies like $e^{-i\frac{\omega}{U_\infty}(\xi - \xi_c)}$, that lies between ξ_1 and ξ_2 . (In Sketch 2.6-1 the double arrows indicate that two equal but opposite wake strengths exist at one point.) This expression can also be used in the double integral of Equation (B-5).

$$\bar{\Phi} = \frac{1}{4\pi} \sum_{s=1} \Delta \bar{Q}_s \int_{\bar{\eta}} I_{rs} d\bar{\eta} , \quad \text{surface} \quad (B-12)$$

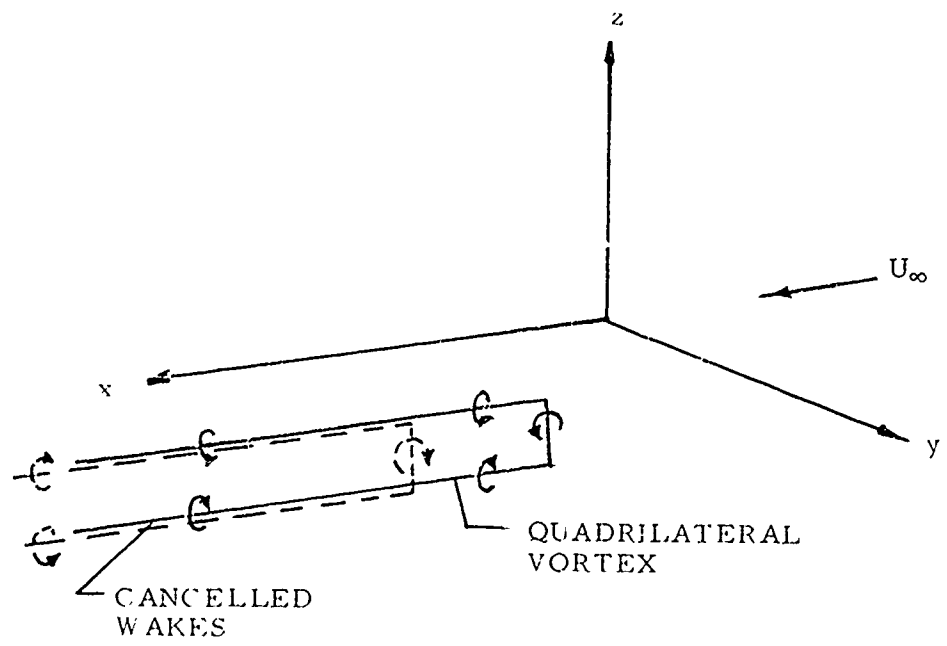
$$\bar{\Phi} = \frac{1}{4\pi} \sum_{s=1} \tilde{\mu}_s I_{rs} , \quad \text{axis} \quad (B-13)$$

The surface integral, given in Equation (B-12) by the integral of I_{rs} , represents an unsteady quadrilateral vortex composed of two unsteady horseshoe vortices (see Sketch (B-1)). If Equation (B-11) is placed into Equations (B-12) and (B-13) and it is assumed that $\Delta\xi_s$ is not a function of $\bar{\eta}$, then

$$\bar{\phi} = \frac{1}{4\pi} \sum_{s=1} \Delta \bar{Q}_s \left\{ e^{i \frac{\omega \Delta \xi_s}{2 U_\infty}} \int_{\bar{\eta}}^{\frac{\omega \Delta \xi_s}{2 U_\infty}} K_\phi(x - \xi_{1s}, \dots) d\bar{\eta} \right. \\ \left. - e^{-i \frac{\omega \Delta \xi_s}{2 U_\infty}} \int_{\bar{\eta}}^{-i \frac{\omega \Delta \xi_s}{2 U_\infty}} K_\phi(x - \xi_{2s}, \dots) d\bar{\eta} \right\}, \quad \text{surface} \quad (B-14)$$

$$\phi = \frac{1}{4\pi} \sum_{s=1} F_s \left\{ e^{i \frac{\omega \Delta \xi_s}{2 U_\infty}} K_\phi(x - \xi_{1s}, \dots) \right. \\ \left. - e^{-i \frac{\omega \Delta \xi_s}{2 U_\infty}} K_\phi(x - \xi_{2s}, \dots) \right\}, \quad \text{axis} \quad (B-15)$$

The first integral of Equation (B-14) is an unsteady horseshoe vortex lying along the line $\xi = \xi_1$, while the second integral is an unsteady horseshoe vortex lying along the line $\xi = \xi_2$ (compare Equations (A-40) and (A-41) with (B-3) and (B-4)). If the element length $\Delta\xi_s$ does vary with $\bar{\eta}$ it is an easy matter to place it within the integrals and handle it in the same way as K_ϕ itself is handled.



SKETCH B-1.

APPENDIX C. IMAGE POINTS

Circular Bodies

The flow about a circle in the presence of a singularity may be solved using Thompson's Circle Theorem (see Milne-Thompson, Reference (43)). This theorem states that if $f(Z)$, ($Z = y + iz$), is the onset flow complex potential of the singularity then the total flow potential is given by $F(Z)$ as

$$F(Z) = f(Z) + \bar{f}(a^2/Z) \quad (C-1)$$

if the circle is located at the origin of coordinates. The term $\bar{f}(a^2/Z)$ is the flow necessary to render the circle a streamline in the presence of the onset flow $f(Z)$. The term $\bar{f}(a^2/Z)$ is the potential due to the image singularity. If $f(Z)$ is the potential due to a vortex located at ξ then

$$f(Z) = -\frac{i\Gamma}{2\pi} \ln(Z - \xi)$$

and

$$\begin{aligned} \bar{f}(a^2/Z) &= -\frac{i\Gamma}{2\pi} \ln \left(\frac{a^2}{Z} - \bar{\xi} \right) \\ &= -\frac{i\Gamma}{2\pi} \left\{ \ln \left(Z - \frac{a^2}{\bar{\xi}} \right) - \ln \left(-Z/\bar{\xi} \right) \right\} \end{aligned}$$

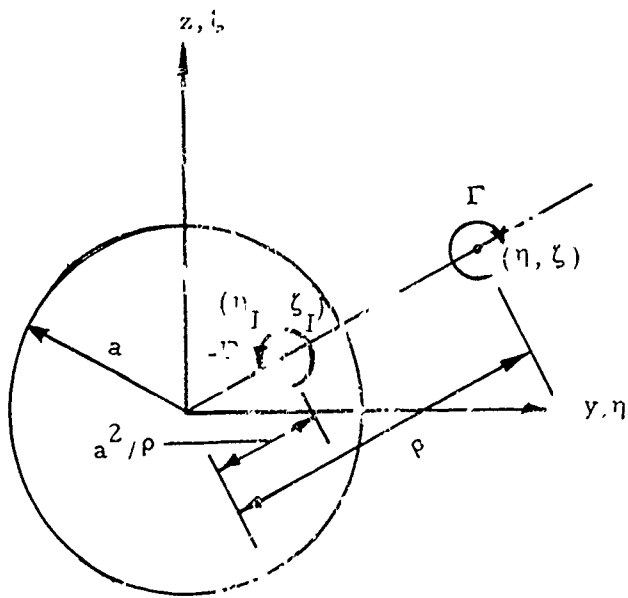
The first log term is the usual image and the second term is a vortex located at the center of the circle. This vortex is expendable since it does not affect the flow normal to ξ , the circle boundary. The result is:

$$\text{image Potential } \bar{f}(a^2/Z_1) = -\frac{i\Gamma}{2\pi} \ln \left(Z - \frac{a^2}{\bar{\xi}} \right)$$

The image vortex is of opposite sign of the exterior vortex and the location of the image vortex is at $+a^2/\bar{\zeta}$

$$\begin{aligned} \text{Image Strength} &= -\Gamma & (C-2) \\ \text{Image Location} &= a^2/\bar{\zeta} = \frac{a^2}{\rho^2} \zeta \\ \rho &= |\zeta| \end{aligned}$$

The sketch shows the image location



SKETCH C-1

Applying the Circle theorem for the point source singularity gives for the image potential:

$$\bar{f}(a^2/Z) = \frac{\sigma}{2\pi} \left(\ln(Z - \frac{a^2}{\bar{\zeta}}) - \ln Z - \ln\left(\frac{-1}{\bar{\zeta}}\right) \right)$$

The very last log term is a constant and may be ignored. The middle log term may not be ignored since it affects the flow about the circle. It represents a sink at the origin. The final solution for a source requires two images; one at the usual image point and one at the origin.

$$\begin{aligned} \text{Image Strength} &= +\sigma \\ \text{Image Location} &= \frac{a^2}{\rho^2} \zeta \end{aligned} \quad \left. \begin{array}{l} \\ \end{array} \right\} \text{first image} \quad (C-3)$$

$$\begin{aligned} \text{Image Strength} &= -\sigma \\ \text{Image Location} &= 0 \end{aligned} \quad \left. \begin{array}{l} \\ \end{array} \right\} \text{second image}$$

The sink at the origin simply keeps the circle from producing a net outward flux of fluid.

The doublet potential is

$$f(Z) = -\frac{\mu}{2\pi} \frac{1}{Z-\zeta}$$

The image potential is

$$\bar{f}(a^2/Z) = -\frac{\bar{\mu}}{2\pi} \left(\frac{1}{\frac{a^2}{Z} - \bar{\zeta}} \right) \quad (C-4)$$

If we wish this potential to go to zero at infinity then the following constant must be added:

$$C = -\frac{\bar{\mu}}{2\pi} \frac{1}{\bar{\zeta}}$$

Adding C to $\bar{f}(a^2/Z)$ gives:

$$\bar{f}(a^2/Z) = -\frac{(-\bar{\mu})}{2\pi} \frac{a^2}{\bar{\zeta}^2} \left(\frac{1}{Z - a^2/\bar{\zeta}} \right)$$

Thus for doublets

$$\begin{aligned} \text{Image Strength} &= -\bar{\mu} \frac{a^2}{\bar{\zeta}^2} \\ \text{Image Location} &= (a^2/\rho^2) \zeta \end{aligned} \quad (C-5)$$

Elliptical Bodies

For any body other than a circle the image approach does not furnish an exact solution. It may however furnish usable approximations if suitably modified. Borland, Reference (35), suggests a generalization of the image approach, for vortices, through a transformation. Specifically, the circle-ellipse transformation is applied to the exterior vortex and image vortex positions. The position of the image vortex, ζ_I , with reference to the exterior vortex in the ellipse or physical plane is

$$\zeta_I = \frac{r^4 + \frac{1}{4} K^2 (\bar{\zeta} + \sqrt{\bar{\zeta}^2 - 4K^2})^2}{\frac{1}{2} r^2 (\bar{\zeta} + \sqrt{\bar{\zeta}^2 - 4K^2})} \quad (C-6)$$

where $r = \frac{a+b}{2}$

$$K^2 = \frac{1}{4} (a^2 - b^2)$$

where a and b are the semi-major and semi-minor axes, respectively.

This formula possesses a restriction on the location of the exterior vortex. If the exterior vortex point ζ lies outside the ellipse

$$\frac{\zeta^2}{\left(\frac{r^2}{|K|} - \frac{K^2}{r^2} |K|\right)^2} + \frac{\eta^2}{\left(\frac{r^2}{|K|} - \frac{K^2}{r^2} |K|\right)^2} = 1 \quad (C-7)$$

then the image point will fall on the wrong Riemann sheet. Thus vortex images may be considered only for vortices lying within the ellipse given in (C-7). If $K \rightarrow 0$, i. e., a circle, the ellipse of (C-7) becomes infinitely large and thus all vortex points may be considered.

A generalization of this approach for doublets must include a variation in image doublet strength in addition to the variation in location. If a doublet is constructed of two vortices of equal and opposite strength

located at ζ and $\zeta + \Delta\zeta$ then there exists an image doublet located at ζ_I and $\zeta_I + \Delta\zeta_I$.

$$\mu = -\Gamma \Delta\zeta_i, \quad \bar{\mu} = \Gamma \overline{\Delta\zeta}_i$$

$$\mu_I = \Gamma \Delta\zeta_{I-1} = \Gamma \frac{\Delta\zeta_I}{\Delta\zeta}, \quad \overline{\Delta\zeta}_i = +\bar{\mu} \frac{\Delta\zeta_I}{\Delta\zeta}$$

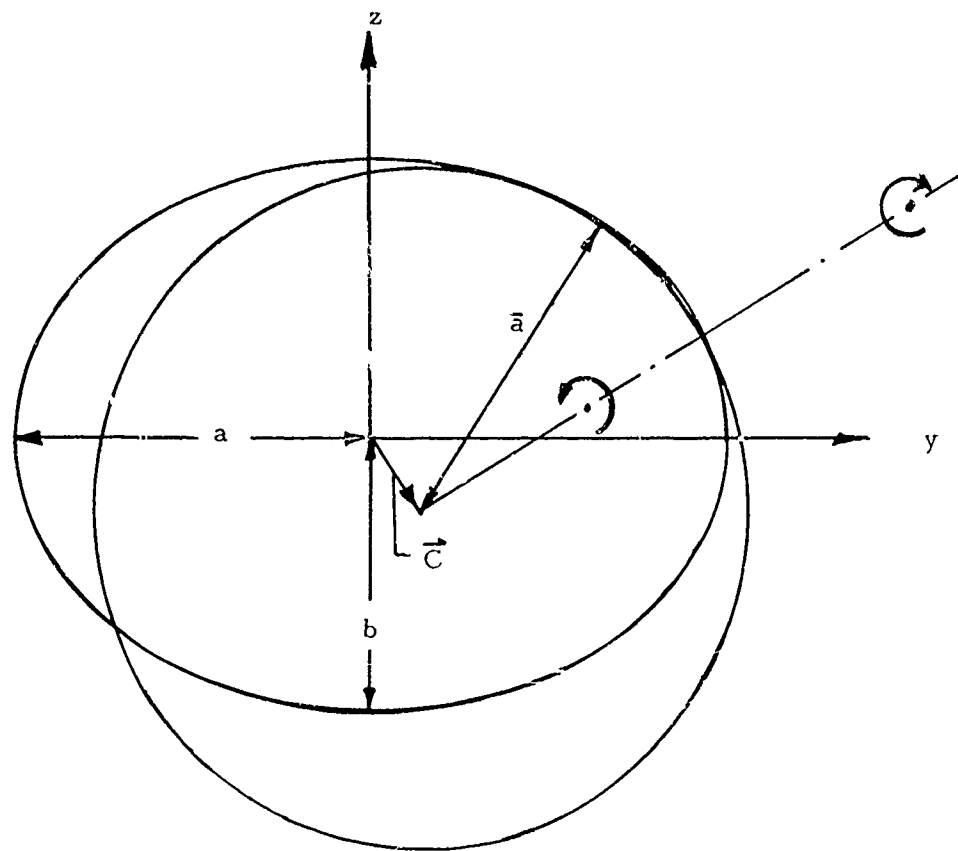
If the limit is taken then

$$\mu_I = \bar{\mu} \frac{d\zeta_I}{d\zeta} \quad (C-8)$$

For a circle $d\zeta_I/d\zeta = -a^2/\zeta^2$ and this is exactly the solution given in (C-5) Differentiating Equation (C-6) gives:

$$\frac{d\zeta_I}{d\zeta} = \frac{-r^4 + \frac{1}{4}K^2 \left(\zeta + \sqrt{\zeta^2 - 4K^2} \right)^2}{\frac{1}{2}r^2 \left(\zeta + \sqrt{\zeta^2 - 4K^2} \right)} \left(\frac{1}{\sqrt{\zeta^2 - 4K^2}} \right) \quad (C-9)$$

A second and more easily understood approach is to define an equivalent circle for each singularity (vortex, doublet, source). The equivalent circle has the correct curvature of the ellipse at a particular point. Sketch C-2 shows an example.



SKETCH C-2

The curvature of the surface of an ellipse ($1/\bar{a}$) is

$$\frac{1}{\bar{a}} = \left| \frac{d^2 y}{ds^2} \hat{j} + \frac{d^2 z}{ds^2} \hat{k} \right| \quad (C-10)$$

where $\frac{d^2 y}{ds^2} = \frac{-a \cos \theta b^2}{(a^2 \sin^2 \theta + b^2 \cos^2 \theta)^2}$

$$\frac{d^2 z}{ds^2} = \frac{-b \sin \theta a^2}{(a^2 \sin^2 \theta + b^2 \cos^2 \theta)^2}$$

where the angular measure θ is defined implicitly as

$$y = a \cos \theta$$

$$z = b \sin \theta \quad (C-11)$$

The result for \bar{a} is

$$\bar{a} = \frac{(a^2 \sin^2 \theta + b^2 \cos^2 \theta)^{3/2}}{ab} \quad (C-12)$$

The vector to the center of the circle with radius \bar{a} is:

$$\vec{c} = \vec{r} - \vec{n} \bar{a}$$

where \vec{r} is the vector to the point on the ellipse and where the radius of curvature is \bar{a} . The vector \vec{n} is the normal vector at the same point and is given as

$$\vec{n} = \left(\frac{d^2 y}{ds^2} \vec{j} + \frac{d^2 z}{ds^2} \vec{k} \right) \bar{a}$$

The result is:

$$\vec{c} = \vec{r} \left(\frac{a^2 - b^2}{a} \right) \cos^3 \theta + \vec{j} \left(\frac{b^2 - a^2}{b} \right) \sin^3 \theta \quad (C-13)$$

This curve is called the "evolute of the ellipse".

APPENDIX D. LONGITUDINAL INTEGRATION OF THE SURFACE
PRESSURE, ON A BODY OF ARBITRARY
CROSS SECTION, FOR FORCE AND MOMENT

The expression for the pressure field due to a point pressure doublet is:

$$C_p(x, y, z) = \frac{\Delta C_p(\xi, \eta, \zeta) \delta A}{4\pi} e^{i\lambda M} \times \frac{\partial}{\partial N} \left(\frac{e^{-i\lambda R}}{R} \right) \quad (D-1)$$

where δA is the elemental area over which the load ΔC_p acts. The coordinates ξ, η, ζ define the location of the pressure point and \vec{N} its direction. Also,

$$\lambda = \frac{\omega M}{\beta^2 U_\infty}$$

$$R = \sqrt{(x - \xi)^2 + \beta^2 r^2}$$

$$r = \sqrt{(y - \eta)^2 + (z - \zeta)^2}$$

This pressure must be integrated over the entire body to give the lift and moment.

$$\frac{\delta F}{q} = \oint \int_{-\infty}^{\infty} C_p dx \vec{n} \cdot \vec{i}_F ds \quad (D-2a)$$

$$\frac{\delta M}{q} = - \oint \int_{-\infty}^{\infty} C_p x dx \vec{n} \cdot \vec{i}_F ds \quad (D-2b)$$

The term $\vec{n} \cdot \vec{i}_F$ is not a function of x since a constant cross section body has been assumed. The vector \vec{n} is the outward normal to the body cross section and has components in the y and z directions only. The vector \vec{i}_F denotes the direction of F and is used to determine the direction of M .

$$M = M (\vec{i}_F \cdot \vec{k}) + N (\vec{i}_F \cdot \vec{j})$$

where M and N are positive nose up and nose right respectively. It is assumed, without loss of generality, that the origin is located at the pressure doublet and that the moments are taken about the origin.

Substituting Eq. (D-1) into (D-2a) and using the transformation $t = x/\beta r$ gives:

$$\frac{\delta F}{q} = \frac{\Delta C_p \delta A}{4\pi} \oint \frac{\partial}{\partial N} I \vec{n} \cdot \vec{i}_F ds \quad (D-3)$$

where

$$I = \int_{-\infty}^{\infty} \frac{e^{i\lambda\beta r(Mt - \sqrt{t^2 + 1})}}{\sqrt{t^2 + 1}} dt$$

Making the substitution $\beta u = \sqrt{t^2 + 1} - Mt$ and $(\lambda\beta r)\beta = \frac{\omega Mr}{U_\infty} = \bar{k}$ gives:

$$\begin{aligned} I &= - \int_{t=-\infty}^{t=\infty} \frac{e^{-i\bar{k}u}}{\sqrt{u^2 - 1}} \text{sign}(t - \frac{M}{\beta}) du \\ &= -2 \int_1^\infty \frac{e^{-i\bar{k}u}}{\sqrt{u^2 - 1}} du = \pi [Y_0(\bar{k}) + i J_0(\bar{k})] \end{aligned}$$

This is just the Hankel function of the second kind times $i\pi$. Thus

$$I = i\pi H_0^{(2)}(\bar{k}) \quad (D-4)$$

where

$$\bar{k} = \frac{\omega r}{U_\infty} M$$

It can be shown that Eq. (D-4) is proportional to the two-dimensional source potential for the unsteady wave equation. A direct method of arriving at (D-4) is outlined as follows:

$$I = \int_{-\infty}^{\infty} e^{i\lambda Mx} \frac{e^{-i\lambda R}}{R} dx$$

Let $\tau = x - \xi$. Then

$$I = \int_{-\infty}^{\infty} e^{i\lambda M(\tau + \xi)} \frac{e^{-i\lambda R}}{R} d\tau$$

Consider the two-dimensional source potential

$$\phi_{2-D} = \frac{\sigma}{4\pi} \int_{-\infty}^{\infty} e^{i\lambda Mx} \frac{e^{-i\lambda R}}{R} d\xi$$

which is obtained simply by integrating the point source along a line from $-\infty$ to $+\infty$. Again make the same transformation $\tau = x - \xi$.

$$\phi_{2-D} = \frac{\sigma}{4\pi} \left[\int_{-\infty}^{\infty} e^{i\lambda M(\tau + \xi)} \frac{e^{-i\lambda R}}{R} d\tau \right]$$

$$\phi_{2-D} = \frac{\sigma}{4\pi} I \quad (D-5)$$

The two-dimensional source solution is obtained from the two-dimensional unsteady wave equation:

$$r^2 \phi_{rr} + r \phi_r + \bar{k}^2 \phi = 0 \quad (D-6)$$

where oscillatory motion has been assumed. The source solution of (D-6) for outgoing waves is:

$$\phi = \frac{i}{4} H_o^{(2)}(\bar{k}) \quad (D-7)$$

Thus from (D-7) and (D-5) we obtain the results of Eq. (D-4).

Substituting (D-4) back into (D-3) gives the proper expression for the force.

$$\frac{\delta F}{q} = \frac{\Delta C_p \delta A}{4\pi} \oint i\pi \frac{\partial H_o^{(2)}(\bar{k})}{\partial \bar{k}} \frac{\partial \bar{k}}{\partial N} \cdot \vec{i}_F ds \quad (D-8)$$

where

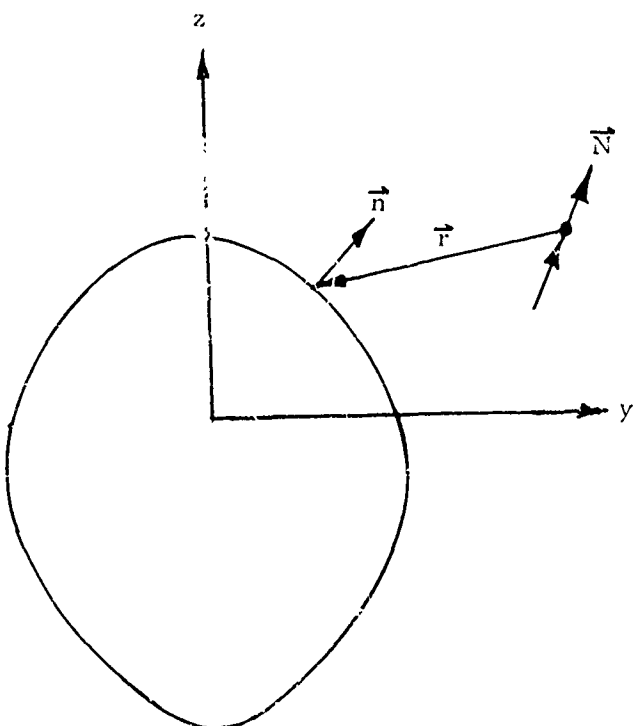
$$\frac{\partial H_o^{(2)}(\bar{k})}{\partial \bar{k}} = -H_1^{(2)}(\bar{k})$$

$$\frac{\partial \bar{k}}{\partial N} = \frac{\omega M}{U_\infty} \frac{\partial r}{\partial N} - \frac{\bar{k}}{r} \vec{i}_r \cdot \vec{N}$$

placing these into (D-8) gives:

$$\frac{\delta F}{q} = \frac{\Delta C_p \delta A}{2\pi} \oint \left[-\frac{i\pi}{2} \bar{k} H_J^{(2)}(\bar{k}) \right] \frac{\vec{i}_r \cdot \vec{N}}{\vec{n} \cdot \vec{i}_F} ds \quad (D-9)$$

where \vec{i}_r is the two-dimensional radial unit vector from the pressure point to a point on the body cross section (see sketch D-1) on which the circuit integral is to be taken. In the steady case ($\bar{k} \rightarrow 0$) the bracketed term approaches unity.



Sketch D-1

The expression for the moment is now considered.

$$\frac{\delta \vec{M}}{q} = -\frac{\Delta C_p \delta A}{4\pi} \oint \frac{\partial}{\partial N} I_m \vec{n} \vec{i}_F ds \quad (D-10)$$

where

$$I_m = \beta r \int_{-\infty}^{\infty} t \frac{e^{i\lambda\beta r (Mt - \sqrt{t^2 + 1})}}{\sqrt{t^2 + 1}} dt$$

The term I_m can be obtained from I as follows:

$$I_m = \left. \frac{\beta r}{i\lambda\beta r} \cdot \frac{\partial I}{\partial M} \right|_{\lambda\beta r = \text{const.}} \quad (D-11)$$

Now $I = i\pi H_0^{(2)}(\bar{k})$ and $\lambda\beta r = \bar{k}/\beta$; thus

$$\left. \frac{\partial I}{\partial M} \right|_{\frac{\bar{k}}{\beta} = \text{const.}} = -i\pi H_1^{(2)}(\bar{k}) \left. \frac{\partial \bar{k}}{\partial M} \right|_{\frac{\bar{k}}{\beta} = \text{const.}} \quad (D-12)$$

$$\left. \frac{\partial \bar{k}}{\partial M} \right|_{\frac{\bar{k}}{\beta} = \text{const.}} = \left. \frac{\partial \beta}{\partial M} \right|_{\text{const.}} = -\frac{M}{\beta} \frac{\bar{k}}{\beta} \quad (D-13)$$

Placing (D-13) into (D-12) and the result into (D-11) gives:

$$\begin{aligned} I_m &= \frac{\beta r}{i\bar{k}/\beta} \left(-i\pi H_1^{(2)}(\bar{k}) \right) \left(\frac{-M}{\beta^2} \frac{\bar{k}}{\beta} \right) \\ &= r M \pi H_1^{(2)}(\bar{k}) \end{aligned} \quad (D-14)$$

Placing this result into Eq. (D-10) gives

$$\begin{aligned}
 \frac{\delta \vec{M}}{q} &= -\frac{\Delta C_p \delta A}{4\pi} \oint r \frac{\partial}{\partial r} [r M \pi H_1^{(2)}(\bar{k})] \frac{\vec{i}_r \cdot \vec{N}}{r} \vec{n} \cdot \vec{i}_F ds \\
 r \frac{\partial}{\partial r} [r M \pi H_1^{(2)}(\bar{k})] &= r M \pi \left[H_1^{(2)}(\bar{k}) + \bar{k} \frac{\partial H_1^{(2)}(\bar{k})}{\partial \bar{k}} \right] \\
 &= r M \pi [\bar{k} H_0^{(2)}(\bar{k})] \tag{D-15}
 \end{aligned}$$

The final expression for the moment is then:

$$\begin{aligned}
 \frac{\delta \vec{M}}{q} &= -\frac{\Delta C_p \delta A}{2\pi} \oint [r M \frac{\pi}{2} \bar{k} H_0^{(2)}(\bar{k})] \frac{\vec{i}_r \cdot \vec{N}}{r} \vec{n} \cdot \vec{i}_F ds \tag{D-16} \\
 &= -\frac{\Delta C_p \delta A}{4\pi} \int M \pi [H_1^{(2)} + \bar{k} \frac{\partial H_1^{(2)}}{\partial \bar{k}}] \vec{i}_r \cdot \vec{N} \vec{n} \cdot \vec{i}_F ds
 \end{aligned}$$

In the steady case ($\bar{k} \rightarrow 0$) the bracketed term approaches zero like $\bar{k} \ln \bar{k}$.

Higher Order Moments

The n^{th} order moment is defined as

$$\frac{\delta \vec{M}_n}{q} = -\frac{\Delta C_p \delta A}{4\pi} \oint \frac{\partial}{\partial N} (I_n) \vec{n} \cdot \vec{i}_F ds$$

where

$$\begin{aligned}
 I_n &= \int_{-\infty}^{\infty} \frac{x^n e^{i\lambda(Mx - R)}}{R} dx \\
 &= \left(\frac{\beta r}{ik/\beta} \right)^n \frac{\partial^n}{\partial M^n} \Big|_{\bar{k}/\beta = \text{const.}} \quad (I)
 \end{aligned}$$

Consider the second order moment; $\delta \vec{M}_2/q$.

$$\begin{aligned}
 \frac{\partial I}{\partial M} &= i\pi \frac{M}{\beta^2} \bar{k} H_1^{(2)}(\bar{k}) \\
 \frac{\partial^2 I}{\partial M^2} &= i\pi \frac{\bar{k}}{\beta} \left\{ \frac{1}{\beta^3} M^2 H_1^{(2)}(\bar{k}) - \frac{M^2 \bar{k}}{\beta^3} H_0^{(2)}(\bar{k}) \right\} \\
 I_2 &= \frac{-i\pi r^2}{\bar{k}} \left\{ (1 + M^2) H_1^{(2)}(\bar{k}) - M^2 \bar{k} H_0^{(2)}(\bar{k}) \right\} \\
 \frac{r}{2} \frac{\partial I_2}{\partial r} &= -i \frac{\pi}{2} r \left\{ M \bar{k} r H_1^{(2)}(\bar{k}) + (1 + M^2) r H_0^{(2)}(\bar{k}) \right\}
 \end{aligned}$$

Finally the result for $\delta \vec{M}_2/q$ is :

(D-17)

$$\frac{\delta M_n}{q} = -\frac{\Delta C_p \delta A}{2\pi} \oint \frac{\vec{i}_r \cdot \vec{N}}{r} \vec{n} \cdot \vec{i}_F \left[-i \frac{\pi}{2} \left\{ M \bar{k} r^2 H_1^{(2)}(\bar{k}) + r^2 (HM^2) H_0^{(2)}(\bar{k}) \right\} \right] ds$$

For steady flow ($\bar{k} \rightarrow 0$) the Hankel Function $i \frac{\pi}{2} H_0^{(2)}(\bar{k}) \rightarrow \ln \bar{k} \rightarrow -\infty$. Thus the second order moment, is unusable. It seems obvious that higher order moments, where n is even, will also give results that are unbounded. The higher order moments, where n is odd, will give finite results since at $\bar{k} = 0$ the results are zero. Moments of higher order than one are of interest in determining generalized forces; however, as shown above this method cannot furnish them.

SUMMARY

$$\frac{\delta F}{q} = \frac{\Delta C_p \delta A}{2\pi} \oint f(\bar{k}) \frac{\vec{i}_r \cdot \vec{N}}{r} \vec{n} \cdot \vec{i}_F ds \quad (D-18)$$

$$\frac{\delta m}{q} = - \frac{\Delta C_p \delta A}{2\pi} \oint r p(\bar{k}) \frac{\vec{i}_r \cdot N}{r} \vec{n} \cdot \vec{i}_F ds \quad (D-19)$$

$$f(\bar{k}) = \frac{-i\pi}{2} \bar{k} H_1^{(2)}(\bar{k})$$

$$p(\bar{k}) = M \frac{\pi}{2} \bar{k} H_0^{(2)}(\bar{k})$$

$$\bar{k} = 2k_r M r / c$$

$$k_r = \frac{\omega c}{2U_\infty}$$

\vec{N} = direction of pressure doublet

\vec{i}_F = direction of F

\vec{r} = $\vec{i}_r + r$ = position vector from doublet to point on body cross section.

F = force in the direction of \vec{i}_F

M = moment normal to \vec{i}_F (positive nose up and nose right).

APPENDIX E. NUMERICAL EVALUATION OF THE FORCE AND MOMENT INTEGRALS

The expressions to evaluate are derived in Appendix D and are:

$$\delta F/q = \frac{\Delta c_p \delta A}{2\pi} \oint f(\bar{k}) \frac{\vec{i}_r \cdot \vec{N}}{r} \vec{n} \cdot \vec{i}_F ds \quad (E-1)$$

$$\delta M/q = \frac{-\Delta c_p \delta A}{2\pi} \oint P(\bar{k}) \vec{i}_r \cdot \vec{N} \vec{n} \cdot \vec{i}_F ds \quad (E-2)$$

The basic approach will be to break up the cross section into a series of elements over which $f(\bar{k})$ and $P(\bar{k})$ are assumed constant.

$$\delta F/q = \frac{\Delta c_p \delta A}{2\pi} \sum_{j=1}^N \int_{-e_j}^{e_j} \frac{\vec{i}_r \cdot \vec{N} \vec{n} \cdot \vec{i}_F}{r} ds \quad (E-3)$$

$$\delta M/q = \frac{\Delta c_p \delta A}{2\pi} \sum_{j=1}^N \int_{-e_j}^{e_j} \frac{\vec{i}_r \cdot \vec{N} \vec{n} \cdot \vec{i}_F}{r} ds \quad (E-4)$$

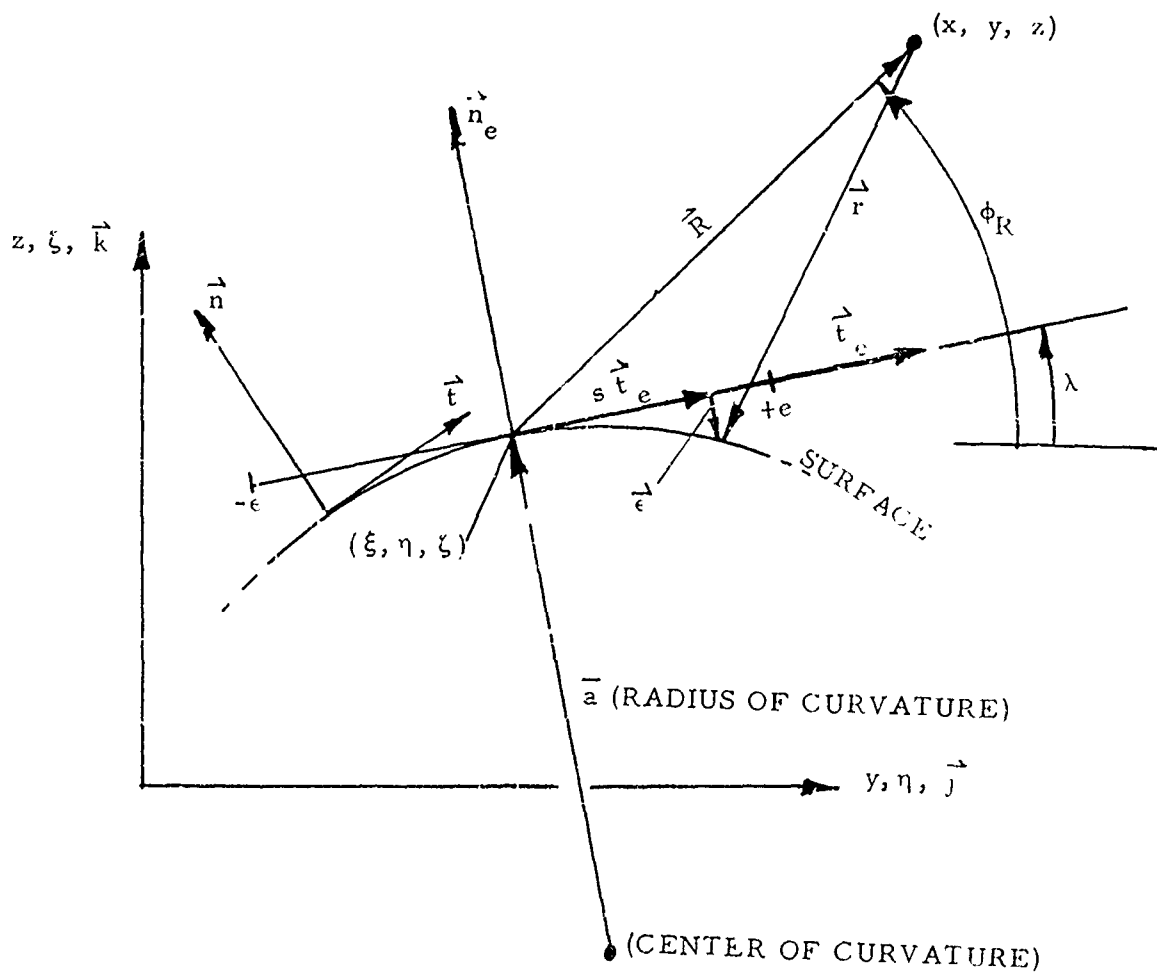
There are no singularities involved in the integrand of Equation (E-4); thus, a simple evaluation is permitted.

$$\delta M/q = \frac{\Delta c_p \delta A}{2\pi} \sum_{j=1}^N (\vec{i}_r \cdot \vec{N} \vec{n} \cdot \vec{i}_F) s=0 2e_j \quad (E-5)$$

Such is not the case for $\delta F/q$; As $r \rightarrow 0$ the integrand is singular like $1/r$ and thus care must be taken in its evaluation. As a matter of fact several procedures were tried and methods which ignored the curvature of the sub-elements were found to be inaccurate for field points (x, y, z) lying close to the cross section. The remainder of this appendix will be devoted to the evaluation of this singular integral which will be termed \bar{I} .

$$I = \int_{-e}^e \frac{\Delta \cdot \vec{N} \cdot \vec{n} \cdot \vec{i}_F}{r^2} ds \quad (E-6)$$

Expressions for \vec{r} , r^2 and \vec{n} may be derived referring to Sketch (E-1).



SKETCH E-1.

It is assumed that over each element the radius and center of curvature is constant. The first quantity to evaluate is \vec{r} . From Sketch (E-1) it is easy to see that:

$$\vec{R} + \vec{r} = s \vec{n}_e - \vec{\epsilon} \quad (E-7)$$

It is assumed that the element length is small compared with the radius of curvature. Thus

$$\vec{\epsilon} = \vec{n}_e \frac{s^2}{2a} \quad (E-8)$$

If terms of order s^2/a^2 and higher are neglected, then

$$\vec{n} = \vec{n}_e + \vec{t}_e \frac{s}{a} \quad (E-9)$$

Noting from the sketch that

$$\left. \begin{aligned} \vec{n}_e &= \vec{k} \cos \lambda - \vec{j} \sin \lambda \\ \vec{t}_e &= \vec{j} \cos \lambda + \vec{k} \sin \lambda \\ \vec{R} &= (y - \eta) \vec{j} + (z - \zeta) \vec{k} \end{aligned} \right\} \quad (E-10)$$

Then solving for \vec{r} in Equation (E-7) and \vec{n} in Equation (E-9), using (E-10), gives:

$$\begin{aligned} \vec{r} &= \vec{j} \left\{ -(y - \eta) + s \cos \lambda + \frac{s^2}{2a} \sin \lambda \right\} + \\ &\quad \vec{k} \left\{ -(z - \rho) + s \sin \lambda - \frac{s^2}{2a} \cos \lambda \right\} \end{aligned} \quad (E-11)$$

$$\vec{n} = \vec{j} \left\{ \frac{s}{a} \cos \lambda - \sin \lambda \right\} + \vec{k} \left\{ \frac{s}{a} \sin \lambda + \cos \lambda \right\} \quad (E-12)$$

Retaining terms linear in s^2/a gives

$$\frac{1}{r^2} = \frac{1}{s^2 + Bs + R^2} + \frac{s^2 D/a}{(s^2 + Bs + R^2)^2} \quad (E-13)$$

where

$$\left. \begin{aligned} D &= R \sin(\lambda - \phi_R) \\ B &= -2R \cos(\lambda - \phi_R) \end{aligned} \right\} \quad (E-14)$$

and where the angle ϕ_R is defined implicitly as follows

$$\left. \begin{aligned} R \cos \phi_R &= y - \eta \\ R \sin \phi_R &= z - \zeta \end{aligned} \right\} \quad (E-15)$$

The angle ϕ_R is shown in Sketch (E-1). If

$$\begin{aligned} \vec{N} &= \vec{j} N_y + \vec{k} N_z \\ \vec{i}_F &= \vec{j} i_{F_y} + \vec{k} i_{F_z} \end{aligned} \quad (E-16)$$

then the numerator of the integrand of Equation (E-6) is (retaining only terms linear in s^2/a)

$$\vec{r} \cdot \vec{N} \cdot \vec{n} \cdot \vec{i}_F = \frac{\bar{I}}{a} s^2 + (J + \frac{LR}{a}) s + RK \quad (E-17)$$

where

$$\begin{aligned} \bar{I} &= N_y i_{F_y} \left\{ \frac{3}{2} \cos^2 \lambda - \frac{1}{2} \right\} + N_z i_{F_y} \left\{ \frac{3}{2} \sin \lambda \cos \lambda \right\} \\ &+ N_z i_{F_z} \left\{ \frac{3}{2} \sin^2 \lambda - \frac{1}{2} \right\} + N_y i_{F_z} \left\{ \frac{3}{2} \sin \lambda \cos \lambda \right\} \end{aligned} \quad (E-18)$$

$$\begin{aligned} J &= N_y i_{F_y} \left\{ -\cos \lambda \sin \lambda \right\} + N_z i_{F_y} \left\{ -\sin^2 \lambda \right\} \\ &+ N_z i_{F_z} \left\{ \cos \lambda \sin \lambda \right\} + N_y i_{F_z} \left\{ \cos^2 \lambda \right\} \end{aligned} \quad (E-19)$$

$$\begin{aligned} L &= N_y i_{F_y} \left\{ -\cos \phi_R \cos \lambda \right\} + N_z i_{F_y} \left\{ -\sin \phi_R \cos \lambda \right\} \\ &+ N_z i_{F_z} \left\{ -\sin \phi_R \sin \lambda \right\} + N_y i_{F_z} \left\{ -\cos \phi_R \sin \lambda \right\} \end{aligned} \quad (E-20)$$

$$\begin{aligned} K &= N_y i_{F_y} \left\{ \cos \phi_R \sin \lambda \right\} + N_z i_{F_y} \left\{ \sin \phi_R \sin \lambda \right\} \\ &+ N_z i_{F_z} \left\{ -\sin \phi_R \cos \lambda \right\} + N_y i_{F_z} \left\{ -\cos \phi_R \cos \lambda \right\} \end{aligned} \quad (E-21)$$

For convenience let

$$\bar{J} = J + \frac{LR}{a} \quad (E-22)$$

Then

$$\vec{r} \cdot \vec{N} \vec{n} \cdot \vec{i}_F = \frac{I}{a} s^2 + \bar{J} s + R K \quad (E-23)$$

The integral I then becomes

$$\begin{aligned} I &= \int_{-e}^e \left\{ \frac{\bar{I}}{a} s^2 + \bar{J} s + R K \right\} \left\{ \frac{1}{s^2 + Bs + R^2} \right. \\ &\left. + \frac{s^2 D/a}{(R^2 + Bs + R^2)^2} \right\} ds \end{aligned} \quad (E-24)$$

Expansion for R/s > 1.0

When R/s is larger than 1.0 an expansion for large R/s is appropriate. Retaining terms of order $\frac{1}{R} \left(\frac{s}{R}\right)^4$ and lower gives:

$$\begin{aligned}
I &= 2K \left(\frac{e}{R} \right) + \frac{2}{3} \left(\frac{e}{R} \right)^3 \left[\bar{I} \frac{R}{\bar{a}} - \left(\frac{B}{R} \right) \bar{J} \right. \\
&\quad \left. + K \left(\frac{D}{\bar{a}} - 1 + \frac{B^2}{R^2} \right) \right] \\
&+ \frac{2}{5} \left(\frac{e}{R} \right)^5 \left[K \left\{ - \left(\frac{R}{\bar{a}} \right)^2 \frac{1}{4} + 1 - \frac{2D}{\bar{a}} + \frac{D^2}{\bar{a}^2} \right. \right. \\
&\quad \left. \left. - \frac{3B^2}{R^2} \left(1 - \frac{D}{R} \right) + \frac{B^4}{R^4} \right\} + \bar{J} \left\{ \frac{2B}{R} \left(1 - \frac{D}{\bar{a}} \right) - \frac{B^3}{R^3} \right\} \right. \\
&\quad \left. + \bar{I} \frac{R}{\bar{a}} \left\{ \frac{B^2}{R^2} - 1 + \frac{D}{\bar{a}} \right\} \right]
\end{aligned} \tag{E-25}$$

Specifically, Equation (E-25) is used when

$$(R/e) > 1.5$$

Inner or Exact Solution

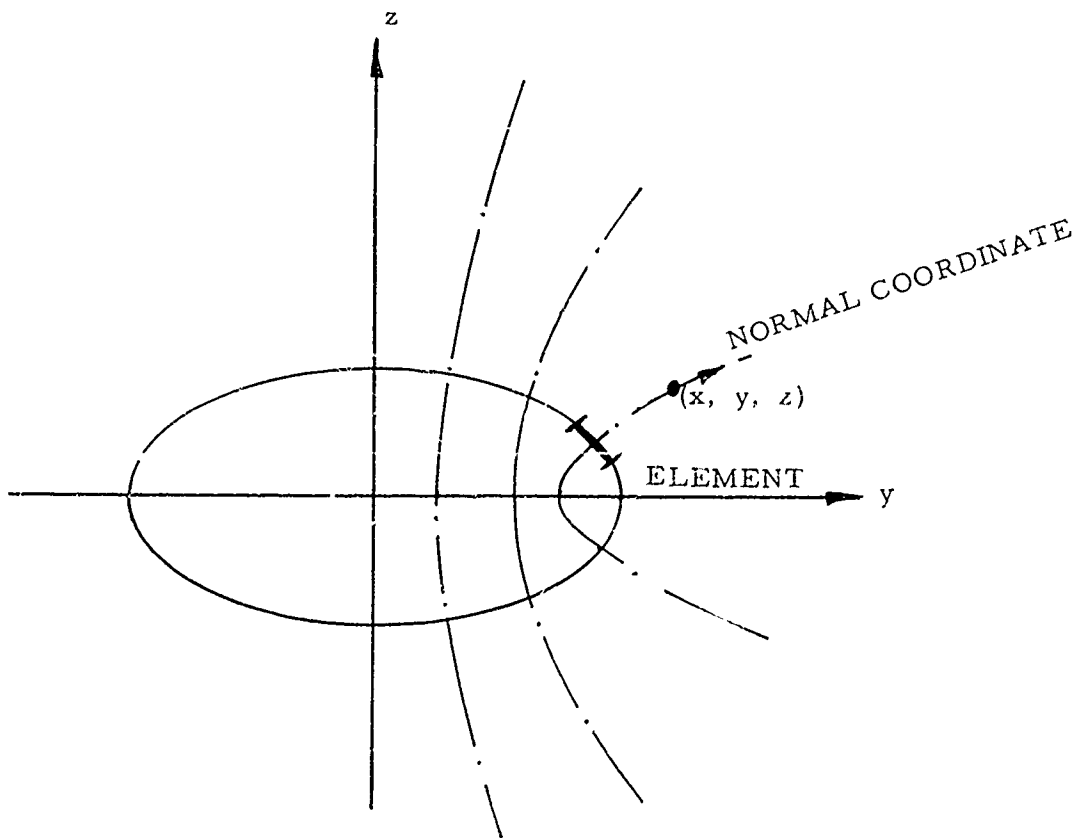
For $R/e < 1.5$ an inner solution is required. The integral E-24 can be performed analytically. A complicated expression results:

$$\begin{aligned}
I &= \left\{ \frac{\bar{I}}{\bar{a}} \left(\frac{B^2 - 2R^2}{2} \right) - \frac{\bar{J}B}{2} + RK - \frac{D}{\bar{a}} \frac{\bar{J}B(6R^2 - B^2)}{2(4R^2 - B^2)} \right. \\
&+ \frac{DR^2K}{\bar{a}(4R^2 - B^2)} \left\{ \frac{2}{\sqrt{4R^2 - B^2}} \tan^{-1} \left(\frac{e \sqrt{4R^2 - B^2}}{R^2 - e^2} \right) \right. \\
&\quad \left. + \left\{ \frac{-\bar{I}B}{\bar{a}2} + \frac{\bar{J}}{2} + \frac{D}{\bar{a}} \frac{\bar{J}}{2} \right\} \ln \left(\frac{e^2 + R^2 + eB}{e^2 + R^2 - eB} \right) + \frac{\bar{I}2e}{\bar{a}} \right. \\
&\quad \left. + \frac{D}{\bar{a}} \bar{J} \left\{ \left[\frac{(3R^2 - B^2)Be + (2R^2 - B^2)R^2}{(4R^2 - B^2)(e^2 + Be + R^2)} \right] \right\} \right\}
\end{aligned} \tag{E-26}$$

$$\begin{aligned}
 & - \left[\frac{-(3R^2 - B^2) Be + (2R^2 - B^2) R^2}{(4R^2 - B^2)(e^2 - Be + R^2)} \right] \} \\
 & + \frac{D R K}{\bar{a}} \left\{ \left[\frac{(B^2 - 2R^2)e + BR^2}{(4R^2 - B^2)(e^2 + Be + R^2)} \right] \right. \\
 & \left. - \left[\frac{-(B^2 - 2R^2)e + BR^2}{(4R^2 - B^2)(e^2 - Be + R^2)} \right] \right\}
 \end{aligned}$$

(E-26)
continued

Simplification of this expression is desirable to reduce the computing effort. Equation (E-26) holds only when the field point is close to the cross section. The elements can be arranged so that the element closest to the field point is centered with respect to the field point. Specifically, the center of the closest element lies on a "normal" coordinate line passing through the field point. Sketch (E-2) shows an example for an ellipse.



SKETCH E-2.

An expression for this normal coordinate will be developed later for an elliptic cross section. Under these circumstances the difference in angles $\lambda - \phi_R$ is close to 90° . Since B is proportional to $\cos(\lambda - \phi_R)$ it is small. An expansion for small B may be made retaining only linear terms. The result is

$$I = \left\{ -\frac{R^2 \bar{I}}{\bar{a}} - \frac{\bar{J} B}{2} + R K - \frac{3}{4} \frac{D \bar{J} B}{\bar{a}} + \frac{R K D}{2\bar{a}} \right\} \frac{1}{R} \quad \left. \begin{array}{l} \\ \\ \end{array} \right\} (E-27)$$

$$\tan^{-1} \left(\frac{2Re}{R^2 - e^2} \right) + \frac{2e \bar{I}}{\bar{a}} +$$

$$\frac{1}{e^2 + R^2} \left\{ e B \bar{J} \left(1 + \frac{D}{\bar{a}} \right) + \frac{D \bar{J} B e (3e^2 + R^2)}{2\bar{a}(e^2 + R^2)} - \frac{D K R e}{\bar{a}} \right\}$$

for $R/e \leq 1.5$

Special Considerations for an Elliptic Cross Section

The location of the element closest to the field point must be chosen such that its center lies along the normal coordinate curve (which is a hyperbola) from the field point to the ellipse. See Sketch (E-2). The first thing that must be done is to find the elliptic parameter θ_1 which is constant along this line. Once θ_1 is known the point on the ellipse where the hyperbola intersects it can be computed. The equation for the hyperbola is:

$$\frac{y^2}{\cos^2 \theta_1} - \frac{z^2}{\sin^2 \theta_1} = a^2 - b^2 \quad (E-28)$$

where y, z are the coordinates of the field point and a and b are the semi-width and semi-height of the ellipse, respectively. Equation (E-28) may be solved for $\sin^2 \theta_1$

$$\sin^2 \theta_1 = \frac{-A + \sqrt{A^2 + 4(a^2 - b^2)z^2}}{2(a^2 - b^2)} \quad (E-29)$$

$$A = (y^2 + z^2 + b^2 - a^2)^2$$

when $a^2 = b^2$

$$\sin^2 \theta_1 = z^2 / (z^2 + y^2) \quad (E-30)$$

The quadrants are assigned as follows

$$\begin{aligned} \sin \theta_1 &= \sqrt{\sin^2 \theta_1} && \text{sign } z \\ \cos \theta_1 &= \sqrt{1 - \cos^2 \theta_1} && \text{sign } y \end{aligned} \quad (E-31)$$

The equation of the ellipse is given again as

$$\begin{aligned} y &= a \cos \theta \\ z &= b \sin \theta \end{aligned} \quad (E-32)$$

The location of the center of the first element is then obtained by placing the value of θ_1 in place of θ in Equation (E-32).

The first element has been located. The other elements are found by dividing the θ coordinate equally from $\theta = 0 \rightarrow 360^\circ$ in N equal parts.

The half width of an element centered at θ is

$$e = -\frac{\pi}{N} \frac{1}{a} \sqrt{a^2 \sin^2 \theta + b^2 \cos^2 \theta} \quad (E-33)$$

The radius of curvature of an element centered at θ is:

$$\bar{a} = \frac{(a^2 \sin^2 \theta + b^2 \cos^2 \theta)^{3/2}}{ab} \quad (\text{E-34})$$

The slope of an element centered at θ is

$$\lambda = \tan^{-1} \left(\frac{b}{c} \cot \theta \right) \quad (\text{E-35})$$

All quantities are now known for the evaluation of $\delta F/q$ and $\delta M/q$ for elliptic cross section.

APPENDIX F. EVALUATION OF THE STEADY LIFT FOR CIRCULAR CROSS SECTIONS

The most important contribution to the lift is the one due to the steady part. Setting $f(k_o) = 1$ in Equation 1, Appendix E, gives:

$$\frac{\delta F(s)}{q} = \frac{\Delta C_p \delta A}{2\pi} \oint \frac{(\vec{i}_r \cdot \vec{N})}{r} (\vec{n} \cdot \vec{i}_F) ds \quad (F-1)$$

where ΔC_p acts in the direction of \vec{N} and $\delta F^{(s)}$ in the direction of \vec{i}_F . The evaluation of this integral for various cross sections will be the subject of this appendix.

The Circular Cross Section

For a circle Eq. (1) becomes

$$\frac{\delta F(s)}{q} = \frac{\Delta C_p \delta A}{2\pi} I_o$$

$$\text{where } I_o = \int_0^{2\pi} \frac{\vec{r} \cdot \vec{N} \vec{n} \cdot \vec{i}_F}{r^2} a d\theta \quad (F-2)$$

and where $\vec{r} = \vec{i}_r r$.

$$\begin{aligned} \vec{r} \cdot \vec{N} \vec{n} \cdot \vec{i}_F &= \vec{i}_F \cdot \vec{i}_{\bar{\theta}} (-r_a \mu_R) \sin \theta \\ &\quad \vec{i}_F \cdot \vec{i}_{\bar{\theta}} a \mu_R \cos \theta \sin \theta + \\ &\quad \vec{i}_F \cdot \vec{i}_R a \mu_{\bar{\theta}} \cos \theta \sin \theta + \quad (F-3) \\ &\quad \vec{i}_F \cdot \vec{i}_{\bar{\theta}} a \mu_{\bar{\theta}} \sin^2 \theta + \\ &\quad \vec{i}_F \cdot \vec{i}_R \mu_y (a \mu_R \cos^2 \theta - r_a \cos \theta) \end{aligned}$$

where a rotated coordinate system is used

$$\vec{i}_R = \vec{j} \frac{y_a}{r_a} + \vec{k} \frac{z_a}{r_a} \quad (F-4)$$

$$\vec{i}_{\bar{\theta}} = \vec{k} \frac{y_a}{r_a} - \vec{j} \frac{z_a}{r_a}$$

Here (y_a , z_a) are the coordinates from the body axis to the pressure doublet.

Also needed in Eq. (2) is r^2 .

$$r^2 = r_a^2 + a^2 - 2ar_a \cos \theta \quad (F-5)$$

Placing (F-3) and (F-5) into (F-2) and deleting integrals that vanish gives:

$$I_o = \vec{i}_F \cdot \vec{i}_{\bar{\theta}} a^2 \mu_{\bar{\theta}} I_s + \vec{i}_F \cdot \vec{i}_R a \mu_R (-r_a I_c + a I_{cc}) \quad (F-6)$$

where

$$I_s = \int_0^{2\pi} \frac{\sin^2 \theta \, d\theta}{A - B \cos \theta}$$

$$I_c = \int_0^{2\pi} \frac{\cos \theta \, d\theta}{A - B \cos \theta}$$

$$I_{cc} = \int_0^{2\pi} \frac{\cos^2 \theta \, d\theta}{A - B \cos \theta}$$

$$\text{and } A = r_a^2 + a^2$$

$$B = 2a r_a$$

The technique of splitting integrals into odd and even parts will be used
The technique will be illustrated for I_s only.

$$I_s = \int_0^{2\pi} \frac{\sin^2 \theta \, d\theta}{A-B \cos \theta} = \int_0^\pi \frac{\sin^2 \theta \, d\theta}{A-B \cos \theta} + \int_0^\pi \frac{\sin^2 \theta \, d\theta}{A+B \cos \theta} + \\ \int_0^\pi \frac{\sin^2 \theta \, d\theta}{A-B \cos \theta} - \int_0^\pi \frac{\sin^2 \theta \, d\theta}{A+B \cos \theta}$$

Combining the first two and last two integrals gives:

$$I_s = 2A \int_0^\pi \frac{\sin^2 \theta \, d\theta}{A^2 - B^2 \cos^2 \theta} + 2B \int_0^\pi \frac{\cos \theta \sin^2 \theta \, d\theta}{A^2 - B^2 \cos^2 \theta}$$

The second of these integrals is the "odd" contribution and is zero.

$$I_s = 4A \bar{I}_s \quad (F-7)$$

$$\text{where } \bar{I}_s = \int_0^{\pi/2} \frac{\sin^2 \theta}{A^2 - B^2 \cos^2 \theta} \, d\theta = \frac{-\pi/2}{4a^2 r_a^2 A} \left\{ \left| r_a^2 - a^2 \right| - (r_a^2 + a^2) \right\}$$

or

$$I_s = \frac{+\pi}{a^2 r_a^2} Q \quad (F-8)$$

$$\text{where } Q = -\frac{1}{2} \left\{ \left| r^2 - a^2 \right| - (r_a^2 + a^2) \right\}$$

In a similar manner

$$I_c = 2B I_n \quad (F-9a)$$

$$I_{cc} = 2A I_n \quad (F-9b)$$

$$\text{where } I_n = 2 \int_0^{\pi/2} \frac{\cos^2 \theta \, d\theta}{A^2 - B^2 \cos^2 \theta} = \frac{\pi Q}{2a^2 r_a^2 |r_a^2 - a^2|} \quad (\text{F-9c})$$

The term $(-r_a I_c + a I_{cc})$ is to be formed for Equation (6).

$$-r_a I_c + a I_{cc} = -2a(r_a^2 - a^2) I_n \quad (\text{F-10})$$

Placing (F-9c) into (F-10) and the result into (F-6) along with the result for I_s gives:

$$I_o = \vec{i}_F \cdot \vec{i}_{\bar{\theta}} \mu_{\bar{\theta}} \left(\frac{\pi Q}{r_a^2} \right) + \vec{i}_F \cdot \vec{i}_R \mu_R - \left(\frac{-\pi Q}{r_a^2} \right) \text{ sign } (r_a^2 - a^2) \quad (\text{F-11})$$

$$\text{where } Q = -\frac{1}{2} \left\{ |r_a^2 - a^2| - (r_a^2 + a^2) \right\}$$

$$r_c > a \quad (\text{doublet outside body}) \quad Q = a^2, \text{ sign } (r_a^2 - a^2) = +$$

$$r_a < a \quad (\text{doublet inside body}) \quad Q = r_a^2, \text{ sign } (r_a^2 - a^2) = -$$

Equation (F-11) can be written as two expressions depending on whether the doublet lies internal or external to the body. Placing these two expressions into (F-1) gives:

Doublet Inside Body

$$\frac{\delta F^{(s)}}{q} = \left(\frac{\Delta C_p \delta A}{2} \right) \vec{i}_F \cdot \vec{N} \quad (\text{F-12})$$

Doublet Outside Body

$$\frac{\delta F(s)}{q} = \left\{ \begin{array}{l} \left(\frac{\Delta C_p \delta A}{2} \right) \\ \left(\frac{r_a}{a} \right)^2 \end{array} \right\} \vec{i}_F \cdot \vec{N}_1 \quad (F-13)$$

$$\text{where } \vec{N} = \mu_{\bar{\theta}} \vec{i}_{\bar{\theta}} + \mu_R \vec{i}_R$$

$$\vec{N}_1 = \mu_{\bar{\theta}} \vec{i}_{\bar{\theta}} - \mu_R \vec{i}_R$$

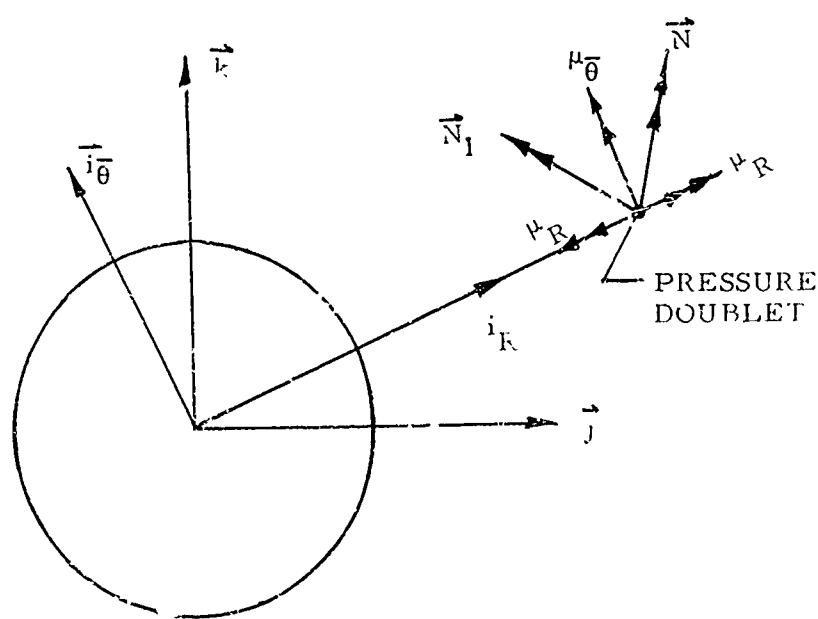
Equations (F-12) and F-13) describe a very peculiar behavior. Take for instance the case where these equations have a common point $r_a = a$.

$$\begin{aligned} \delta F(s)/q &= \frac{\Delta C_p \delta A}{2} \vec{i}_F \cdot \vec{N} = \frac{\Delta C_p \delta A}{2} \left\{ (\vec{i}_F \cdot \vec{i}_{\bar{\theta}}) \mu_{\bar{\theta}} + (\vec{i}_F \cdot \vec{i}_R) \mu_R \right\}, \quad r_a = a - \epsilon \\ &\quad (F-14) \\ \delta F(s)/q &= \frac{\Delta C_p \delta A}{2} \vec{i}_F \cdot \vec{N}_1 = \frac{\Delta C_p \delta A}{2} \left\{ (\vec{i}_F \cdot \vec{i}_{\bar{\theta}}) \mu_{\bar{\theta}} - (\vec{i}_F \cdot \vec{i}_R) \mu_R \right\}, \quad r_a = a + \epsilon \end{aligned}$$

Notice that the contribution of the component $\bar{\mu}_z$ (one oriented normal to the radius vector from the circle center, see sketch) is continuous when the doublet passes through the body surface. However, such is not the case for the component $\bar{\mu}_y$ (oriented parallel to the radius vector).

When the doublet passes inside the body the force on the body due to μ_R changes sign. When the doublet is anywhere inside the body, the force is equal to $\frac{\Delta C_p \delta A}{2}$ and is in the direction of the doublet, \vec{N} .

When the doublet is outside of the body the force is equal to $\frac{\Delta C_p \delta A}{2} / (r_a/a)^2$ and is in the direction of \vec{N}_1 .



SKETCH F-1

APPENDIX G. CIRCUMFERENTIAL INTEGRATION OF
THE PRESSURE FOR BODIES OF CIRCULAR
CROSS SECTION IN BOTH STEADY
AND OSCILLATORY FLOW

Steady Flow

The expression for the pressure field due to a point pressure doublet in steady flow is

$$C_p(x, y, z) = \frac{\Delta C_p \delta A}{4\pi} \frac{\partial}{\partial N} \left(\frac{1}{R} \right) \quad (G-1)$$

where

$$R^2 = (x - \xi)^2 + \beta^2 r^2$$

$$r^2 = (y - \eta)^2 + (z - \zeta)^2$$

Lawrence and Flax⁷ have integrated this equation, in an approximate manner, around a circular cross section. Essentially, they obtained only the force in the z -direction (see Sketch G-1) due to a pressure doublet oriented in the same direction. Their results will be rederived and extended to obtain the force in the y -direction due to a pressure doublet oriented in the same direction. Also, it will be shown that the force in the z -direction due to a doublet oriented in the y -direction (and vice versa) is zero.

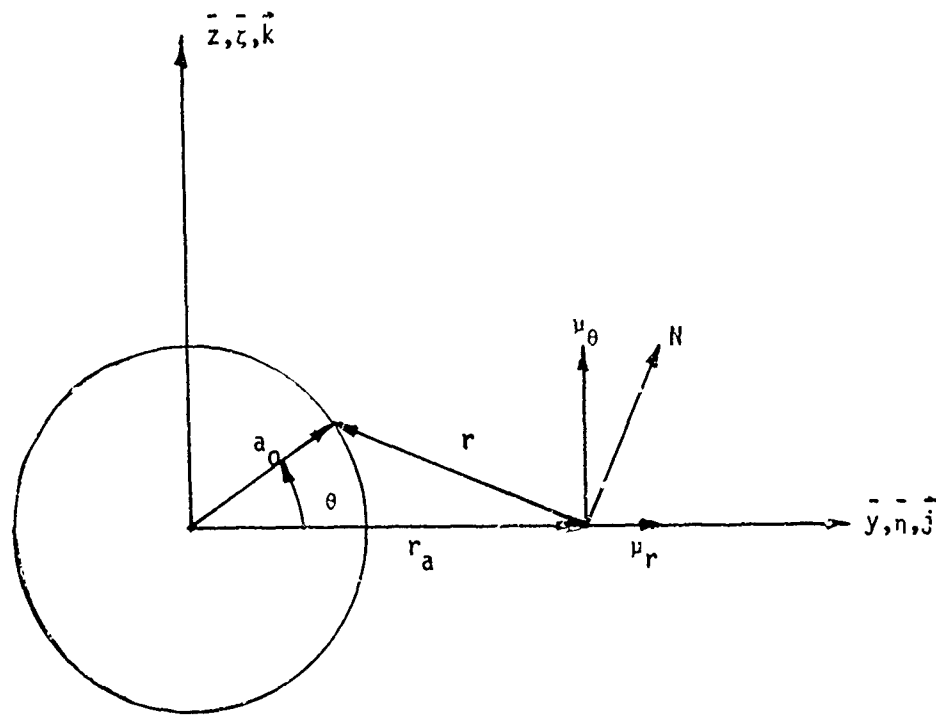
For simplicity of notation the origin of coordinates is fixed at the circle center and the pressure doublet is assumed to lie on the \bar{y} -axis. This results in no loss of generality since the \bar{y} - and \bar{z} -axis may be thought of as simply a coordinate system that has been translated and rotated so that these assumptions are satisfied.

Equation (G-1) may be rewritten as: *

$$C_p(\xi, y, z) = \frac{\Delta C_p \delta i}{4\pi} - \frac{\beta^2}{R^2} \left\{ (\bar{z} - \bar{\zeta}) \mu_\theta (\bar{y} - \bar{\eta}) \mu_r \right\} \quad (G-2)$$

where $\vec{N} = \vec{i}_\theta N_\theta + \vec{i}_r N_r$

* μ_θ and μ_r are used to be consistent with Appendix F.



SKETCH G-1

Introducing the coordinates of the circle, $\bar{y} = a_o \cos \theta$, $\bar{z} = a_o \sin \theta$. noting that $\xi = 0$ and $\bar{\eta} = r_a$ and expanding in terms of a_o/R_a gives:

$$C_p(x, y, z) = \frac{\Delta C_p \delta A}{4\pi} \frac{\beta^2}{R_a^3} \left\{ 1 - \frac{3a_o r_a \beta^2 \cos \theta}{R_a^2} + \dots \right\} x \\ \left\{ a_o \sin \theta \mu_0 + (a_o \cos \theta - r_a) \mu_r \right\} \quad (G-3)$$

where

$$R^2 = R_a^2 + \beta^2 a_o^2 - 2a_o r_a \beta^2 \cos \theta$$

and

$$R_a^2 = (x - \xi)^2 + \beta^2 r_a^2$$

Equation (G-3) may be integrated circumferentially to give the total force per unit length.

$$\frac{\partial(\vec{F}/q)}{\partial x} = \oint C_p (\vec{k} \sin \theta + \vec{j} \cos \theta) a_o d\theta \\ = \frac{\Delta C_p \delta A}{4} \frac{\beta^2 a_o^2}{R_a^3} \left\{ \mu_0 \vec{k} + \mu_r \left(1 - \frac{3r_a^2 \beta^2}{R_a^2} \right) \vec{j} \right\} \quad (G-4)$$

$r_a > a_o$

If (G-1) is expanded in terms of r_a/R_a then the results are

$$\frac{\partial(\vec{F}/q)}{\partial x} = \frac{\Delta C_p \delta A}{4} \frac{\beta^2 a_o^2}{R_a^3} \left\{ \mu_0 \vec{k} + \mu_r \vec{j} \right\} \quad (G-5)$$

$r_a \leq a_o$

where

$$\bar{R}_a^2 = (x - \xi)^2 + \beta^2 a_o^2$$

Notice that there are no cross terms; i.e., z-force due to y-doublet or vice versa. Equations (G-4) and (G-5) cover the entire range of r_a .

One way to measure the accuracy of these equations is to integrate them

longitudinally from $-\infty$ to $+\infty$, holding a_0 constant, and compare the results with the exact values obtained in Appendix F.

Integration of Equation (G-4) gives:

$$\vec{F}/q = \int_{-\infty}^{\infty} \partial(F/q)/\partial x dx = \frac{\Delta C_p \delta A}{2} \frac{a_0^2}{r_a^2} \left(\mu_\theta \vec{k} - \mu_r \vec{j} \right) \quad (G-6)$$

$, r_a > a_0$

$$F/q = \frac{\Delta C_p \delta A}{2} \left(\mu_\theta \vec{k} + \mu_r \vec{j} \right) \quad , r_a \leq a_0 \quad (G-7)$$

These results correspond precisely to the exact values even though approximate methods have been employed in the derivation. It can be shown that even though the total integrated values are exactly correct the distributions are only approximately valid.

Oscillatory Flow

The results for steady flow are very encouraging. The exact total integrated lift is obtained from an approximate result. A similar line of development may be made for oscillatory flow.

The expression for the pressure field due to a point pressure doublet in oscillatory flow is:

$$C_p(x, y, z) = \frac{\Delta C_p \delta A}{4\pi} e^{i\lambda M(x - \xi)} \frac{\partial}{\partial N} \left\{ \frac{e^{-i\lambda R}}{R} \right\} \quad (G-8)$$

where

$$\lambda = \frac{\omega M}{\beta^2 U_\infty}$$

Taking the N-derivative and substituting $\zeta = 0$, $\eta = r_a$ and, $z = a_0 \sin \theta$ and $y = a_0 \cos \theta$ gives

$$C_p(x, y, z) = \frac{\Delta C_p \delta A}{4\pi} e^{i\lambda(M(x - \xi) - R)} \quad (G-9)$$

$$\times \left\{ \frac{1}{R^3} + \frac{i\lambda}{R^2} \right\} \beta^2 \left\{ \mu_\theta a_o \sin\theta + \mu_r (a_o \cos\theta - r_a) \right\}$$

If R is expanded in terms of a_o/R_a , as in the steady case and if $e^{-i\lambda R}$ is expanded in terms of $\lambda \eta a \beta^2 \cos\theta / R_a$ then:

$$e^{-i\lambda R} = e^{-i\lambda R_a} \left(1 + \frac{i\lambda a_o r_a \beta^2 \cos\theta}{R_a} + \dots \right)$$

Also

$$\left\{ \frac{1}{R^3} + \frac{i\lambda}{R^2} \right\} = \left\{ \frac{1}{R_a^3} + \frac{i\lambda}{R_a^2} \right\} \left\{ 1 + \frac{3\beta^2 a_o r_a \cos\theta}{R_a^2} \right\} - \frac{i\lambda \beta^2 a_o r_a \cos\theta}{R_a^4}$$

Thus

$$\begin{aligned} C_p(x, y, z) &= \frac{C}{a_o^2} \left\{ 1 + \frac{i\lambda a_o r_a \beta^2 \cos\theta}{R_a} \right\} \times \\ &\quad \left\{ \mu_\theta a_o \sin\theta + \mu_r (a_o \cos\theta - r_a) \right\} \times \\ &\quad \left\{ \left(\frac{1}{R_a^3} + \frac{i\lambda}{R_a^2} \right) \left(1 + \frac{3\beta^2 a_o r_a \cos\theta}{R_a^2} \right) - \frac{i\lambda \beta^2 a_o r_a \cos\theta}{R_a^4} \right\} \end{aligned}$$

where

$$C = \frac{\Delta C_p \delta A}{4\pi} e^{i\lambda[M(x - \xi) - R_a]} \beta^2 a_o^2$$

$$\begin{aligned} \frac{\partial(F_z/q)}{\partial x} &= \oint C_p a_o \sin\theta d\theta \\ &= \mu_\theta C \left\{ \left[\frac{1}{R_a^3} + \frac{i\lambda}{R_a^2} \right] \left[\oint \left(\sin^2\theta + \cos\theta \sin^2\theta \frac{i\lambda a_o r_a \beta^2}{R_a} - \right. \right. \right. \\ &\quad \left. \left. \left. + \cos^2\theta \sin^2\theta \frac{i\lambda 3\beta^4 a_o^2 r_a^2}{R_a^3} \right) d\theta \right] \right\} + \end{aligned}$$

$$\begin{aligned}
& - \frac{i\lambda\beta^2 a_o r_a}{R_a^4} \oint \left[\cos\theta \sin^2\theta + \cos^2\theta \sin^2\theta \frac{i\lambda a_o r_a \beta^2}{R_a} \right] d\theta \Big\} \\
& = \mu_\theta C\pi \left\{ \left[\frac{1}{R_a^3} + \frac{i\lambda}{R_a^2} \right] \left[1 + \frac{3}{4} \frac{i\lambda\beta^2 a_o^2 r_a^2}{R_a^3} \right] \right. \\
& \quad \left. - \frac{\lambda^2 \beta^4 a_o^2 r_a^2}{R_a^5} \frac{1}{4} \right\} \tag{G-10}
\end{aligned}$$

$$\begin{aligned}
\frac{\partial(F_y/q)}{\partial x} &= \oint C p a_o \cos\theta d\theta \\
& = \mu_r C \left\{ \left[\frac{1}{R_a^3} + \frac{i\lambda}{R_a^2} \right] \oint \left[\cos^2\theta - \frac{r_a}{a_o} \cos\theta \right. \right. \\
& \quad \left. + \frac{i\lambda a_o r_a \beta^2}{R_a} \cos^3\theta \right. - \frac{i\lambda r_a^2 \beta^2}{R_a} \cos^2\theta + \frac{3\beta^2 a_o r_a}{R_a^2} \cos^3\theta \\
& \quad \left. - \frac{3\beta^2 r_a^2 \cos^2\theta}{R_a^2} + i\lambda \frac{3\beta^4 a_o^2 r_a^2}{R_a^3} \cos^4\theta \right. \\
& \quad \left. - i\lambda \frac{3\beta^4 a_o r_a^3 \cos^3\theta}{R_a^3} \right] d\theta \\
& \quad - \frac{i\lambda\beta^2 a_o r_a}{R_a^4} \oint \left[\cos^3\theta - \frac{r_a}{a_o} \cos^2\theta + \frac{i\lambda a_o r_a \beta^2 \cos^4\theta}{R_a} \right. \\
& \quad \left. - \frac{i\lambda r_a^2 \beta^2 \cos^3\theta}{R_a} \right] d\theta
\end{aligned}$$

$$\begin{aligned}
 \frac{\partial(F_y/q)}{\partial x} &= \mu_r C \pi \left\{ \left[\frac{1}{R_a^3} + \frac{i\lambda}{R_a^2} \right] \left[1 - \frac{i\lambda r_a^2 \beta^2}{R_a} \right. \right. \\
 &\quad \left. \left. - \frac{3\beta^2 r_a^2}{R_a^2} + i\lambda \frac{9}{4} \frac{\beta^4 a_o^2 r_a^2}{R_a^3} \right] \right. \\
 &\quad \left. - \frac{i\lambda \beta^2 a_o r_a}{R_a^4} \left[- \frac{r_a}{a_o} + \frac{i\lambda a_o r_a \beta^2}{R_a} - \frac{3}{4} \right] \right\} \quad (G-11)
 \end{aligned}$$

To check the accuracy of the expressions given in Equations (G-10) and (G-11) an integration will be performed in the x-direction from $-\infty$ to $+\infty$ and the results compared with the method derived in Appendices D and E which are the exact results.

If the highest order terms in equations, Eqs. (G-10) are dropped, then:

$$\begin{aligned}
 \frac{\partial(F_z/q)}{\partial x} &= \mu_0 \frac{\Delta C_p \delta A}{4} e^{i\lambda[M(x-\xi)-R_a]} \left\{ \frac{1}{R_a^3} + \frac{i\lambda}{R_a^2} \right\} \beta^2 a_o^2 \\
 &= \mu_0 \frac{\Delta C_p \delta A}{4} \frac{a_o^2}{r_a} \frac{\partial}{\partial r_a} \left\{ \frac{e^{i\lambda[M(x-\xi)-R_a]}}{R_a} \right\} \\
 F_z/q &= \int_{-\infty}^{\infty} \frac{\partial(F_z/q)}{\partial x} dx \\
 &= \mu_0 \frac{\Delta C_p \delta A}{4} \frac{a_o^2}{r_a} \frac{\partial}{\partial r_a} \int_{-\infty}^{\infty} \frac{e^{i\lambda[M(x-\xi)-R_a]}}{R_a} dx
 \end{aligned}$$

The integral appearing here is precisely the integral I appearing in Appendix D, Equation(D-3).

$$I = i \pi H_0^{(2)}(\bar{k})$$

$$\bar{k} = \frac{\omega r_a}{U_\infty} M$$

where $H_0^{(2)}(\bar{k})$ is the Hankle function of the second kind and zeroth order

$$\frac{\partial I}{\partial r_a} = -i \pi H_1^{(2)}(\bar{k}) \frac{\omega M}{U_\infty}$$

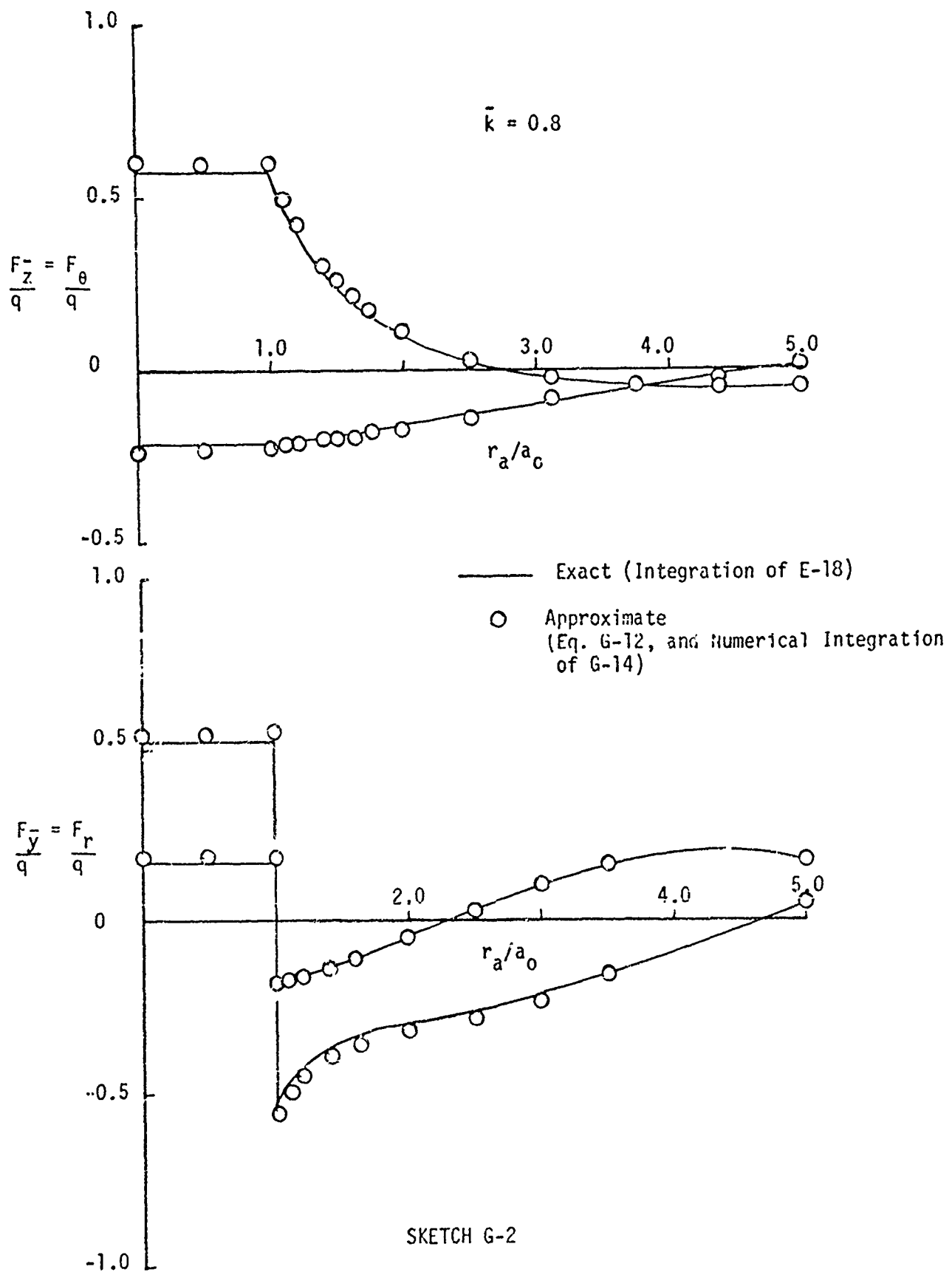
then

$$F_z/q = \mu_\theta \frac{\Delta C_p \delta A}{2} \frac{a_o^2}{r_a^2} \left(\frac{i\pi}{2} \right) H_1^{(2)}(\bar{k}) \bar{k} \quad (G-12)$$

Sketch (G-2) shows that the agreement between (G-12) and the results of Appendices D and E is almost perfect. If the highest order terms are dropped from Equation (G-11) and the results integrated numerically the results again agree with the results of Appendices D and E. This result is also shown in Sketch (G-2). The simplified formulas are then:

$$\frac{\partial(F_z/q)}{\partial x} = \mu_\theta \frac{\Delta C_p \delta A}{4} \beta^2 a_o^2 e^{i\lambda[M(x-\xi) - Ra]} \left\{ \frac{1}{R_a^3} + \frac{i\lambda}{R_a^2} \right\} \quad (G-13)$$

$$r_a > a_o$$



$$\frac{\partial(F_y/q)}{\partial x} = \mu_r \frac{\Delta C_p \delta A}{4} \left\{ \left| \frac{1}{R_a^3} + \frac{i\lambda}{R_a^2} \right| \left| 1 - \frac{i\lambda r_a^2 \beta^2}{R_a} - \frac{3\beta^2 r_a^2}{R_a^2} \right| + \frac{i\lambda \beta^2 r_a^2}{R_a^4} \right\} \beta^2 a_o^2 e^{i\lambda[M(x-\xi) - R_a]} \quad (G-14)$$

$r_a > a_o$

Following the steady analysis the expressions for $r_a \leq a_o$ may be obtained.

$$\frac{\partial(F_z/q)}{\partial x} = \mu_\theta \frac{\Delta C_p \delta A}{4} \beta^2 a_o^2 e^{i\lambda(M(x-\xi) - \bar{R}_a)} \left\{ \frac{1}{\bar{R}_a^3} + \frac{i\lambda}{\bar{R}_a^2} \right\} \quad (G-15)$$

$r_a \leq a_o$

$$\frac{\partial(F_y/q)}{\partial x} = \frac{\mu_r}{\mu_\theta} \frac{\partial(F_z/q)}{\partial x} \quad r_a \leq a_o$$

where

$$R_a^2 = (x-\xi)^2 + \beta^2 r_a^2$$

$$\bar{R}_a^2 = (x-\xi)^2 + \beta^2 a_o^2$$

As in the steady case the integrated values agree with the exact values. However, the distributions are again only an approximation.

The coordinate system used to derive the formulas (\bar{y} , \bar{z}) for the forces is one that has been rotated an angle θ_1 . This rotation was performed so that the pressure doublet will lie on the \bar{y} -axis of the rotated system. A transformation back to the y , z system is necessary to complete the derivation.

$$\frac{\partial(F_z/q)}{\partial x} = \mu_r \left\{ \cos^2 \theta_1 \frac{\partial(F_z/q)}{\partial x} + \sin^2 \theta_1 \frac{\partial(F_y/q)}{\partial x} \right\} \quad (G-17a)$$

$$+ \mu_r \left\{ \cos \theta_1 \sin \theta_1 \left(\frac{\partial(F_y/q)}{\partial x} - \frac{\partial(F_z/q)}{\partial x} \right) \right\}$$

$$= \mu_r \frac{\partial(F_z^{(z)}/q)}{\partial x} + \mu_r \frac{\partial(F_z^{(y)}/q)}{\partial x} \quad (G-17b)$$

$$\frac{\partial(F_y/q)}{\partial x} = \mu_r \left\{ \sin^2 \theta_1 \frac{\partial(F_z/q)}{\partial x} + \cos^2 \theta_1 \frac{\partial(F_y/q)}{\partial x} \right\} \quad (G-18a)$$

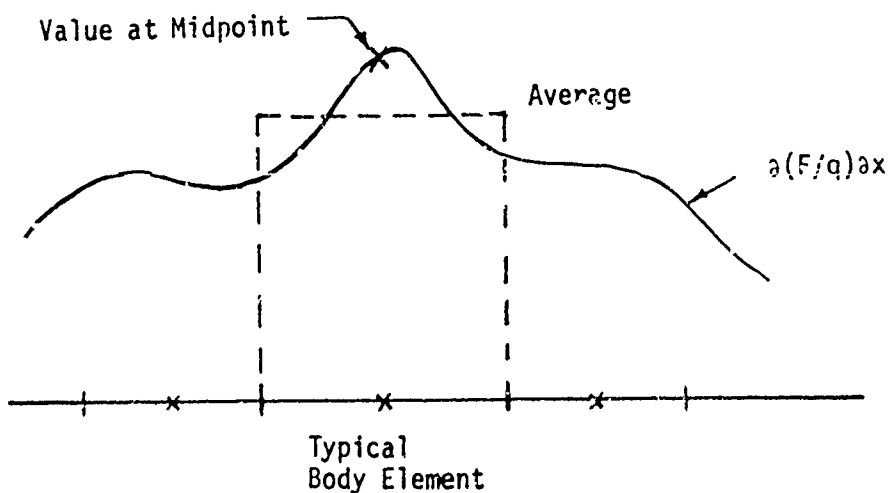
$$+ \mu_r \frac{\partial(F_z^{(y)}/q)}{\partial x}$$

$$= \mu_r \frac{\partial(F_y^{(y)}/q)}{\partial x} + \mu_r \frac{\partial(F_z^{(y)}/q)}{\partial x} \quad (G-18b)$$

The new variables, $\partial(F_z^{(z)}/q)/\partial x$, $\partial(F_y^{(y)}/q)/\partial x$ and $\partial(F_z^{(y)}/q)/\partial x$ are defined implicitly by comparing Equation (G-17a) with (G-17b) and by comparing Equation (G-18a) with (G-18b).

APPENDIX H. INTEGRATION OF $\partial(\vec{F}/q)/\partial x$
OVER A BODY ELEMENT

The circumferential integration of the pressure for a circular cross section was performed in Appendix G. In the present method the force distribution is given, not at every value of x , but at a set of points which correspond to the midpoints of a set of body elements. The value of the circumferential integration, $\partial(\vec{F}/q)/\partial x$, must be averaged over these elements. If it is not then errors could be introduced due to local variations over the element. As an example, Sketch (H-1) shows what might happen if averaging is not performed.



SKETCH H-1

The expressions to be integrated may be written in the following form.

$$\frac{\partial(\bar{F}_z/q)}{\partial x} = \mu_\theta \cdot \bar{z} \quad (H-1)$$

$$\frac{\partial(\bar{F}_y/q)}{\partial x} = \mu_r \bar{f}_y \quad (H-2)$$

where

$$\bar{f}_z = C\pi \left[\frac{1}{R_a^3} + \frac{i\lambda}{R_a^2} \right] \quad (H-3)$$

$$\bar{f}_y = \bar{f}_z + C\pi L \quad (H-4)$$

and where

$$L = \frac{\beta^2 r_a^2}{R_a^3} \left\{ \lambda^2 - \frac{3}{R_a^2} - \frac{i3\lambda}{R_a} \right\} \quad (H-5)$$

$$\pi C = \frac{\Delta C p \delta A}{4} e^{i\lambda[M(x-\xi) - R_a]} \beta^2 a_o^2 \quad (H-6)$$

The average value of $\partial(\bar{F}_z/q)/\partial x$ and $\partial(\bar{F}_y/q)/\partial x$ over an element stretching from $x_A - \frac{\Delta x}{2}$ to $x_A + \frac{\Delta x}{2}$ is

$$\partial(\bar{F}_z/q)/\partial x = \frac{1}{\Delta x} \int_{-\frac{\Delta x}{2}}^{\frac{\Delta x}{2}} \frac{\partial(\bar{F}_z/q)}{\partial x} dt \quad (H-7)$$

$$\partial(\bar{F}_y/q)/\partial x = \frac{1}{\Delta x} \int_{-\frac{\Delta x}{2}}^{\frac{\Delta x}{2}} \frac{\partial(\bar{F}_y/q)}{\partial x} dt \quad (H-8)$$

where

$$x = x_A + t$$

The terms x_A and Δx are the element midpoint and length, respectively.

If $x_A + t$ is substituted for x in the expression for R_a and the result expanded for small t/R_{aA} the result is

$$R_a = R_{aA} \left\{ 1 + \left(\frac{t}{R_{aA}} \right) \frac{(x_A - \xi)}{R_{aA}} + \left(\frac{t}{R_{aA}} \right)^2 \frac{1}{2} \frac{\beta^2 r_a^2}{R_{aA}^2} \right\} \quad (H-9)$$

where

$$R_{aA}^2 = (x_A - \xi)^2 + \beta^2 r_a^2$$

Placing Equation (H-9) into (H-6) and expanding for small λt gives:

$$\begin{aligned} \frac{\Delta C_p \delta A \beta^2 a_o^2}{4} e^{i\lambda[M(x-\xi)-R_a]} &= \frac{\Delta C_p \delta A \beta^2 a_o^2}{4} e^{i\lambda[M(x_A - \xi) - R_{aA}]} \\ &e^{i\lambda \left[Mt - \frac{t}{R_{aA}} (x_A - \xi) - \left(\frac{t}{R_{aA}} \right)^2 \frac{1}{2} \frac{\beta^2 r_a^2}{R_{aA}} \right]} \\ &\approx a_o^2 \Delta x \bar{C} \beta^2 \left| 1 + i\lambda(tA - t^2B) \right| \end{aligned} \quad (H-10)$$

where

$$\bar{C} = \frac{\Delta C_p \delta A}{4 \Delta x} e^{i\lambda[M(x_A - \xi) - R_{aA}]}$$

$$A = M - \tau$$

$$B = \frac{\beta^2 r_a^2}{2 R_{aA}^3}$$

$$\tau = \frac{(x_A - \xi)}{R_{aA}}$$

$$\begin{aligned} \partial(\bar{F}_z/q)/\partial x &= \bar{C} \beta^2 a_0^2 \int_{-\frac{\Delta x}{2}}^{\frac{\Delta x}{2}} \left[\frac{1}{R_a^3} + i\lambda A \frac{t}{R_a^3} - i\lambda B \frac{t^2}{R_a^3} \right. \\ &\quad \left. + \frac{i\lambda}{R_a^2} - \frac{\lambda^2 A t}{R_a^2} + 0(t^2 \lambda^2) \right] dt \end{aligned} \quad (H-11)$$

$$\begin{aligned} \partial(\bar{F}_y/q)/\partial x &= \partial(\bar{F}_z/q)/\partial x \\ &+ \bar{C} \beta^4 r_a^2 a_0^2 \int_{-\frac{\Delta x}{2}}^{\frac{\Delta x}{2}} \left[\frac{\lambda^2}{R_a^3} + \frac{i\lambda^3 A t}{R_a^3} - \frac{3}{R_a^5} - \frac{3i\lambda A t}{R_a^5} \right. \\ &\quad \left. + \frac{3i\lambda B t^2}{R_a^5} - \frac{i3\lambda}{R_a^4} + \frac{3\lambda^2 A t}{R_a^4} + 0(t^2 \lambda^2) \right] dt \end{aligned} \quad (H-12)$$

Define a new reduced frequency variable, \bar{k} .

$$\bar{k} = 2 k_r M a_0 / \bar{C} = \lambda \beta^2 a_0 \quad (H-13)$$

If \bar{k} is introduced into Equations (H-11) and (H-12) then:

$$\begin{aligned} \partial(\bar{F}_z/q)/\partial x &= \bar{C} a_0 \left\{ (\beta^2 a_0 I_1 - \frac{\bar{k}^2}{\beta^2 a_0} A I_5) \right. \\ &\quad \left. + i \bar{k} (A I_2 + I_4 - I_3 B) \right\} \end{aligned} \quad (H-14)$$

$$\partial(\bar{F}_y/q)/\partial x = \partial(\bar{F}_z/q)/\partial x \quad \Delta \quad (H-15)$$

$$\Delta = \bar{C} r_a^2 \left\{ \left[-3 \beta^4 a_0^2 I_6 + \bar{k}^2 (I_1 + 3A I_{10}) \right] \right. \\ \left. + i \beta^2 a_0 3 \bar{k} (-A I_7 + B I_8 - I_9) + i \bar{k}^3 A I_2 / \beta^2 a_0 \right\}$$

where

$$I_1 = \int_{-\frac{\Delta x}{2}}^{\frac{\Delta x}{2}} \frac{dt}{R_a^3} = \frac{1}{\beta^2 r_a^2} \left\{ \frac{(x_2 - \xi)}{R_{a_2}} - \frac{(x_1 - \xi)}{R_{a_1}} \right\} \\ I_2 = \int_{-\frac{\Delta x}{2}}^{\frac{\Delta x}{2}} \frac{t dt}{R_a^3} = \frac{-1}{\beta^2 r_a^2} \left\{ \frac{(x_A - \xi) \frac{\Delta x}{2} + R_{a_A}^2}{R_{a_2}} + \frac{(x_A - \xi) \frac{\Delta x}{2} - R_{a_A}^2}{R_{a_1}} \right\} \\ I_3 = \int_{-\frac{\Delta x}{2}}^{\frac{\Delta x}{2}} \frac{t^2 dt}{R_a^3} = I_{11} - 2(x_A - \xi) I_4 - R_{a_A}^2 I_1 \\ I_{11} = \int_{-\frac{\Delta x}{2}}^{\frac{\Delta x}{2}} \frac{dt}{R_a} = \ln \left| \frac{x_2 - \xi + R_{a_2}}{x_1 - \xi + R_{a_1}} \right| \\ I_4 = \int_{-\frac{\Delta x}{2}}^{\frac{\Delta x}{2}} \frac{dt}{R_a^2} = \frac{1}{\beta r_a} \left\{ \text{Atan} \left(\frac{x_2 - \xi}{\beta r_a} \right) - \text{Atan} \left(\frac{x_1 - \xi}{\beta r_a} \right) \right\} \\ I_5 = \int_{-\frac{\Delta x}{2}}^{\frac{\Delta x}{2}} \frac{t dt}{R_a^2} = \frac{1}{2} \ln \left(\frac{R_{a_2}^2}{R_{a_1}^2} \right) - (x_A - \xi) I_4 \\ I_6 = \int_{-\frac{\Delta x}{2}}^{\frac{\Delta x}{2}} \frac{dt}{R_a^5} = \frac{1}{3 \beta^2 r_a^2} \left\{ \frac{(x_2 - \xi)}{R_{a_2}^3} - \frac{(x_1 - \xi)}{R_{a_1}^3} \right\} + \frac{2}{3 \beta^2 r_a^2} I_1 \\ I_7 = \int_{-\frac{\Delta x}{2}}^{\frac{\Delta x}{2}} \frac{t dt}{R_a^5} = -\frac{1}{3} \left\{ \frac{1}{R_{a_2}^3} - \frac{1}{R_{a_1}^3} \right\} - (x_A - \xi) I_6 \\ I_8 = \int_{-\frac{\Delta x}{2}}^{\frac{\Delta x}{2}} \frac{t^2 dt}{R_a^5} = I_1 - 2(x_A - \xi) I_7 - R_{a_A}^2 I_6$$

$$I_9 = \int_{-\frac{\Delta x}{2}}^{\frac{\Delta x}{2}} \frac{dt}{R_a^4} = \frac{1}{2\beta^2 r_a^2} \left\{ \frac{(x_2 - \xi)}{R_{a_2}^2} - \frac{(x_1 - \xi)}{R_{a_1}^2} \right\} + \frac{1}{2\beta^2 r_a^2} I_4$$

$$I_{10} = \int_{-\frac{\Delta x}{2}}^{\frac{\Delta x}{2}} \frac{t dt}{R_a^4} = -\frac{1}{2\beta^2 r_a^2} \left\{ \frac{(x_A - \xi)\frac{\Delta x}{2} + R_{aA}^2}{R_{a_2}^2} + \frac{(x_A - \xi)\frac{\Delta x}{2} - R_{aA}^2}{R_{a_1}^2} \right\} - \frac{(x_A - \xi)}{2\beta^2 r_a^2} I_4$$

where

$$x_1 = x_A - \Delta x / 2$$

$$x_2 = x_A + \Delta x / 2$$

$$R_{a_1}^2 = (x_1 - \xi)^2 + \beta^2 r_a^2$$

$$R_{a_2}^2 = (x_2 - \xi)^2 + \beta^2 r_a^2$$

Approximate formulas, yielding less than 2% error, are used when $\Delta x / R_{aA} \leq 1/2$. Let $\delta = \Delta x / R_{aA}$ and $\tau = (x_A - \xi) / R_{aA}$

$$I_1 = \frac{1}{R_{aA}^2} \delta \left\{ 1 - \frac{1}{8} (-1 + 5\tau^2) \delta^2 \right\}$$

$$I_2 = \frac{1}{R_{aA}^2} \delta^3 (-\tau/4)$$

$$I_3 = \delta^3 / 12$$

$$I_4 = \frac{1}{R_{aA}^2} \delta \left\{ 1 + \frac{1}{12} (-1 + 3\tau^2) \delta^2 \right\}$$

$$I_5 = -\frac{\tau}{6} \delta^3$$

$$I_6 = \frac{1}{R_a^4 A} \delta \left\{ 1 + \frac{5}{24} (-1 + 7\tau^2) \delta^2 \right\}$$

$$I_7 = \frac{1}{R_a^3 A} \delta^3 \left(-\frac{5}{12} \tau \right)$$

$$I_8 = \frac{1}{R_a^2 A} \delta^3 \frac{1}{12}$$

$$I_9 = \frac{1}{R_a^2 A} \delta \left\{ 1 + \frac{1}{6} (-1 + 6\tau^2) \delta^2 \right\}$$

$$I_{10} = \frac{1}{R_a^2 A} \delta^3 \left(-\frac{\tau}{3} \right)$$

When $\delta \leq 1/7$ further approximations may be made:

$$I_1 = \frac{\delta}{R_a^2 A}$$

$$I_2 = I_3 = 0$$

$$I_4 = \frac{\delta}{R_a^2 A}$$

$$I_5 = 0$$

$$I_6 = \frac{\delta}{R_{a_A}^4}$$

$$I_7 = I_8 = 0$$

$$I_9 = \frac{\delta}{R_{a_A}^3}$$

$$I_{10} = 0$$

The formulas given in Equations (H-14) and (H-15) are valid for $r_a > a_o$.
 For $r_a \leq a_o$ simply replace R_{a_A} with \bar{R}_{a_A} and set $\Delta = 0$.

$$\left. \begin{aligned} R_{a_A}^2 &\rightarrow \bar{R}_{a_A}^2 &= (x_A - \xi)^2 + \beta^2 a_o^2 \\ \Delta &\rightarrow 0 \end{aligned} \right\} r_a \leq a_o$$

UNCLASSIFIED

Security Classification

DOCUMENT CONTROL DATA - R&D

(Security classification of title, body of abstract and indexing annotation must be entered when the overall report is classified)

1 ORIGINATING ACTIVITY (Corporate author) Douglas Aircraft Company Long Beach, California		2a REPORT SECURITY CLASSIFICATION UNCLASSIFIED
		2b GROUP N/A
3 REPORT TITLE Subsonic Unsteady Aerodynamics for General Configurations Part II, Vol. I - Application of the Doublet-Lattice Method and the Method of Images to Lifting-Surface/Body Interference		
4. DESCRIPTIVE NOTES (Type of report and Inclusive dates) December 1969 to August 1971		
5 AUTHOR(S) (Last name, first name, initial) J. P. Giesing, T. P. Kalman, W. P. Rodden		
6. REPORT DATE APRIL 1972	7a TOTAL NO OF PAGES 239	7b NO OF REFS 60
8a CONTRACT OR GRANT NO. F33615-70-C-1167	9a ORIGINATOR'S REPORT NUMBER(S) AFFDL-TR-71-5, Part II, Vol. I	
b PROJECT NO 1370	9b OTHER REPORT NO(S) (Any other numbers that may be assigned this report) Douglas Report No. MDC-J0944	
c Task No. 137003		
d		
10 AVAILABILITY/LIMITATION NOTICES Distribution Limited to U.S. Government agencies only; test and evaluation; statement applied in September 1971. Other requests for this document must be referred to AF Flight Dynamics Laboratory, (FY) Wright-Patterson AFB, Ohio 45433		
11 SUPPLEMENTARY NOTES	12 SPONSORING MILITARY ACTIVITY Air Force Flight Dynamics Laboratory Wright-Patterson AFB, Ohio 45433	
13 ABSTRACT <p>A technique for predicting steady and oscillatory aerodynamic loads on general configurations has been developed which is based on the Doublet-Lattice Method and the method of images. Chord- and spanwise loading on lifting surfaces and longitudinal body load distributions are determined. Configurations may be composed of an assemblage of bodies (elliptic cross sections and a distribution of width or radius) and lifting surfaces (arbitrary planform and dihedral, with or without control surfaces). Loadings predicted by this method are required for flutter, gust, frequency response and static aeroelastic analyses and may be used to determine static and dynamic stability derivatives.</p> <p>The methods described in this report are intended to be used by airplane designers to calculate with improved accuracy, the unsteady aerodynamic pressures that act on a lifting surface being propelled at subsonic speeds. The new feature of these calculations is that the effects on the pressure field induced by interference between the fuselage, for example, and the wing or the wing, pylon and nacelle, are taken into account. These calculations are an essential ingredient of flutter analyses and will improve the confidence level of such calculations in preventing wing-store flutter and flutter of advanced vehicles where fuselages are relatively large, provide some lifting capability and cause noticeable interference effects. The general requirement for such calculations are contained in Military Specification MIL-A-8870A(USAF).</p>		

UNCLASSIFIED

Security Classification

14 KEY WORDS	LINK A		LINK B		LINK C	
	ROLE	WT	ROLE	WT	ROLE	WT
subsonic lifting surface theory wing-body interference aircraft flutter dynamic loads analysis nonplanar lifting surface theory vortex lattice doublet lattice fuselage and nacelle loads generalized forces control surface aerodynamic loads oscillatory aerodynamics unsteady aerodynamic loads						
INSTRUCTIONS						
1. ORIGINATING ACTIVITY Enter the name and address of the contractor, subcontractor, grantees, Department of Defense activity or other organization (<i>corporate author</i>) issuing the report.	imposed by security classification, using standard statements such as:					
2a. REPORT SECURITY CLASSIFICATION: Enter the overall security classification of the report. Indicate whether "Restricted Data" is included. Marking is to be in accordance with appropriate security regulations.	<ul style="list-style-type: none"> (1) "Qualified requesters may obtain copies of this report from DDC." (2) "Foreign announcement and dissemination of this report by DDC is not authorized." (3) "U. S. Government agencies may obtain copies of this report directly from DDC. Other qualified DDC users shall request through _____." (4) "U. S. military agencies may obtain copies of this report directly from DDC. Other qualified users shall request through _____." (5) "All distribution of this report is controlled. Qualified DDC users shall request through _____." 					
2b. GROUP: Automatic downgrading is specified in DoD Directive 5200.10 and Armed Forces Industrial Manual. Enter the group number. Also, when applicable, show that optional markings have been used for Group 3 and Group 4 as authorized.						
3. REPORT TITLE: Enter the complete report title in all capital letters. Titles in all cases should be unclassified. If a meaningful title cannot be selected without classification, show title classification in all capitals in parenthesis immediately following the title.						
4. DESCRIPTIVE NOTES: If appropriate, enter the type of report, e.g., interim, progress, summary, annual, or final. Give the inclusive dates when a specific reporting period is covered.						
5. AUTHOR(S): Enter the name(s) of author(s) as shown on or in the report. Enter last name, first name, middle initial. If military, show rank and branch of service. The name of the principal author is an absolute minimum requirement.						
6. REPORT DATE: Enter the date of the report as day, month, year, or month, year. If more than one date appears on the report, use date of publication.						
7a. TOTAL NUMBER OF PAGES: The total page count should follow normal pagination procedures, i.e., enter the number of pages containing information.						
7b. NUMBER OF REFERENCES: Enter the total number of references cited in the report.						
8a. CONTRACT OR GRANT NUMBER: If appropriate, enter the applicable number of the contract or grant under which the report was written.						
8b, & 8d. PROJECT NUMBER: Enter the appropriate military department identification, such as project number, subproject number, system numbers, task number, etc.						
9a. ORIGINATOR'S REPORT NUMBER(S): Enter the official report number by which the document will be identified and controlled by the originating activity. This number must be unique to this report.						
9b. OTHER REPORT NUMBER(S): If the report has been assigned any other report numbers (<i>either by the originator or by the sponsor</i>), also enter this number(s).						
10. AVAILABILITY/LIMITATION NOTICES: Enter any limitations on further dissemination of the report, other than those						
If the report has been furnished to the Office of Technical Services, Department of Commerce, for sale to the public, indicate this fact and enter the price, if known.						
11. SUPPLEMENTARY NOTES: Use for additional explanatory notes.						
12. SPONSORING MILITARY ACTIVITY: Enter the name of the departmental project office or laboratory sponsoring (paying for) the research and development. Include address.						
13. ABSTRACT: Enter an abstract giving a brief and factual summary of the document indicative of the report, even though it may also appear elsewhere in the body of the technical report. If additional space is required, a continuation sheet shall be attached.						
It is highly desirable that the abstract of classified reports be unclassified. Each paragraph of the abstract shall end with an indication of the military security classification of the information in the paragraph, represented as (TS), (S), (C), or (U).						
There is no limitation on the length of the abstract. However, the suggested length is from 150 to 225 words.						
14. KEY WORDS: Key words are technically meaningful terms or short phrases that characterize a report and may be used as index entries for cataloging the report. Key words must be selected so that no security classification is required. Identifiers, such as equipment model designation, trade name, military project code name, geographic location, may be used as key words but will be followed by an indication of technical context. The assignment of links, roles, and weights is optional.						